Universidad Autónoma de Madrid
Departamento de Física Teórica

Two different cases of calorimetry in High Energy Physics: the ATLAS liquid argon electromagnetic end cap and the ZEUS Forward Plug Calorimeter

Memoria presentada para la obtención del título de Doctor en Ciencias Físicas por D. Gastón García López

Director: Luis Labarga Echeverría

Dedicatoria

Esta tesis está dedicada a mi madre, María Isabel, mis hermanos, Pitina y César, mi novia, Luisa y mi sobrino Juan Gastón.

Prologue

Calorimetry plays a key role in high energy physics experiments. Multipurpose detectors installed at large accelerator facilities typically show a layered structure around the interaction point, consisting of three chief components: tracking system, calorimeters and muon chambers. The prime goal of the calorimeters is measuring the energy of the electromagnetic and/or strongly interacting particles (other than muons) produced in the collision. They may also help with particle identification and, provided they have a proper granularity, can be used in order to measure the direction of a particle's three-momentum. Most of the studies that can be done with a multipurpose detector rely to a large extent on calorimeter information.

In order to accomplish the above general goals, various calorimetric devices must operate in a combined way within the same detector. Each of these devices plays a more specific role. This thesis is devoted to two calorimeters which are part of different detectors. They have been designed to operate in very different environments and are devoted to different tasks. However the key concepts lying underneath their operation are essentially the same.

The first device dealt with in this thesis is the ATLAS electromagnetic end cap (EMEC) calorimeter. ATLAS [1] is one of the experiments of the Large Hadron Collider (LHC) at CERN (Geneva). The ATLAS detector has been designed mainly to study the symmetry breaking sector of the Standard Model of elementary particles (SM) and to explore physics beyond the SM (Technicolour, Supersymmetry, etc...). The LHC experiments are planned to be operational by the year 2005. One of the basic requirements set on the detector by the ATLAS physics programme is an excellent energy resolution over a wide energy range for electromagnetic particles (i.e. $e^{\pm}$, γ). The decay $H \rightarrow \gamma\gamma$ can be considered as a benchmark process for electromagnetic calorimetry requirements. This decay channel of the SM Higgs boson is believed to be the cleanest one for a Higgs mass around $130\,GeV$, which is the mass range favoured by indirect measurements. In order to measure directly m_H in this decay channel one has to calculate the invariant mass of the two-photon system. This implies measuring the energy of the two photons and the angle subtended by their three-momentum vectors. An energy resolution at the level of $10\%/\sqrt{E} \oplus 1\%$ [1], where E is the photon energy in GeV, has been estimated to provide enough accuracy in the m_H measurement.

The first of the two terms in the formula shown above dominates the resolution at low and moderate energies, and it is basically driven by the calorimeter composition. The choice for the ATLAS electromagnetic calorimetry was lead combined with liquid argon. The liquid argon (LAr) technique is not new: it was already used for electromagnetic calorimetry by the CELLO experiment at the PETRA e^+e^- collider (Hamburg) and is

[1] The symbol $\oplus$ represents the quadratic sum.

presently used by the H1 experiment at the HERA *ep* collider (Hamburg). The second term in the resolution formula dominates at high energy and it depends on the detector geometry and on mechanical imperfections. In order to push this so called *constant* term below 1%, a novel geometric configuration was developed, known as *accordion* geometry. This concept is based on the strategy of extracting the signal from liquid argon without the need of "cracks" in the calorimeter. In addition to this new geometrical concept, a constant term below 1% can only be reached by pushing the mechanics technology to the limit, so that the calorimeter components are manufactured with the required uniformity and reproducibility properties. Accordion geometry and the accuracy needed imply a challenge for the manufacturing of the calorimeter "building blocks". On the other hand, in order to reconstruct the photon direction, the impact position on the calorimeter must be accurately measured at different depths. This implies that the electromagnetic calorimeter must have some granularity in depth, as well as a very fine granularity in the transverse directions.

The second calorimeter studied in this thesis is the Forward Plug Calorimeter (FPC) of the ZEUS detector. ZEUS [2] is one of the experiments operating at the HERA accelerator, where electrons collide head on against protons at high energy. The main ZEUS calorimeter (UCAL) is made up of uranium and plastic scintillator. The scintillator technique is a very standard one in high energy physics calorimetry (for example the ATLAS experiment itself uses scintillator for hadronic calorimetry). Uranium used as absorber material, when combined with plastic scintillator, has the property of yielding similar signals for the energy deposited by hadrons or electromagnetic particles. This is the so called *signal compensation* that will be explained in detail in chapter 1 below. A *compensating* calorimeter is especially well suited for hadron energy measurement.

The FPC can be regarded as an additional piece "plugged" into the UCAL in order to increase the calorimetric coverage in the forward (proton beam) direction. This update was found to be necessary for a better understanding of the unexpected *deep inelastic scattering* (DIS) events with a *large rapidity gap* first observed by ZEUS (see chapter 6 below). As this extra coverage was not foreseen at the time of the design of ZEUS, an appropiate calorimeter technique for building small, dead area free and low cost hadronic calorimeters was searched for and found: lead-scintillator sampling with longitudinal wave length shifter fiber redout. The FPC was installed within the ZEUS environment in 1998. It uses lead instead of uranium, due to lower cost and easier handling. Lead and scintillator are combined in the FPC in the proper way so as to reproduce as closely as possible the properties of the UCAL. Therefore it is not a device designed for precision measurements, but rather a robust, easy to handle, low cost extension of the more sophisticated UCAL. Its main goal is measuring the energy of hadrons, in combination with the UCAL.

Two different calorimetric techniques for two different physics goals are therefore studied in this thesis: lead-liquid argon with accordion geometry, for a very accurate electromag-

netic energy measurement; lead-scintillator for an acceptable energy resolution, both for hadrons and electromagnetic particles, at reasonably low cost. The author of this thesis was directly involved in Montecarlo (MC) simulation effort, quality control, module construction, beam testing, and beam test data analysis of the EMEC, as well as in beam testing and beam test data analysis of the FPC.

The thesis is organized as follows: chapter 1 introduces the basic concepts of calorimetry in high energy physics; chapters 2- 5 (part I) are devoted to the ATLAS EMEC calorimeter; chapters 6- 7 (part II) deal with the ZEUS FPC; finally chapter 8 compares the performance of the two calorimeters. Further details about the contents of each chapter are given at the beginning of parts I and II. Figures illustrating the text are concentrated at the end of each chapter.

The studies included in this thesis gave rise to the following publications, contributions to conferences and internal documents:

- *"Automatic thickness control system for the ATLAS electromagnetic calorimeter absorber plates", NIM A 418 (1998) 513-521.*
- *"The ZEUS Forward Plug Calorimeter with lead-scintillator plates and WLS fibers readout", DESY 99-194, submitted to NIM.*
- *"The Forward Plug Calorimeter of the ZEUS detector", in Proceedings of the VIII International Conference on Calorimetry in High Energy Physics, ed. World Scientific.*
- *"Construction and beam test of the ATLAS EMEC module-0 calorimeter", proceedings of the XXVII Reunión bienal de la Real Sociedad Española de Física.*
- *"Lead thickness control system for the ATLAS end cap production", ATLAS internal note LARG-NO-069.*
- *"Lead absorber production for the end cap module-0", ATLAS internal note LARG-NO-074.*
- *"Energy signal ϕ-modulation in the liquid argon electromagnetic calorimeter", ATLAS internal note LARG-NO-098.*
- *"Data analysis of the ATLAS EMEC module-0 calorimeter September 1998 beam test", ATLAS internal note LARG-99-017.*
- *"Data analysis of the Forward Plug Calorimeter Beam Test at CERN", Memoria presentada para la obtención del grado de Licenciado en Ciencias Físicas.*
- *"Test of a FPC prototype at DESY", ZEUS note 98-068.*
- *"Data analysis of the ZEUS Forward Plug Calorimeter Beam Test at CERN", ZEUS note 2000-001.*

Contents

1 Review of calorimetry **11**

1.1 Sampling calorimeters 11

1.2 Electromagnetic showers 12

1.2.1 Shower generation 12

1.2.2 Energy resolution 15

1.3 Hadronic showers 18

1.3.1 Compensation in hadronic showers 19

1.3.2 Energy resolution 19

I The module-0 of the electromagnetic end cap liquid argon calorimeter of the ATLAS detector **21**

2 The ATLAS experiment: the liquid argon EMEC **25**

2.1 Physics programme of the ATLAS experiment 25

2.2 Detector requirements 26

2.2.1 General requirements 27

2.2.2 Requirements on electromagnetic calorimetry 27

2.3 Overview of the ATLAS detector 28

2.3.1 The magnet system 28

2.3.2 The inner detector 28

2.3.3 Muon spectrometer . . . 29
2.3.4 ATLAS calorimetry . . . 29
2.4 The liquid argon electromagnetic calorimeter . . . 30
2.4.1 Barrel calorimeter overview . . . 31
2.4.2 The EMEC calorimeter . . . 31
2.4.3 Mechanical components of the EMEC calorimeter . . . 32
2.4.4 Read out electronics . . . 35

3 Expected performance of the EMEC 49
3.1 Energy resolution . . . 49
3.2 Position resolution . . . 50
3.3 Signal dependence on high voltage across the gap . . . 50
3.4 ϕ-modulation . . . 51
3.4.1 Introduction . . . 51
3.4.2 Data sample . . . 52
3.4.3 Fourier polynomials: a natural choice for the parametrization . . . 52
3.4.4 Results for the end cap outer wheel . . . 53
3.4.5 Results for the barrel . . . 54
3.4.6 Energy dependence of ϕ-modulation . . . 55
3.4.7 Modulation with different windows . . . 56
3.4.8 Conclusions on ϕ-modulation . . . 56

4 Construction and quality control of module-0 69
4.1 Strategy for the quality control of the absorbers . . . 69
4.1.1 Introduction . . . 69
4.1.2 X-ray lead thickness control system . . . 70

4.1.3 Description of the ultrasound control system for the lead thickness . . . 71
4.1.4 Calibration of the ultrasound system . . . 72
4.1.5 Stability of the ultrasound device . . . 76
4.1.6 Control of the finished absorber geometry . . . 78
4.1.7 Conclusion on dimensional control of absorbers . . . 80
4.2 The absorbers produced for module-0 . . . 80
4.2.1 Introduction . . . 80
4.2.2 Lead thickness measured with ultrasounds . . . 81
4.2.3 Cross-check of X-ray and ultrasound thickness measurements . . . 84
4.2.4 Conclusions on thickness measurements . . . 86
4.2.5 Results on the dimensional control of the geometry of the finished absorber . . . 87
4.3 The EMEC module-0: from assembly site to test beam area . . . 89
4.3.1 Module assembly . . . 89
4.3.2 Module manipulation and transport . . . 89
4.3.3 Installation in the cryostat, cabling and read out system tests . . . 90
4.3.4 High voltage tests . . . 91

5 Beam test of the EMEC module-0 113
5.1 Introduction . . . 113
5.2 Description of the EMEC module . . . 113
5.3 Beam test set up and data taken . . . 114
5.3.1 Setup . . . 114
5.3.2 Data taken . . . 115
5.3.3 Known detector problems . . . 116
5.4 Signal reconstruction . . . 117
5.4.1 Introduction . . . 117

5.4.2 The non parametric technique for pulse shape reconstruction 118
5.4.3 The NPLF formula 118
5.4.4 Determination of t_{max} 119
5.5 Calibration 122
5.5.1 Electronics calibration with test pulse runs 122
5.5.2 Calibration with beam data 122
5.6 Event selection and energy signal systematics 130
5.6.1 Event rejection due to DAQ misfunctioning 130
5.6.2 Fine tuning T_{tdc} correction 131
5.6.3 ϕ-modulation 131
5.6.4 η dependence of the energy signal 133
5.6.5 Energy signal dependence on the shower longitudinal profile 134
5.7 Energy resolution and linearity 137
5.7.1 Noise calculation 137
5.7.2 Energy resolution and linearity for the region $\eta = 2.2$ 139
5.7.3 Energy resolution and linearity for the region $\eta = 1.55$ 141
5.7.4 Energy resolution and linearity for the region $\eta = 2.9$ 142
5.8 Position reconstruction 143
5.8.1 Reconstruction of ϕ 144
5.8.2 Reconstruction of η 147
5.9 Energy signal dependence with the HV setting 151
5.10 Time reconstruction 152
5.10.1 Introduction 152
5.10.2 Time resolution 152
5.11 Momentum spread of the test beam 153
5.12 Conclusions on the beam test of module-0 154

II The Forward Plug Calorimeter of the ZEUS detector 205

6 The FPC in the ZEUS environment 209
6.1 Description of the ZEUS detector 209
6.2 Diffractive physics with the ZEUS detector at HERA 211
6.2.1 Kinematics of deep inelastic scattering 211
6.2.2 Kinematics of diffractive DIS 213
6.2.3 Models for diffractive DIS 214
6.2.4 Contribution of the FPC to diffractive physics at ZEUS 215
6.3 Description of the FPC and performance requirements 216
6.4 Construction of the FPC 218

7 Beam test of the FPC 223
7.1 Set up, data taken and signal processing 223
7.1.1 Beam test set up 223
7.1.2 The data taken during the test 224
7.1.3 Signal processing 225
7.2 Calibration 225
7.2.1 Calibration of the EMC and HAC section 225
7.2.2 Calibration cross-check with pion data 226
7.3 FPC performance with an electron beam 227
7.3.1 Uniformity 227
7.3.2 Linearity 227
7.3.3 Energy resolution 228
7.3.4 Shower width 230
7.3.5 Position reconstruction 231
7.4 FPC performance with pions 232

7.4.1 Linearity 233
7.4.2 Energy resolution 233
7.4.3 Position reconstruction 235
7.5 Conclusions on the beam test of the FPC 236

8 Global comparison between the two calorimeters 255
8.1 Energy resolution for electromagnetic showers 255
8.2 Position resolution for electromagnetic showers 256
8.3 Conclusion 257

Chapter 1

Review of calorimetry

In this chapter an overview of the principles of calorimetry in high energy physics is given. First the concept of *sampling calorimeter* will be explained and then the so called *particle showers*, in their two kinds (electromagnetic and hadronic) will be described.

1.1 Sampling calorimeters

Calorimeters currently used in high energy physics are either *homogeneous* or *sampling*. Homogeneous calorimeters consist of a single material, such as lead glass, NaI, BGO, etc... When a fast particle enters the acceptance volume of a homogeneous calorimeter its energy degrades and generates a measurable signal. On the contrary, the tasks of absorbing the incident energy and generating a signal are, in sampling calorimeters, done by two different materials: the *passive* material (Fe, Cu, Pb, U, etc...) plays the role of energy absorber, whereas the *active* material (scintillating plastic, LAr, silicon) gives rise to the signal. This work is focused on sampling calorimeters.

The two materials present in a sampling calorimeter are tipically arranged in successive layers, so that the incident particle and the secondary ones generated by its interaction with the detector, cross alternatively regions of active and passive material as they go deeper and deeper into the detector. The interaction just mentioned usually produces a so called *shower* of secondary particles in which the energy carried is degraded and part of it detected. Particle showers will be described in 1.2 and 1.3.

The principles of the shower generation are of statistical nature. Therefore the fraction of energy that an incident particle leaves inside the active medium can be regarded as a random variable, subject to fluctuations. The geometry of a calorimeter can be very complicated. For the sake of simplicity one can consider the simplest plane-parallel layered

structure as an example. In any case, the signal generated by an incident particle must be, on average, proportional to its original energy.

In order to gain some insight into the features of the energy signals generated in a sampling calorimeter, it is necessary to describe particle showers. Two types of showers can be distinguished: *electromagnetic* and *hadronic*.

1.2 Electromagnetic showers

We call electromagnetic showers to those generated by an electron, positron or photon reaching a calorimeter. In this paragraph the mechanism of shower generation and the resolution achievable in an energy measurement involving an electromagnetic shower are discussed.

1.2.1 Shower generation

Several mechanisms contribute to the energy loss of electrons and photons incident on matter. However at high energies (well above $10\,MeV$) the fraction of energy lost per unit depth of material is almost energy independent and only due to brehmesstrahlung (electrons or positrons) and pair creation (photons). The secondary particles produced in the cascade carry successively less energy until they reach the range where several other effects become important. If the whole shower is absorbed inside the calorimeter, the energy deposited is obviously equal to that of the primary particle.

For electrons and positrons the processes that become relevant in the sub-GeV range are Bhabha and Compton scattering and ionization. Positrons in addition suffer annihilation. Ionization is in fact the dominant process and the reason why all particles finally get absorbed. For photons the Compton and photoelectric effect are the ones that compete with pair production at low energies.

At high energies ($E > 1\,GeV$) the absorption can thus be characterised in a material-independent way by introducing the so called *radiation length* (X_0) of the substance. It is defined as the material thickness to be travelled by an electron so that it looses on average 63.2% of its energy through brehmesstrahlung; i.e. the electron energy decreases by a factor $1/e$ each radiation length. This obviously means that the typical shower particle energy at a given depth z is

$$E = E_0 \cdot e^{-\frac{z}{X_0}} = E_0 \cdot e^{-t}$$

where E_0 is the initial energy of the incident electron or positron. Obviously t is the depth measured in units of X_0.

At low energies, energy losses are dominated by collisions. The *critical energy* ϵ_0 of a material is the energy value at which the mechanisms of brehmesstrahlung and ionization are equally important. It represents the limit where the growth of the shower stops and the particle multiplicity starts to decrease. Its value in MeV is given approximately by [3]:

$$\epsilon_0 = \frac{550}{Z}$$

This approximation is accurate to 10% for an atomic number $Z > 13$.

A very simplified model of shower developement can provide some insight into electromagnetic calorimetry, assuming that the only dominant processes at high energies are brehmesstrahlung and pair production and describing these two mechanisms by asymptotic formulae.

An electron entering a calorimeter with energy E much larger than the critical energy ϵ_0, after having crossed one radiation length of material (X_0), will have lost 63% of its initial energy into photons. We can say that on average the photon and the electron will carry each half of the original energy, $E/2$. After another radiation length of material the photon will create an e^+e^- pair and the electron will emit another brehmesstrahlung photon. The energy of each of the four particles will be on average $E/4$. The multiplication process proceeds. When the shower particles reach an energy below ϵ_0 they are completely absorbed by collisions and the shower terminates. The model is equally valid if the original particle is a photon, except for a small shift in depth.

The number of particles doubles after each radiation length. Therefore at a depth t (in units of X_0) the number of shower particles is

$$N = 2^t$$

The mean energy of a particle will then be

$$\epsilon = \frac{E}{N} = E \cdot 2^{-t}$$

The depth at which the mean energy ϵ equals the critical energy ϵ_0 is where the shower reaches its maximum particle multiplicity and it is

$$t_{max} \simeq \frac{ln\,(E/\epsilon_0)}{ln2} \tag{1.1}$$

The average total distance covered by all the particles of the shower is called the average *total track length* T. Since each particle travels on average a distance X_0 before splitting into two, the quantity T, in units of X_0, is equal to the total number particles in the shower.

As the showering process occurs, a small part of the energy is lost by ionization and this fraction is proportional to the total track length, because each energetic particle of the shower deposits an amount of energy per unit length independent of the energy it carries. That is:

$$E_{visible} = E_{ionization} \propto T = \frac{E}{\epsilon_0}$$

This linear relation between the incident energy and the total track length or energy loss by ionization makes calorimeters useful devices.

In general not the whole track length will be detectable, but only a fraction of it, T_d, will give some signal which can be seen. Only shower particles above a certain energy threshold η will be detected, so we can write

$$T_d \simeq F(\eta) \cdot T = F(\eta) \cdot \frac{E}{\epsilon_0}$$

In order to ensure the full containment of the shower in the calorimeter, experimental and calculational information can be used [4]. The length necessary to ensure a 98% energy shower containment can be parametrized as

$$< L_{98\%} > \simeq t_{max} + 4\lambda_{att}$$

where the quantity λ_{att} comes from the exponential decay of the shower energy density deposition (following $e^{-z/\lambda_{att}}$) after reaching the maximum. This λ_{att} turns out to be approximately energy-independent and can be characterized in terms of the radiation length as $\lambda_{att} \simeq (3.4 \pm 0.5)X_0$. Notice that the depth necessary for a calorimeter to fully contain and measure a shower grows only *logarithmically* with the energy (see eq. 1.1).

1.2.2 Energy resolution

The processes of energy deposition, detection and read out are of statistical nature. The relative precision of the energy measurement is

$$\frac{\sigma\,(E_{visible})}{E_{visible}}$$

Intrinsic fluctuations

Two kinds of uncertainties enter the energy measurement. First, the showering is in itself a statistical process, of almost gaussian character. Landau fluctuations [5] due to ionization processes with large energy transfer to the electrons of the detector material, lead to asymmetric spectra. They are however not quantitatively significant in the case of the ATLAS or ZEUS detector.

The visible energy is, as shown above, proportional to the number of particles produced (N), but also to the number detected (N_d). Both are large numbers that will follow normal distributions (based on large number theory). The standard deviation will thus scale as $\sigma \sim \sqrt{N}$. Then

$$\frac{\sigma(E)}{E} \sim \frac{\sigma(N_d)}{N_d} = \frac{\sqrt{N_d}}{N_d} = \frac{1}{\sqrt{N_d}} \sim \frac{1}{\sqrt{E}}$$

The relation stated above sets a lower limit to the accuracy of the energy measurement, i.e. the *intrinsic fluctuations*. The best homogeneous calorimeters made of scintillating crystals or noble liquids achieve energy resolutions of order $\sigma/E \simeq 1\%/\sqrt{E}$ [4].

Sampling fluctuations

In the case of a sampling calorimeter only the fraction of the particle tracks that is inside the active part will contribute to the visible signal. Let d be the distance in radiation lengths separating two consecutive active layers. Then the number of sampled tracks is

$$N_s \simeq \frac{T_d}{d}$$

Replacing T_d we get

$$N_s \simeq F(\eta) \cdot \frac{E}{\epsilon_0 \cdot d}$$

Being proportional to E, the number of crossings also follows gaussian statistics. Thus

$$\frac{\sigma(N_s)}{N_s} = \frac{1}{\sqrt{N_s}}$$

The energy resolution can be parametrized [6] as

$$\left(\frac{\sigma_E}{E}\right)_{sampling} \simeq 3.2\% \sqrt{\frac{d}{X_0}\frac{\epsilon_0\,[MeV]}{E\,[GeV]}} = R\sqrt{\frac{d\,[X_0]}{E\,[GeV]}} \tag{1.2}$$

where d is the thickness of the passive material layers and R is a constant that depends on the passive material chosen. The formula above must be corrected for multiple scattering. Once the passive material is fixed, this correction can be reabsorbed by the constant R.

It is very instructive to observe that, for layered lead-based calorimeters, like the ATLAS EMEC and the FPC, the contribution of sampling fluctuations to the energy resolution scales like

$$\left(\frac{\sigma_E}{E}\right)_{sampling} \sim \sqrt{\frac{d}{E}}$$

Therefore increasing d from 1.7 to 15 mm [1] should lead to a deterioration of the sampling component of the energy resolution by a factor of 3 . We will see in chapter 8 below that this rough calculation is not far off the experimental result.

Fluctuations due to the signal read out

A very important statistical contribution can be due to the conversion of the energy signal into electrical current or voltage. This is the case of the ZEUS uranium calorimeter, and also of the FPC (see part II), in which the energy signal consists of photons emmited by the scintillator. In the FPC these photons are captured by wavelength shifting (WLS) fibers and reemitted at a different wavelength, optimal for photomultiplier (PMT) operation. The fibers guide the photons to the PMTs. At the photocathode each photon

[1] As will be explained later in this thesis, these are the nominal thicknesses of the lead layers in the EMEC and FPC, respectively.

excites an electron with a certain probability, due to the photoelectric effect, leading to an electron avalanche in the subsequent dinodes and generating at the anode a measurable charge pulse. All these processes are statistical in nature and therefore they generate contributions to the energy measurement uncertainty called *photostatistics fluctuations*. These fluctuations are governed by Poisson statistics, the mean signal being proportional to a (discrete) number of elementary processes. In the case we are discussing this discrete number is, at different stages of the read out chain, the average number of photons generated in the scintillator, the number of electrons excited in the photocathode or the number of electrons of which the pulse at the anode consists. At any of these stages, let N_p be the average number of elementary processes. Then the fluctuations (the sigma measured in units of the mean value) are given by [2] $1/\sqrt{N_p}$. It is obvious that the fluctuations that dominate are those corresponding to the stage where N_p is smallest. For the FPC N_p is a very large number for all the stages except for the electron excitation at the photocathode ($N_p \sim 100$ per GeV of the incident particle energy). Therefore the fluctuations are important. In LAr calorimetry the smallest N_p corresponds to the number of electrons generated in LAr, that drift to the read out electrode. This number is very large. Fluctuations of this type scale as $\sim 1/\sqrt{E}$.

Other fluctuations. Summary

Another important contribution to the degradation of the energy resolution is added by the design and mechanical imperfections. Some examples are: leakage due to finite calorimeter depth, signal non-uniformities, etc...

Non-uniformities and mechanical imperfections in general, do not follow the same scaling law as the sampling and photostatistics fluctuations, generating a constant term that dominates the energy resolution at high energies.

To sum up, the energy resolution of a sampling calorimeter can be parametrized by the formula [3]

$$\frac{\sigma_E}{E} = \frac{a}{\sqrt{E}} \oplus b$$

This parametrization will be used for energy resolution studies throughout the thesis.

[2] Let μ be the mean of a Poisson distribution. Then the variance is $\sigma^2 = \mu$. Therefore $\sigma/\mu = 1/\sqrt{\mu}$.
[3] Electronics noise is not taken into account at this stage.

1.3 Hadronic showers

Particles subject to the strong interaction, i.e. hadrons, also produce showers when entering a calorimeter. In contrast to the electromagnetic case, in which a few processes dominate over all others, many channels compete, approximately on equal foot, in the developement of hadronic showers. This fact brings about large variations in the deposited and visible energy.

The main component of the hadronic shower developement is given by inelastic scattering of particles with the nuclei of the absorber material. This and other processes taking place, are very hard to describe analytically. Modelling hadronic showers is difficult and calculations are only possible with MC methods and parametrized experimental results. Here only a brief description of the phenomena leading to the hadronic shower generation and developement will be given. For a more detailed explanation see [3] and [7]. Some calculational methods can be found in [8], [9] and [10].

The hadron's energy is lost in inelastic collisions and carried away by some of the nucleons or secondary hadrons produced. If their energy is larger than the nuclear binding energy, they will leave the nucleus, predominantly in the forward direction, and collide with other nuclei repeating the process. The time scale characterizing this process is 10^{-22} s. After this period of time photons are produced by nucleon deexcitation. These photons give rise to small electromagnetic showers inside the hadronic one. Also the decay of π^0 particles gives rise to an electromagnetic component inside the hadron shower.

In total some 300 different reactions occur in the developement of a hadronic shower, each contributing comparably to the global process. Event to event statistical fluctuations are much larger than in the electromagnetic case, setting limits to the resolution achievable in the hadron energy measurement.

To describe hadronic showers in a material-independent way the quantity λ (nuclear interaction legth) is introduced, in a similar way to the radiation length for electromagnetic showers, i.e. λ is the depth at which an incoming hadron will have dissipated on average 63% of its initial energy.

Hadronic showers have much larger longitudinal and transverse dimensions than electromagnetic ones. As a reference, in a lead-based calorimeter the hadronic shower is roughly five times deeper and wider than the electromagnetic one.

1.3.1 Compensation in hadronic showers

The fraction of deposited energy which is rendered visible in the calorimeter is typically smaller for hadronic than for electromagnetic showers. This is mainly due to the larger amount of energy lost in breaking nuclei (nuclear binding energy). In addition to this, passive materials with high mass number, lead to the generation of many neutral particles, that produce less signal in the active medium.

This fact leads to smaller visible signals for hadrons than for electrons of the same energy. The so called e/h ratio is smaller than 1. Therefore the electromagnetic component of the hadronic shower yields larger signals than the purely hadronic part, resulting in a larger spread of the global measured response. The effect can be minimized by achieving an e/h ratio equal to unity. This is the so called *compensation* of the signals. Using uranium as passive material helps in compensating the losses in the hadronic shower [11], due to the fact that neutrons induce fission of uranium nuclei, leading to an additional contribution to the energy deposition. However a compensating calorimeter can also be obtained with lead, provided the layers of active and passive material have the proper thickness relative to each other [12]. The FPC is designed to be a compensating calorimeter.

1.3.2 Energy resolution

The same parametrization proposed for electromagnetic showers is used for the hadron energy resolution, i.e.

$$\frac{\sigma_E}{E} = \frac{a}{\sqrt{E}} \oplus b$$

In this case the sampling term coefficient a is usually much larger than for electromagnetic showers.

Part I

The module-0 of the electromagnetic end cap liquid argon calorimeter of the ATLAS detector

This first part starts with an overview of the ATLAS detector and a closer look at the LAr electromagnetic (EM) calorimeter, with special emphasis on the end cap part (chapter 2). Chapter 3 summarizes some studies about the performance of the EM calorimeter, done before the beam test of the module described in this thesis, which are based on both MC and prototype test beam results, including a detailed study of the so called ϕ-modulation effect. Chapter 4 is devoted to the construction process of the EMEC module-0. Special attention is paid to the quality control of the lead absorber plates. Finally chapter 5 deals with the beam test of the EMEC module-0 done at CERN in September 1998.

Chapter 2

The ATLAS experiment: the liquid argon EMEC

ATLAS is one of the experiments of the Large Hadron Collider (LHC), where two proton beams of $7 TeV$ each will collide head on at different points of the ring. This chapter is devoted to introducing the topic of electromagnetic calorimetry of the ATLAS detector. To this this end, we start with a review of the physics programme of the ATLAS experiment (section 2.1). This leads in a natural way to detector requirements, which is the topic of section 2.2. Requirements on electromagnetic calorimetry are described in more detail than for the rest of the detector components. Once we have gone through what we want to do in the ATLAS experiment and what type of detector is needed for that purpose, section 2.3 presents the solution adopted by the ATLAS collaboration, giving a very general description of the ATLAS detector. Electromagnetic calorimetry is described in further detail in section 2.4.

2.1 Physics programme of the ATLAS experiment

The LHC offers a wide range of physics opportunities. The most important ones can be classified into three groups:

- Study of the origin of mass at the electroweak scale.
- Detailed study of the top and bottom quarks.
- Search of new physics: supersymmetry, technicolour, heavy gauge bosons, compositeness, etc...

For the rest of the section we focus on the first of these topics, which has been taken as a major guideline for detector design.

Within the framework of the Standard Model (SM) of elementary particles, the origin of the particle masses is due to the existence of a scalar field which couples to fermions and massive gauge bosons. The model predicts the existence of a scalar particle, namely the Higgs boson, whose mass may in principle have a value over a wide range. On the other hand and on general grounds, one can say that all theories that generalize the SM, predict the existence of one or several particles at the electroweak scale which play the role of the SM Higgs boson. One of the main goals of the LHC multipurpose experiments and, in particular, of ATLAS, is the discovery of the particle or particles that lie at the heart of the origin of mass.

Focusing on the SM Higgs (H), the different production and decay channels which are expected to be the most fruitful ones for discovery, depend on the Higgs mass (m_H):

- $pp \to WH, ZH, t\bar{t}H,\ H \to b\bar{b}$ for $80 < m_H < 100\,GeV$.
- $H \to \gamma\gamma$ for $90 < m_H < 150\,GeV$.
- $H \to ZZ^* \to 4\ell$ for $130\,GeV < m_H < 2m_Z$.
- $H \to ZZ \to 4\ell, 2\ell 2\nu$ for $m_H > 2m_Z$.
- WW, ZZ fusion with $H \to ZZ, WW \to \ell\nu 2jets$ for m_H up to $1\,TeV$.

Assuming the correctness of the SM, the value of the Higgs mass can be determined by combining the measured masses of the W boson and the t quark. However the dependence of m_H on these parameters is logarithmic. Therefore this indirect determination of m_H has a large uncertainty. The mass value preferred by this indirect mesurement is between 100 and $200\,GeV$. On the other hand the latest Higgs search results from LEP experiments [13] exclude masses below $95\,GeV$. The channel $H \to \gamma\gamma$ is therefore extremely important. Since the final state consists of neutral electromagnetic particles, the observation of this decay channel relies almost completely on the electromagnetic calorimeter.

2.2 Detector requirements

In order to cope with the physics programme outlined above, the ATLAS detector must meet stringent requirements, a summary of which is presented in this section, with emphasis on electromagnetic calorimetry.

2.2.1 General requirements

The basic design considerations for ATLAS can be summarized as follows:

- Very good electromagnetic calorimetry for electron and photon identification and measurement.
- Hermetic jet and missing E_T calorimetry.
- Efficient tracking at high luminosity for lepton momentum measurement, heavy flavour tagging and vertex reconstruction.
- Precision muon momentum measurement up to highest luminosity.

2.2.2 Requirements on electromagnetic calorimetry

For electromagnetic calorimetry the general requirements proposed above translate into specific constraints, some of which are listed and briefly explained below:

- **Rapidity coverage**. Due to the heavy radiation load expected in the more forward detector regions, precision calorimetry will cover up to pseudorapidity [1] $|\eta| < 2.5$. More robust calorimetric devices, with coarser granularity, extend the coverage up to $|\eta| \simeq 5$.
- **Electron reconstruction capability from $1\,GeV$ to $5\,TeV$**. The lower limit comes from the need of reconstructing electrons from b quark decay. The upper one is set by heavy gauge boson decays.
- **Excellent energy resolution over the range $10 - 300\,GeV$**. This is needed to achieve a 1% mass resolution for the $H \to \gamma\gamma$ in the range $90 < m_H < 180\,GeV$ [1]. For this the sampling term of the electromagnetic calorimeter should be at the level of $10\%/\sqrt{E[GeV]}$ and the constant term should be below 1%.
- **Accurate measurement of the shower position**. The photon direction must be accurately reconstructed for the invariant mass measurement in $H \to \gamma\gamma$ decay. Shower position along the ϕ direction [2] can be reconstructed accurately by combining calorimeter information with the knowledge of the transverse beam position, which will have a spread of order $25\,\mu m$. However the longitudinal spread of the interaction

[1] Pseudorapidity is defined as $\eta = -ln\,tan\theta/2$, where θ is the polar angle w.r.t. the beam axis.
[2] ϕ is the azimuthal angle, taking the z-axis along the beam line.

point will be of order $6\,cm$. The EM calorimeter should thus be able to measure the θ component of the photon direction in a standalone way. In order to achieve the discovery target of 1% in mass resolution, the precision in θ should be of the order of $50\,mrad/\sqrt{E[GeV]}$. This implies having fine transverse granularity and some longitudinal segmentation.

- Excellent γ/jet, e/jet, τ/jet separation, which requires again high transverse granularity and longitudinal segmentation.

2.3 Overview of the ATLAS detector

In order to undertake the physics programme outlined in 2.1, according to the requirements established in 2.2 and after an intensive R&D effort, the ATLAS collaboration has arrived at a final detector design, summarized in this section. The evolution of the detector design can be followed along the benchmark documents: Letter of intent (1992) [14], Technical proposal (1994) [1] and the several Technical design reports (starting in 1996) [15], [16]. The ATLAS detector consists of an inner detector (ID), calorimeters, muon spectrometer and magnet system. These four components are described in the following subsections. A view of the ATLAS detector is given in Fig 2.1.

2.3.1 The magnet system

The magnet system consists of an inner solenoid around the ID cavity and a set of large air-core toroids, consisting of independent coils arranged with an eight-fold symmetry outside the calorimeter system. All magnets are superconducting. This layout of the magnet system allows to have a high-resolution, large-acceptance and robust muon spectrometer, whereas almost no constraints are imposed on the ID and calorimeter.

2.3.2 The inner detector

The ID is contained in a cylinder of length $6.8\,m$ and radius $1.15\,m$, within a magnetic field of 2 T provided by a solenoid. The innermost part is devoted to high precision tracking, provided by silicon pixel detectors. These are arranged in a barrel part with two layers, and four disks on each forward direction. Four additional barrel layers with silicon strips complement the precision measurement. In each of the forward directions two GaAs disks and 12 micro strip gas counters (MSGC) are also present.

Pattern recognition is provided by straw tube tracking detectors (TRT), that envelope the innermost Si and GaAs detectors. The TRTs allow for continuous track-following with less material. In addition to this, the electron identification capabilities of the ID are enhanced by the detection of transition radiation photons in the straw tubes.

The layout of the ID provides full tracking coverage for $|\eta| < 2.5$, including impact parameter measurement and vertexing for heavy flavour and τ tagging. The measurement of the secondary vertex will be more precise during the initial low luminosity run due to the inclusion of an additional layer of silicon tracking detectors, closer to the beam pipe than the ones mentioned previously.

Some typical values for the amount of dead material present in front of the calorimeter due to the presence of the ID are: 0.185 X_0 at $\eta = 0.0$ (center of barrel), 0.46 X_0 at $\eta = 2.0$ (center of end cap outer wheel), 0.27 X_0 at $\eta = 2.5$ (transition between outer and inner wheel).

2.3.3 Muon spectrometer

The muon spectrometer defines the overall dimensions of the ATLAS detector. The outer chambers of the barrel part are at a radius of $11\,m$ and the last forward chambers are $21\,m$ away from the interaction point (IP).

In the barrel region ($|\eta| < 1.1$) there are three layers of muon chambers, placed at the inner and outer edges of the volume with magnetic field and in the mid-plane. In the forward directions there are two chamber layers at the front and back faces of the toroidal magnet system and a third one against the cavern wall, in order to maximize the lever arm for the point-angle measurement.

Each of the muon chambers consists of two multilayers of detectors, mounted on either side of a support structure. The basic measurement in each muon chamber is therefore a track segment, providing a vector for robust pattern recognition and momentum determination.

The momentum resolution of the muon spectrometer relies heavily on the alignment of the chambers. The goal is to achieve an accuracy of $50\,\mu m$ for the muon sagittas.

2.3.4 ATLAS calorimetry

Fig 2.2 gives an overview of the ATLAS calorimetry. It consists of an inner barrel cylinder and end caps, using LAr technology, surrounded by a hadronic scintillator tile calorimeter (TILECAL).

The barrel part of the LAr calorimetry is an electromagnetic (EM) accordion calorimeter including a presampler. The LAr end cap cryostats include an EM accordion calorimeter (EMEC) with presampler, a hadronic calorimeter with flat absorber plates and a forward calorimeter with a tube electrode structure.

The LAr accordion calorimeter (end cap and barrel) will be described at depth in section 2.4, with special emphasis on the EMEC.

Each of the two end cap hadronic calorimeters consists of two wheels, made up of 32 modules each. Copper absorber plates alternate with LAr gaps, filled with an electrode structure forming an electrostatic transformer read out scheme. The total active thickness (including the EMEC) is about 13 λ.

The LAr forward calorimeters must work in an extreme particle and energy flux environment. For the front module (EM) the speed and radiation hardness required are achieved with a metallic tube and rod electrode structure with a LAr gap of only 250 μm, embedded in a copper absorber. For the two hadronic modules tungsten alloy absorbers are used. The λ of tungsten is about half that of copper or iron. This fact reduces the transverse spread of the hadronic shower. The total active depth is 10 λ, to which an additional passive tungsten shielding of 2 λ is added in order to reduce punch-through into the forward muon detectors.

The hadronic TILECAL is a sampling calorimeter, using plastic scintillator tiles as active and iron as passive material. The tiles are placed in planes perpendicular to the beam axis and staggered in depth, simplifying mechanical construction and fiber routing. The TILECAL consists of a barrel and one extended barrel on either side. Each of these three parts is made up of 64 sector modules. The active depth (including the EM accordion) is about 9.5 λ at $\eta = 0$, followed by a passive iron shielding of 1.5 λ.

2.4 The liquid argon electromagnetic calorimeter

The ATLAS LAr calorimetry is housed into three cryostats. The central one contains the barrel EM calorimeter as well as the 2 T superconducting solenoid, being mechanically supported by the barrel part of the TILECAL. Each end cap cryostat contains the EMEC, the hadronic calorimeter and the three forward calorimeter modules. In this case mechanical support is provided by the extended barrels of the TILECAL. One half of the LAr calorimeter can be seen in Fig 2.3.

2.4.1 Barrel calorimeter overview

A perspective of one half of the barrel cryostat is given in Fig 2.4. The cryostat is 6.8 m long and has an outer radius of 2.25 m. The radius of the inner cavity is 1.15 m. The shells are made of aluminum alloy with vacuum insulation.

From the mechanical point of view the barrel calorimeter is subdivided into two identical half barrels, with a gap of a few millimeters in between. Each half barrel consists of 1024 absorbers. Between two consecutive absorbers there is a read out electrode. Both the absorbers and read out electrodes are arranged with an accordion geometry, sketched in Fig 2.5. Therefore a straight track coming from the IP traverses many times the same absorber.

Projective cells are defined in η by etching the read out electrodes. In the ϕ direction read out cells are built by adding up together the signals of several consecutive electrodes (four, for the central towers). Connections are made at the inner and outer face of the calorimeter using the so called *summing boards* and *motherboards*. The latter carry the calibrating element (one resistor per channel). Both read out and calibration cables are routed out of the cryostat using *feedthroughs*. Electronics boxes including all the read out elements up to the ADCs [3] are located at the warm side of the feedthroughs.

2.4.2 The EMEC calorimeter

Fig 2.6 shows one end cap cryostat, housing the two hadronic sections and forward calorimetry, apart from the EMEC. The cryostat is built of aluminium and is vacuum insulated. The outer radius is 2.25 m (the same as for the barrel) and the length is 3.17 m. The cryostat wall in front of the EMEC amounts to one radiation length.

A closer look at one EMEC is taken in Fig 2.7. Each of the two EMECs is divided into two parts: inner wheel, covering the pseudorapidity interval 2.5-3.2; and outer wheel, spanning 1.4-2.5. Both the inner and outer wheel consist of consecutive layers absorber-LAr-electrode-LAr..., as one moves along the azimuthal angle direction. There are 768 electrodes-absorbers in the outer wheel and 256 in the inner wheel. Fig 2.7 shows only a few absorbers to give an idea of the geometry, which is very complicated: the angle of the folds varies continuously with the radius, the angles becoming more and more acute as we approach the barrel. Notice in Fig 2.6 the relative dimensions of the inner and outer wheel. The latter is much more delicate from the mechanical point of view, due to the larger dimensions of the absorbers and electrodes. Notice, as well, that the two wheels are not mechanically separated.

[3] Analog to digital converters.

From the mechanical point of view, each end cap is divided into eight sector modules, each constructed separately. The eight sectors of a wheel will be finally assembled together at CERN. In Fig 2.8 one of the eight modules forming each EMEC is shown. The module tested with a particle beam at CERN in September 1998 was like this. It will be referred to as *module-0*.

2.4.3 Mechanical components of the EMEC calorimeter

Apart from the support structures, the elementary building blocks of the EM calorimeter are its absorber plates and electrodes. This section describes both for the end cap case. Most of the explanations can be easily applied to the barrel by changing numbers.

Absorbers

As it will be explained in further detail in chapter 4, extensive MC simulations have shown that, in order to achieve a constant term in the energy resolution below 1%, the dispersion in the lead absorber thickness cannot be larger than 1% of the nominal value. The uniformity of the LAr gap must also hold at the level of 100 μm. The latter cannot be achieved unless lead plates are supported by a more rigid material. That is why absorbers are made with a stainless steel-prepreg-lead-prepreg-stainless steel sandwich. The prepreg layers keep the steel and lead plates together and provide, after polimerization, the proper rigidity. The absorbers are equipped with side bars (along the constant ϕ direction), used to support them on the structure rings. Also a transverse bar is attached to the acute side of the absorbers.

Two different types of absorbers are needed for the EMEC: large absorbers for the outer wheel (Fig 2.9) and small ones for the inner wheel (Fig 2.10). The size of the lead and steel plates before bending is roughly $1.5 \times 1\, m^2$ for large and $0.5 \times 1\, m^2$ for small absorbers. The lead thickness is $1.7\, mm$ for large and $2.2\, mm$ for small absorbers, the stainless steel thickness being $0.2\, mm$ in both cases.

The construction of an absorber consists of the following phases:

- Lead and steel rectangular plates are manufactured, with the proper thickness and contour dimensions. A first thickness quality control is performed at the factory for the lead plates using X-ray radiography technique. Lead plates are manufactured by *Rohr GmbH* (Krefeld, Germany), and steel plates by *Allegheny Rodney metals* (Sprockhovel, Germany). See 4.1 for details.

- A detailed thickness control is performed on the lead plates at the *Universidad Autónoma de Madrid* (UAM) laboratory using ultrasound technique (see 4.1).
- Parallely, side and transversal bars are manufactured by *Compreforme* (Chatillon sur Seine, France). These bars are made up of composite material in such a way that their expansion coefficient is similar to that of the absorber.
- Lead and steel plates are laser cut to the correct contour shape for the two types of absorbers, large and small. Special cleaning of the lead surface is done in order to remove any oxide. This part of the process takes place at the factory *Talleres Mendiaraiz* (Zumaya, Guipúzcoa, Spain). Steel cleaning is done by *Chimimeca* (Moirans, France).
- The five layers steel-prepreg-lead-prepreg-steel are piled up. The sandwich is bent to the final accordion geometry. A different bending press is used for small and large absorbers. Fig 2.11 shows the one used for the former. At this stage absorber plates are not yet rigid.
- The absorber with its side bars is introduced in a precision mould with the final geometry and goes through a pressure-temperature cycle, making the prepreg polimerize, thus providing rigidity to the absorber.
- A proper set of measurements is performed in order to control the absorber geometry. These last three steps take place at the factory *Fibertecnic* (Vitoria, Spain). The precision tooling used was developed and manufactured in close collaboration by UAM and the company *Talleres Aratz* (Vitoria, Spain). Details can be found in [17].
- Finally the transverse bar is glued to the acute-angle edge of the absorber (small or large). After this step the absorber is ready to be assembled in the module structure. This last operation is already done at the laboratory where the module will be mounted. Half of the 16 EMEC modules are scheduled to be mounted at UAM and the other half at the *Centre de Phisique des Particules de Marseille* (CPPM).

This process includes three different stages of dimensional control which are explained in detail in chapter 4 below, along with further details about the absorber production process.

Electrodes

The read out electrodes are flexible printed circuit boards. They have the same geometry as the absorbers (i.e. there are two types of electrodes for the EMEC, for the inner and outer wheel respectively).

The electrodes have a thickness below 300 μm and consist of three copper layers: two external ones, to which high voltage (HV) is supplied and where the ionization charge is collected, and an internal one, to which the signal is transmitted through capacitive coupling. The output of the internal copper layer is the input to the read out electronics system. The three copper layers are separated by two intermediate kapton polyamide ones. Fig 2.12 sketches the layered structure of the kapton electrodes.

The structure of the printed copper circuit in the signal layer determines the detector segmentation in η and in depth. In order to minimize cross-talk effects the external HV layers have the same segmentation as the signal layer, different channels being connected through resistances. Moreover, inside a channel, the HV layer is subdivided into smaller regions separated by resistances in order to protect the read out electronics from sparking. The absorbers are connected to the electrode ground through copper-printed plastic flaps, soldered to the electrode ground and forced to contact the adjacent absorbers by a small plastic bar.

Fig 2.13 shows the HV layer of an outer-wheel electrode before bending. The top part of the figure corresponds to the region closest to the barrel, where there are only two sections in depth (the first four cells in η). From there on we find three sections in depth (front, mid and back). It can be seen that there are two cells in the mid section for each one in the back section throughout. For each mid section cell there are 8, 6, 4 or 1 front section cells, depending on the η region considered. Further details on detector granularity are given in chapter 5 below.

The same is shown for an inner wheel electrode in Fig 2.14. In this case there are only two sections in depth throughout.

Spacers

Once bent, electrodes are kept centered between two consecutive absorbers using spacers, that consist of honeycomb strips made of phenolic resine impregnated paper. Two strips are used for each flat part of the accordion, both in the outer and inner wheel. The strips have linearly variable thickness in order to accomodate to the geometry of the gap. The complicated EMEC geometry makes necessary the use of 29 different types of spacers.

Mechanical structure

Absorbers are supported by a structure consisting of ten rings, five on the front and five on the back side of the EMEC (see Fig 2.7, 2.8). Details about the mechanical support structure can be found in [16].

2.4.4 Read out electronics

The read out chain of the ATLAS LAr EM calorimeter consists of the following main components: summing boards, motherboards, preamplifiers, shaping amplifiers, SCA chips, ADCs and optical links, as detailed below.

The charge generated in the LAr gap by an energetic particle, drifts to the read out electrode due to the voltage difference applied between the electrode and the absorber. A current pulse of triangular shape is thus generated on each cell of the electrode HV layer, being transmitted to the internal signal layer through capacitive coupling. Those pulses are routed out of the electrode through pins, connected to *summing boards*. These are thin flat plastic boards plugged on the front or back face of the EMEC, perpendicular to the electrodes and absorbers. The summing boards merge together, through on-board printed connections, the signals from consecutive electrode layers which form the read out cells. The number of layers that form a read out cell is: 3 (outer wheel, mid and back sections), 4 (inner wheel), 12 (outer wheel, front section). The output of the summing boards are triangular current pulses, corresponding to the final read out cells.

Motherboards are placed on top of summing boards, again connected through pins. Each connection coming out of the summing board and entering the motherboard corresponds to a calorimeter read out channel. From the read out point of view the motherboards do not play any role. They are used in order to inject a current pulse with well known amplitude (test pulse) into the read out chain, emulating the pulse coming from the calorimeter cells themselves, in order to obtain an accurate calibration of the read out electronics. The test pulse is generated as a voltage pulse in a *calibration board* placed in the front end crate (FEC), at the outer wall of the cryostat. Voltage is converted to current through precision resistors, placed at the motherboard. The cables entering the motherboard from the outside of the calorimeter are thus of two types: signal cables (output) and calibration cables (input). The same calibration line is used to distribute its pulse to a number of non-neighbour cells. Therefore the number of calibration cables entering a motherboard is smaller than the number of signal cables coming out.

The signal cables go from the motherboards, placed on the EMEC front or back face, to the inner wall of the cryostat, and they are routed out with feedthrough connections. On the outer wall of the cryostat signal pins are grouped in sets of 128, arranged so as to connect a board to them. This is the so called *front end board* (FEB) and it contains most of the read out electronics. FEBs are grouped together, along with other boards (like the calibration one, mentioned above) at the FEC.

The triangular pulse enters the FEB and is amplified at the preamplifier. The signal is shaped and amplified again at the shaping amplifier. At this stage, for each input signal (i.e. for each read out channel) three output signals with different gains are generated:

low (L), *medium* (M) and *high* (H). The ratio of the gains is approximately 1:10:100.

After shaping, the height of the pulse is measured every 25 *ns* and the sampled amplitudes are stored in an analog pipeline. Upon receiving the trigger signal [4] five sampled amplitudes are retained and digitized in 12-bit commercial ADCs. The sampling of the pulses, storage of the sampled amplitudes and selection of the appropriate set of five samples is done on *SCA chips*. SCA chips can be programmed in order to digitize only the five samples of one fixed gain (*fixed gain mode*), all three gains (*three gain mode*), or take the decision, based on the result of digitizing one sample of the medium gain, of which of the three gains needs to be digitized (*free gain mode*). In each case the output of the SCA consists of a few (from 5 to 15) analog numbers. In the September 1998 beam test, only fixed gain mode was used. A total of 8 read out channels are multiplexed to the same ADC.

After digitization, the data (5 to 15 digital numbers per channel) are sent to an appropriate computer interface for storage. Transmission is done in ATLAS using optical links. However in the September 1998 test, copper links were used.

[4] In a test beam environment the trigger usually comes from an external device (typically a coincidence of scintillator paddles). In ATLAS the trigger signal at this stage is the *First level trigger* (FLT). The FLT decision is taken using analog sums of cell signals, built at the shaping amplifier level.

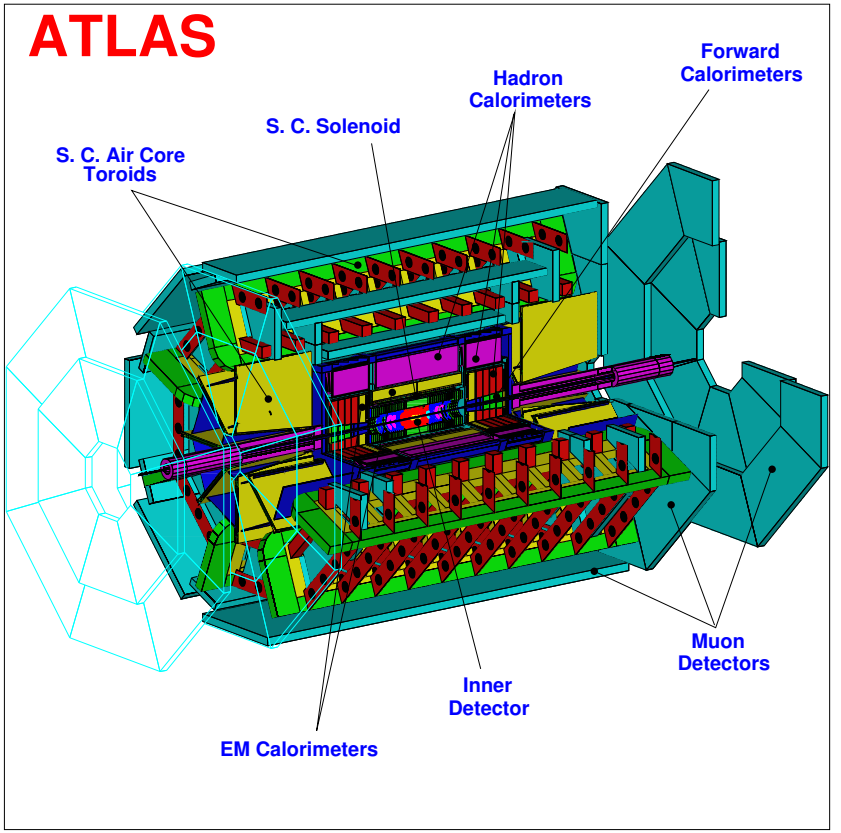

Figure 2.1: View of the ATLAS detector.

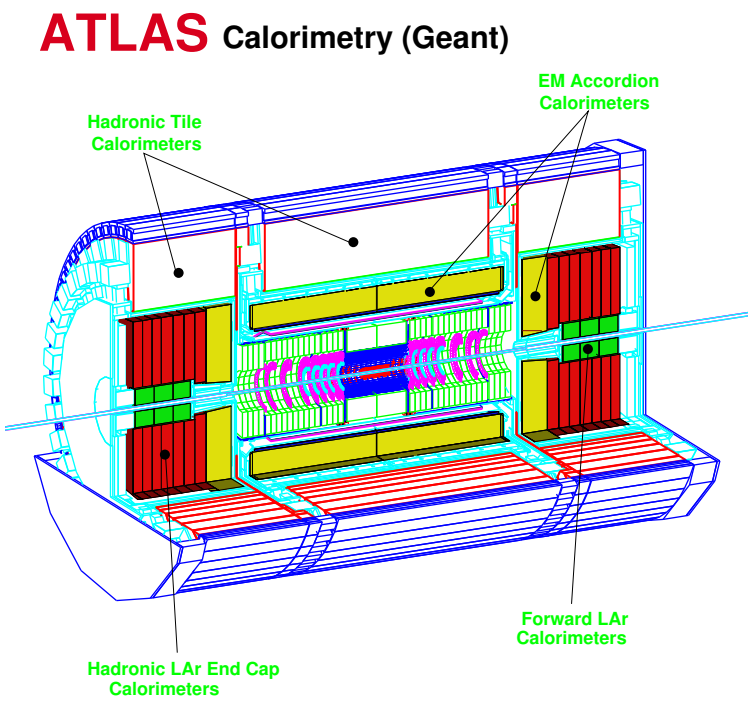

Figure 2.2: View of the ATLAS calorimetry.

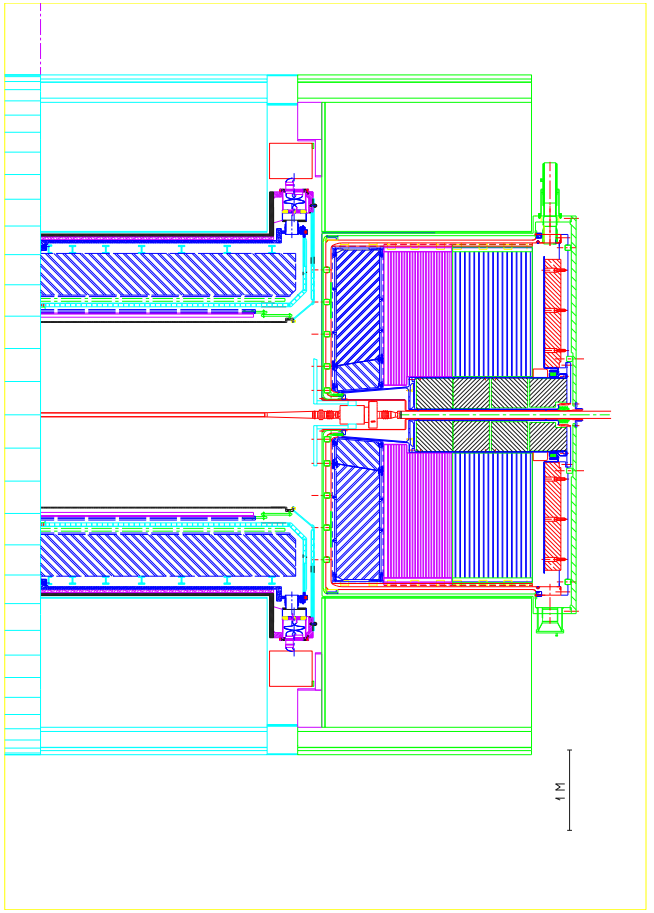

Figure 2.3: One half of the LAr calorimeter.

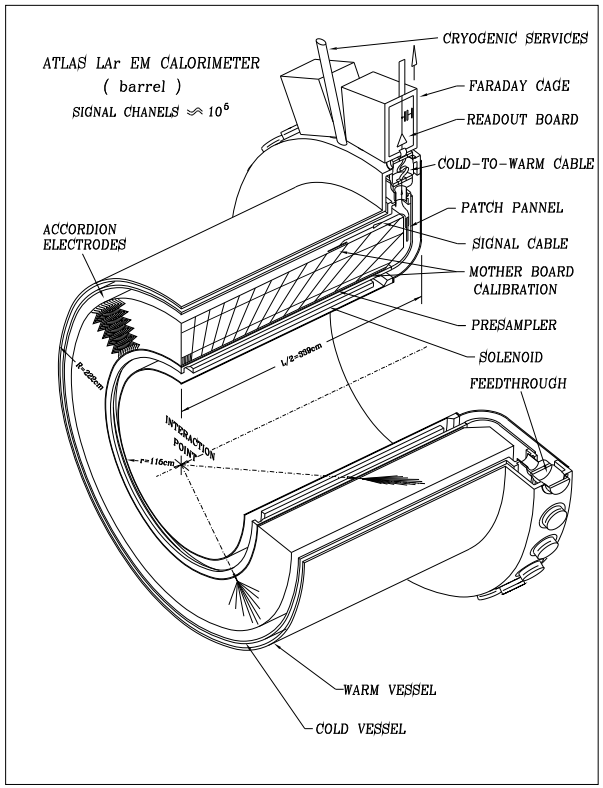

Figure 2.4: One half of the barrel cryostat.

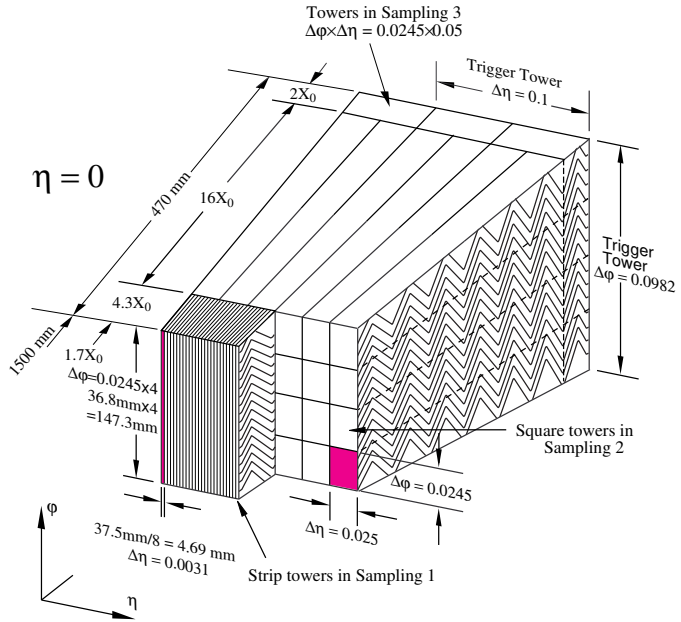

Figure 2.5: Sketch of the accordion structure of the EM calorimeter.

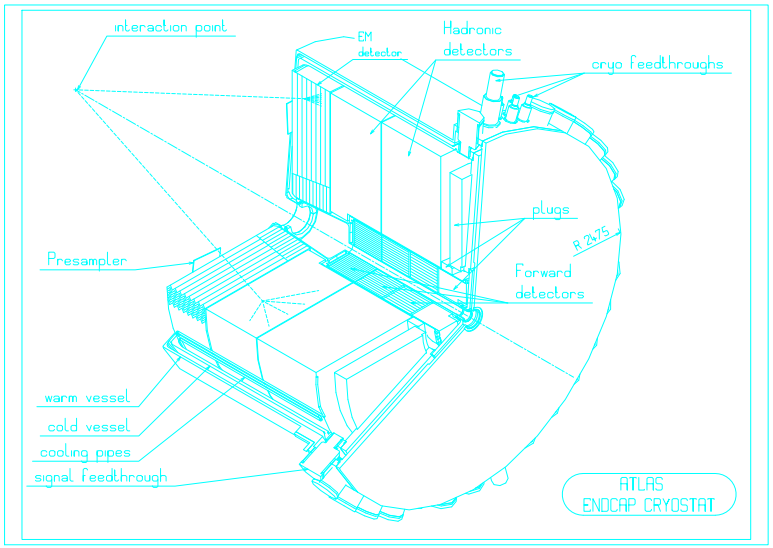

Figure 2.6: End cap cryostat.

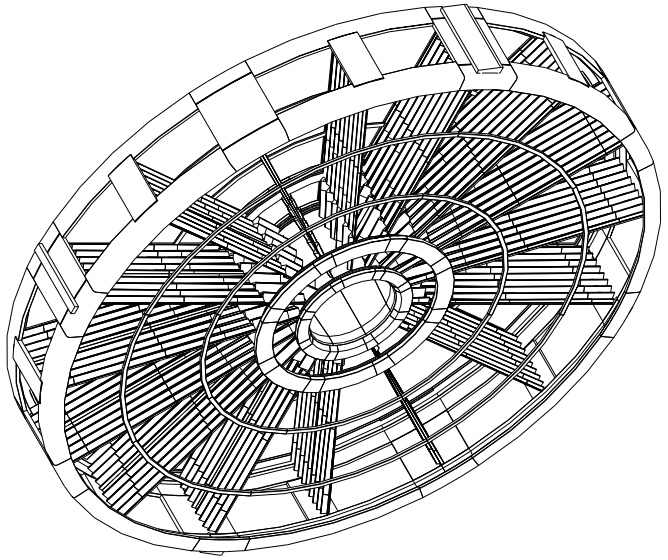

Figure 2.7: General view of the EMEC calorimeter, with a few absorbers to give an idea of the accordion structure.

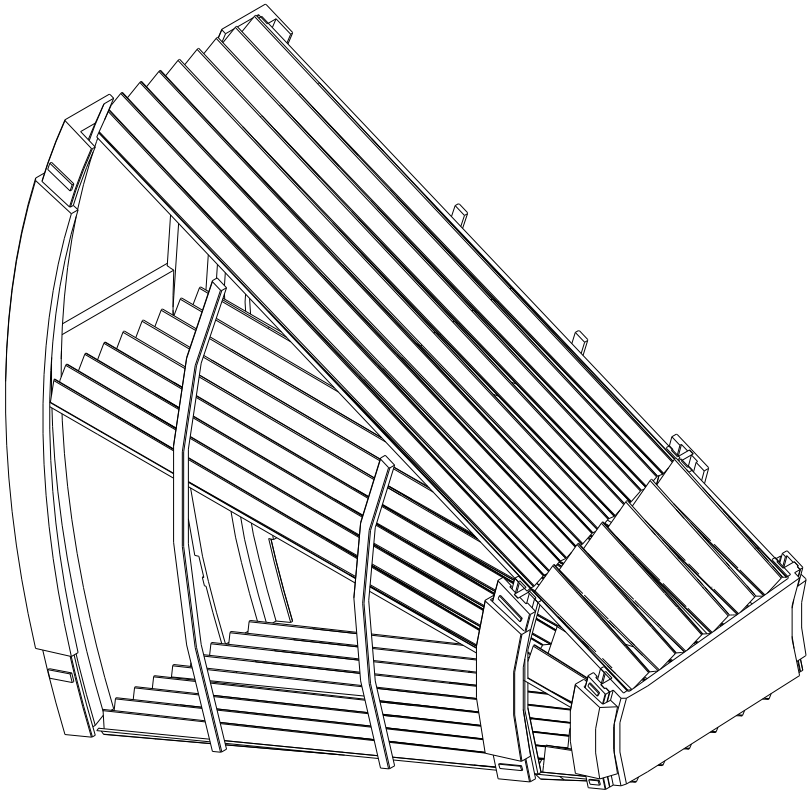

Figure 2.8: EMEC calorimeter module. Each of the two EMECs consists of eight such modules.

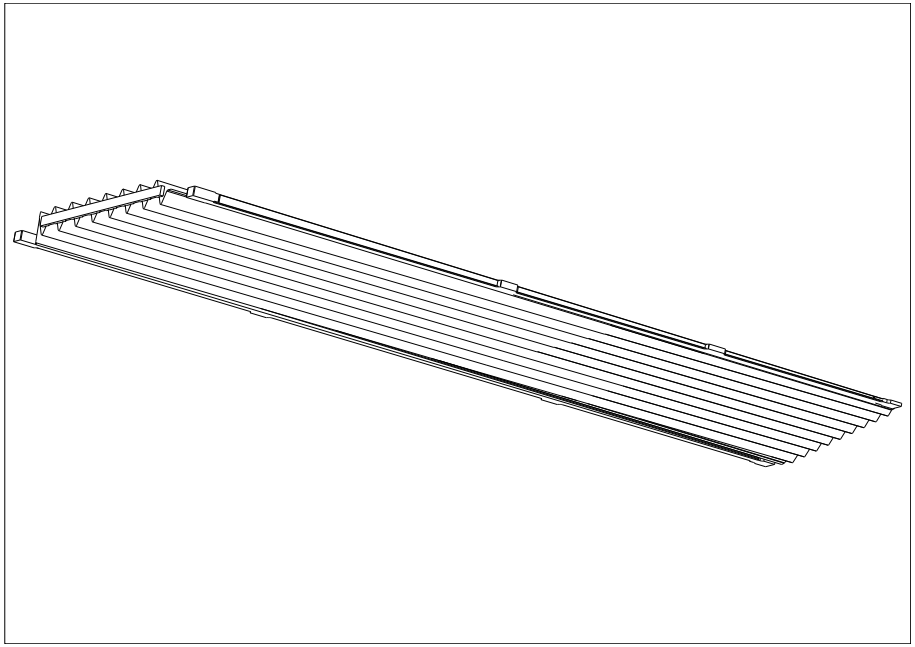

Figure 2.9: EMEC outer wheel absorber.

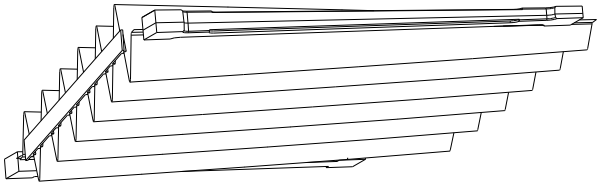

Figure 2.10: EMEC inner wheel absorber.

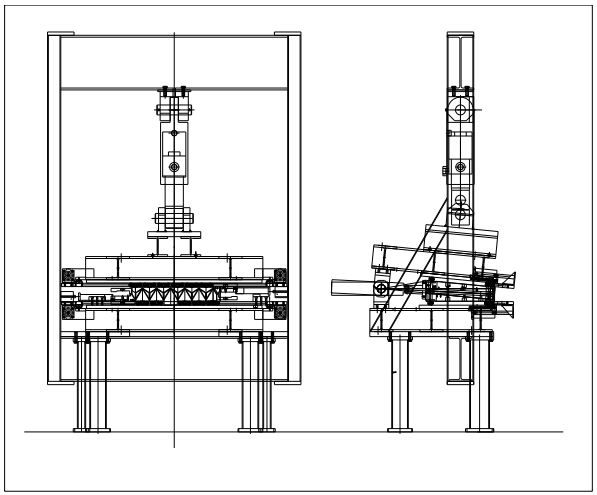

Figure 2.11: Bending press for inner-wheel EMEC absorbers.

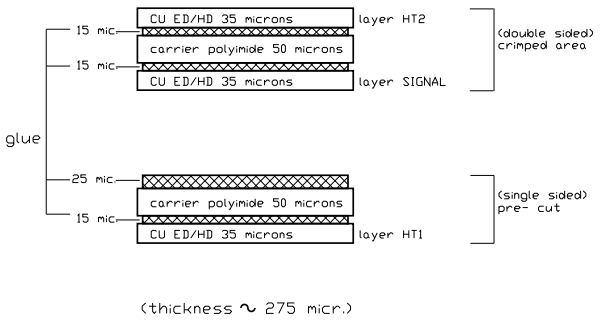

Figure 2.12: Cross section of a kapton electrode.

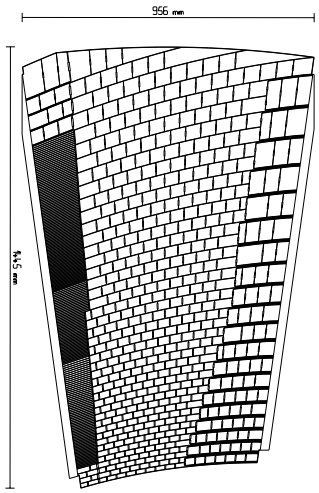

Figure 2.13: HV layer of an outer-wheel EMEC electrode (before bending).

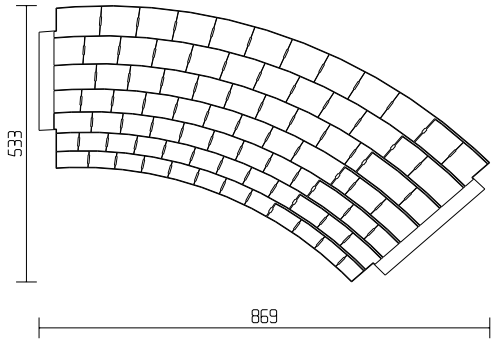

Figure 2.14: HV layer of an inner-wheel EMEC electrode (before bending).

Chapter 3

Expected performance of the EMEC

A large simulation and prototype beam testing effort has been done in order to study thoroughly the expected performance of the ATLAS components. The results obtained from these two sources are the natural guideline to study the performance of the detector with the final design (i.e. the EMEC module-0 in this thesis). In this chapter an overview of the results concerning the EMEC is presented: section 3.1 presents the expected energy resolution; position resolution is dealt with in section 3.2; the signal dependence on the HV applied across the LAr gap is studied in section 3.3. A detailed study of the so called energy signal ϕ-modulation effect (thoroughly analyzed in [18]) is postponed to section 3.4.

3.1 Energy resolution

The energy resolution of a sampling calorimeter is usually parametrized as

$$\frac{\sigma}{E} = \frac{a}{\sqrt{E}} \oplus b \oplus \frac{c}{E}$$

The first two terms, known as *sampling* and *constant* were discussed in chapter 1. The third term is known as *noise*. It contains the contribution of electronics and pile-up [1].

The lead-LAr concept chosen for the ATLAS EM calorimeter, with the ratio active to

[1] In the high luminosity environment of the LHC, the genuine signals coming from a given pp collision may be "polluted" by spurious signals coming from another collision, in the same bunch crossing or in the previous one. This contribution to the fractional energy resolution σ/E obviously scales like $1/E$ and is known as *pile-up noise*.

passive material determined by the design geometry, gives rise to a sampling term a in the range $8-11\%$, according to simulation results [15]. In the region $\eta \simeq 2.2$ of the end cap, with photons of $E \simeq 230\,GeV$ the sampling term is $a \simeq 11\%$, as shown by Fig 3.1, where the energy resolution is shown for photons with $E_T = 50\,GeV$. The sampling term of the energy resolution measured in the test beam with an EMEC prototype in 1993-94 was in the range $10-11\%$ [19], in good agreement with simulation.

The constant term, as explained above, has its main source in mechanical imperfections, not present in the simulation. The goal is to keep the global constant term below 0.7%. The contribution coming from temperature inhomogeneities, calibration and mechanics of the modules is expected to be at the level of 0.6%. Therefore a margin of around 0.35% is left for the *local* constant term, i.e. the constant term measured at a fixed (η, ϕ) position. The local constant term measured in the 1993-94 test beam with the EMEC prototype was around the aimed-at 0.35%.

Electronics noise, using a typical cell cluster (3×5 at the mid section level), is expected to be around $200\,MeV$ [15]. However the electronics chain has not been completely implemented following the final ATLAS design in the 1998 beam test.

3.2 Position resolution

Position resolution is important for a number of physics goals to be covered by the ATLAS research programme. An interesting example is the decay $H \to \gamma\gamma$. For invariant mass reconstruction the energy of the two photons and the angle between their trajectories is needed, as explained in 2.2. The measurement of the photon momentum pointing angle depends on two measurements of pseudorapidity (in the front and mid sections). In order to achieve the required $50\,mrad/\sqrt{E}$ a resolution at the level of $\Delta\eta \simeq 0.33/\sqrt{E}$ (where E is in GeV and $\Delta\eta$ is in mid section cell units) is needed for each of the two η measurements.

Simulation predicts a comparable position resolution for ϕ (measured using the mid section), and η (both with the front and mid section). Position resolution is predicted to scale down with the beam energy following the law $1/\sqrt{E}$. At high energy ($E \simeq 200\,GeV$) and for the region $\eta \simeq 2.2$, ϕ position resolution is predicted to be around 2% of the mid section cell size (see [18]).

3.3 Signal dependence on high voltage across the gap

The pulse height observed in the calorimeter cells when a particle reaches the detector depends on the voltage difference applied across the LAr gap between the absorber and the read out electrode. The precise knowledge of this dependence is important in order to select the proper voltage values for the different η regions of the EMEC, so that the effect of the varying gap thickness is approximately compensated and a uniform response can be attained throughout.

The signal observed at the calorimeter depends linearly on the electron drift velocity in LAr. This quantity has been measured to depend on the voltage across the gap approximately as $\sim V^{0.3}$ [15], [20].

3.4 ϕ-modulation

3.4.1 Introduction

The geometry of the ATLAS EM calorimeter was designed with the idea of preserving ϕ symmetry. In the EMEC outer wheel, for instance, there are 768 absorber plates. The geometrical configuration of the detector stays exactly the same if we rotate it by an angle of $2\pi/768$ (roughly $8.5\,mrad$) with respect to the beam axis. This discrete symmetry, which can be seen as a good approximation to the continuous ϕ symmetry that would be ideal (but is not achievable), gives rise to systematic effects that were partially studied in [15], [16], [21]. The goal of this section is to perform a complete and systematic study of the effect and to provide a simple and robust parametrization to describe it. The study is based on MC simulation, using samples of photons generated at different energies and η values. All the details of this analysis can be found in [18].

For the purpose of studying ϕ-modulation it is useful to define the *reduced* ϕ coordinate as

$$\phi_{red} = \phi.MOD.N_{abs}$$

where N_{abs} is the number of absorbers (768 in the end cap outer wheel, 256 in the inner wheel, 1024 in the barrel) and the operation $.MOD.$ consists of calculating the integer ratio and extracting the rest of this division. The type of problem we are facing can be summarized by Fig 3.2 (upper), where we can see the dependence of the energy signal w.r.t. ϕ_{red} for electrons of $E_T = 200\,GeV$, incident in the calorimeter region $\eta \simeq 2.1$. It can be seen that the energy signal has a strong dependence on ϕ_{red}, which induces an important deterioration of the energy resolution. After applying a multiplicative correction which depends on the reconstructed value of the azimuthal angle, the response can be forced to a flat shape, as it can be seen in the lower half of Fig 3.2. The effect of this type of correction on energy resolution can be very important. The energy signal distribution

for the events shown in Fig 3.2, is displayed in Fig 3.3 before (upper) and after (lower) correcting for ϕ-modulation.

3.4.2 Data sample

The analysis is done with MC generated samples of about 300-800 photon events around the following η values: 1.7, 1.8, 1.9, 2.0, 2.1, 2.2, 2.3 (for the end cap) and 0.1, 0.3, 0.5, 0.7, 0.9, 1.1, 1.2, 1.3 (for the barrel). In each case events were generated with random η uniformly distributed around the nominal value along an interval of length 0.05 . This was done at three different energies, $E_T = 200, 80, 50\,GeV$ (for some of the η values). Events were generated using DICE [22] (version of end 96, used for the calorimeter TDR) and reconstructed with the standard reconstruction code ATRECON [23] (version of June 97). The energy signal in a $3(\eta) \times 7(\phi)$ cell window was used throughout.

3.4.3 Fourier polynomials: a natural choice for the parametrization

The main problem to be taken into account if one wants to choose a class of functions to describe ϕ-modulation is that its shape changes non trivially with η. The solution proposed in this section is a truncated Fourier series. There are several reasons that suggest this choice as a natural one:

- The data we want to describe have a well defined period: $2\pi/N_{abs}$. Any function with this property can be written as a series of orthogonal terms (Fourier series)

$$A_0 + \sum_{k=1}^{\infty} (A_k cos(kN_{abs}\phi) + B_k sin(kN_{abs}\phi))$$

- It is well known from Fourier analysis that the value of each coefficient in this series reflects the contribution to the shape under analysis of features with a characteristic wavelength. This provides a natural criterion to truncate the series: if, for example, the smallest feature detected has a length of about one fourth of the fundamental period, then we will be able to reproduce the shape very well with the first four harmonics. This trick works especially well if the shape is smooth.

- Furthermore, additional symmetries visible in the data can easily give us information about which coefficients contribute and which ones are not present at all. For example the shape shown in Fig 3.2 is, to a good approximation, symmetric with respect to the center of the ϕ_{red} scale. This implies that the sine terms will not contribute to the Fourier expansion. Of course this type of conclusion cannot be accepted without further investigation; but a detailed calculation will prove most times that the guess was correct.

- Since a Fourier polynomial is a very general parametrization for periodic functions, we can expect to obtain a smooth variation of the Fourier coefficients with respect to the η coordinate.

The different sets of data were fitted with the standard chi-squared routine provided by the PAW package for different sets of Fourier parameters. The contribution of all coefficients was analyzed up to the fourth harmonic. After careful analysis only five terms were retained. The polynomial used for all η regions is

$$P_0 + P_1 cos(N_{abs}\phi) + P_4 sin(N_{abs}\phi) + P_2 cos(2 \cdot N_{abs}\phi) + P_3 cos(3 \cdot N_{abs}\phi)$$

3.4.4 Results for the end cap outer wheel

Shape variation with respect to η

Fig 3.4 to 3.10 show how the shape of the ϕ-modulation evolves with η, at both 200 and $80\,GeV$, where data are available. From direct visual inspection one can easily guess which Fourier coefficients are contributing most. At $\eta = 1.7$ the most important terms are the second and third symmetric harmonics (notice the two peaks), whereas the fundamental frequency contributes more and more as one moves closer to the beam line. This tendency inverts around $\eta = 2.1$. The contribution of the asymmetric term included in the analysis is small everywhere, but its effect is non-negligible in the intermediate region (from 1.9 to 2.1). Fig 3.11 gives an idea of the η coordinate values corresponding to the main features of the EMEC calorimeter.

The results are summarized in Fig 3.12. The coefficient P_0 can be considered as a fine correction for residual η dependence of the energy signal, but it does not affect the problem of ϕ-modulation. The three symmetric coefficients (those multiplying cosine-terms) are shown in the same plot for comparison. Finally, the only asymmetric one taken into account is given in the lower plot.

Fig 3.13 shows the improvement in energy resolution after ϕ-modulation has been corrected for. The correction is most effective in the η regions where the contribution of the fundamental harmonic is largest (i.e. where modulation is most apparent).

Some cross-checks

The method involves two choices, in principle arbitrary:

- One has to choose which Fourier coefficients have to be taken into account.
- Before the fits are done, points corresponding to single events have to be clustered in order to get a few "effective" points (the ones shown in ϕ-modulation plots), so that convergence is achieved without problems. The number of clusters chosen is arbitrary.

All Fourier coefficients up to the fourth harmonic were checked to have negligible contributions, except for those retained. The number of clusters was also varied and no variations were found in the results.

Impact of ϕ resolution on the correction

The variable ϕ is used as the argument of the trigonometric factor applied to energy signal for correction. Therefore it is very important to make sure that this coordinate is reconstructed with a precision much better than the typical distance over which the correction varies. Fig 3.14 shows ϕ position resolution versus energy at $\eta = 1.85$. The vertical axis is scaled in units of the spacing between two consecutive absorbers. A few points are given also for different η values. It can be seen that at reasonably high energies (where ϕ-modulation is really important, since at low energy sampling fluctuations dominate) we can reconstruct the azimuthal angle with a precision below 5 % of the spacing between absorbers. The ϕ-modulation correction was checked to work the same whether the generated or reconstructed ϕ coordinate is used, as one would expect, at high energy.

3.4.5 Results for the barrel

The same calculations explained in the previous paragraph were done for the barrel. In this case there are 1024 absorbers (instead of 768). Again photon samples were taken, covering a small η interval, and the shape of ϕ-modulation was monitored using a Fourier polynomial with the same five terms. Samples with $E_T = 80\,GeV$ were available for all η values in this case, along with $E_T = 200\,GeV$ events at most of them.

The η-evolution of the Fourier coefficients is shown in Fig 3.15 and 3.16, for the two different energies. The only two terms with a sizeable contribution are the sine and cosine of the fundamental harmonic. Notice that the modulation has a smaller amplitude in the barrel. Therefore one can not expect much improvement in energy resolution after applying a correction. This is shown in Fig 3.17, again for both energies.

In the transition region between end cap and barrel, energy resolution is deteriorated by the crack and the ϕ-modulation effect becomes negligible.

3.4.6 Energy dependence of ϕ-modulation

In this paragraph we look at the energy dependence of the ϕ-modulation. The goal is to establish to what extent the effect can be corrected in an energy-independent way.

ϕ-modulation is only important at relatively high energies, where the contribution to energy resolution from the sampling term is small enough. By comparing the shape of ϕ-modulation at 80 and $200\,GeV$ one can see that it doesn't change much with energy in most cases. In general the modulation is more apparent at $200\,GeV$. The contribution of sampling fluctuations in the energy signal tends to somewhat mask the effect under study at lower energies.

In order to test if the Fourier coefficients must be parametrized as energy dependent, the ϕ-modulation multiplicative correction was applied to $80\,GeV$ events using both the Fourier parameters obtained at this energy and at $200\,GeV$. The result is shown in Fig 3.18. At all η regions where the correction yields an important improvement in energy resolution, the result is the same for both options. Only at certain barrel regions (at low η) a small difference is observed. Therefore we conclude that it is not necessary to use energy dependent coefficients.

Below $E_T = 80\,GeV$ the modulation is even further masked by sampling fluctuations. Even so, one can still test if the values obtained at higher energies for the Fourier parameters improve energy resolution. This was done for $E_T = 50\,GeV$ photons, shot at two selected η in the end cap, as shown in Fig 3.19. At $\eta = 2.3$ the energy-independent correction (i.e. the one calculated with $200\,GeV$ photons) is very effective, even better than that obtained with the $50\,GeV$ photons themselves. This is what one could expect for a region where the effect of ϕ-modulation is important: the shape of the modulation is roughly energy-independent and it can be more precisely calculated at a higher energy. Things work somewhat worse at $\eta = 1.8$, a region where the effect is much smaller. In this case no modulation is seen and the correction calculated with $50\,GeV$ photons helps nothing, whereas applying the factor obtained from $200\,GeV$ events seems to worsen slightly the resolution. However in all cases the results obtained are compatible within errors. This confirms our conclusion that an energy-independent correction is the most reasonable solution.

3.4.7 Modulation with different windows

All the analysis described above was done using a 3×7 window, that is, only the energy signal inside a cluster of 3 (η) by 7 (ϕ) cells was used. The fact that only a very small amount of the energy in the cluster is deposited in the outermost ϕ cells strongly suggests that the ϕ-modulation effect under study will not change if a smaller cluster is used. This was checked at the test value $\eta = 2.3$. Fig 3.20 shows that the shape of the modulation is roughly the same with the three choices 3×7, 3×5 and 3×3. The same set of Fourier coefficients is therefore used and if one looks carefully at the numbers given in the insets, the same values, within errors, are obtained in the three cases. This cross check was performed at different η values, yielding the same results.

3.4.8 Conclusions on ϕ-modulation

The dependence of the energy signal on the ϕ coordinate of the particle impact point at the EM calorimeter is, at high energies, an important effect that must be corrected for. This can be done in a very general way by using Fourier polynomials with a few terms. The coefficients can be parametrized as a function of η using a poligonal that goes through the points found in the simulations. The data analyzed cover both the barrel and the end cap outer wheel. The energy dependence of the coefficients was found to be negligible.

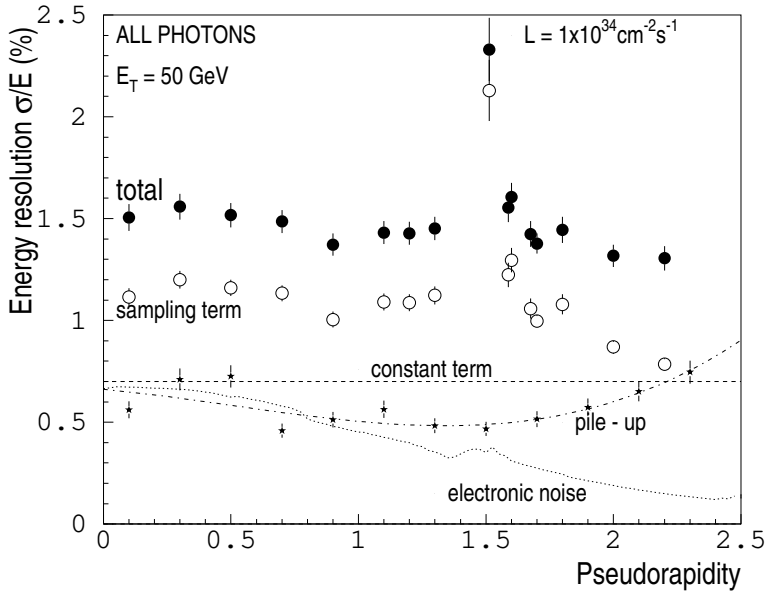

Figure 3.1: Various contributions to the energy resolution. Simulation done with photons of $E_T = 50\,GeV$. Figure taken from [15].

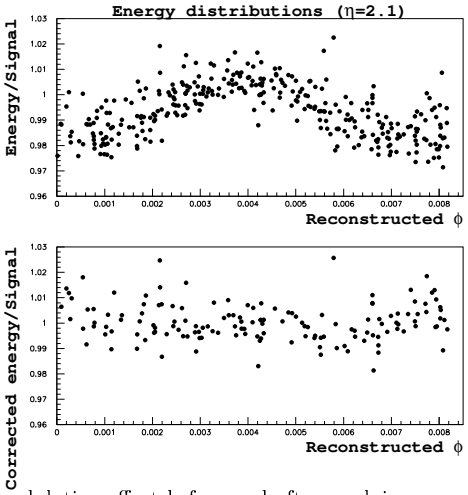

Figure 3.2: ϕ-modulation effect before and after applying a multiplicative correction.

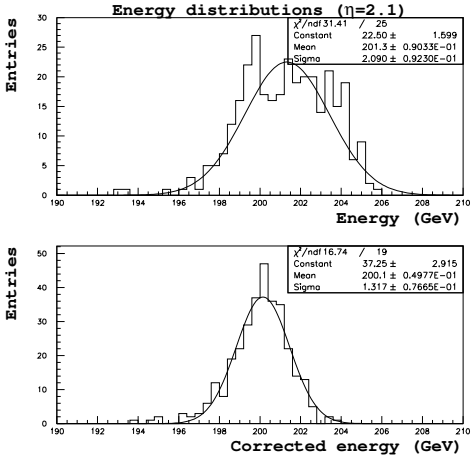

Figure 3.3: Transverse energy signal distribution before and after correcting for ϕ-modulation.

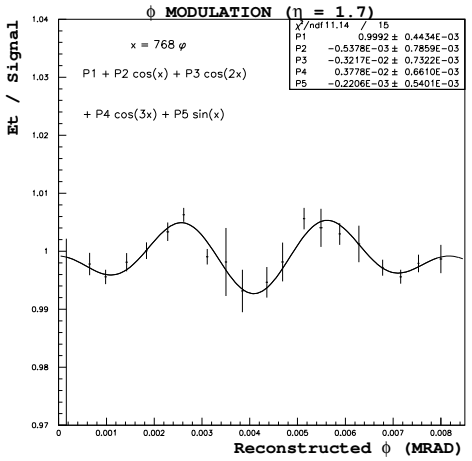

Figure 3.4: Energy signal ϕ-modulation at $\eta = 1.7$. $E_T = 200\,GeV$.

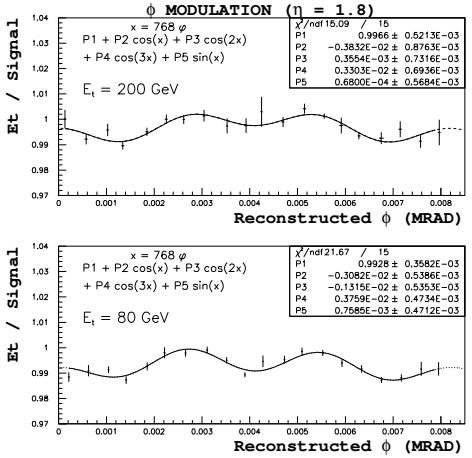

Figure 3.5: Energy signal ϕ-modulation at $\eta = 1.8$. $E_T = 200, 80\,GeV$.

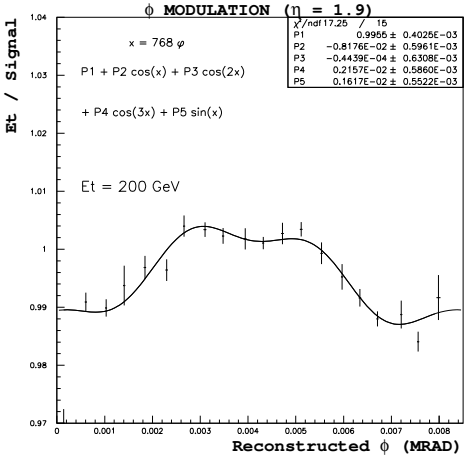

Figure 3.6: Energy signal ϕ-modulation at $\eta = 1.9$. $E_T = 200\,GeV$.

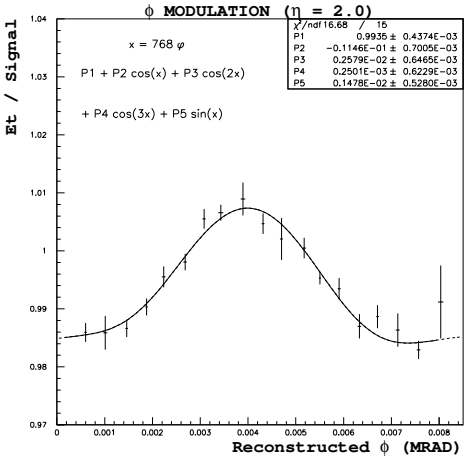

Figure 3.7: Energy signal ϕ-modulation at $\eta = 2.0$. $E_T = 200\,GeV$.

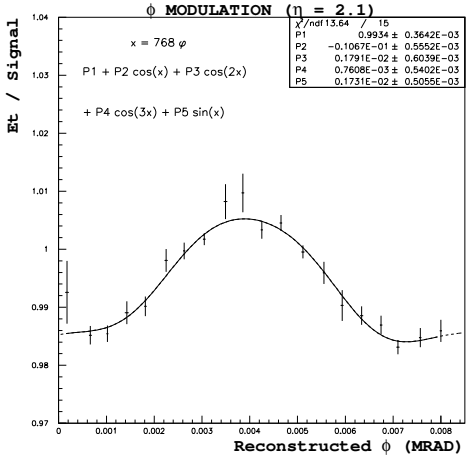

Figure 3.8: Energy signal ϕ-modulation at $\eta = 2.1$. $E_T = 200\,GeV$.

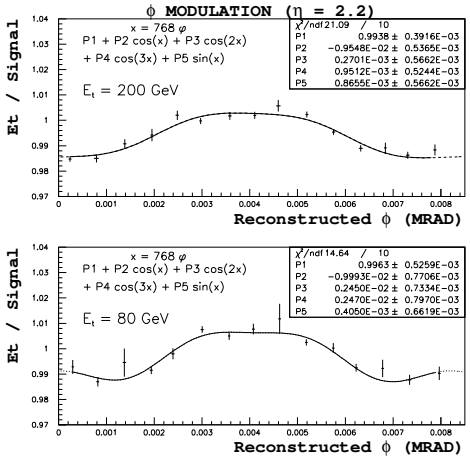

Figure 3.9: Energy signal ϕ-modulation at $\eta = 2.2$. $E_T = 200,\,80\,GeV$.

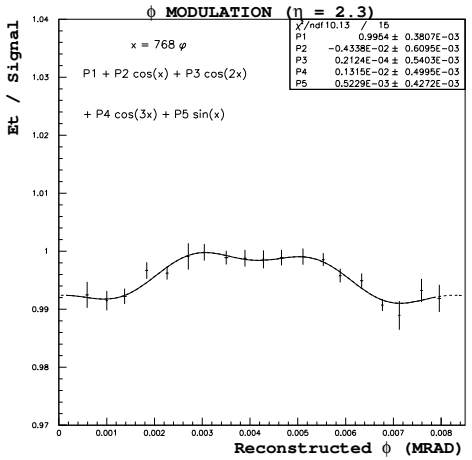

Figure 3.10: Energy signal ϕ-modulation at $\eta = 2.3$. $E_T = 200\,GeV$.

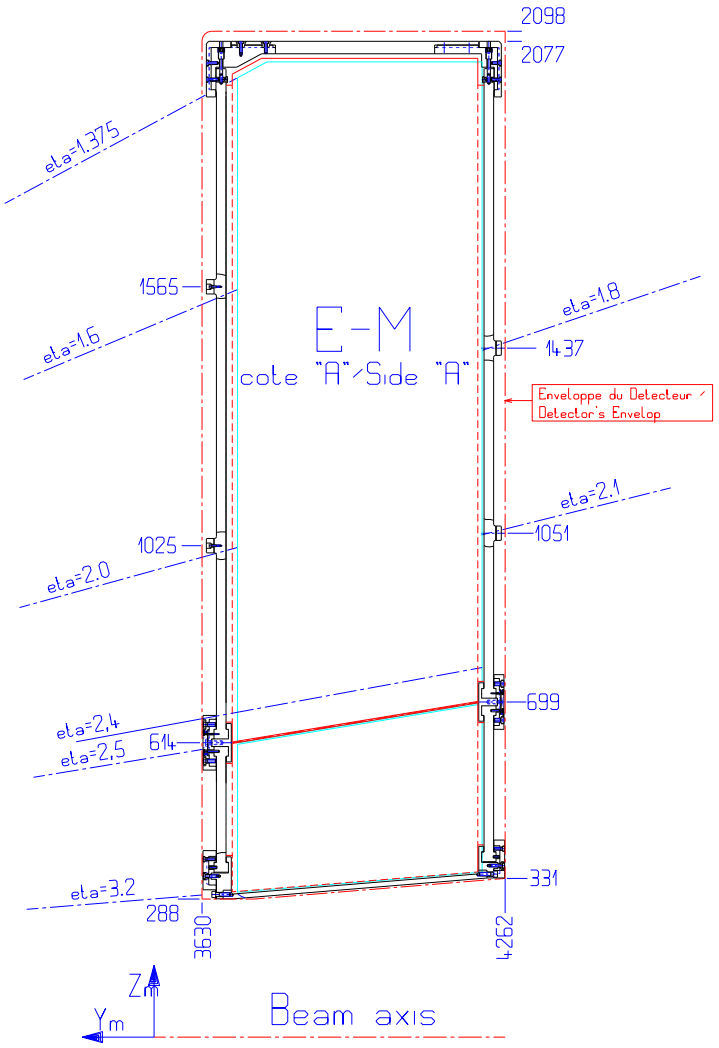

Figure 3.11: Side view of the EMEC. The η coordinate is given for the most relevant features of the detector.

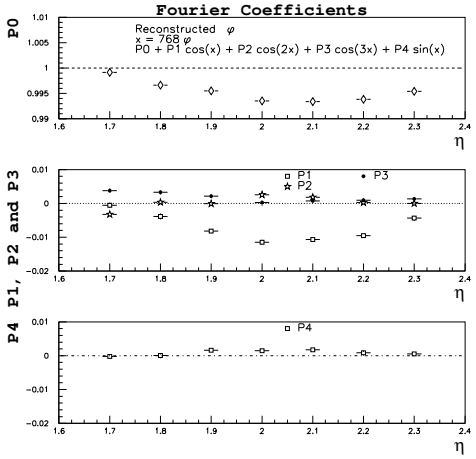

Figure 3.12: η dependence of Fourier coefficients (EMEC outer wheel). $E_T = 200\,GeV$.

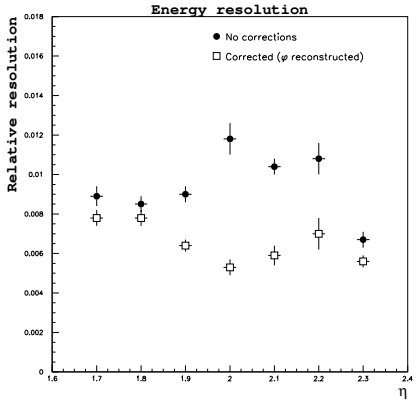

Figure 3.13: Energy resolution at several η values before and after correcting for ϕ-modulation (EMEC outer wheel). $E_T = 200\,GeV$.

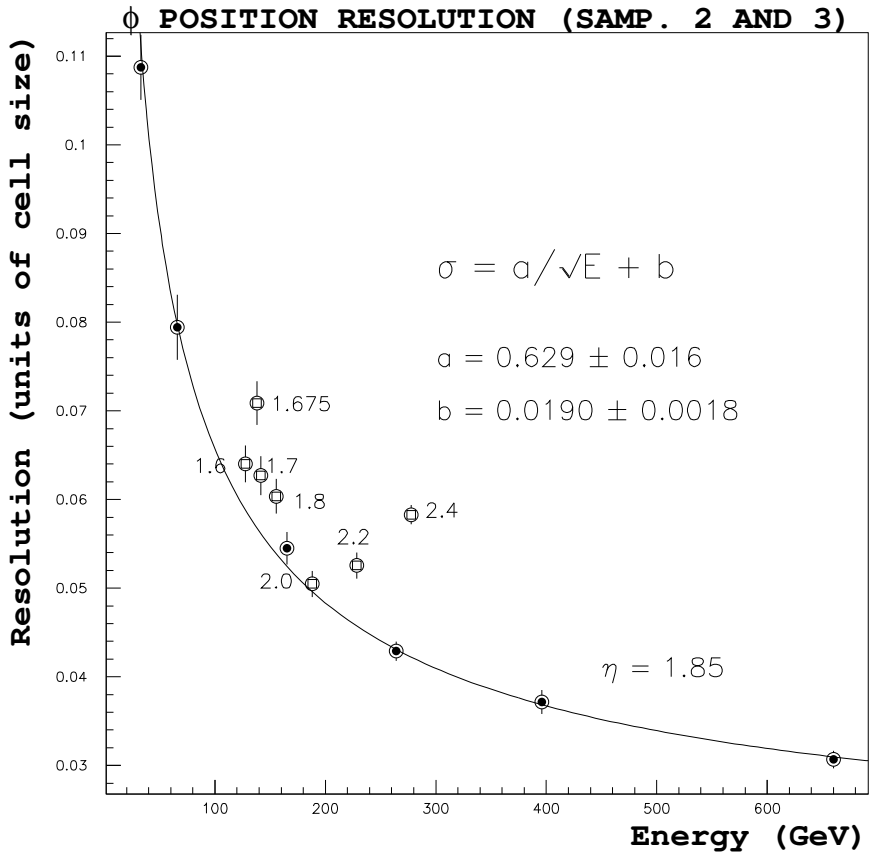

Figure 3.14: ϕ position resolution as a function of energy in units of the spacing between consecutive absorbers. A mid section read out cell corresponds to 3 spacings. In order to read the resolution in cell units the numbers in the ordinate axis must be divided by 3.

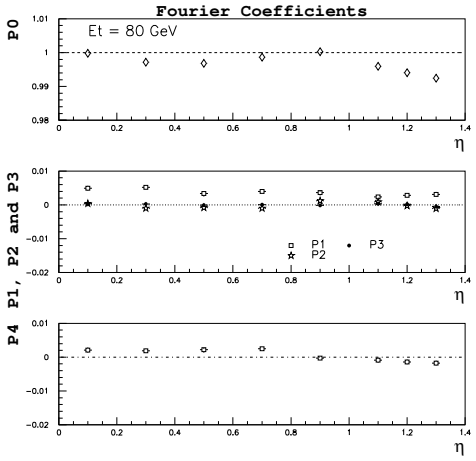

Figure 3.15: η dependence of Fourier coefficients at $80\,GeV$ (barrel).

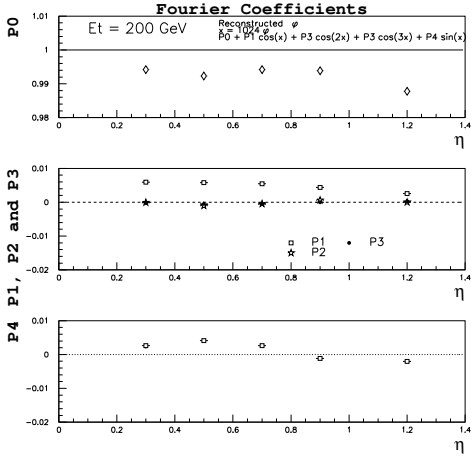

Figure 3.16: η dependence of Fourier coefficients at $200\,GeV$ (barrel).

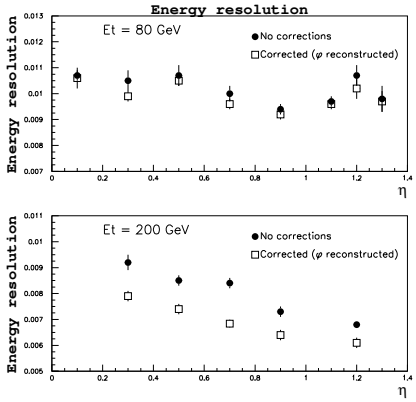

Figure 3.17: Improvement in energy resolution after correcting for ϕ-modulation (barrel).

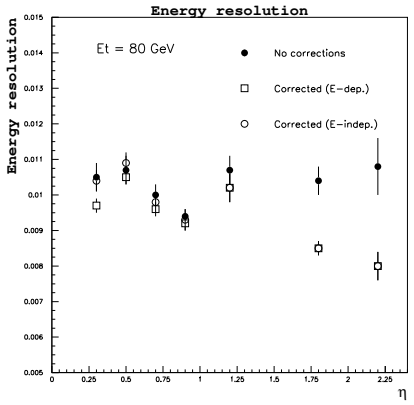

Figure 3.18: Energy resolution improvement for $E_T = 80\,GeV$ photons at different η values, applying a correction optimized at that energy or at $200\,GeV$.

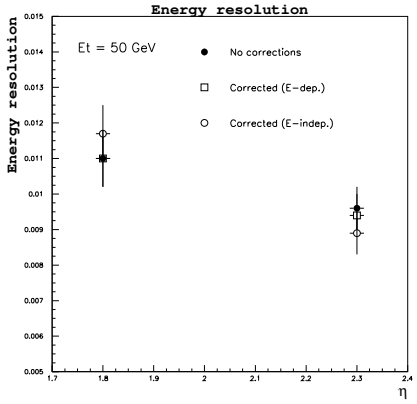

Figure 3.19: Energy resolution improvement for $E_T = 50 GeV$ photons at different η values, applying an energy independent ϕ-modulation correction and an energy dependent one.

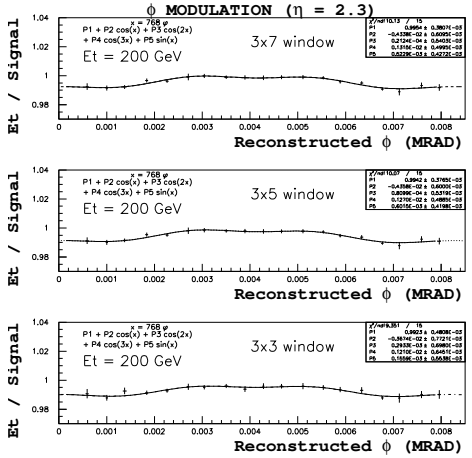

Figure 3.20: Energy signal ϕ-modulation at $\eta = 2.3$. $E_T = 200 GeV$. Three different windows are compared.

Chapter 4

Construction and quality control of module-0

4.1 Strategy for the quality control of the absorbers

4.1.1 Introduction

The ATLAS electromagnetic calorimeter can be regarded as the sum of many layers of active and passive material. Mechanical imperfections generate local systematic effects on the energy signal. A small deviation from nominal of the lead layer thickness (l) gives rise to an energy signal (S) variation of (see section 1.2)

$$\frac{\Delta S}{S} = \frac{\Delta l}{l}$$

whereas a similar effect on the liquid argon gap (g) yields

$$\frac{\Delta S}{S} = 0.3\frac{\Delta g}{g}$$

The factor 0.3 comes from the dependence of the electron drift velocity in liquid argon on the electric field (see section 3.3).

Therefore in order to ensure that mechanical imperfections have contributions to the constant term below 1%, one must require tolerances at the level of 1% for the lead thickness and 3% for the liquid argon gap. In order to guarantee that these goals are

achieved it is mandatory to have a complete and precise dimensional control system for the absorbers.

The dimensional control system consists of the following steps:

- An online, feed-back provider, X-ray based thickness measurement is performed on the lead manufactured for the plates at the factory [24].
- After lead plates have been shipped to the laboratories, thickness is controlled with a more accurate ultrasound-based system [25], [26].
- Once the absorber has been finished (i.e. after laser cutting, sandwich piling, bending and curing) the geometry is controlled to be correct [27].

The first two steps control the thickness of the passive material layers in the calorimeter. The third one indirectly controls the thickness of the active material layers, i.e. the liquid argon gaps between an absorber and the adjacent electrodes. The whole process is explained in some detail in this chapter. Details of the production process which are closely related to dimensional control are also given.

4.1.2 X-ray lead thickness control system

The lead for the absorbers is laminated at *Rohr GmbH*, as mentioned in 2.4.3. The lamination procedure starts with a thick piece of lead, of approximate surface $2 \times 1\,m^2$, weighting about one ton. Lead is guaranteed to be pure by the company, with a weight fraction of impurities well below 1%. The initial piece of lead is passed between two rolling steel cylinders, in such a way that the lead piece becomes thinner and is lengthened along one direction that we will call X. After a few passes the piece of lead has become a long band (with dimensions of order $50 \times 1\,m^2$) and with thickness at the level of $3\,mm$. The last pass forces the thickness to the nominal requested value (1.7 or $2.2\,mm$). For each pass, after going between the cylinders, the lead band is rolled in a coil for storage. Thickness control takes place during the last pass.

In front of the cylinders position, on the side where the lead band comes out from lamination, an X-ray source is kept operational above the position of the lead. A set of 7 PMTs placed along the Y direction (i.e. along the $1\,m$ width of the lead band) are installed below the lead. This way the transmitted X-ray intensity can be used as a measurement of the lead thickness. The signal at the PMT anode is digitized by ADC units. Data acquisition and system operation is done using a PC. The measurement for each PMT takes place at a well defined Y position. However the PMT response is integrated w.r.t. time in such a way that the thickness measurement is an average along a typical X interval

of $10 - 15\,cm$. The output of the thickness control system is therefore an X-Y thickness map of the whole lead roll. After plates are cut from the roll, the correct piece of the whole thickness map can be assigned to each plate using reference numbers printed with ink on the lead surface.

The measured thickness was displayed online on the PC screen. The operator of the laminating machine used this online feedback as a reference for operation in a very efficient way.

4.1.3 Description of the ultrasound control system for the lead thickness

Thickness is accurately controlled at the UAM laboratory by laying plates on a precision table and measuring on a grid of $5\,cm$ pitch (above 400 points per plate). Measurements are performed with an ultrasound device supplied by *Krautkramer-Branson*. It consists of a probe, read out electronics and a computer interface module. This device, which is the most important part of the ultrasound thickness control system, has reference number CL 304, with a data interface module DI 304 and a special delay probe. It operates sending wavetrains lasting a fraction of a microsecond each (with frequency about 20 MHz) at a rate of 196 Hz to 25 kHz (set automatically by the device).

The probe must be placed on the surface of the plate. The presence of a liquid layer between lead and probe is required in order to ensure an approximate matching of the mechanical impedances and, therefore, get a correct measurement. A drop of water has proven to be adequate. The device sends the ultrasonic pulse and receives the waves reflected at the upper and lower surfaces of the plate, measuring the time delay. The speed of sound must be determined by other means and introduced manually, if one wants to obtain a thickness reading. This problem will be discussed in 4.1.4 below.

The interface module allows to read the thickness displayed on the device screen with a computer. Data transfer is activated by a hand switch that has been replaced by a computer controlled one.

The probe must be taken to the point where the measurement has to be performed; then a drop of water must be laid at the correct place and the probe must be placed on the lead surface. Besides it is advisable to remove any dust from the plate before laying the drop of water. This is all achieved with two engines, a compressed air circuit, and a set of four valves, all computer controlled. Part of this system was designed and built at LPNHE [1].

At Madrid we use a Motorola VME processor, talking through interfaces with the X-Y

[1] Laboratoire de Physique Nucleaire des Hautes Energies (Paris)

scan table and the ultrasound module. The set of electronic valves and the switch for Krautkramer data transfer are controlled by an interface card connected on the VME bus, which provides TTL compatible signals through a set of connectors. These signals are then used to activate or close the valves and switch as required at each phase of the program, which is written in C language.

4.1.4 Calibration of the ultrasound system

Statement of the problem

In order to perform the absolute calibration of the ultrasound measuring device, a Palmer micrometer has been used. The ultrasound system gives precise measurements of the time the signal needs to travel between the upper and lower surfaces of the lead plate. The probe has a finite area surface, so it averages thickness over a certain region of the plate. On the other hand, the micrometer will measure the distance between the outermost points, since the shaft will stop moving once it has found an obstacle.

These two observations lead to a very simple model. The two parameters that we would like to determine are the speed of sound (v) and the average overestimation of thickness by the Palmer due to lead roughness (ϵ). The thickness measured by the ultrasound system is

$$z_k = v_k t$$

where v_k is the sound velocity arbitrarily given to the device (taken from a table of material properties, for example) and t the time measured.

If we now measure with the Palmer we get

$$z_{Pal} = vt + \epsilon$$

where v is the exact speed of sound.

Subtracting and eliminating t

$$z_{Pal} - z_k = (v - v_k)t + \epsilon = \left(\frac{v - v_k}{v_k}\right) z_k + \epsilon$$

Then we can easily calculate v and ϵ by just measuring at different thicknesses with the Palmer and the ultrasound probe, and fitting the dependence of $z_{Pal} - z_k$ as a function of

z_k to a straight line. From the slope we can extract v, whereas the y axis intercept is ϵ.

The parameter ϵ accounts not only for rugosity of the lead surface, but also for any other systematic effect leading to a thickness-independent offset between the measurements done with Palmer and Krautkramer.

Uncertainty of thickness measurements

Before going any further we need to determine the uncertainties carried by the readings we get from both the ultrasound device and Palmer micrometer. To this end, thickness was measured at the same point and in the same conditions many times. It is not advisable to measure too many times at the same point with the Palmer, in order not to deform the plate.

The intrinsic resolution of the ultrasound device was evaluated by performing 30 measurements at the same point. Between every two measurements the automatized table moved to different points and made some other measurements, and between measurements number 10 and 11, and number 20 and 21, the device was turned off. The three sets of ten measurements were consistent with each other. Within the thickness range explored ($2-3\,mm$) no variation in this result has been found. We obtain a measurement dispersion (RMS of the different readings) of

$$\Delta z_k = 0.7\,\mu m$$

Nevertheless, it has also been detected that, at points with surface defects, a wrong thickness reading can sometimes be obtained. We will deal with these "special" points in 4.1.5 below.

The same procedure was followed to evaluate the precision of the Palmer micrometer, but now measuring only ten times, in order to avoid plate deformation at the point of interest, as explained above. The measured uncertainty is

$$\Delta z_{Pal} = 1.6\,\mu m$$

This kind of experiment has been repeated many times in different conditions with similar results.

First results

In order to check the assumptions made so far, the parameters v and ϵ were measured, following the proposed method, on a variable thickness test plate (about $2.8\,mm$ at the thicker end and $1.9\,mm$ at the thinner one) composed of Pb (95%) and Sb (5%). Thickness was measured at different points along the maximum slope direction. The plate had been machined with a rotating head. Therefore a large rugosity was expected. The dependence of $z_{Pal} - z_k$ w.r.t. z_k was fitted to a straight line, as shown in Fig 4.1. Error bars on $z_{Pal} - z_k$ are assumed to be $1.7\,\mu m$, the quadratic sum of the resolutions from Palmer and ultrasound probe given above. Error bars on z_k are taken as $0.7\,\mu m$. The value of v_k used on the measurements was $2.238 Km/s$. After some computations we get from the result of the fit

$$v = 2.213 \pm 0.003\, Km/s$$

$$\epsilon = 0.043 \pm 0.003\, mm$$

with a chi-squared per degree of freedom of 4.1 (19 points), not too good but reasonable.

The experiment was redone using as input value for the speed of sound $v_k = 2.213\, Km/s$, yielding results compatible with the ones obtained in the first iteration. A very important consistency check is provided by the values obtained for v and ϵ. The v value measured is slightly below the speed of sound in pure lead as given by a table of material properties ($v_{lead} = 2.253\, Km/s$). This is what one would expect for a mixture with a small amount of antimony, which is less dense than lead. For ϵ the value measured has the expected order of magnitude for a plate machined with a rotating head.

Data analysis

The previous measurements validate our model and determine the sound velocity and the parameter ϵ for the lead-antimony variable thickness plate. However we would like to have the values of these two quantities for the pure lead, constant thickness plates to be finally used in the assembly of module-0. The speed of sound is expected to change due to the different composition. Additionally, constant thickness plates are shaped through a laminating procedure, expected to yield vanishing rugosity. If this calibration method is to be applied to thickness measurements on plates for module-0, we ought to repeat the process explained above, now with constant thickness plates. In order to measure the speed of sound we will take advantage of the fact that we have plates of two nominal thicknesses: 2.2 and $1.7\,mm$.

Data from constant thickness plates

All the points taken on the same type of plate have essentially the same thickness. Therefore we only have two effective points, no matter how many measurements are made: one of them is at $z_k \simeq 1.7\,mm$ and the other one at $z_k \simeq 2.2\,mm$. Several measurements at each type of plate will give us a $z_{Pal} - z_k$ distribution and an ordinate value of $\overline{z_{Pal} - z_k}$ will be assigned to each of these two points. The slope will then be derived applying the formula for the straight line that goes through two given points:

$$\frac{v - v_k}{v_k} = \frac{\left(\overline{zPal - z_k}\right)_2 - \left(\overline{zPal - z_k}\right)_1}{(z_k)_2 - (z_k)_1}$$

Error propagation can be done in the usual way.

In order to be more precise, instead of exactly 2.2 and $1.7\,mm$, we will use the average z_k of all points for each type of plate. It can be seen that error propagation gives negligible contributions from z_k, so they can be neglected.

Four plates were used for calibration, two of each type. Twelve points were measured on each, with an initial $v_k = 2.253\, Km/s$. The results obtained are:

$$\begin{array}{ll} (z_k)_1 = 1.7335\, mm & \left(\overline{zPal - z_k}\right)_1 = -0.0261 \pm 0.0005\, mm \\ (z_k)_2 = 2.244\, mm & \left(\overline{zPal - z_k}\right)_2 = -0.0314 \pm 0.0006\, mm \end{array}$$

Finding the slope and solving for v yields

$$v = 2.230 \pm 0.004\, Km/s$$

As a curiosity we can point out that the ϵ parameter comes out to be

$$\epsilon = -0.009 \pm 0.003\, mm$$

It seems that rugosity is negligible and some other effect, like for example compression, makes the Palmer give a systematically lower reading than the ultrasound system.

Conclusion on calibration

Experimental results are consistent with the assumptions of the model. An accurate absolute calibration for ultrasound thickness measurements is thus available. It must be

pointed out that the measurements were performed at a temperature of 18^0C.

Long term calibration stability is checked by comparing the two types of thickness measurement (ultrasound and micrometer) at a test point for every measured plate. Any noticeable deviation from the expected behaviour will warn us that one of the two devices is not working properly.

Since thickness readings are obtained measuring the time t with a very small intrinsic precision (below $1\,\mu m$, as shown previously) and then calculating $z = vt$, propagation of the error coming from v gives, for all measurements, a global offset from the exact value of

$$\Delta z \leq 4\,\mu m$$

which is fully acceptable.

4.1.5 Stability of the ultrasound device

Once calibration has been fully discussed it is necessary to check how these results depend on conditions of operation. Two effects have been considered:

- Thickness measurement evolution along several hours of operation.
- Temperature dependence.

In the first case, if any variation occurs at all, it should show a more reliable performance as the device "heats up". The thickness versus temperature behaviour is expected to be linear (for small temperature changes) and slowly varying.

Finally a brief study of the ultrasound system behaviour at points where the plate shows a surface defect is presented.

Performance versus time of operation

The thickness control set up is planned to be working for eight to ten hours a day. Therefore it is important to check if the readings vary from the first minutes to, say, the last hour. To this end a variable thickness test plate was thoroughly measured six times (over eight hours of operation) without stopping the system. Three measurements were taken at each point for each of the six runs. The temperature was kept at 12^0C along the whole process.

The results are plotted in Fig 4.2 and 4.3. In the former, sets of three measurements are plotted versus time of operation for four different points of the plate; in the latter the distribution of thickness differences between couples of measurements at the same point on the plate (three pairings can be done with the three thickness measurements), for all the points of the scan, is displayed for the six successive runs. Note that on the sixth run the system was stopped before finishing the measurements, so we have a smaller number of points.

Fig 4.2 manifestly shows that there is no drift along the time of operation. Fig 4.3 shows that the same shape is repeated in the six runs: about eighty percent of the data are exactly zero and most of the remaining twenty percent is equally divided between $1\,\mu m$ and $-1\,\mu m$ (i.e. the intrinsic thickness resolution is below $1\,\mu m$ throughout the time of operation).

Temperature dependence

A variable thickness plate was measured at three different temperatures and a few points were selected at random to see how thickness readings vary. The results are plotted on Fig 4.4. The response of the ultrasound device is fairly linear. The thickness reading is changing by $0.5\,\mu m$ per degree. If this difference were exclusively due to lead dilatation it would give a coefficient of $0.00018\,K^{-1}$, about six times larger than expected. However the speed of sound also varies with temperature. Both effects should be cumulative (i.e. the speed of sound should decrease with temperature and therefore enhance the reading compared to true thickness). Therefore it can be concluded that this effect is more important than bare dilatation.

The conclusion of this paragraph can be summarized as follows:

- The speed of sound must be evaluated on constant thickness plates at the same temperature to be maintained in the laboratory during the measurement process. This temperature must be precisely controlled.
- Eventually, a small correction can be applied to measurements obtained at temperatures differing from 18^0C more than a few degrees. It would be

  $$(\Delta z)_T = 0.5\Delta T$$

  with z given in μm and T in degrees Celsius.

The so called "bad points"

The ultrasound probe that is being used must contact the lead surface in a parallel way. The mechanical system that brings the probe down leaves a small angle of freedom so that it can adapt to the plate surface. When there is a bump or some other sharp imperfection, the Krautkramer device will not be fully reliable anymore.

These "bad points" can be classified into two types:

- (I) Sometimes the superficial defect is not too sharp and several readings at the same point give correct thickness values, but with a distribution width larger than at normal points (typically, $10\,\mu m$ instead of $1\,\mu m$).
- (II) Other points exist where the same distribution as in the previous case is obtained, but now with some additional manifestly wrong readings.

The number of bad points found on the variable thickness plate used in this study, was 5 (out of 357). They always appeared close to the edge of the plate. This fact makes them less important, because these regions of the plate do not become part of the absorber. However we should be ready to handle such data when they appear.

Let us imagine the distribution of many readings made at a type II point. It is expected to be gaussian-like with a width of about $10\,\mu m$ and a few events very far away from the central value. The probability of getting one such event is small (say $p << 1$). If we make three measurements at each point and retain the median value, the probability of having a bad reading is of order p^2, assuming the three measurements are independent. This is the best result that can be achieved without increasing too much the time of operation per plate. Of course, the possibility of still getting a bad reading can not be discarded. Different selection criteria could be considered but such refinements are probably unnecessary and could always be implemented a posteriori. In any case, visual inspection of a thickness map should always be performed as a last check. Examples of such maps can be found in Fig 4.13, 4.14.

4.1.6 Control of the finished absorber geometry

The absorbers for the ATLAS LAr calorimeter have a very complicated geometry. Therefore, in order to ensure that a given absorber has the correct shape, a number of quantities need be measured. The measurements that are performed on each absorber (see 2.4.3), along with the quantities that are calculated with them, are briefly described in this section. Further details may be found in [27].

Description of the geometric dimensional control

The geometric dimensional control done on absorbers consists of the following:

- Optical inspection looking for defects.
- Thickness measurement of the ensemble steel-prepreg-lead-prepreg-steel at some predefined points of the absorber. The measurement is done manually using a Palmer micrometer.
- Measurement of the overall dimensions (length and width), done at different positions along the absorber. The measurements are performed with a precision meter.
- 3-D mapping of the absorber surface, using a 3-D measurement machine.

A thorough dimensional control, consisting of all the items mentioned, is performed on 10% of the absorbers. For the rest, the 3-D mapping is not done and a smaller number of width, length and thickness measurements is performed.

Geometrical quantities obtained from the measurements

The measurements described above directly provide or are used for the calculation of the following geometrical parameters:

- Absorber thickness.
- Angles between half-wave surfaces (calculated using the 3-D mapping).
- Position of the folds (calculated using the 3-D mapping).
- Length and width.

In each case the measured quantities are compared to their nominal values and required to show deviations compatible with the tolerances.

Tolerances are calculated for each geometrical parameter in such a way that the correspond to a 2% tolerance in the liquid argon gap. This choice leaves room for three independent effects added up in quadrature, to yield the total tolerance on the gap (3%).

4.1.7 Conclusion on dimensional control of absorbers

The dimensional control for the absorbers of the ATLAS LAr EM calorimeter consists of three stages that have been explained in this section. The complete control scheme was applied to the absorbers for the EMEC module-0 studied in this thesis, and is now routinely applied to the absorbers being produced for the 16 ATLAS EMEC modules [2].

Lead thickness measurement based on X-rays has proven as an invaluable online help for the producer. The ultrasound system, providing more accurate measurements, fulfills the addressed requirements for lead thickness control.

The dimensional control of the absorber geometry is the last stage of the quality control system. Tolerances for the different precision measurements are calculated in order to guarantee a deviation of the liquid argon gap between an absorber and the neighbouring electrode in the module at the level of 3%.

4.2 The absorbers produced for module-0

4.2.1 Introduction

The goal of this section is to review the results of the dimensional quality control performed on the absorbers of the ATLAS LAr EMEC module-0, following the scheme explained in the previous section. The analysis is based on [28], [27]. A total of 106 large and 54 small absorbers were manufactured for module-0. The absorbers installed in the module were chosen among these. For each absorber the following data were gathered:

- Lead thickness values measured with the ultrasound system, at points on a $5 \times 5\, cm^2$ grid covering the whole plate (some 440 points on large absorbers and 100 on small ones).
- Some additional information about the absorber and the ultrasound measurements.
- Lead thickness measurements performed at the factory using the X-ray system, on a grid of about $10 \times 10\, cm^2$ (i.e. coarser than that of ultrasound measurements).
- Geometrical measurements done on the finished absorbers.

[2] Lead production and X-ray thickness control were finished for the 16 modules in April 1997. Ultrasound thickness control was already performed on the plates of the modules 1 and 2 in November 1998-January 1999 and modules 3 and 4 in November 1999 (the four modules correspond to $\simeq$ 440 plates).

The analysis of the data consists of five parts (see [28], [27]):

- First we will see qualitatively what the thickness profiles of lead plates look like.
- It is very important to check that the calibration of the ultrasound measuring device is stable. This type of check was done on each plate and is thoroughly analyzed.
- The thickness quality of each lead absorber plate can, to a first approximation, be summarized in two numbers: thickness mean and RMS. The main result concerning lead thickness is the description of what typical values we get for these two parameters and how they vary from absorber to absorber. The results are compared to the specifications established in section 4.1.
- A consistency cross-check of X-ray and ultrasound measurements was done. The former are not expected to be precise enough as to replace the latter (although this possibility should not be discarded in principle), but still one would like to take profit of the fact that both measurement systems are independent, in order to make sure that they work properly.
- Finally the measurements describing the finished absorber geometry will be briefly described and compared to the specifications.

4.2.2 Lead thickness measured with ultrasounds

The basic unit of information regarding thickness control is the ABSORBER. However it must be kept in mind that small absorbers can be naturally grouped is sets of three, coming from the same lead plate (see Fig 4.5). Some of the information available about an absorber will be the same for each group of three small absorbers.

Some qualitative features of lead thickness profiles

A periodic modulation of thickness along the roll has been observed in ultrasound thickness maps. Fig 4.6 shows two examples. The rolling direction is that defined by the X-axis. The modulation is apparent in the plate shown in the upper part of the figure. X-ray online measurements had already suggested this effect. The wavelength of the modulation is comparable to the perimeter of the rolling steel cylinders. Therefore the effect is understood in terms of a small misalignment of the cylinders.

Another outstandig feature observed on most plates is the appearance of incorrect thickness readings whenever the plate shows surface defects. If one goes back to the point

where a strange thickness value was obtained and measures carefully it can be seen that the reading is not stable. These measurements, appearing on the map as sharp peaks, should thus be regarded as spurious (this type of "bad points" were discussed in 4.1.5).

Information about absorber thickness control on the www

All data from thickness measurements on plates used for module-0 are available through the World Wide Web [3]. For each absorber plate there is a file containing the ultrasound and X-ray thickness measurements performed on the plate, along with some useful information about the absorber. A detailed explanation of the contents and format of the files can be found in [28]. A complete database with lead thickness information for all the absorbers in the two EMECs will also be available on the www.

Calibration monitoring of the ultrasound system

In order to check that calibration was stable throughout the measurement process, thickness was measured with the Palmer (*p-thickness*) and with the ultrasound system (*u-thickness*) at a reference point on every plate. Fig 4.7 shows the difference between these two values for all plates. The mean and RMS of the distribution agree very well with the expected result ($9 \pm 3\,\mu m$, see 4.1.4). In Fig 4.8 the same data are separated into two groups: measurements on $2.2\,mm$-thick plates and on $1.7\,mm$-thick ones. The difference detected between the mean values is compatible with the error bar given in section 4.1 for the speed of sound. This proves that the absolute calibration was stable throughout the period of mesurement. Even so, one should keep in mind that thickness is not the only difference between these two groups of plates: there is also the fact that Palmer measurements were performed by different operators and that the micrometer itself gave some problems. Before going any further a glance should be taken at Fig 4.9, which shows all measurements done on $1.7\,mm$-thick plates classified according to the Palmer operator.

The micrometer was found not to be working properly at some moment during the measurement of the first $1.7\,mm$-thick plates (once all $2.2\,mm$-thick ones were measured). This misadjustment was detected partly due to the slight disagreement between the p- and u-thickness actual difference and the expected value. The measurements performed before the detection of this problem were done by operators 1 and 2. No information about the operator doing each individual measurement was kept at this stage. After the Palmer was readjusted and checked to be working fine we obtained basically the values attributed individually to operators 1, 2 and 3 (Fig 4.9). The agreement between different operators is quite good, although the three distributions do not look exactly the same.

[3] See URL address http://www.uam.es/Alt.Ener/plomo.html (accessible from ATLAS pages).

The conclusions of this study about calibration are:

- The absolute calibration of the ultrasound device kept stable throughout the whole process.
- Monitoring the difference between p- and u-thickness is important in order to detect possible misfunctioning of any of the two devices involved. In this case the Palmer gave some problems, which were promptly detected and solved.

Therefore, when thickness control has been performed for further modules, even more attention has been paid to this type of check.

Quality of absorbers: mean thicknesses and RMS's

The most powerful and simple way to visualize at a glance if lead production was satisfactory is to look at the thickness mean and RMS of each absorber, as given by ultrasound measurements. This information is shown in Fig 4.10 for small absorbers and in Fig 4.11 for large ones. The spread of the mean thickness values is small in both cases, and all RMS's are well below the $17(22)\,\mu m$ for large (small) absorbers, addressed in 4.1.1 as tolerance. In fact results are so good that one can try to go further and ask oneself why there are a few absorbers with "just good" RMS values whereas others are excellent. Is there any correlation between these "non-excellent" RMS's and the mean thickness value ? Does this correlation show up if parameters characterizing the absorber other than the mean, like the roll number, are taken into account ?

The answer to the first question can be extracted from Fig 4.12 (for small absorbers in the upper plot and for large ones in the lower one). Each point represents an absorber, whose mean thickness and RMS are given by the x, y coordinates. Small absorbers with larger RMS do not show any tendency to have especially large or small mean thickness. For large ones it seems that higher RMS's are correlated with lower means. This suggests that these "non-excellent" $1.7\,mm$-thick plates come from a certain roll, or even from a part of a roll, in which the laminating machine operation was not as stable as in the rest.

These are good suggestions to go on investigating where these somewhat larger RMS's come from for large absorbers, and this will be done below; but what about small ones ? Why there are four absorbers (see Fig 4.10 or 4.12 upper) with an RMS noticeably larger than the rest ?

To begin with, these "singular" small absorbers come from only two plates (two from each). Besides this, some of the $2.2\,mm$-thick plates showed a lot of superficial scratches, giving rise to unphysical thickness readings. One could think that these four absorbers

are really as good as the rest, but they just have too many scratches and this spoils the RMS. The best way to test this hypothesis is taking a look at a histogram with all u-thickness measurements of a high-RMS absorber and comparing it with the same graph for a low-RMS one. Fig 4.13 shows such a histogram along with the u-thickness map for a low-RMS absorber (upper) and for a high-RMS one (lower). It is easy to notice that the large value obtained for the RMS in the second case is due to a few bad thickness readings that appear isolated on the map and can be regarded as spurious. Supressing these few data one would get something much similar to what is shown in the upper figure. In fact, the gaussian fit gives close sigma values for both absorbers. The other three small absorbers with RMS above $8\,\mu m$ look much the same as this one, so the same conclusion can be extracted for all.

Let us now move on to large absorbers. We can take advantage from what we just learned from small ones. However in this case, Fig 4.14 shows that the absorber of the upper plots does not have an unphysically large RMS due to a few isolated measurements, but rather a truly larger thickness spread without apparent structure. It seems that at some part of the production process operating conditions were significantly better than the rest of the time. If we classify the 106 RMS values coming from large absorbers depending on the roll the plate was cut out from, we get the plots shown in the upper part of Fig 4.15. All absorbers with RMS $> 8\,\mu m$ come from roll 10. We still see two types of absorbers in this roll. The lower part of the figure shows the RMS and mean for each absorber as a function of the position they occupy in roll 10. At the beginning worse RMS values are found and the situation steadily improves as we go on along the roll. The mean thickness also shows a slight drift.

Therefore and to sum up, we have been able to detect very fine effects of the rolling procedure at the factory. This makes our data more reliable and confirms that the quality of the lead plates is excellent.

4.2.3 Cross-check of X-ray and ultrasound thickness measurements

Study of a particular plate

A nice exercise that can be done with the thickness data is to choose an absorber and compare the thickness maps obtained with the two measurement methods: X-ray and ultrasounds. However this idea involves some problems: visual comparison of two thickness maps can not be expected to give very precise information; and, most important, the grid on which x-thickness was measured does not coincide with the one chosen for u-thickness control. Therefore point-to-point thickness comparison requires a previous interpolation process.

Thickness measurements at different points of a plate done with the two methods can be regarded as the result of sampling a two-dimensional random variable, say (X,U), where the first component is x-thickness and the second one u-thickness. If everything were perfect, X and U should exactly coincide for all events, except for, perhaps, a global offset due to a different calibration. Therefore we would expect the random variable $X - U$ to have a mean close to zero and vanishing RMS. There are mainly two reasons why one can not expect to see such a behaviour in reality:

- Thickness resolution attained is good, but not perfect. For ultrasounds, individual measurements carry an uncertainty of about one micron (negligible), but the X-ray system is not so accurate (in particular the relative calibration of the PMTs).
- In practice we compare each x-measurement not to a true u-measurement, but to a smoothed (interpolated) value. This intermediate step introduces an additional uncertainty.

If X and U were not correlated at all, the RMS of $X - U$ would be just the quadratic sum of the separate RMS's. Anything significantly below this limit is a proof of the correlation we expect to see.

Fig 4.16 shows the two thickness maps for a given absorber. One can see some similarities between them but, as expected, no conclusions can be drawn from visual comparison. In Fig 4.17 we can see the corresponding distributions of u-thickness (top), x-thickness (center) and x-minus-smoothed-u (bottom). The mean of the difference is $2\,\mu m$ and the sigma is $8.7\,\mu m$, significantly smaller than the $11.6\,\mu m$ one gets when adding quadratically the sigmas of the two separate distributions. This proves that thickness measurements performed with the two methods are correlated.

Study of all absorbers

The analysis showed in the previous section was good to illustrate the subject. In practice it is enough to compare the mean thickness of absorbers calculated with x or u-data. In particular it is interesting to see how X-ray performance changes from roll to roll. We would also expect to see a somewhat worse behaviour for small absorbers, both because we have fewer x-measurements per absorber (the uncertainty of the mean scales like the inverse squared root of the number of measurements) and because the intrinsic resolution of the X-ray method itself is expected to deteriorate with increasing lead thickness.

Fig 4.18 and 4.19 compare u- and x-mean thickness values of absorbers classified in rolls. For each roll we have on the left a diagram where each absorber has a representative

point, whose coordinates are the mean thicknesses measured with the two methods. The line $y = x$ is shown as a reference. On the right half, we show how the mean thickness difference between the two methods is distributed.

Rolls 8 and 9 show a similar behaviour: u and x mean thickness values are apparently correlated with a miscalibration of about $10\,\mu m$ (see mean of histograms on the right). The RMS of the difference is very small. This means that ultrasounds and X-rays are reproducing the same information, to within a few microns, except for a global offset.

Roll 10 shows a very different behaviour. Now the global offset is not present anymore, but the RMS of the difference is larger than in the previous cases. Fig 4.20 separates absorbers from roll 10 into those coming from the first part of the roll (with RMS larger than $8\,\mu m$) and those cut from the second part (RMS smaller than $8\,\mu m$). It seems that the X-ray system didn't measure in the same way at the beginning and at the end of the roll (notice the different means of the two histograms). The reason for this is not understood.

On roll 11 (small absorbers), also shown in Fig 4.19, the global offset is recovered and the dispersion increases by a factor of three. This is more or less what one would expect from the $1/\sqrt{n}$ scaling effect explained above. It is somewhat puzzling to find two clusters of points, peaking at 5 and $20\,\mu m$. Absorbers belonging to these two groups do not have any systematic property in common (like coming from the same part of the roll, etc...). Perhaps this is, after all, just an effect of not high enough statistics.

To summarize this section, correlations between X-ray and ultrasound thickness measurements are very apparent on all plates, but there are still some details suggesting that the X-ray system is not fully stable.

4.2.4 Conclusions on thickness measurements

The thickness of the lead plates used for module-0 was controlled following the scheme explained in section 4.1. All the data are available through the World Wide Web so that they can be used by any member of the collaboration.

The absolute calibration of the ultrasound thickness measuring system was checked to be stable and the cross-check with X-ray measurements yielded consistent results (although a few details suggest to keep both methods and do further checks in the future). However, perhaps the most important conclusion has been somewhat obscured by the large amount of information given. The main motivation for doing such a detailed thickness control on lead absorber plates was to assure that, say, an electron, would traverse lead layers of the same thickness (with very high precision) when flying across the EMEC. How precisely are these succesive layers equally thick ? Can we synthesize all the analysis of these pages

in a couple of numbers answering this question ?

If a particle flies across the EMEC it will generate a shower that will develop crossing about 40 lead layers (ten accordion waves times four absorbers sharing a given η , ϕ direction). Each particle of the shower will go through the layers at different points. To sum up, we have a lot of particles multiplied by a lot of crossings, and would like to have an idea of how the thicknesses associated to all these absorber points are distributed (in particular we are interested on the spread of the distribution). All these points belong to a few adjacent absorbers (as placed in the detector). However, probably the best is to stick to the most conservative point of view: just take the thickness at many different points of all absorbers of a given type. This can be done by just putting together all ultrasound thickness measurements done on absorber plates for module-0 at Madrid. Fig 4.21 shows this distribution for large and small absorbers, and the result is really excellent: the RMS's are both below $10\,\mu m$, i.e. well below tolerances. It remains to be verified that this level of homogeneity can be maintained for the whole set of plates necessary for at least one end cap (8 times the amount analyzed here) [4].

4.2.5 Results on the dimensional control of the geometry of the finished absorber

In this paragraph a brief summary of the results obtained in the dimensional control of the finished absorber geometry for module-0 is presented. For further details see [27].

Thickness

The absorber thickness was controlled at points near the absorber edge, both at the acute and at the obtuse fold angle side. The RMS of all the measurements done on large (i.e. outer wheel) absorbers at the acute side is $26\,\mu m$ (tolerance $110\,\mu m$, from LAr gap uniformity requirements, see 4.1.1), and at the obtuse side $33\,\mu m$ (tolerance $36\,\mu m$). For small (i.e. inner wheel) absorbers the measured RMS was $43\,\mu m$ (tolerance $110\,\mu m$) at the acute side and $48\,\mu m$ (tolerance $60\,\mu m$) at the obtuse side. Therefore the requirements are correctly met for both types of absorber.

[4] The results of analyzing X-ray and ultrasound thickness measurements for modules 1 and 2 [29] are similar to the ones presented in this thesis for module-0.

Angles of half-wave surfaces

The angle between two consecutive half-wave surfaces was studied at different positions on the absorber. Notice that the nominal angle varies smoothly from the acute to the obtuse side. The result of the measurement was compared to the nominal value for each different absorber region.

For large absorbers the measured angle shows a dispersion around the nominal value well below or, in the worst case, compatible with the specifications. Fig 4.22 shows the deviation from the nominal value for eight different regions on the absorber. The worst result is that obtained for the most obtuse side, where the RMS obtained is slightly above the tolerance.

For small absorbers a systematic "jitter" of the measured angles around the nominal value was detected (i.e. the measured angle is larger than nominal in odd waves and smaller in even waves). This effect was believed to be related to the systematics of the 3-D measurement, introduced by the support frame used. The reproducibility of the angle at each given position for different absorbers was found to be well within tolerances.

Folds coordinates

The typical measured dispersions around nominal of the fold positions, both for large and small absorbers, are 100(50) μm on the acute (obtuse) side of the absorber, within tolerances.

A global shrinkage effect, of order 1 mm, was detected for the two types of absorbers. This effect is not critical because of its reproducibility and the fact that absorbers are not completely rigid. The absorbers of module-0 were mounted in the support structure without any mechanical problems.

Conclusion on absorber geometry

The different geometrical measurements briefly summarized in this section show that the nominal absorber geometry was achieved with the accuracy needed in order to guarantee a contribution to the energy resolution constant term below the specifications.

4.3 The EMEC module-0: from assembly site to test beam area

4.3.1 Module assembly

The assembly of module-0 was done at CPPM in the summer of 1998, using the same techniques foreseen for the 16 modules to become part of the EMEC.

Absorbers are guided to their position in the module along the six main support rings. The innermost and intermediate rings at the front and back, support small absorbers, whereas the intermediate and outermost rings support the large ones. The edges of the absorber side bars are fixed mechanically to these rings. The remaining four rings (two in the front and two in the back) can be regarded as complementary. They are used to fix two more intermediate points of each large absorber side bar.

The three main support rings are attached to the stacking frame shown in Fig 4.23, so that both large and small absorbers can be guided to their correct position sequentially, making use of their own weight. In the case of large absorbers, the dimensions and weight induced the usage of a vacuum lifter system supported by a crane (see Fig 4.24).

Between two consecutive absorbers an electrode was placed. The honeycomb spacers had been glued previously on both sides of the large electrodes using a mixture of ARALDITE and DURCISSEUR. It was not necessary to glue them in the case of small absorbers. The electrodes are not mechanically attached to the support rings, being held in place due to the pressure exerted on the spacers by the two adjacent absorbers.

The module was equipped with 60 large absorbers and 24 small ones. Only the central part was filled with electrodes, in a total number of 19 (large) and 6 (small).

The whole assembly process and HV tests, to be described on a later section, were performed inside a clean room, in which a small overpressure, supplied through filters, was kept w.r.t. the outside. Special clean clothes were used throughout the process. Any small debris coming from cutting, carving or scratching operations was immediately vacuum cleaned.

4.3.2 Module manipulation and transport

After module assembly, the top part of the whole structure (module and stacking frame) was closed with a frame similar to the one below the module, in order to obtain a symmetric shape for manipulation. Fig 4.25 shows the whole structure, with a void in the place where the module was mounted. The weight asymmetry due to the module geometry was

compensated by attaching lead blocks to the stacking frame.

The so called *spatule* (see Fig 4.26), that plays the role of a table on which the module is layed, its back side facing down, was attached to this back face of the module. The three legs of the spatule were equipped with wheels.

The next operation consisted of turning the whole structure by 90^o in order to leave the module resting on the spatule. This was accomplished using a device called *rotomax*. The rotomax [5] is a shaft that rotates around an axis parallel to the ground, while suspended by a crane, hanging from its midpoint. The structure to be manipulated is hung from the rotomax using two wide and strong material bands, each of them hanging from one edge of the device. As the shaft rotates, friction forces the bands and the structure to follow this rotation.

Once the rotation is finished the structure is layed down, supported by the spatule. The complementary structure around the module is disassembled and removed using the crane. At the end only the module itself is left, resting on the spatule.

Transportation from CPPM to CERN was done on a truck, using a special support system to minimize vibration of the module.

4.3.3 Installation in the cryostat, cabling and read out system tests

The EMEC module-0 was tested inside a cryostat [6] with the shape of a rectangular box, the upper wall being removable by usage of a crane. This upper wall, once removed from the rest of the cryostat, was used to attach the module to its inner (i.e. lower) face, through a proper mechanical interface. The module was thus hanging from this piece of the cryostat. The ensemble was introduced in a clean room where cabling and testing were done. All these manipulations were done already at CERN.

Once in the clean room, summing boards and motherboards were installed. The cables for signal read out and those for test pulse injection were connected to the motherboards, at one end, and to the inner side of the cryostat feedthrough, at the other end. The outer side of the feedthrough was connected to the FEC, which sitted physically on the outer side of the removable cryostat wall from which the module was hanging. In the FEC different types of boards were connected. The two types that are important for this thesis are the calibration board and the FEB. The former is used to generate test pulses to be

[5] The rotomax is manufactured by *Ateliers Demarchi*, Arches, France. The reference number of the device is RVE 5000/2.0.

[6] The cryostat had been formerly used by the NA31 experiment.

injected to the read out chain, whereas the latter is used for signal read out. The cabling was carefully checked at room temperature, using test pulse injection.

The module was introduced in the cryostat, attached to the movable wall, using a crane. The same mechanical operation played the role of closing the cryostat and positioning the module inside. Once the cryostat was filled with liquid argon, cabling tests were redone with satisfactory results.

4.3.4 High voltage tests

Warm tests

HV tests start at the factory where electrodes are manufactured, checking that the internal kapton gaps (between the external copper layers and the internal one) hold a voltage difference of order 2000 v.

The same kind of test was done again, after the electrodes had been folded, inside the module assembly clean room at CPPM, before mounting. The whole signal layer was grounded and a voltage ranging from 2.5 to 1.0 Kv for the 7 HV channels (i.e. selecting HV values similar to those to be applied to the different regions of the electrode during test beam operation) was supplied to the external HV layers.

Incidentally, some signal connectors and HV coupling resistances had to be removed after this HV test, in order to avoid undesired electrical contacts or high current leakage.

After each electrode was mounted between two absorbers in the module, the stability to HV of the gap absorber-electrode was also tested. In this case, since the test was done in air (and not in LAr), a voltage of 1000 v was considered enough. However higher voltages were also applied, providing useful information. The test was done grounding the absorbers and supplying HV to the electrode external layers, and then redone grounding also the signal layer.

After all these tests, a set of 12 consecutive large electrodes was guaranteed to function properly. This set of electrodes, along with the corresponding set of 4 small ones (covering the same ϕ region) defines the active channels used for beam test operation and analysis.

Warm HV tests were redone systematically at CERN after module transportation. Detector channels with problems were carefully recorded in order to use this information in the data analysis.

Cold tests

Once the module was in LAr, the nominal HV values were applied to the different electrode regions. Some additional HV problems appeared at this stage. They were also recorded for usage in the analysis.

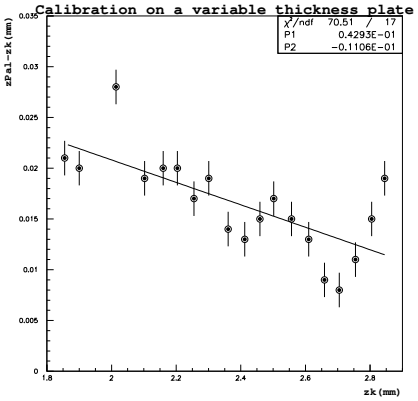

Figure 4.1: $z_{Pal} - z_k$ vs. z_k. Fit to a straight line ($v_k = 2.238 Km/s$).

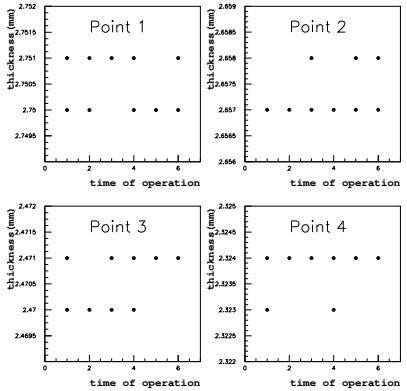

Figure 4.2: Stability of the thickness measurement versus time of operation at four different points of a plate.

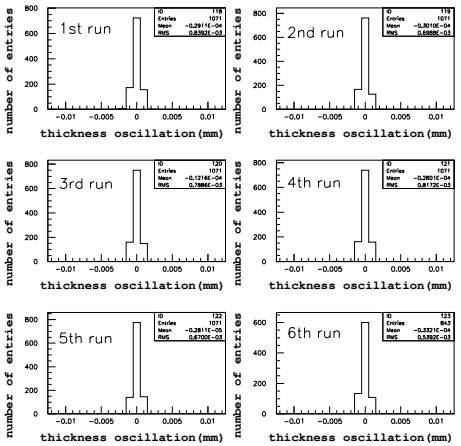

Figure 4.3: Distribution of measurement oscillations at the same point for six plate scans done the same day.

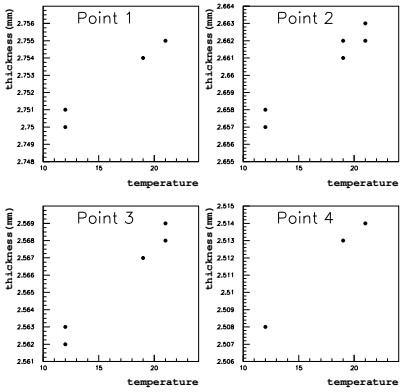

Figure 4.4: Temperature dependence of the thickness measurement. Data taken at four different points.

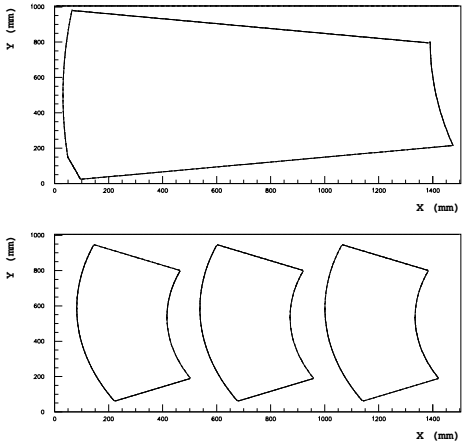

Figure 4.5: Absorber lead shape and lead plate coordinate system.

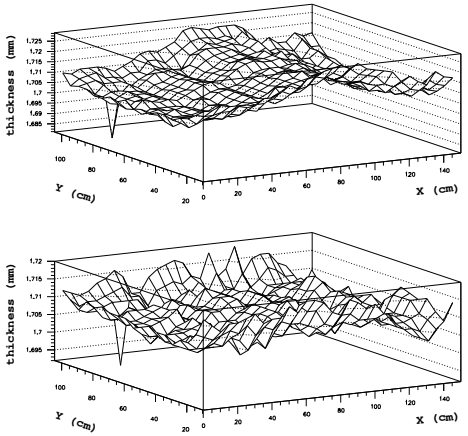

Figure 4.6: Thickness map of two lead plates.

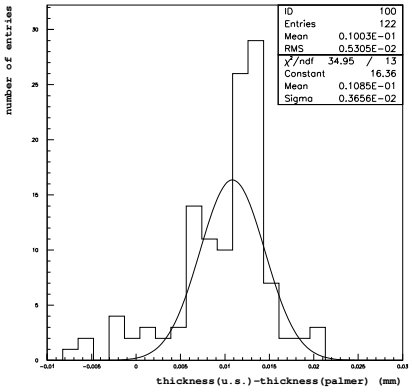

Figure 4.7: Calibration control: difference between u-thickness and p-thickness for all plates.

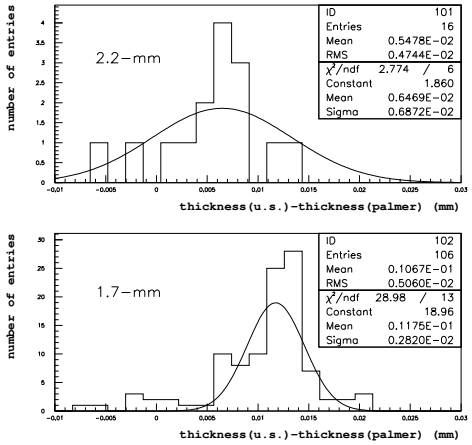

Figure 4.8: Calibration control: difference between u-thickness and p-thickness for plates classified by their nominal thickness.

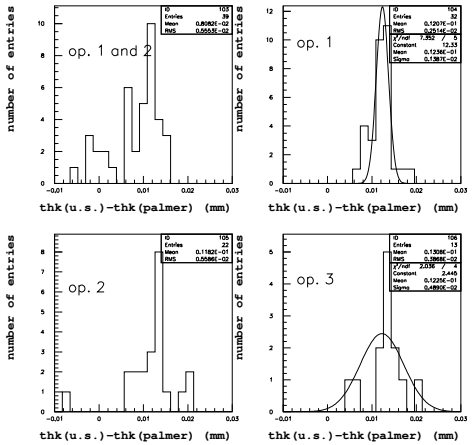

Figure 4.9: Calibration control: difference between u-thickness and p-thickness for 1.7 mm-thick plates measured by different operators. The upper left plot corresponds to the period during which no information about the person doing each individual measurement was kept.

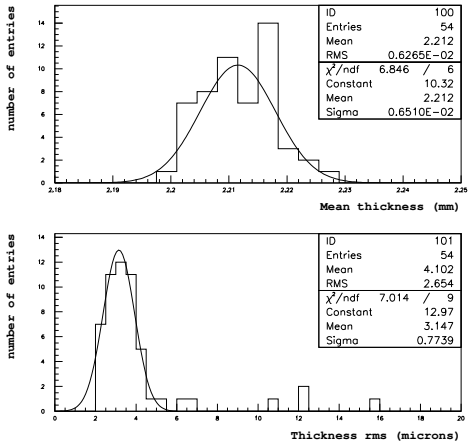

Figure 4.10: U-thickness mean and RMS of all small absorbers.

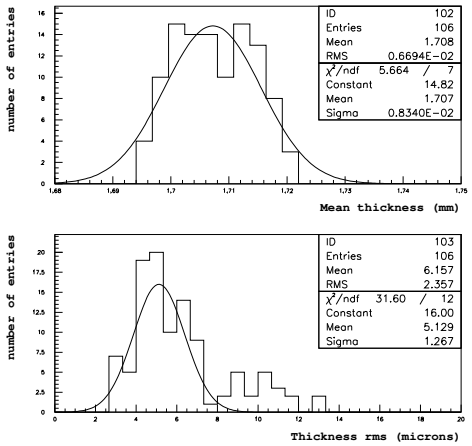

Figure 4.11: U-thickness mean and RMS of all large absorbers.

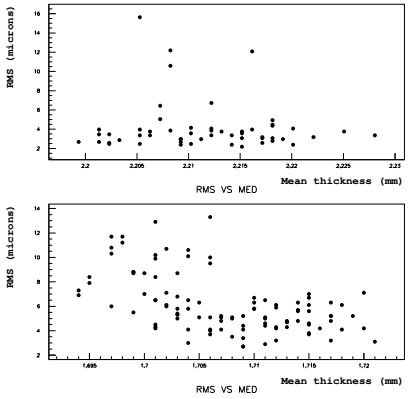

Figure 4.12: Correlations between u-thickness mean and RMS of all small (upper) and large (lower) absorbers.

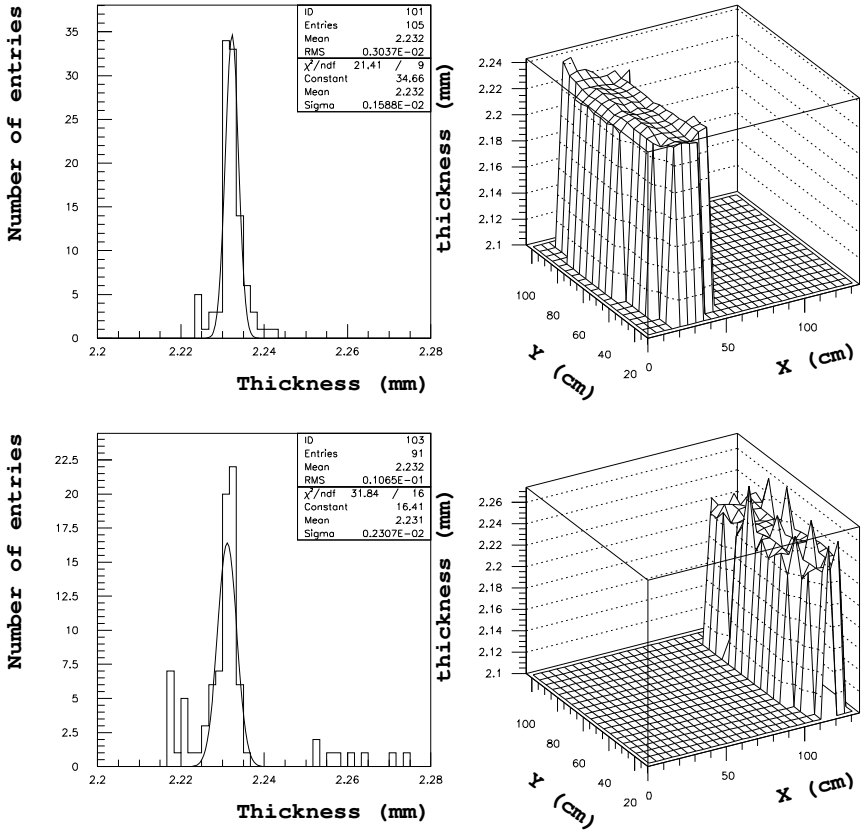

Figure 4.13: U-thickness measurements and maps of two small absorbers.

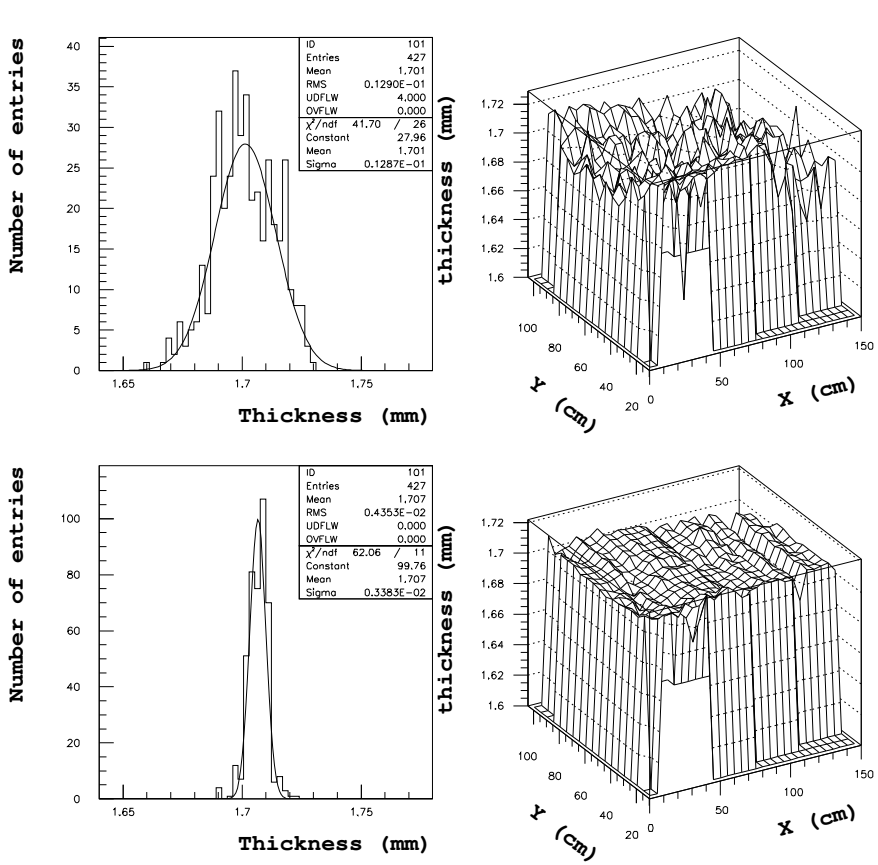

Figure 4.14: U-thickness measurements and maps of two large absorbers.

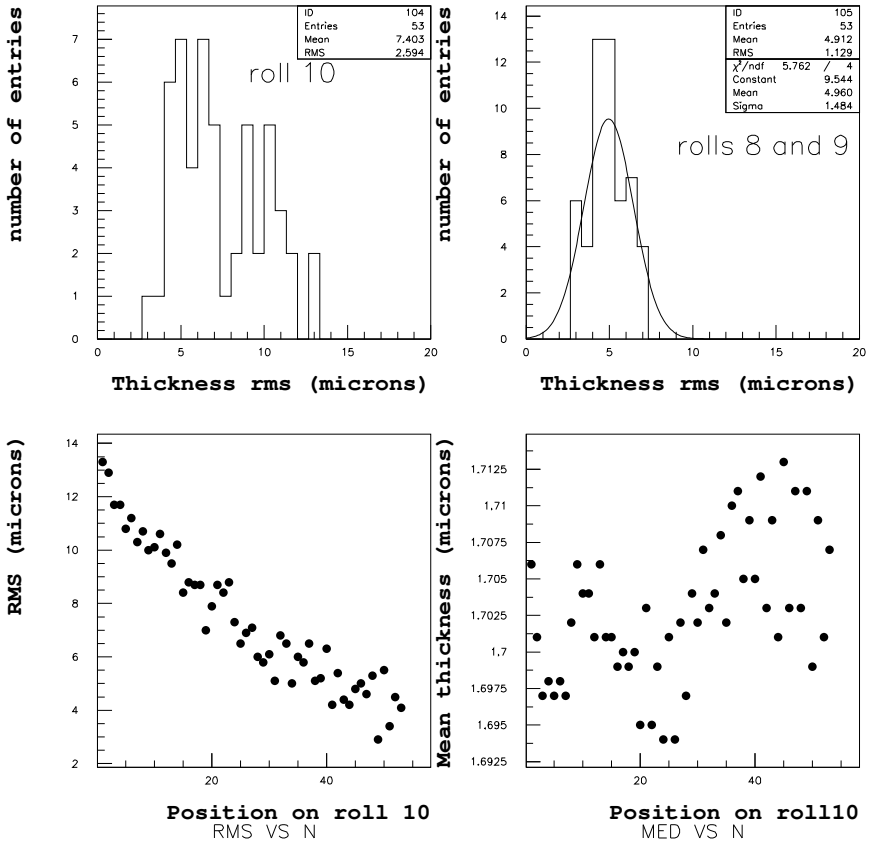

Figure 4.15: U-thickness RMS values of large absorbers classified by rolls (upper) and RMS and mean for roll 10 as a function of position on the roll.

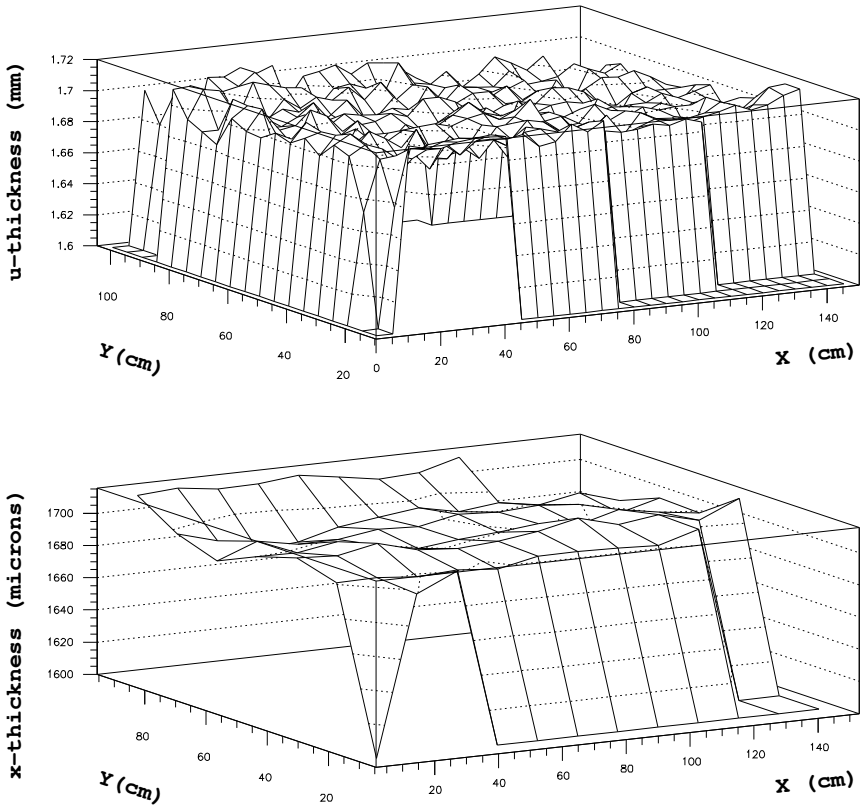

Figure 4.16: Thickness measured with ultrasounds (upper) and with X-rays (lower) for a large absorber.

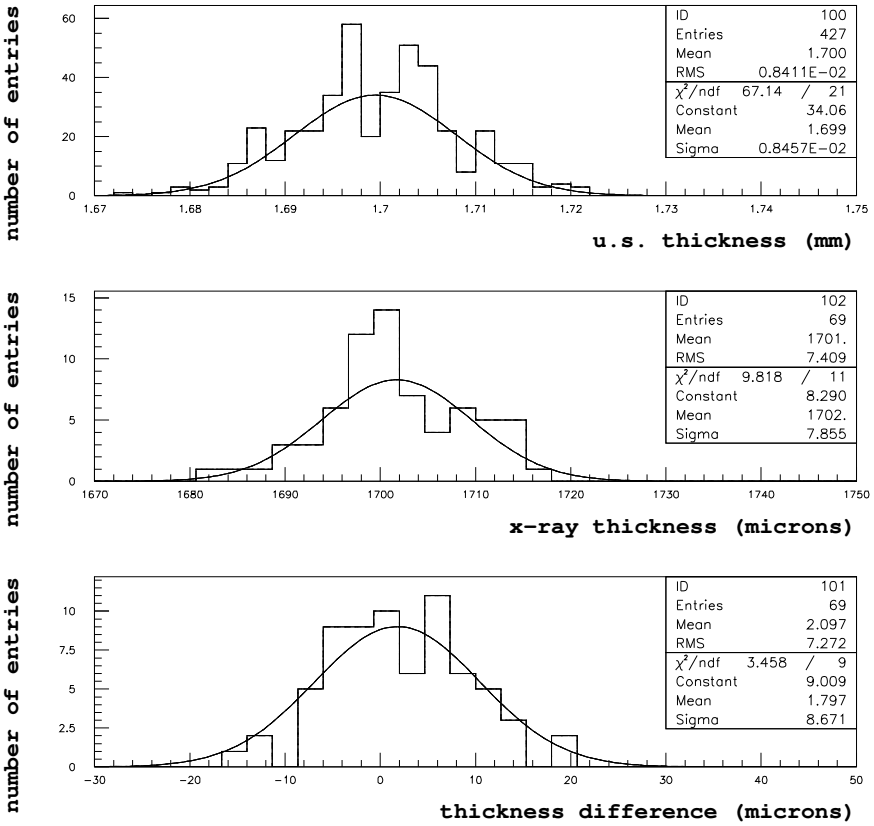

Figure 4.17: U-thickness, x-thickness and difference at the same point (with the smoothed ultrasound value).

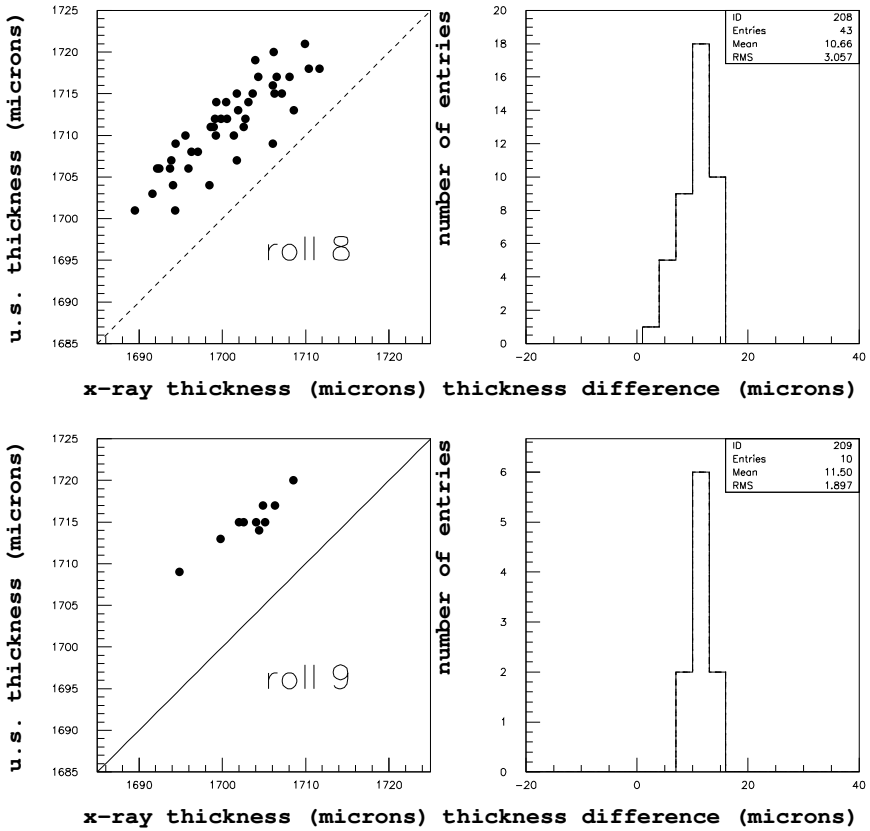

Figure 4.18: Mean thickness of absorbers: correlation between ultrasound and X-ray (left); difference between the two methods (right). Rolls 8 and 9.

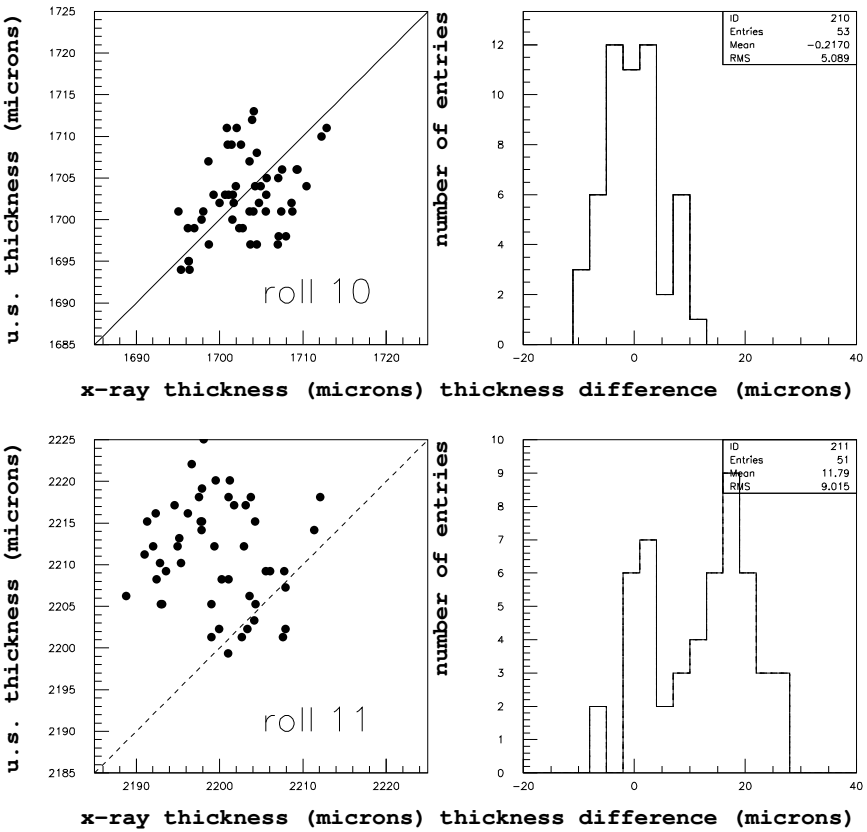

Figure 4.19: Mean thickness of absorbers: correlation between ultrasound and X-ray (left); difference between the two methods (right). Rolls 10 and 11.

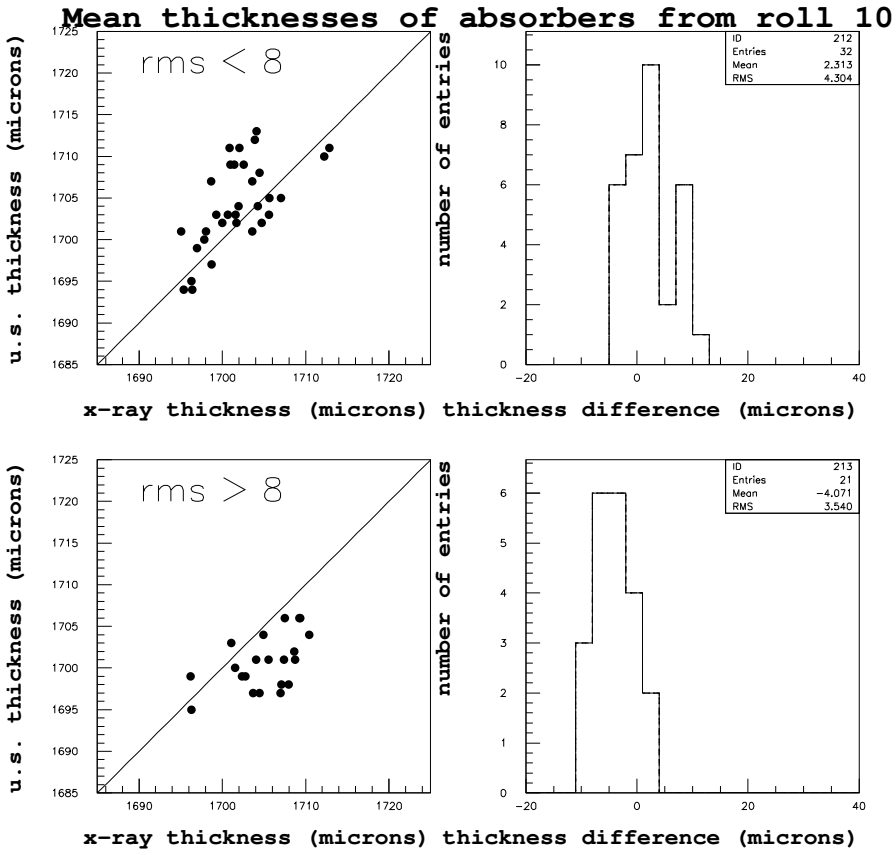

Figure 4.20: Mean thickness of absorbers with low and high RMS (roll 10): correlation between ultrasound and X-ray (left); difference between the two methods (right). Roll 10.

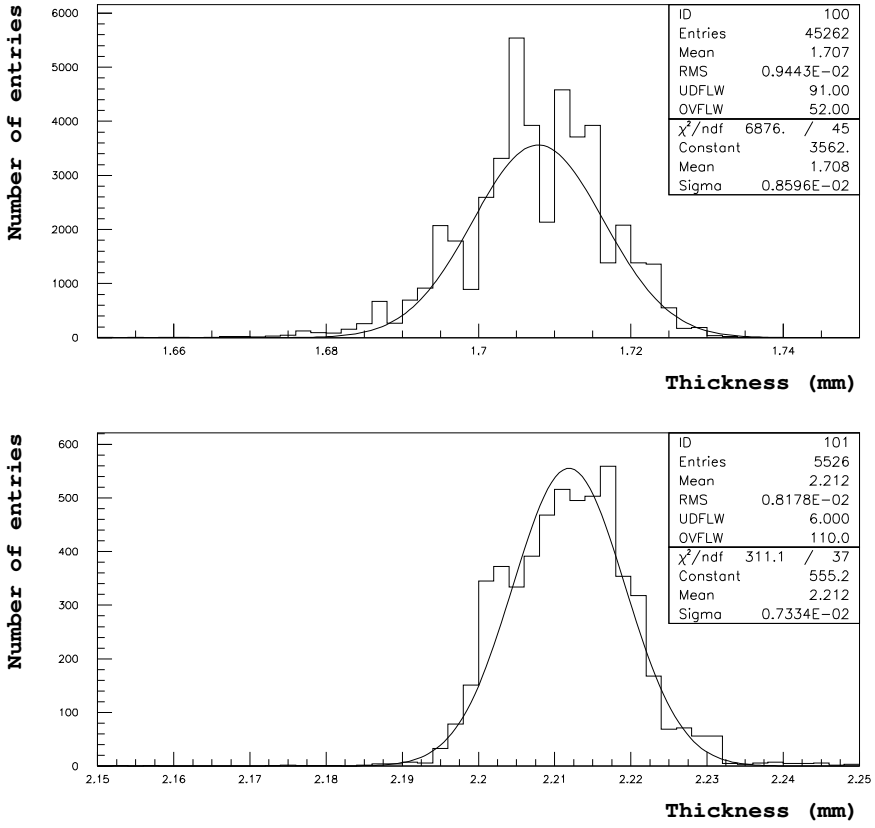

Figure 4.21: All thicknesses measured with ultrasounds on large (upper) and small (lower) absorbers produced for module-0.

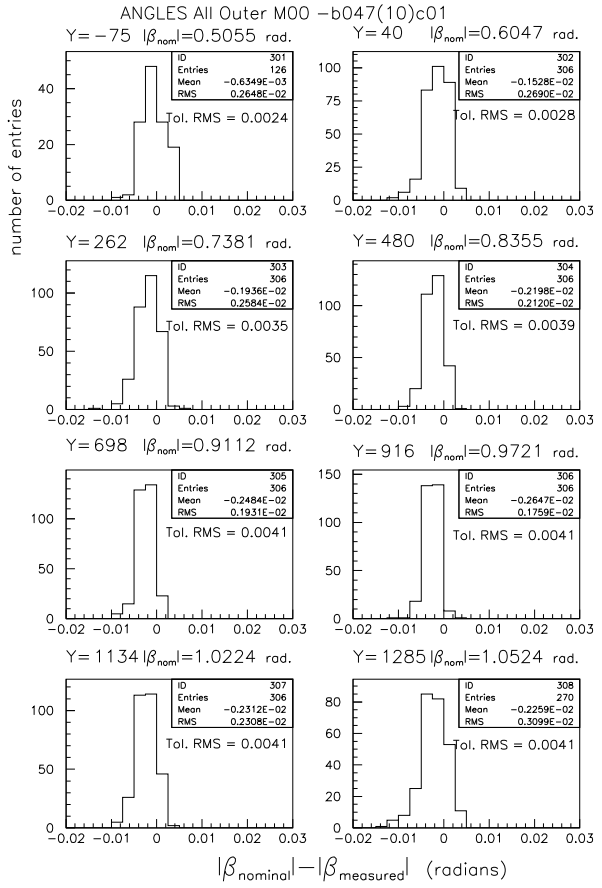

Figure 4.22: Histograms for the deviations w.r.t. nominal of the measured half-wave surface angle at eight different scan lines. Data from all the module-0 large absorbers are shown. RMS tolerances are given in radians. The lowest Y value is at the obtuse side of the absorber; the highest Y is at the acute side.

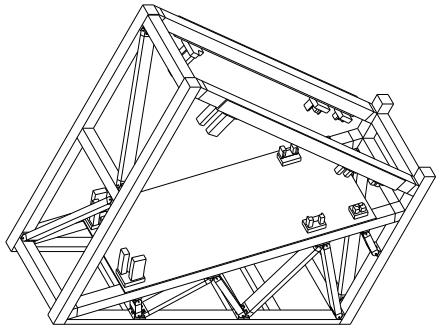

Figure 4.23: Stacking frame.

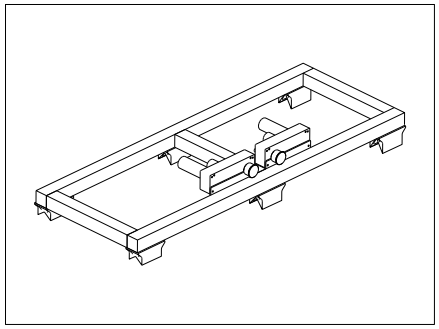

Figure 4.24: Vaccuum lifter. Notice the shape of the suckers, adapted to the absorber folds.

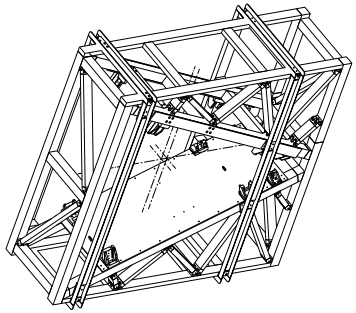

Figure 4.25: Stacking frame once closed after module assembly. A void can be seen in the place where the module should have been mounted.

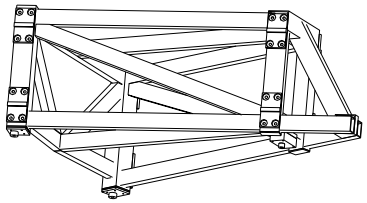

Figure 4.26: Spatule.

Chapter 5

Beam test of the EMEC module-0

5.1 Introduction

In September 1998 an EMEC module partially equipped with the final ATLAS design was tested in the CERN SPS H6 test beam facility. A detailed analysis of the data can be found in [30]. An independent analysis also performed at UAM can be found in [31].

The chapter is organized as follows: section 5.2 gives a general description of the module; section 5.3 gives an idea of the beam test set up; signal reconstruction is dealt with in section 5.4, with details about features of the data collected in the test; calibration is discussed in section 5.5; section 5.6 reviews in some detail the different systematics of the reconstructed energy signal; results are given in the following sections: energy resolution and linearity in section 5.7, position reconstruction in section 5.8, energy signal dependence on the voltage applied across the LAr gap in section 5.9 and time reconstruction in section 5.10; section 5.11 discusses the momentum spread of the test beam; finally the conclusions are drawn in section 5.12.

5.2 Description of the EMEC module

The EMEC module-0, tested in September 1998, had the final ATLAS design. Fig 2.8 shows the mechanical layout of the module. It contains nominally 96 absorbers + electrodes in the outer wheel and 32 in the inner wheel. In the figure only three of each type are shown. For the beam test only a limited ϕ region corresponding to 12 (4) electrodes in the outer (inner) wheel was fully equipped.

The calorimeter module is segmented longitudinally into three sections: front, mid and

back. In the inner wheel only two sections exist (mid and back).

In the transverse plane segmentation is done using the varibles η and ϕ i.e. following a projective geometry. Segmentation in ϕ is as follows:

- **Front.** Cell size is $0.1\,rad$. This implies that all 12 electrodes form a single read out cell.
- **Mid and back (outer wheel).** Cell size is 0.025. Three consecutive electrodes are read out together. Therefore there are 4 cells in the module, which will be numbered from 0 to 3, clockwise from the front face of the detector.
- **Mid and back (inner wheel).** Cell size is 0.1 . The four electrodes present in the module form a single read out cell.

In the η direction the segmentation is more complicated. Cells are again numbered starting out at 0 and increasing with η for each longitudinal section. Since data were only taken at three η positions (see 5.3 below), a description of cell sizes is given below only in the vicinity of those points. As a global reference, mid section cells have size $\Delta\eta = 0.025$ over most of the outer wheel.

- $\eta \simeq 1.55$. Mid cells have size $\Delta\eta = 0.025$. Back cells have size $\Delta\eta = 0.05$ (twice the size of mid cells) and front cells have size $\Delta\eta = 0.025/8$.
- $\eta \simeq 2.2$. Mid and back cells have the same size as in the previous case. Front cells have size $\Delta\eta = 0.025/4$.
- $\eta \simeq 2.9$ (inner wheel). Cell size is $\Delta\eta = 0.1$ both for mid and back.

5.3 Beam test set up and data taken

5.3.1 Setup

The module was tested in the CERN SPS H6 beam facility with electrons in the range $10 - 200\,GeV$. It was placed inside the cryostat. In the outer upper wall of the cryostat, front end electronics, integrated on FEBs, were installed, along with HV power supplies. From the FEBs, signals were routed to the MINIRODS [1] using flat copper cables. From the MINIRODS the data were transferred to a UNIX workstation.

[1] The MINIRODS are data FIFO interfaces between the front-end electronics and the computer that stores the data.

In front of the cryostat four beam chambers were set up, in order to give an independent position measurement for each single event. Only two of them, namely numbers 1 and 2, are used in the analysis below. Scintillator paddles in front of the cryostat were used to define the trigger.

The module was placed inside the cryostat, moveable around a fixed axis (corresponding to the would-be LHC beam line) in order to expose different ϕ regions to the beam. The whole cryostat was moved sideways along a circular rail having its center at the nominal distance from the ATLAS IP to the EMEC front face. This movement was used to scan in η while conserving the projectivity of the set up.

The *medium* (M) and *high* (H) shaper amplifier gains were used for data taking. The read out electronics were organized in such a way that the gain could be selected independently for each longitudinal section. In all the runs used in the analysis the gain was selected to be H for the back section, in which little energy is deposited for any input beam energy. For the front and mid sections, H gain was used up to $60\,GeV$ of input beam energy and M gain above this value. The gain configuration used for $40\,GeV$ runs with the beam pointing at the outer wheel was, for example, HHH (meaning *high* for all three sections). At $120\,GeV$ the configuration was MMH (meaning *medium* for front and mid, *high* for back). In the inner wheel only two longitudinal sections exist. Therefore the corresponding gain configurations are MH and HH (the two letters standing for the gains of mid and back in this case).

5.3.2 Data taken

Data were taken with an electron beam pointing at three positions in the detector: $\eta \simeq 1.55$ (near the external edge of the end cap outer wheel), $\eta \simeq 2.2$ (in the outer wheel) and $\eta \simeq 2.9$ (in the inner wheel). The energy range covered was $10 - 200\,GeV$. In the region $\eta \simeq 2.2$ data were taken at different ϕ positions and with different values of HV applied to the read out electrodes.

Along with beam data, dedicated test pulse runs were taken in order to calibrate the detector electronics (see 5.5 below). Three types of test pulse runs were taken:

- Delay runs pulsing at all channels. In these runs current is injected simultaneously to all detector cells over a wide region. Current injection is delayed in steps of $1\,ns$ in order to scan the whole profile of the pulse.
- Delay runs pulsing at selected channels. In this case the same delay technique explained in the previous item is used, but only selected channels are pulsed at. These runs allow for cross-talk studies. They are not used in this analysis.

η range	ϕ cell	Fraction dead
$1.5 - 1.6$	2	1/6
$2.2 - 2.3$	0	1/6

Table 5.1: List of HV problems in the detector regions that were tested.

- Ramp runs. These runs provide the detector response for a given delay value and for different values of injected current. They are not used in the analysis below.

5.3.3 Known detector problems

There are some detector cells exhibiting known problems affecting the analysis. Those problems are briefly explained in this section.

High voltage problems

Voltage is supplied independently to each electrode face. Since signals from several electrodes are read out together in a given channel, HV problems generate only *partially dead* cells. For example, an outer wheel mid section cell adds up signals from three consecutive electrodes. If no voltage is supplied to one electrode face, the cell will have 1/6 of its read out volume inactive. Table 5.1 lists the mid section detector cells in which some fraction of the read out volume was inactive. Only cells relevant for the analysis done in this thesis are included in the table. Front and back section cells sitting physically in front or behind the mid section cells listed in the table have exactly the same problem. Therefore HV inactive regions are projective in depth and are well localized in η and ϕ.

Notice that in the $\eta \simeq 1.55$ region the HV problem is in a ϕ central cell, whereas at $\eta \simeq 2.2$ the problematic cells are at the edge of the equipped region. The problem affects energy resolution and gives rise to systematic effects discussed in different sections below.

Short between a mid and a back cell

The back section cell at $\phi = 2$, $\eta = 1.55 - 1.6$ was found to have an electrical contact at the summing board level with the mid section cell $\phi = 2$, $\eta = 1.55 - 1.575$. This problem has to be dealt with in order to reconstruct the total energy measured by the detector in the region $\eta \simeq 1.55$.

5.4 Signal reconstruction

5.4.1 Introduction

The technique used for signal amplitude reconstruction in this thesis is referred to as *non parametric linear filtering* (NPLF). The goal of a signal reconstruction algorithm is to obtain a good estimate of the pulse peak amplitude using as input the amplitudes (s_i) at a few points of the time axis, plus the time phase (t) between the time of the amplitude samplings and that of the pulse peak. The general signal reconstruction algorithm can be expressed as follows:

$$A = f(s_i, t)$$

In the case of the EMEC the index i runs from 1 through 5 and the parameter t is the time phase between the trigger signal and the $40\,MHz$ sampling clock, which is measured for each event by a TDC unit. The quantity t, expressed in ns takes values in the range $(0, 25)$.

In Fig 5.1 the meaning of this parameter t, that will be called in the following T_{tdc}, is clarified. The upper plot shows the five sampled amplitudes for two different pulses. The lines on top are intended to guide the eye. The reference system chosen for the abscissa axis is the time of the 40 MHz clock (T). The pulse labeled with open circles is arriving earlier than the one with full squares. This information, extracted visually from the upper plot, can be quantified by looking at the T_{tdc} of both events. Replacing T by $T + T_{tdc}$, that is, shifting the pulses according to the time phase information available, the situation of the lower plot is reached.

The global strategy of the NPLF technique can be summarized as follows:

- Obtain a smooth function describing the pulse shape, using as input the five sampled amplitudes. Non parametric statistics techniques are used at this stage.
- Shift the smooth function describing the pulse by T_{tdc}. After this second step we have the pulse shape functions peaking at approximately the same point of the time axis for all events.
- Evaluate the pulse shape function at a reference point of the time axis, where the position of the peak is on average (t_{max}).

5.4.2 The non parametric technique for pulse shape reconstruction

Let t_i, $i = 1...5$ be the times of the five samplings, as given by the $40\,MHz$ clock, and let T be the time interval between two consecutive samplings ($T = 25\,ns$ in our case). Finally let $K(t)$ be a function, that will be referred to as *kernel*. Then the expression

$$A(t) = \sum_i s_i \cdot K(t - t_i)$$

provides a function that, with a proper kernel choice, can be used as a reconstruction of the pulse shape. Notice that, for a given t_0, the quantity $A(t_0)$ is a **linear** function of the sampled amplitudes s_i. The formula given above is clearly the convolution of the discrete empirical profile measured and the kernel. Therefore, applying the formula can be interpreted as doing a Fourier analysis of the empirical discrete profile and applying to it a frequency filter, given by the Fourier transform of the kernel.

The kernel used throughout in this analysis is

$$K(t) = \frac{sin(\frac{\pi t}{T})}{\frac{\pi t}{T}}$$

Notice that it exhibits the property of yielding a pulse shape $A(t)$ going exactly through the 5 sampled points [2]. This is a standard kernel choice for digital to analog signal conversion. In terms of Fourier analysis this kernel corresponds to filtering out the frequencies above the sampling one. A detailed study about this technique can be found in [31].

5.4.3 The NPLF formula

The final formula that yields the reconstructed amplitude of the pulse maximum can now be obtained by following the steps explained above:

- Pulse shape: $A(t) = \sum_i s_i \cdot K(t - t_i)$
- Time shift: $A(t) = \sum_i s_i \cdot K(t + T_{tdc} - t_i)$
- Evaluate at peak: $A(t_{max}) = \sum_i s_i \cdot K(t_{max} + T_{tdc} - t_i)$

[2] $K(t)$ has nodes at $t = \pm n \cdot T$, n being a non-zero integer.

If the value of t_{max} is known for a given detector channel, this algorithm provides an estimate of the peak amplitude which is a linear combination of the five sampled amplitudes, with weights that are smooth non-linear functions of the T_{tdc} measurement.

The time axis conventions used in this chapter are the following:

- The time coordinates of the five samples are taken to be $t_1 = -50$, $t_2 = -25$,..., $t_5 = 50\,ns$.
- T_{tdc} ranges from 0 to $25\,ns$.
- t_{max} has typical values in the range $0 - 30\,ns$.

Notice that the definition of t_{max} implies that when an event has $T_{tdc} = t_{max}$, the third sample is on the pulse peak.

These are the conventions used in the section devoted to the calculation of t_{max}. However in the plots where pulse profiles are shown, the time axis ranges from 0 to $125\,ns$, instead of from -50 to 75. Therefore in order to compare the position of the peak in one of these plots with a value given for t_{max}, the origin of time must be displaced to $t = 50\,ns$. For example, if the pulse profile of a channel has the maximum at $t \simeq 60\,ns$, this corresponds to a t_{max} of $10\,ns$.

5.4.4 Determination of t_{max}

In order to determine t_{max} for each detector channel the average pulse shape was reconstructed from test pulse and physics [3] runs. In the former case delay runs are taken, pulsing at all channels at the same time. Pulse profiles for a few channels are shown in Fig 5.2. In the case of physics, pulse shapes can only be reconstructed reliably for those channels that dominate the energy deposition in the run. The pulse shapes for a few of the most relevant channels can be found in Fig 5.3, where the five sampled amplitudes are plotted at their corresponding time abscissa $t_i + T_{tdc}$ for all events. Large amplitude dispersions are seen. Therefore applying some smoothing procedure is mandatory before doing any systematic calculation. In this thesis smoothing was performed on profile histograms using splines, as provided by the PAW package. An example of the raw profile obtained from the physics data and after smoothing can be found in Fig 5.4. Notice that the splines interpolation follows very well the profile histogram in the region near the peak.

[3] Physics means, in this context, test beam electron data.

Once smooth profiles are available, one can calculate the time for which the pulse has maximum amplitude. This is done scanning bin by bin and choosing the highest ordinate value. This value could directly be taken as the aimed-at t_{max} for an energy dominant channel. However the fact that not all relevant channels are energy dominant in some physics run, makes necessary a comparative study of the pulse maxima in calibration [4] and physics runs. This study was done separately in the three regions of the detector tested with the electron beam. The ultimate purpose is obtaining a t_{max} prescription that can be applied to all the channels used in the analysis. The t_{max} selection criterion must have the property of reproducing the position of the maxima as obtained from physics smoothed pulse profiles for the particular case of energy dominant channels in a given physics run.

As an example, the t_{max} determination for the region $\eta = 2.2$ is discussed in some detail below. For the other two regions details can be found in [30]. A summary of the results in all the regions can be seen in table 5.2.

Region $\eta = 2.2$

Fig 5.5 shows the position on the time axis of the averaged pulse peak for each detector channel, from two calibration runs and a physics one. The physics pulses are shown in addition. The average time of the peak is shown as a function of the η cell number. Since several ϕ cells exist for the same η, they are represented at abscissa $cell_\eta + 0.25 \cdot cell_\phi$. Timing information from the physics run is only meaningful for the region hit by the beam. This region is displayed in more detail in the lower plot for the sake of clarity. A few conclusions can be drawn from this type of plots, applicable to physics runs with the beam pointing at the region $\eta = 2.2$:

- In the mid section the physics pulses in energy dominant channels are systematically ahead of calibration by $\simeq 15\,ns$. This global shift is seen consistently for all the physics runs prior to number 101006. Notice in Fig 5.5 that the two edge cells in ϕ for each group of 4 at the same η (which are non-dominant in this physics run, as it can be seen in the pulses on the upper half of the figure) are systematically delayed w.r.t. the central ones (dominant). This effect is believed to come from cross-talk: non-dominating channels tend to show distorted signals and therefore it is not reasonable to use them for the t_{max} calculation. This hypothesis can be cross-checked by looking at runs in which the beam was pointing at a different ϕ position. One would expect to see the cells with little energy showing delayed pulses in this case too. This behaviour is clearly seen in Fig 5.6: now the beam (upper plot) hits the right side of the 4×4 cell group, and the cells of the left side feature delayed pulses (lower plot). Therefore the average peak maximum obtained in a physics run for a non-dominating cell is not used for signal reconstruction. The quantity t_{max} is obtained, for each channel by taking the time of the maximum as given by calibration and applying a global shift of $-15\,ns$ (the same for all the channels).

- Front and back section cells show a qualitatively similar behaviour. Selection of t_{max} is again done by applying a global shift to the time of the maxima measured with test pulse delay runs.

- For runs in the range 101007-101210 the pulse maxima behave qualitatively in the same way explained above for the runs prior to 101006. However physics pulses of all sections are now delayed by $\simeq 15\,ns$ w.r.t. the previous case. Notice in Fig 5.7 that the average position of the maxima from physics and calibration in the mid section now coincide. This change in the system timing behaviour happened *during* run 101006 and is not understood. It affects exactly in the same way the front and back detector sections. The same technique explained above is applied for the selection of t_{max} in this run range, but with the proper global time shifts.

- The change in the timing behaviour approximately coincides with the moment in which the gain of the system was changed from HHH (low energy) to MMH (high energy). However the time shift of $15\,ns$ happened during run 101006 (gain HHH), for which the two types of timing behaviour can be found, in the first and last events of the run respectively. Therefore, although the two groups of runs coincide in practice with the two gain configurations, this is not a gain effect.

The prescription for the t_{max} calculation is summarized in table 5.2.

Other regions

The results obtained in the other two η regions tested are qualitatively similar to the ones discussed above for $\eta = 2.2$. A detailed analysis can be found in [30].

Summary and conclusions on t_{max} selection

Looking at averaged pulse profiles coming from both physics and calibration runs one can make a reasonable choice of the parameter t_{max} for the relevant channels. However some arbitrariness exists in this choice. It is believed that all ambiguities will disappear with a more stable functioning of all systems in future beam tests.

The value t_{max} used for reconstruction is given in table 5.2 for the various detector regions, and run intervals, as a function of the peak time of a calibration run (referred to as t_{cal}).

[4] *Calibration* will be used in the following as a synonym of *test pulse*.

The number of the calibration run used to obtain t_{cal} is also given. When two calibration runs are quoted, the first one is M gain and the second one is H gain.

5.5 Calibration

5.5.1 Electronics calibration with test pulse runs

The output of the pulse reconstruction is a number for each channel (in ADC count units). Since each cell has a physically different electronics read out chain, these amplitudes ought to be calibrated before adding them up. In order to do this, current pulses of a given amplitude (measured in DAC counts [5]) are injected to the cells in test pulse runs. From the analysis of these runs a conversion factor from ADC to DAC counts is extracted for each channel and gain. After applying such factors, the amplitudes of all channels (for a given detector layer) are expressed in homogeneous units and can thus be safely added up.

Fig 5.8 shows, for some detector channels, the conversion factors from ADC to DAC counts extracted from two different calibration runs. The response is practically the same in both runs. The result is similar for all parts of the detector.

5.5.2 Calibration with beam data

The final step in the calibration procedure is translating the signals from DAC counts to energy units. This is done in the following steps:

- The signals at all the cells inside a suitable window are added up for each detector section. The window chosen at the mid section level is: $6(\eta) \times 4(\phi)$ cells ($\eta \simeq 2.2$), 4×4 ($\eta \simeq 1.55$), 4×1 ($\eta \simeq 2.9$). For the front and back section the window has the same $\eta \times \phi$ size as in the mid.
- The residual T_{tdc} dependence of the signal (see below) is corrected for each of the three longitudinal sections. The response is normalized to the value obtained for the case $T_{tdc} = t_{max}$ for a reference (energy dominating) cell.
- A global weight is applied to each of the three sections of the detector, on the basis of optimizing energy resolution.
- A global factor is applied to the sum of all sections in order to make the conversion from DAC counts to GeV.

[5] *DAC* stands for *digital to analog converter*. The calibration board generates an analog signal with the amplitude previously selected as a digital number.

η region	run interval	gain	layer	$t_{max}(ns)$	Cal. run
2.2	..-101005	HHH	front	$t_{cal} - 7$	101164
2.2	..-101005	HHH	mid, back	$t_{cal} - 15$	101164
2.2	101006-..	MMH, HHH	front	$t_{cal} + 8$	101138, 101164
2.2	101006-..	MMH, HHH	mid, back	t_{cal}	101138, 101164
1.55	..-101471	MMH,HHH	front	$t_{cal} + 5$	101461,101458
1.55	101498-101513	MMH,HHH	front	$t_{cal} - 15$	101461,101458
1.55	101514-5	MMH,HHH	front	$t_{cal} - 30$	101461,101458
1.55	101526-101528	MMH,HHH	front	$t_{cal} - 37$	101461,101458
1.55	101529-101532	MMH,HHH	front	$t_{cal} - 18$	101461,101458
1.55	..-101471	MMH	mid,back	35	101461,101458
1.55	101498-101527	MMH	mid,back	15	101461,101458
1.55	101528	MMH	mid,back	10	101461,101458
1.55	101529	MMH	mid	-8	101461
1.55	101529	MMH	back	10	101458
1.55	101530	MMH	mid,back	15	101461,101458
1.55	101531	MMH	mid,back	10	101461,101458
1.55	101532	HHH	mid,back	15	101458
2.9	101557	HH	mid,back	$t_{cal} + 4$	101587
2.9	101558-61	MH	mid,back	t_{cal}	101583,101587
2.9	101558-61	HH	mid,back	t_{cal}	101587
2.9	101562-4	MH	mid,back	$t_{cal} + 6$	101583,101587
2.9	101565-7	MH	mid,back	t_{cal}	101583,101587
2.9	101568	MH	mid,back	$t_{cal} + 3$	101583,101587
2.9	101569-71	MH	mid,back	t_{cal}	101583,101587

Table 5.2: t_{max} prescription for all the runs.

The whole procedure has been done independently for the three detector regions tested ($\eta = 2.2$, $\eta = 1.55$, $\eta = 2.9$) and its stability with the beam energy and gain configuration has been checked. The various steps are discussed in detail below.

Residual T_{tdc} dependence of the signal

The NPLF technique for pulse reconstruction is very general and powerful. The shape of the pulse whose amplitude is to be reconstructed need not be known at any stage in the calculation. In contrast, the disadvantage is that the reconstructed amplitude depends on the relative phase of the maximum and the sampled points, and that this dependence is different for different pulse shapes.

The reconstructed signals inside a proper cell cluster are added up by sections and the dependence with the parameter T_{tdc} is parametrized with a polynomial of degree 4 (see Fig 5.9). This strategy is based on the fact that pulse shapes are very similar within the limited region of a section used to study beam data at a given η region. The shape of the signal dependence w.r.t. T_{tdc} was observed to be very stable throughout the beam test for the region $\eta = 2.2$. Notice that the procedure must be redone if the t_{max} changes. Therefore two sets of correction parametrizations are calculated, for the two run intervals 100968-101005, 101007-101210.

In the region $\eta = 1.55$ the situation is basically the same. However in this case there are more changes in t_{max}. The correction had to be calculated independently for each group of runs with the same t_{max} prescription.

For the data taken at $\eta = 2.9$ there exists the additional problem that the detector region which is equipped consists of only one ϕ cell. Due to the large transverse leakage it is essential to start the analysis with a tight ϕ restriction. Otherwise the large ϕ dependence of the energy signal would mask the systematics due to T_{tdc}. After that cut is applied, the procedure is the same one described above for the other two regions.

Relative calibration of detector sections

For an ideal detector without mechanical imperfections, energy leakage, cross-talk or noise effects, signals from different detector sections should be added linearly

$$E_{tot} = \alpha_1 \cdot E_1 + \alpha_2 \cdot E_2 + \alpha_3 \cdot E_3$$

where E_1 stands for the energy observed in the front section, and so on... The weights should be approximately 0.17:1:1 . This is due to the fact that the injected voltage

(measured in DAC counts) is converted to current at the motherboard level through precision resistors, which were measured to have values proportional to 0.17:1:1 for the boards corresponding to the three sections.

The strategy followed in this analysis in order to properly add up the signals from different detector sections is based on energy resolution optimization. The technique is explained in further detail below for the different η regions.

Relative calibration at region $\eta = 2.2$

The energy signal is calculated as

$$E_{tot} = \alpha_1 \cdot E_1 + E_2 + E_3$$

At this stage the quantities E_i are given in DAC counts. The parameter α_1 is estimated such as to minimize the energy resolution for different physics runs. Fig 5.10 (upper) shows the energy resolution as a function of the weight α_1.

The weight applied to the back section was not allowed to vary. As cross-talk effects are very large in the back section no attempt was made to estimate the corresponding weight, which was fixed to unity.

Table 5.3 gives the optimal value of α_1 for a few different runs. The result obtained with the MMH gain is significantly lower than the one obtained for the HHH case. Therefore a different α_1 is used for each gain. Notice that this can be regarded as a global fine tuning of the ADC to DAC conversion factor for the front section in the H and M gain, based on beam data.

In the $60\,GeV$ run, saturation effects were observed in the central cells of the front section, as shown in Fig 5.11. This explains the fact that α_1 is optimal for a larger value. Discarding the $60\,GeV$ run, the weighted mean of all the rest yields

$$\alpha_1^{MMH} = 0.1850 \pm 0.0006$$

$$\alpha_1^{HHH} = 0.1948 \pm 0.0008$$

which are used in the analysis below.

Beam energy (GeV)	**Gain**	**run used**	α_1
20	HHH	100968	0.1938 ± 0.0017
20	HHH	100977	0.1964 ± 0.0019
40	HHH	101003	0.1946 ± 0.0016
60	HHH	100998	0.2011 ± 0.002
120	MMH	101210	0.1861 ± 0.0013
150	MMH	101209	0.1857 ± 0.0014
200	MMH	101034	0.1807 ± 0.003
200	MMH	101177	0.179 ± 0.005

Table 5.3: Optimal value of α_1 for the region $\eta = 2.2$.

Relative calibration at region $\eta = 1.55$

The same procedure explained above was done for the $\eta = 1.55$ region. However the ϕ dependence of the signal was so strong, due to a voltage problem (see 5.3.3), that it had to be corrected for before starting the process of resolution optimization.

An additional difficulty in the $\eta = 1.55$ region is the presence of a short (discussed in 5.3.3). In order to deal with this problem the energy signal was now written as a function of *two* arbitrary coefficients:

$$E_{tot} = \alpha_1 E_1 + E_2 + \left(\overline{E_3} + \alpha_3^{12} E_3^{12}\right)$$

where $\overline{E_3}$ is the energy measured in the back section without taking into account the troublesome cell S3-1-2, and E_3^{12} is the energy in that cell.

Optimization is done iteratively. First resolution is minimized versus α_3^{12}, taking a fixed reference value for α_1. Then optimization is done with α_1. These two steps are iterated. The result for the few MMH gain runs with high enough statistics are shown in table 5.4.

The weighted mean for the weight applied to the troublesome back section cell is

$$\alpha_3^{12} = 0.523 \pm 0.004$$

For lower beam energies (HHH gain configuration) energy resolution is too little dependent on the weight applied to the cell S3-12. Therefore the value given above is fixed and only α_1 is varied. The results are shown in table 5.5.

Beam energy (GeV)	**Gain**	**run used**	α_1	α_3^{12}
80	MMH	101506	0.2145 ± 0.0014	0.528 ± 0.007
80	MMH	101508	0.2139 ± 0.0013	0.522 ± 0.007
100	MMH	101507	0.2137 ± 0.0015	0.519 ± 0.007

Table 5.4: Optimal value of the weights α_1 and α_3^{12} for the region $\eta = 1.55$ in the MMH gain configuration.

Beam energy (GeV)	**Gain**	**run used**	α_1
10	HHH	101501	0.247 ± 0.007
20	HHH	101500	0.2277 ± 0.0019
40	HHH	101498	0.223 ± 0.007
40	HHH	101499	0.2189 ± 0.0011

Table 5.5: Optimal value of α_1 for the region $\eta = 1.55$ in the HHH gain configuration.

The obtained α_1 seem to be systematically higher than the value obtained at higher energies. In addition the excess seen is larger for lower beam energies. This could be an indication of a preshowering effect in the cryostat wall. At $\eta = 2.2$ the effect is not observed, probably due to the fact that the lowest energy avalilable is $20\,GeV$ in that case. The solution adopted is taking the average from the runs shown in the tables to calculate separately α_1^{HHH} and α_1^{MMH}, discarding the $10\,GeV$ data in this calculation. Averaging one obtains

$$\alpha_1^{HHH} = 0.2211 \pm 0.0009$$

$$\alpha_1^{MMH} = 0.2140 \pm 0.0008$$

which are the values used in the analysis.

An example of the resolution parabolas for the $\eta = 1.55$ region can be seen in Fig 5.10 (lower).

Beam energy (GeV)	**Gain**	**run used**	**Global factor** f (GeV/DAC)
20	HHH	100968	0.03389 ± 0.00012
20	HHH	100977	0.03392 ± 0.00012
40	HHH	101003	0.03392 ± 0.00012
60	HHH	100998	0.03392 ± 0.00012
120	MMH	101210	0.03377 ± 0.00012
150	MMH	101209	0.03401 ± 0.00012

Table 5.6: Global calibration factor for the region $\eta = 2.2$.

Relative calibration at region $\eta = 2.9$

In the inner wheel, only sections mid and back exist and they are added up with weights equal to unity.

Global calibration

Once the signals from the different detector sections have been properly added up, the global calibration factor can be readily calculated as the ratio of the beam energy to the mean of the signal distribution (as given by a gaussian fit). No leakage out of the cluster effects are thus taken into account. This calculation was done with several runs for each detector region and gain configuration, as detailed below.

Global calibration at region $\eta = 2.2$

The global calibration factor is given for some runs in table 5.6. The error given is dominated by the beam momentum spread and is thus similar for all the runs. The data taken at 200 and $60\,GeV$ are not used for the global calibration: the latter due to the saturation effect in the front section mentioned above and the former because the beam energy is believed not to be well tuned to $200\,GeV$ (as discussed in several meetings of the ATLAS LAr group). In the $60\,GeV$ case the result obtained is however seen to be compatible with the rest of the data, meaning that saturation is a small effect.

The weighted mean yields

$$f = 0.03390 \pm 0.00005$$

Beam energy (GeV)	**Gain**	**run used**	**Global factor** (f) (GeV/DAC)
10	HHH	101501	0.03351 ± 0.00013
20	HHH	101500	0.03286 ± 0.00012
40	HHH	101498	0.03269 ± 0.00012
40	HHH	101499	0.03272 ± 0.00012
80	MMH	101506	0.03166 ± 0.00011
80	MMH	101508	0.03163 ± 0.00011
100	MMH	101507	0.03162 ± 0.00011

Table 5.7: Global calibration factor for the region $\eta = 1.55$.

which is used in the analysis below.

Global calibration at region $\eta = 1.55$

The same procedure explained above was followed for the $\eta = 1.55$ region, the results being shown in table 5.7.

Besides the possible preshowering problem at $10\,GeV$ (and not so strong at $20\,GeV$), there seems to be a significant difference between the two gain configurations. Therefore the global calibration is done independently for each of them. The $10\,GeV$ run is again not taken into account. The weighted means are calculated and used in the subsequent analysis. At the end they are replaced by more accurate values, chosen after all corrections to the energy signal are applied. These values are

$$f^{HHH} = 0.03181 \pm 0.00007$$

$$f^{MMH} = 0.03106 \pm 0.00006$$

Again in this refinement of the global energy scale the $10\,GeV$ data are not used.

Global calibration at region $\eta = 2.9$

As discussed previously in the inner wheel only one read out cell in ϕ was instrumented and therefore severe transverse leakage is expected. Due to this problem the conversion factor from DAC to GeV calculated for $\eta = 2.2$ was used as an approximate absolute

calibration. After all corrections have been applied, two different factors are calculated for the two gain configurations, the average of the two being constrained to be equal to the preliminary factor f taken from the region $\eta = 2.2$. The values obtained are

$$f^{MH} = 0.03351$$

$$f^{HH} = 0.03429$$

5.6 Event selection and energy signal systematics

Before estimating energy, position and time resolution, the data samples must be thoroughly studied and understood. The purpose of this section is twofold:

- Data taking was not fully stable in the September 1998 run. Therefore it is mandatory to identify and reject events in which the data acquisition (DAQ) system was misfunctioning.
- Due to the accurate energy measurements achievable with the ATLAS LAr accordion calorimeter, it is necessary to understand and correct for all the systematics of the energy signal dependence with the detector parameters, such as ϕ and η position, time phase between the trigger and sampling clock, etc... ; such systematics would otherwise dominate the resolution, masking the full potential of the detector. It must be particularly kept in mind that only small regions of the detector were operational in the module under test. Therefore position cuts will be used along with corrections in order to minimize the effect of energy leakage.

5.6.1 Event rejection due to DAQ misfunctioning

The event information in the September run consisted of two separate blocks of data: one coming from the calorimeter (CALO), and the other one (CAMAC) providing complementary information from several devices (time phase, beam chambers, etc...). Each of these two blocks was managed by a different processor and only at the end of the DAQ chain were they merged together. For some recorded events it was observed that the two blocks of data are not properly matched, i.e. they belong to different physics events. The typical mismatch seen consists of recording together the CALO information of the physics event n and the CAMAC information of the physics event $n-2$. This behaviour of the

recorded data will be referred to as *CAMAC shift*. The strategy adopted to deal with this problem is the following:

- Time was reconstructed for each event using the pulse samples of a mid section cell, having generally maximum energy deposition in the particular run under study. The function $t_{rec} = (s_2 + s_3 - s_4 - s_5)/(s_2 + s_3 + s_4 + s_5)$ where s_i, $i = 1..5$ are the sampled amplitudes, was observed to be monotonic and cuasi-linear w.r.t. the parameter T_{tdc}. Time reconstruction is studied in further detail in 5.10. Notice that t_{rec} (in arbitrary units) and T_{tdc} are giving us two independent measurements of the same phenomenon, coming from the block CAMAC (T_{tdc}) or from CALO (t_{rec}). This t_{rec} was the time function used for DAQ quality event selection.
- The correlation between t_{rec} and T_{tdc} was monitored for all runs. Runs without DAQ instabilities show all events concentrated in a band, whereas those with DAQ problems feature an additional homogeneous background of events with no t_{rec} vs T_{tdc} correlation (see Fig 5.12).
- A suitable cut was applied in the plane t_{rec},T_{tdc} in order to remove events with wrong CAMAC information. The cut was chosen for groups of runs with the same timing behaviour. The cuts were chosen visually. For the runs in Fig 5.12, events between the two straight lines were accepted.

5.6.2 Fine tuning T_{tdc} correction

After the residual dependence of the signal w.r.t. the parameter T_{tdc} had been corrected for blocks of runs without timing changes (see 5.5.2), small deviations from the aimed-at flat response were still found for the complete signal (i.e. adding up the three detector sections). This is a minor effect (see Fig 5.13). It is probably due to the fact that a smooth parametrization using a limited number of parameters was used for the first iteration T_{tdc} correction. The two sets of corrections in the previous iteration correspond to the energy ranges $20-60$ and $120-200\,GeV$. Notice that within each group of energies the dependence is very similar for the different beam energies. The effect was corrected using the profile histogram obtained from the data at each beam energy, for technical convenience.

5.6.3 ϕ-modulation

The dependence of the signal w.r.t. the coordinate ϕ was studied and corrected for at each beam energy. For this analysis the following cuts and corrections were applied:

- Time cut to reject events with DAQ misfunctioning.
- T_{tdc} correction.
- Events inside a limited pseudorapidity interval are selected: the cuts are the same ones used for energy resolution and are given in section 5.7 for the different η regions.

The ϕ coordinate is expressed in mid section cell units for the outer wheel. The four cell centers are at $\phi = 0, .., 3$. For ϕ-modulation studies, ϕ is obtained as a linear barycenter of the cell coordinates, using the energy deposits as weights. A cluster of $6(\eta) \times 4(\phi)$ (4×4) mid section cells is used for the barycenter calculation in the region $\eta = 2.2$ (1.55). Further details on ϕ reconstruction can be found in 5.8.

Results for the three detector regions studied are given below in some detail. In all cases a profile histogram is obtained for each available beam energy. The correction is directly taken from these histograms as follows:

- A central bin with large statistics is chosen as a reference. The same bin is chosen for all beam energies. Let S_{ref} be the mean signal at this bin, for a given beam energy.
- For a given event at this beam energy, let S_{bin} be the mean signal at the ϕ bin corresponding to this single event.
- The correction consists of multiplying the energy signal by the factor $c = S_{ref}/S_{bin}$.

Region $\eta = 2.2$

The results for the region $\eta = 2.2$ are shown in Fig 5.14, where the energy signal (normalized to the beam energy) is shown as a function of ϕ. The shape of the modulation is qualitatively as expected: there are three oscillations per ϕ cell, due to the fact that a cell consists of three electrodes. Notice that the oscillations are superimposed on a non-constant baseline, due to side leakage and to a HV problem present in the cells at $\phi = 0$ (see 5.3.3 above). The shape of the modulation is very stable at high energy.

Region $\eta = 1.55$

The ϕ dependence of the energy signal in the region $\eta = 1.55$ was completely dominated by the effect of a HV problem (see 5.3.3). Fig 5.15 shows this dependence for different input beam energies. The signal drops with increasing ϕ, as the region with the HV problem is approached, completely masking the ϕ-modulation.

Region $\eta = 2.9$

As expected, transverse leakage out of the small region instrumented in the inner wheel was observed to be very important. Fig 5.16 shows the energy signal as a function of the coordinate ϕ for the different beam energies. Notice that in this case ϕ is given in arbitrary units, as obtained by direct mesurement with a beam chamber. Roughly 20-25 % of the total energy is leaking out of the instrumented region.

5.6.4 η dependence of the energy signal

The dependence of the energy signal with pseudorapidity could only be monitored for very small regions, corresponding to the beam spot width along the η direction in the three detector regions tested.

The parameter η used in this paragraph for the outer wheel is expressed in front section cell units. It is calculated as a linear barycenter of front cell coordinates weighted with their energy deposits, using a fixed window of 16 cells. For the inner wheel the η position is taken from the beam chamber measurement. More sophisticated techniques and a different unit system are used in 5.8 in order to study η position resolution.

Cuts applied for the different η regions are detailed in 5.7. The η dependence of the energy signal is corrected for by usage of profile histograms obtained at each beam energy and for each detector region. The correction is done in the same way explained above for the ϕ dependence of the signal.

Region $\eta = 2.2$

Fig 5.17 shows the η dependence of the energy signal around $\eta = 2.2$, for different energies. The response is quite uniform in the mid section η cell 32 (corresponding to the front section cells 180-183). The edge effect between mid section η cells is noticeable near the point $\eta = 2.2$. In the cell MID31 (front section cells 176-9) a strong η dependence of the signal is detected. Far away from the mid cell boundary, approximately the same signal as in cell MID32 is reached. The asymmetric behaviour around the point $\eta = 2.2$ is not fully understood. No further conclusions can be extracted due to the limited η range available in the data.

Region $\eta = 1.55$

The energy response as a function of η in the region $\eta = 1.55$ is remarkably uniform (see Fig 5.18). This is due to the fact that along the region where statistics are available, the HV problems existing in the read out electrodes do not change with η.

The cut $16 < cell_{\eta_1} < 18$ is applied (see 5.7 below) in the resolution studies, in order not to be too affected by the cell of the back section which has a short with a mid section cell (see 5.3.3).

Region $\eta = 2.9$

The energy response as a function of η is practically constant near $\eta = 2.9$, within the region where statistics are available. Fig 5.19 shows this dependence for all beam energies. The beam chamber is used for the position measurement. The coordinate η is thus given in arbitrary units.

5.6.5 Energy signal dependence on the shower longitudinal profile

Energy losses due to preshowering or longitudinal leakage can be detected and corrected for, to some extent, through the study of the longitudinal shower profile.

Let $r_3 = E_3/E_{tot}$, i.e. the fraction of the total observed energy detected in the back section, and let $r_1 = E_1/E_{tot}$, i.e. the fraction of energy in the front. These two quantities are strongly correlated. If each event is seen as a representative point in the (r_1, r_3) plane, the region of low r_3 and high r_1 clearly corresponds to early showers, whereas high r_3 and low r_1 means late showers. The parameter r_1 is well suited for the study of preshowering, whereas r_3 is very sensitive to longitudinal leakage. This would be the case for an ideal detector without problematic channels or cross-talk. Such effects can affect the expected behaviour of the signal dependence on (r_1, r_3). This happens to be the case, particularly in the region $\eta = 1.55$.

Region $\eta = 2.2$

Fig 5.20 shows the way events populate the (r_1, r_3) plane for different beam energies. The following features are easily seen:

- Events can be classified into two types: those clustered in a well defined cloud (*main cloud*) and those with low r_1 and very high r_3 (*high r_3 tail*). Most of the events belong to the main cloud.
- The main cloud is better defined (in particular narrower in r_3) for high energies.
- The main cloud shifts continuously towards lower r_1, higher r_3, as the beam energy increases. This is due to the logarithmic energy dependence of the depth of the longitudinal shower profile.
- As the beam energy rises, the high r_3 tail becomes more and more populated and shifts to higher r_3 values. These events are understood as showers with late develpement.

The dependence on (r_1, r_3) of the total measured energy can only partially be understood in terms of shower shapes. The signal is observed to be smaller for high r_1 as expected, but events in the high r_3 tail do not show a smaller signal (as one would expect from longitudinal leakage). This is probably due to the high cross-talk seen in the back section cells. The total observed energy (normalized to the beam energy) is shown as a function of the variables (r_1, r_3) using three different binnings in Fig 5.21, at $E = 120\,GeV$. A roughly similar behaviour is observed for all the other beam energies available.

Bins are only filled in the shown lego histograms (Fig 5.21) if more than ten events are available to calculate the average response. Notice that the finest grid provides a very detailed signal map, but has the shortcoming of giving information only for the region of the (r_1, r_3) plane most heavily populated. The second lego plot has a coarser binning, but covers a wider region of the shower shape phase space. Finally, the third histogram provides very rough information practically for any shower shape of interest.

Region $\eta = 1.55$

In the region $\eta = 1.55$ the fractional energy measured in the back section is distorted by the fact that one of the back cells had a short at the summing board level with a cell of the mid section. This problem was attempted to be solved, as explained above, by applying to this troublesome cell a weight chosen to minimize energy resolution at high beam energies. In addition to this, a stringent cut in η was applied in order to stay away from the detector area most affected (see 5.3.3). Needless to say, the effect of this problem is apparent when the signal in the back section is monitored separately. This is clearly the case in any study involving the variable r_3 defined above. Therefore in the region $\eta = 1.55$ it will be difficult to interpret the signal dependence with respect to (r_1, r_3) in terms of electromagnetic shower topology.

Fig 5.22 shows the distribution of the events in the (r_1, r_3) plane for all beam energies. The signal map for the $80\,GeV$ case is presented in Fig 5.23.

Region $\eta = 2.9$

In the inner wheel only two longitudinal sections exist. Therefore the shower profile can only be studied using the variable r_3 (recall that the two sections are conventionally taken to be mid and back). The dependence on r_3 of the measured energy signal is shown in Fig 5.24 for all beam energies. Notice that the beam energies available only cover the range $40 - 100\,GeV$ in the inner wheel: therefore no major change is seen in the shower longitudinal profile. The typical fraction of the energy seen in the back section sampling is 4-5%. The total measured energy increases slightly with r_3. This could be due to cross-talk effects.

Longitudinal shower shape correction

In order to correct for the systematics described above, two-dimensional signal maps like the ones shown in Fig 5.21, 5.23 were obtained for each η region and beam energy with three different binnings: fine (F), coarse (C) and very coarse (VC). For a given event the correction is calculated as follows:

- Let S_{ref} be the mean signal for a reference bin (a typical, i.e. very populated bin is taken) in the C histogram.
- The (r_1, r_3) coordinates of the event are determined. If the event is inside the r_1,r_3 region covered by the F signal map, then let S_{bin} be the average signal of the bin where the event is found to be.
- If the F map does not provide information for this event, then the C map is used to obtain S_{bin}.
- If neither the F nor the C map cover the region in which the event sits, the VC map is used in order to obtain S_{bin}.
- The correction to be applied is the factor S_{ref}/S_{bin}.
- For technical convenience a cut in (r_1, r_3) is applied (see 5.7).

For the region $\eta = 2.9$ only the quantity r_3 is available. Therefore the one-dimensional profile histogram obtained at each beam energy is used for the correction.

The quantities r_1, r_3 are not only sensitive to longitudinal leakage and preshowering. They are also strongly correlated to the ϕ impact position of the particle in the calorimeter. Fig 5.25 illustrates this dependence for the region $\eta = 2.2$.

Therefore, after applying the r_1,r_3 correction, one can expect a small distortion on the flat ϕ dependence of the energy signal obtained previously by applying the ϕ correction (i.e. the two corrections do not factorize). This effect was seen to be small, but non-negligible. The residual ϕ dependence was monitored and corrected for at each beam energy using a profile histogram. This was done for all three detector regions studied.

Residual dependence of the signal on η after application of the longitudinal profile correction, was also monitored. The result is that small distortions had been introduced by the correction also in this case. The effect was especially important in the $\eta = 1.55$ region, due to the already mentioned problematic back section cell. For completeness, this residual effect was corrected for all energies in the regions $\eta = 2.2$, $\eta = 1.55$, using profile histograms.

5.7 Energy resolution and linearity

Energy resolution was studied separately for the three detector regions tested. In order to evaluate correctly the calorimeter resolution it is necessary to provide a reliable estimate of the contribution due to electronics noise. A brief explanation of the noise measurements done with the data is therefore presented before dealing with resolution results.

5.7.1 Noise calculation

Noise was calculated in the usual way: pedestal runs [6] were taken and processed with the same filtering techniques used for physics data. For each of the relevant detector regions the signals of the cells in the cluster used for energy reconstruction were added up. The conversion factors to DAC counts, appropriate weights and conversion factors to energy units were applied, and the resulting noise distribution was fitted with a gaussian. The sigma of this fit was taken as the noise of the energy measurement.

For each of the three detector regions two different gain configurations were used, each of them using partially different electronics and leading to different noise results. The noise calculation described above was therefore done for six independent cases. The results are shown in table 5.8. An example of the noise spectra obtained is shown in Fig 5.26.

[6] We call pedestal runs to those in which the output signals from the detector are registered, in absence of any input signal.

η **region**	**Cluster** ($\eta \times \phi$)	**Gain**	**noise** (MeV)
2.2	6×4	MMH	669 ± 5
2.2	6×4	HHH	338 ± 2
1.55	4×4	MMH	649 ± 5
1.55	4×4	HHH	389 ± 3
2.9	4×1	MH	413 ± 3
2.9	4×1	HH	228 ± 2

Table 5.8: Noise measurement for different detector regions and gain configurations.

Notice in table 5.8 the strong increase due to the change from H to M gain, which is attributed to "pick up" noise (i.e. noise entering the read out system after amplification). Noise for a given channel can be written as $N = N_{pre} \oplus N_{pick-up}$, i.e. two independent contributions coming from the devices in the read out chain before (N_{pre}) or after ($N_{pick-up}$) amplification. The electronics are the same for all gains before amplification. Indeed, if we assume that the two gains have a similar amount of *intrinsic* (i.e. measured in voltage units) pick up noise, then the term $N_{pick-up}$ expressed in energy units differs by a factor of $\simeq 10$ for the M and H gain: $N^M_{pick-up} \simeq 10 N^H_{pick-up}$. The noise measurement presented in this section suggests that $N^H_{pick-up}$ is small as compared to the total noise for the H gain, but $N^M_{pick-up}$ dominates the noise of the channel in the medium gain. Notice that this would imply that in the low (L) gain [7] the total noise, in energy units, would be $N^L \simeq 10 \cdot N^M$.

Cross-check of the noise calculation

In order to cross-check the noise calculation explained above, both energy resolution and noise were measured for the region $\eta = 2.2$ using two different windows (namely 6×4 and 8×4). The idea behind this strategy is very simple:

- Both windows are large enough to fully contain the shower. Therefore the only effect of increasing the cluster should be adding more noise to the energy measurement.
- Energy resolution (measured with physics runs) should be slightly worse for the larger window. This resolution deterioration is entirely due to the increase of the noise. Therefore the resolution after noise subtraction should not change.

[7] This low gain was not used in the September 1998 run.

window	**noise MMH** (MeV)	**noise HHH** (MeV)	**a** (%)	**b** (%)
6×4	669	338	9.97 ± 0.03	0.34 ± 0.06
8×4	755	398	10.06 ± 0.02	0.36 ± 0.07

Table 5.9: Noise measurement and sampling and constant term of the energy resolution (after noise subtraction) for two different window sizes.

Energy resolution was calculated for different beam energies, using the two windows (6×4, 8×4). This study was done using a limited set of runs and a preliminary set of corrections. Final results on energy resolution are given later on in this section. Noise was measured for both window sizes. The dependence of resolution after noise subtraction w.r.t. the beam energy was parametrized in the usual way. A sampling and a constant term were thus obtained for each window size. The results are shown in table 5.9.

Larger noise is found for the 8×4 window, and the calorimeter resolution (the sampling and constant term) after noise subtraction calculated with the two window sizes yields compatible results.

5.7.2 Energy resolution and linearity for the region $\eta = 2.2$

Summary of cuts and corrections

The following cuts were applied in the region $\eta = 2.2$:

- Cut in the plane (T_{tdc}, t_{rec}) in order to reject events with wrong CAMAC information.
- $1.5 < \phi < 2.0$
- $179.5 < cell_{\eta_1} < 181.0$ [8]
- $r_3 < 0.15$.

The corrections applied are listed below:

- Systematics with T_{tdc} are corrected for section by section. The same correction is used for a given group of runs without changes in the timing behaviour of the system.

[8] $cell_{\eta_1}$ is the η position expressed in front section cell units.

- Residual dependence of the total energy on T_{tdc} is corrected for at each beam energy.
- ϕ-modulation is corrected for at each beam energy.
- η dependence is corrected for at each beam energy.
- Dependence on (r_1, r_3) is corrected for at each beam energy.
- Residual dependence on ϕ is corrected for at each beam energy.
- Residual dependence on η is corrected for at each beam energy.

Results

After all the corrections and cuts explained above were applied, the energy signal spectra shown in Fig 5.27 were obtained. The signal spectra have been fitted with gaussians. A 6×4 window was used throughout.

Fig 5.28 shows the mean reconstructed energy, obtained from the gaussian fit, as a function of the beam energy. Deviations from linearity are below 1%, except for the $200\,GeV$ point, for which a problem with beam tuning is believed to explain the deviation.

The beam energy dependence of the measured energy resolution was fitted to the function

$$\frac{\sigma}{E} = \frac{a}{\sqrt{E}} \oplus b \oplus \frac{noise}{E} \oplus beamspread$$

where only the two parameters a, b were allowed to vary. The coefficient $noise$ is a step function implementing the measured noise for the gain configurations corresponding to each energy range (HHH below $100\,GeV$; MMH above). The $beamspread$ is also a step function, due to the fact that a secondary beam was used for the $200\,GeV$ point, whereas a tertiary beam was used in the remaining cases. The beam momentum spread is in both cases calculated using the beam test facility documentation. See 5.11 for details.

The measured energy resolutions, along with the result of the fit, are shown in Fig 5.29. The fitted sampling and constant terms obtained are

$$a = 9.2 \pm 0.2\%$$

$$b = 0.53 \pm 0.04\%$$

The results are compatible with the expectations stated in [15].

5.7.3 Energy resolution and linearity for the region $\eta = 1.55$

Summary of cuts and corrections

The cuts applied are:

- Cut in the plane (T_{tdc}, T_{rec}) in order to reject events with wrong CAMAC information.
- $1.3 < \phi < 2.0$
- $16.0 < cell_{\eta_1} < 18.0$
- $r_3 < 0.15$

The corrections applied are:

- Dependence of the signal on ϕ is corrected before doing any further studies, for each beam energy.
- Systematics with T_{tdc} are corrected section by section. The same correction is used for groups of runs without changes in the timing behaviour of the system.
- Residual dependence of the total energy on T_{tdc} is corrected for at each beam energy.
- Dependence of the signal on η is corrected for at each beam energy.
- Dependence of the signal on (r_1, r_3) is corrected for at each beam energy.
- Residual dependence on ϕ is corrected for at each beam energy.
- Residual dependence on η is corrected for at each beam energy.

Results

The signal spectra obtained after all corrections, along with the corresponding gaussian fits, are shown in Fig 5.30. A window of 4×4 cells was used. Notice that the window is smaller than in the $\eta = 2.2$ region. This is due to the fact that the same pseudorapidity interval corresponds to a larger calorimeter region for smaller η values. At $\eta = 1.55$ four cells are sufficient for a proper shower containment.

Deviations from linearity are below 1% (see Fig 5.31).

The beam energy dependence of the measured energy resolution was fitted using the same technique introduced at $\eta = 2.2$. The result is shown in Fig 5.32. The fitted sampling and constant terms are

$$a = 11.0 \pm 0.3\%$$

$$b = 0.70 \pm 0.07\%$$

Both the constant and sampling term are significantly deteriorated, as expected from the fact that a part of the read out volume, very close to the impact point of the beam, was inactive due to the mentioned HV problems (see 5.3.3).

5.7.4 Energy resolution and linearity for the region $\eta = 2.9$

Summary of cuts and corrections

The following cuts were applied in this region:

- Cut in the plane (T_{tdc}, T_{rec}) in order to reject events with wrong CAMAC information.
- $-1.5 < \phi_{bc2} < -0.8$ [9]
- $-1.0 < \eta_{bc2} < 1.6$
- $r_3 < 0.075$

The corrections applied were:

- Dependence of the signal on ϕ is corrected for, before doing any further studies, at each beam energy.
- Systematics with T_{tdc} are corrected for the mid section. The same correction is used for groups of runs without changes in the timing behaviour of the system.
- Residual dependence of the total energy on T_{tdc} is corrected for at each beam energy.
- Dependence of the signal on η is corrected for at each beam energy.

[9] *bc2* stands for beam chamber number 2.

- Dependence of the signal on r_3 is corrected for at each beam energy.
- Residual dependence of the signal on ϕ is corrected for at each beam energy.

Results

The large transverse leakage out of the instrumented region at $\eta = 2.9$ completely spoils the detector performance. Therefore energy resolution studies in this case shall be taken just as a qualitative check of the detector behaviour. The signal spectra obtained after all cuts and corrections were applied, along with the corresponding gaussian fits, are shown in Fig 5.33. The window used was 4×1. The global energy scale was taken from the data taken at $\eta = 2.2$. The spectra do not peak at the nominal beam energy due to transverse leakage.

Deviations from linearity are below 1% (see Fig 5.34).

The beam energy dependence of the measured energy resolution was fitted to the same function used above for the other two η regions. In this case (due to a mistake) the MH configuration was used for electrons of 40 and $100\,GeV$, whereas HH was used at 60 and $80\,GeV$. The measured energy resolutions and the result of the fit are shown in Fig 5.35. The resulting sampling and constant term are

$$a = 13.5 \pm 1.0\%$$

$$b = 1.64 \pm 0.12\%$$

Notice that whereas the three points at 40, 60 and $80\,GeV$ follow roughly the expected scaling law, resolution is worse than expected at $100\,GeV$. The data available at this beam energy show severe DAQ problems. Therefore some contamination of events with wrong T_{tdc} information is expected to remain even after cuts are applied.

5.8 Position reconstruction

The natural coordinates to describe the geometry of the detector are the azimuthal angle (ϕ) and pseudorapidity (η). An important feature of the detector is that, whereas cell boundaries are projective in the η direction, this is not the case in the ϕ direction, due to the accordion geometry. Hence if position is reconstructed using a barycenter algorithm, a systematic non-linear bias towards the center of the cell (known as *S-shape*) will appear for

η, but not for ϕ. Therefore the two coordinates need different reconstruction techniques and will be dealt with in two separate subsections. In both cases the whole study was done using the best set of data, namely those runs taken in the region $\eta = 2.2$.

5.8.1 Reconstruction of ϕ

Preliminary reconstruction

The coordinate ϕ of the impact point of an electron in the calorimeter is reconstructed in the following way:

- A linear barycenter of the type

$$\phi_{bar} = \frac{\sum (\phi_i \cdot s_i)}{\sum s_i}$$

  where i runs over a fixed cluster of $6(\eta) \times 4(\phi)$ cells in the mid section, ϕ_i is the coordinate of the $i-$th cell center and s_i the signal at cell i, is calculated as a first iteration. At this stage an η barycenter is calculated in the same way using 16 cells of the front section.

- The η, ϕ values calculated in the first iteration are used to select events inside a $2(\eta) \times 1(\phi)$ mid section cell rectangle centered at $\eta = 2.2$ ($cell_{\eta_2} = 31, 32$) and at $\phi = 2$. This is the best ϕ region from the point of view of HV problems. At this stage the usual cut is also imposed in order to reject events with DAQ problems.

- A 3×3 mid section cell cluster is built around the cell with maximum energy deposition, chosen among the two cells selected previously.

- The coordinate ϕ is reconstructed using a linear barycenter calculated with the same formula given in the first item, but with i running only over the 3×3 cells selected for each event. Let ϕ_{rec} be the result of this calculation.

Beam chamber calibration

The reconstructed ϕ coordinate (ϕ_{rec}) is compared to the coordinate provided by beam chamber number 2 (beam chambers 1 and 2 were the ones functioning in a more stable way), given at this stage in arbitrary units. A linear dependence is observed, as shown by Fig 5.36.

In order to translate the beam chamber coordinates to the cell unit scale, we need to establish a linear transformation taking the uncalibrated ϕ_{bc2} to a calibrated quantity, that will be denoted as ϕ_{bc}. The transformation is completely determined as soon as the image of two ϕ_{bc2} values is given. The first one is provided by the fit done in Fig 5.36: since a symmetric three ϕ cell set around cell 2 was used for the barycenter, the point $\phi = 2.0$ is estimated in an unbiased way with ϕ_{rec}. Therefore the fitted straight line can be used in order to obtain the value of ϕ_{bc2} corresponding to $\phi_{bc} = 2.0$. Notice that near the cell edge ϕ_{rec} can be presumed to give a biased estimate of ϕ.

The second reference point needed can be obtained by building a two cell barycenter, using only the cells $\phi = 1, 2$. This type of barycenter was observed to be linear with respect to the beam chamber coordinates in the vicinity of $\phi = 1.5$. The symmetry of the two ϕ cell cluster around that point allows to obtain an unbiased estimate of ϕ and thus provides the value of ϕ_{bc2} corresponding to $\phi_{bc} = 1.5$.

An interesting detail that can be observed in Fig 5.36 is that the intrinsic width of the cloud of points is larger for values close to $\phi_{rec} = 1.5$. This may be due to energy leakage out of the cluster. The effect suggests that a 5 (instead of 3) ϕ cell cluster should be tried in future beam tests.

Corrections to ϕ_{rec}

The quantity ϕ_{rec} is linear with respect to the true ϕ coordinate (see Fig 5.36), being unbiased at $\phi = 2$. In order to obtain an unbiased estimate for an arbitrary ϕ, a linear correction must be applied:

$$\phi_{rec} \to \overline{\phi_{rec}} = 2.0 + \alpha \cdot (\phi_{rec} - 2.0)$$

Using calibrated beam chamber information the parameter was calculated to be $\alpha = 1.15$.

Once we have $\overline{\phi_{rec}}$ and ϕ_{bc} calculated in the way explained above, it is natural to regard ϕ_{bc} as the *true* coordinate and $\overline{\phi_{rec}}$ as the measurement done with the calorimeter. Resolution can be readily calculated by looking at the width of the distribution obtained with the quantity $\overline{\phi_{rec}} - \phi_{bc}$, shown in Fig 5.37 for a beam energy of $120\,GeV$. Observe that the resolution of the measurement, obtained as the sigma of a gaussian fit, is at the level of 5% the cell size. The figure also shows that, as indicated above in the text, the resolution is slightly worse for ϕ values near the cell edge. Tails are believed to be due to events with wrong CAMAC information escaping the t_{rec} cut.

The study detailed above was for run 101210 ($120\,GeV$ electrons). The same was done for a large set of runs. For each of them the ϕ position resolution was obtained. The results

E (GeV)	**run**	$\sigma(\phi)$ **(cell units)**	ϕ_{rec} **range**
20	100968	0.1136 ± 0.0018	1.8-2.2
	100977	0.117 ± 0.002	1.8-2.2
40	101003	0.0742 ± 0.0016	1.8-2.2
60	100993	0.0578 ± 0.0018	1.9-2.5
	100997	0.0647 ± 0.0016	1.6-2.5
	100998	0.0651 ± 0.0017	1.6-2.2
	101002	0.0636 ± 0.0016	1.6-2.2
120	101210	0.0462 ± 0.0005	1.6-2.2
150	101210	0.0483 ± 0.0006	1.6-2.2
200	101028	0.0245 ± 0.0013	1.55-1.8
	101031	0.0212 ± 0.0014	1.55-1.8
	101157	0.0259 ± 0.0005	2.2-2.5
	101177	0.0235 ± 0.0009	1.8-2.2

Table 5.10: Resolution in the ϕ position measurement for different runs.

are summarized in table 5.10. For the sake of completeness, the ϕ region (in mid section cell units) in which the statistics are concentrated is given. Notice that this is a relevant piece of information due to the fact that a slightly worse resolution can be expected near the cell edge.

As expected the general trend is an improvement of position resolution with increasing beam energy. Slightly different results are obtained with different runs at the same beam energy. In some cases the discrepancy can be explained by the different ϕ_{rec} range of the data. In the remaining cases, deterioration of the position resolution was traced to be due to some events with wrong CAMAC data escaping the DAQ-quality cut.

ϕ resolution, measured in mid section cell units, is shown as a function of beam energy in Fig 5.38. All the runs included in table 5.10 are plotted as separate points. The runs at 120, $150\,GeV$ are strikingly above the general trend. These were the last runs taken and the beam chambers had started to show an unstable behaviour, as it can be seen also in 5.8.2. Therefore these two points are not included in the fit. The data are fitted using the formula $\sigma = a/\sqrt{E} \oplus b$, yielding

$$a = 0.442 \pm 0.003$$

$$b = 0.0000 \pm 0.0009$$

Notice that the resolution observed at high energy ($200\,GeV$) is around 2% of the cell size. This is a remarkable result, in good agreement with the prediction given in section 3.4 using simulation.

In terms of the momentum direction of a particle coming from the IP (assuming that the position spread of the IP is negligible, see 2.2.2), the angular resolution is $\Delta\psi = c \cdot \Delta\phi / D$, where c is the cell size, D the distance from the IP to the point where the shower is measured at the calorimeter [10] and $\Delta\phi$ the position resolution in cell units. Replacing the values of c, D and $\Delta\phi$, we readily obtain

$$\Delta\psi \simeq \frac{2.2\,mrad}{\sqrt{E}}$$

well below the aimed-at $50\,mrad/\sqrt{E}$, as expected.

5.8.2 Reconstruction of η

Reconstruction of the η position may be done separately using the front and the mid section of the detector. Obtaining two values for η at different depths allows for pointing angle reconstruction. This type of measurement is important e.g. for invariant mass reconstruction in a $H \to \gamma\gamma$ decay, as explained above in this thesis. Simulation (see 3.2) predicts the following features in the reconstruction of η using the front (η_1) and mid (η_2):

- The front section has very fine η granularity. On the other hand, most of the particle energy is deposited in the mid section. These two effects compensate each other in such a way that roughly the same resolution can be achieved with η_1 and η_2.
- The linear barycenter technique gives rise to a systematic non-linear bias of the reconstructed position towards the center of the cell. The effect has the periodicity of the cell size. Since granularity is much finer in the front section, the S-shapes are in this case a much smaller effect.

Algorithm for η reconstruction

The data used to study η reconstruction were selected and processed in the following steps:

[10] To be more precise, the distance from the IP to the 3-D barycenter of the part of the shower contained in the mid section.

- Events are selected with the usual DAQ quality cuts, based on time reconstruction calculations.
- A first iteration η and ϕ barycenters are calculated in the same way explained above for ϕ position reconstruction. The same position cut is applied. Recall that each of the two mid section η cells selected corresponds to 4 front section cells. The coordinate 0 is assigned to the point $\eta = 2.2$ and all calculations are done in mid section cell units. From now on these units will be used and denoted as $\overline{\eta}$.
- For a given event a 3×3 cluster of mid section cells is selected around the one cell (out of the two ones selected) having maximum energy deposition. The corresponding 12 cells in the front section are selected.
- A barycenter is calculated using the selected 3×3 mid section cells (η_{bar2}) and another one with the 12 front section ones (η_{bar1}).
- The value of η given by the beam chambers (η_{bc1}, η_{bc2}) [11] is calibrated according to our unit system by comparing it to η_{bar1} as follows: this barycenter is a quasi-linear function of the true η coordinate and, for symmetry considerations, it is an unbiased estimate of η at the points $\overline{\eta} = \pm0.5$. At $\overline{\eta} = 0.0$ the cluster is changed and therefore a small discontinuity may be found. An example of this dependence can be seen in Fig 5.39, where the data are fitted with a linear function in the range $-0.5 < \eta_{bar1} < 0.5$. The calibrated beam chamber coordinate (η_{bc}) is obtained as a linear function of the raw coordinate (η_{bc1} or η_{bc2}, depending on the beam chamber used). Again symmetry implies that the result of the fit shown in Fig 5.39 is the inverse of the aimed-at linear transformation. The coordinate η_{bc} was obtained for each beam energy using this technique.
- The systematics in the difference $\eta_{bar1} - \eta_{bc}$ and $\eta_{bar2} - \eta_{bc}$ are studied and corrected for. This step is explained in detail below, separately for the front and the mid section.
- After all corrections are applied we obtain two calorimeter-based unbiased estimates of η: η_1 and η_2. Resolution is calculated as the sigma of a gaussian fit to the difference $\eta_i - \eta_{bc}$, $i = 1, 2$. This is done at different beam energies and the energy evolution of the η position resolution is studied.

Reconstruction of η with the front section

Once we have η_{bar1} and η_{bc} for all events, the systematics of the difference between these two quantities are studied as a function of the former. The systematics expected are the following:

[11] The two beam chambers can in principle be used alternatively. For each run the one behaving more stably at that moment was chosen. See details below in this subsection.

- Quasi-linear dependence in the ranges $-1 < \eta_{bar1} < 0$ and $0 < \eta_{bar1} < 1$, with a small discontinuity at $\eta_{bar1} = 0$.
- Small oscillations of period 0.25, roughly symmetric w.r.t $\eta_{bar1} = 0$.

These two effects are neatly seen at high energy and are somewhat masked by the worse resolution at low energy, as shown in Fig 5.40.

The dependence shown in Fig 5.40 is corrected for in two stages:

- First two independent linear functions are fitted to the data in the ranges $\eta_{bar1} < 0$ and $\eta_{bar1} > 0$.
- Then the residual dependence is fitted using a truncated Fourier series of the type $P_0 + \sum_{k=1}^{3} P_k \cdot sin(2k \cdot \pi\overline{\eta}/0.25)$. Notice that the fundamental frequency is the one corresponding to the front section cell size (0.25).

After applying these two corrections to η_{bar1}, the quantity η_1 is obtained.

Reconstruction of η with the mid section

The systematics of $\eta_{bar2} - \eta_{bc}$ as a function of η_{bar2} are of the type shown in Fig 5.41. A strong oscillatory behaviour with the periodicity of the mid section cell size (1 in the current η units) is found, as expected. This dependence is fitted using the same type of truncated Fourier series given in the previous paragraph

$$P_0 + \sum_{k=1}^{3} P_k \cdot sin(2k \cdot \pi\overline{\eta}/1.0)$$

and a correction is applied. The quantity obtained after applying the correction to η_{bar2} is called η_2. There are some details to be noted:

- The S-shape shown in Fig 5.41 is not exactly antisymmetric with respect to zero. Therefore after applying the correction described above some small residual systematics subsist.
- The deviations to the pure antisymmetric behaviour were found to be especially important at high energies ($200\,GeV$). In this case it was necessary to use an independent fit of the same type for each of the two regions $\eta_{bar2} < 0$, $\eta_{bar2} > 0$ in order to attain convergence.

η position resolution

After the quantities η_1 and η_2 have been obtained, η position resolution is evaluated in terms of the sigma of the distribution $\eta_i - \eta_{bc}$. This was done at several beam energies. The distributions obtained are fairly gaussian, as shown in Fig 5.42.

Beam chambers were not functioning in a fully stable way throughout the test. Three phases can be distinguished w.r.t. the measurement in the η direction:

- Beam chamber 2 was used in order to obtain η_{bc} for the first part of the test ($E = 20 - 60\,GeV$).
- For the runs with $E = 200\,GeV$, beam chamber 1 was used.
- The beam chambers did not behave well for the last runs taken in the detector region $\eta = 2.2$, corresponding to $E = 120,\ 150\,GeV$. These runs are not used for η reconstruction analysis.

Fig 5.43 shows the beam energy dependence of η position resolution, given in mid section cell units, both with the front and with the mid section. The data are fitted with the standard law $\sigma(\eta) = a/\sqrt{E} \oplus b$. The fitted values, using the front detector section are

$$a = 0.377 \pm 0.005$$

$$b = 0.0216 \pm 0.0009$$

With the mid section the results are

$$a = 0.422 \pm 0.006$$

$$b = 0.0121 \pm 0.0016$$

The resolution is, as expected, very similar in both cases.

Combining the two position measurements η_1, η_2, the momentum direction can be reconstructed without using any information coming from the IP. The angular uncertainty is

$$\Delta\theta = \frac{c}{d} \cdot (\Delta\eta_1 \oplus \Delta\eta_2)$$

where c is the mid section cell size, d the distance between the 3-D barycenters of the part of the shower inside the front and the mid section, projected on the beam axis direction, and $\Delta\eta_i$ the measured position resolutions in mid section cell units. Replacing we obtain

$$\Delta\theta \simeq \frac{60\,mrad}{\sqrt{E}}$$

slightly above the required $50\,mrad/\sqrt{E}$.

5.9 Energy signal dependence with the HV setting

In order to study the signal dependence on the voltage applied across the liquid argon gap, $60\,GeV$ electron runs at $\eta = 2.2$ were taken with HV varying from 0.9 to $1.3\,Kv$. In the analysis of these runs the same corrections calculated for the nominal HV setting were applied to the data.

Fig 5.44 shows the energy signal spectra for the different HV settings. The energy signal (E) is predicted to vary with HV (see section 3.3) as

$$E = E_0 \cdot \left(\frac{V}{V_0}\right)^{\gamma}$$

when V varies around a reference value V_0. The exponent is predicted to be $\gamma \simeq 0.3$. A more convenient way to write the formula is

$$E = E_0 \cdot (1 + \epsilon_v)^{\gamma}$$

where $\epsilon_v = (V - V_0)/V_0$ is adimensional. For $\epsilon_v << 1$, linearizing, one gets

$$E \simeq E_0 \cdot (1 + \gamma \cdot \epsilon_v)$$

Fig 5.45 (upper) shows the measured dependence of the mean signal on the HV applied to the electrodes. The data are fitted with the linearized theoretical expression yielding

$$\gamma = 0.3672 \pm 0.0018$$

The non-linearized function, with the values obtained from the linear fit for the parameters γ, E_0, is shown for comparison superimposed on the figure. The linear approximation is seen to hold very accurately in the HV range tested. The result obtained is in good agreement with the predictions obtained by combining simulation and electron drift time velocity measurements, shown in section 3.3.

The energy resolution is shown for the different HV settings in Fig 5.45 (lower). It seems to be roughly constant throughout the voltage range tested.

5.10 Time reconstruction

5.10.1 Introduction

A method has been developed for reconstructing the time at which the signal peak occurs in a given cell. The method uses a simple function of the samplings performed on the charge pulse. The function is

$$t_{rec} = \frac{s_2 + s_3 - s_4 - s_5}{s_2 + s_3 + s_4 + s_5}$$

where s_i are the sampled amplitudes.

In the case of a cell with a substantial amount of energy deposition in it, t_{rec} is observed to be a quasi-linear monotonic function of T_{tdc}. The shape of this dependence is determined by the relative position of the samples on the pulse profile w.r.t. the pulse maximum. The closest to linear behaviour occurs when s_2, s_3 are on average on the straight part of the rising slope and s_4, s_5 are on the falling side. This is approximately the case for the energy dominant mid section cells at $\eta = 2.2$ in runs 101007-101210.

The dependence of t_{rec} with respect to T_{tdc} is somewhat distorted if the pulse is shifted w.r.t. the position of the samples on the time axis. This effect can be seen for any of the runs prior to number 101006. The two types of behaviour can be compared in Fig 5.46.

5.10.2 Time resolution

In this section an estimate is given for the resolution that can be achieved in the time measurement using the quantity t_{rec}. In order to do this, only runs with the almost linear behaviour shown in Fig 5.46 (lower) will be used (i.e. region $\eta = 2.2$, run number larger than 101006). A calorimeter-based estimate of T_{tdc} will be obtained using the t_{rec} of a given cell in the mid section, containing on average most of the deposited energy. Events hitting that given cell are selected by imposing cuts on the reconstructed ϕ, η coordinates.

The t_{rec} technique was already applied in order to reject events with DAQ misfunctioning, as explained in 5.6.1. Time resolution will be evaluated using two runs, namely 101209 ($150\,GeV$) and 101210 ($120\,GeV$). The dependence of t_{rec} w.r.t. T_{tdc} is shown in Fig 5.47 for the two runs. A linear function is used for the fit. The formula can be inverted in order to define

$$T_{rec} = \frac{t_{rec} - A_0}{A_1}$$

This quantity T_{rec} provides for each event an unbiased estimate of the true time T_{tdc} and can thus be used in order to evaluate the time resolution of the calorimeter.

Time reconstruction performed in this way is sensitive to the amount of energy deposited in the cell used. This effect can be seen in Fig 5.48, where the error $T_{rec} - T_{tdc}$ is shown as a function of energy in the cell for all events, and also averaging over energy bins. Notice that a slight energy dependent bias exists in the time reconstruction. These systematics have not been corrected for. Fig 5.48 shows as well the distribution of $T_{rec} - T_{tdc}$ for the $120\,GeV$ run studied. Resolution is found to be

$$\sigma\left(T_{rec} - T_{tdc}\right) = 0.299 \pm 0.003\,ns$$

The result is roughly similar when using the $150\,GeV$ run.

5.11 Momentum spread of the test beam

The beam momentum spread can be calculated from the collimator apertures. If both collimators are set to the same value C, one obtains [12]

$$b_s = \frac{\Delta p}{p} = \sqrt{2}k \cdot C[mm]$$

where $k \simeq 0.0005$.

This formula can be tested using data taken at the same beam energy with different collimator apertures. These data are available at $150\,GeV$.

[12] CERN SPS documentation provides the formula to calculate the beam momentum spread as a function of the collimator apertures.

Energy resolution at a given input beam energy is written as

$$\frac{\sigma}{E} = a \oplus b_s$$

where b_s is the beam spread and all other effects are contained in a. Replacing the expression obtained above for b_s and rearranging

$$\frac{\sigma}{E} = a \cdot \sqrt{1 + \frac{2k^2}{a^2} \cdot C^2}$$

where $\frac{2k^2}{a^2} \cdot C^2 << 1$. Thus

$$\frac{\sigma}{E} \simeq a \cdot \left(1 + \frac{k^2}{a^2} \cdot C^2\right)$$

Energy resolution was measured for three collimator apertures. Only for one of them high statistics were available ($\simeq 30k$ events). The full statistics of this run (namely 101209) were used for all the corrections. In order not to bias the calculation, energy resolution was measured using similar statistics ($\simeq 3k$ events) for the three apertures. The measured resolutions are given as a function of the collimator aperture in Fig 5.49. A two parameter fit, according to the linearized expression given above, was done with the measured energy resolutions, yielding

$$a = 0.0096 \pm 0.0005$$

$$k = 0.00033 \pm 0.00006$$

The result obtained for k is compatible with the information provided by the beam line documentation.

5.12 Conclusions on the beam test of module-0

A module with the final design of the ATLAS EMEC was tested for the first time with a particle beam in September 1998. Only a limited part of the module was fully equipped for read out and there were some regions without HV supply. However the results are compatible with the expected performance.

Energy resolution in the only region where no severe problems were found with the HV supplied to the read out electrodes (namely $\eta = 2.2$), was measured to be

$$\frac{\sigma}{E} = \frac{9.2 \pm 0.2\%}{\sqrt{E[GeV]}} \oplus 0.53 \pm 0.04\% \oplus \frac{noise}{E}$$

with $noise = 338\,MeV$ $(669\,MeV)$ for the gain used in the low (high) energy range.

The systematics of the energy signal with respect to ϕ have qualitatively the expected behaviour. Extensive uniformity studies were not possible due to the limited region of the module equipped and to problems with the read out electrodes.

In the regions of the detector with severe voltage or leakage problems (namely $\eta = 1.55$ and $\eta = 2.9$) the detector behaved qualitatively as expected.

Position resolution in the ϕ direction, expressed in mid section cell units, can be parametrized as

$$\sigma(\phi) = \frac{0.442}{\sqrt{E[GeV]}}$$

In the η direction, position resolution is comparable when using the front or the mid section of the detector. It can be parametrized, in mid section cell units, as

$$\sigma(\eta) \simeq \frac{0.42}{\sqrt{E[GeV]}} \oplus 0.012$$

Assuming the expected position spread of the IP in ATLAS (see 2.2.2), the pointing angle resolution in the two orthogonal directions corresponding to the ϕ and η coordinates is, respectively

$$\Delta\psi \simeq \frac{2\,mrad}{\sqrt{E}}$$

$$\Delta\theta \simeq \frac{60\,mrad}{\sqrt{E}}$$

The energy signal was measured to scale with the voltage applied across the gap following the predicted law $E = E_0 \cdot \left(\frac{V}{V_0}\right)^\gamma$ where the exponent was measured to be

$$\gamma = 0.3672 \pm 0.0018$$

Time was reconstructed using a mid section calorimeter cell, achieving a resolution of $\sigma(T) \simeq 0.3\,ns$ at high energy.

These results indicate that the mechanical design, component construction and assembly procedure of the EMEC modules are well suited to the performance goals of ATLAS calorimetry. Some improvements are expected in order to reduce the cross-talk level and achieve a better quality of the read out electrodes.

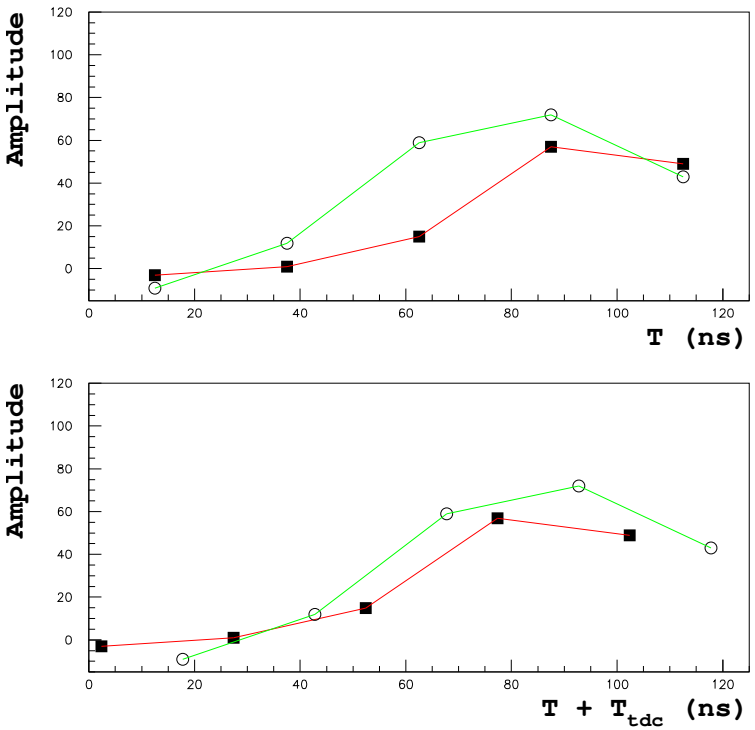

Figure 5.1: Five samplings of two pulses in a mid section cell, for $60\,GeV$ electrons, before (upper) and after (lower) applying T_{tdc} time shift.

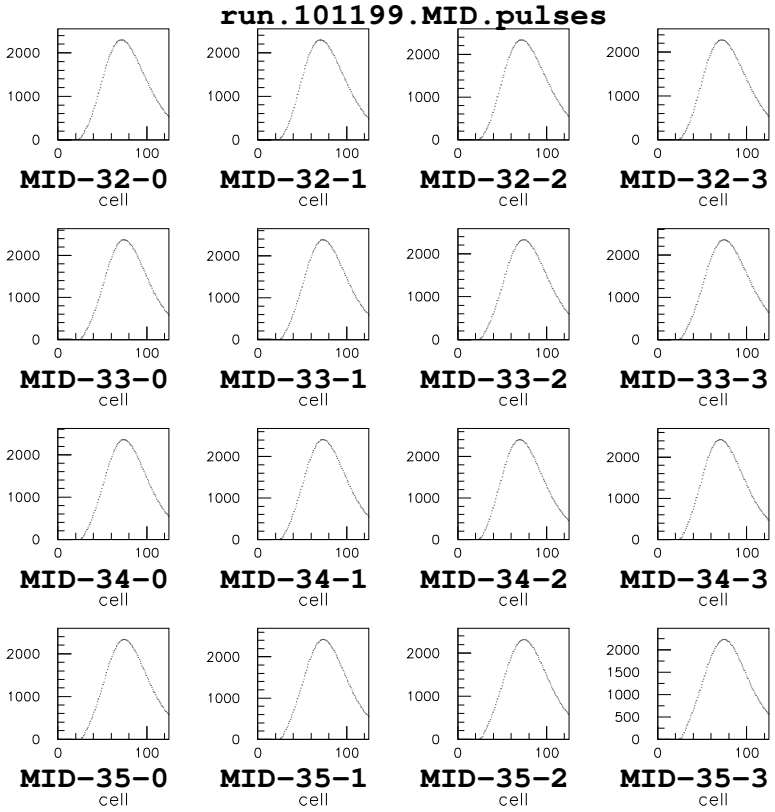

Figure 5.2: Pulse profiles obtained with a medium gain test pulse run, pulsing at all channels at the same time, with 25 delay steps of $1\,ns$. DAC value selected was 8400.

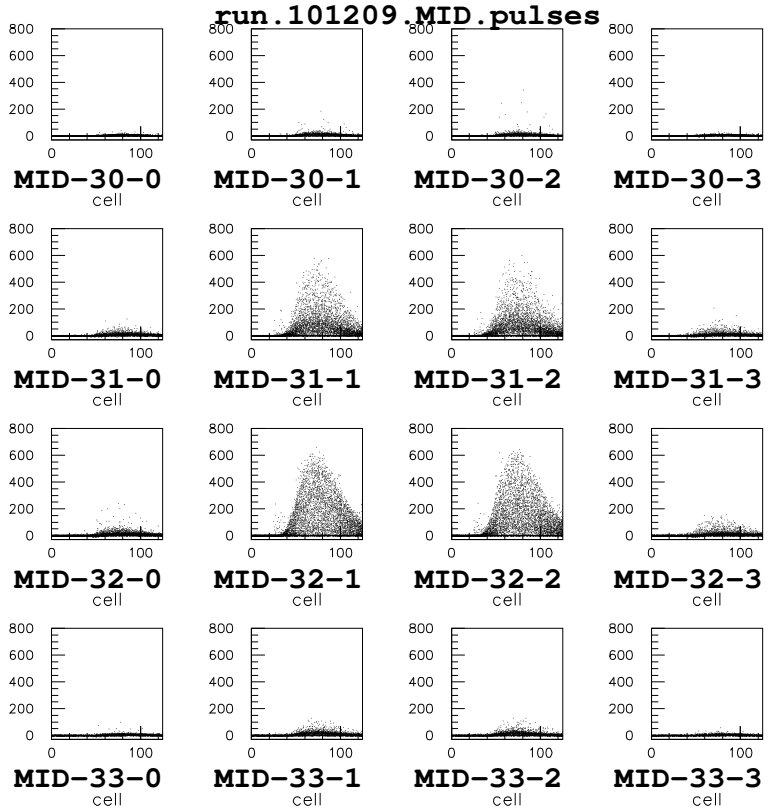

Figure 5.3: Pulse profiles obtained with a $150\,GeV$ electron run. The beam points at the region $\eta = 2.2$. Gain MMH.

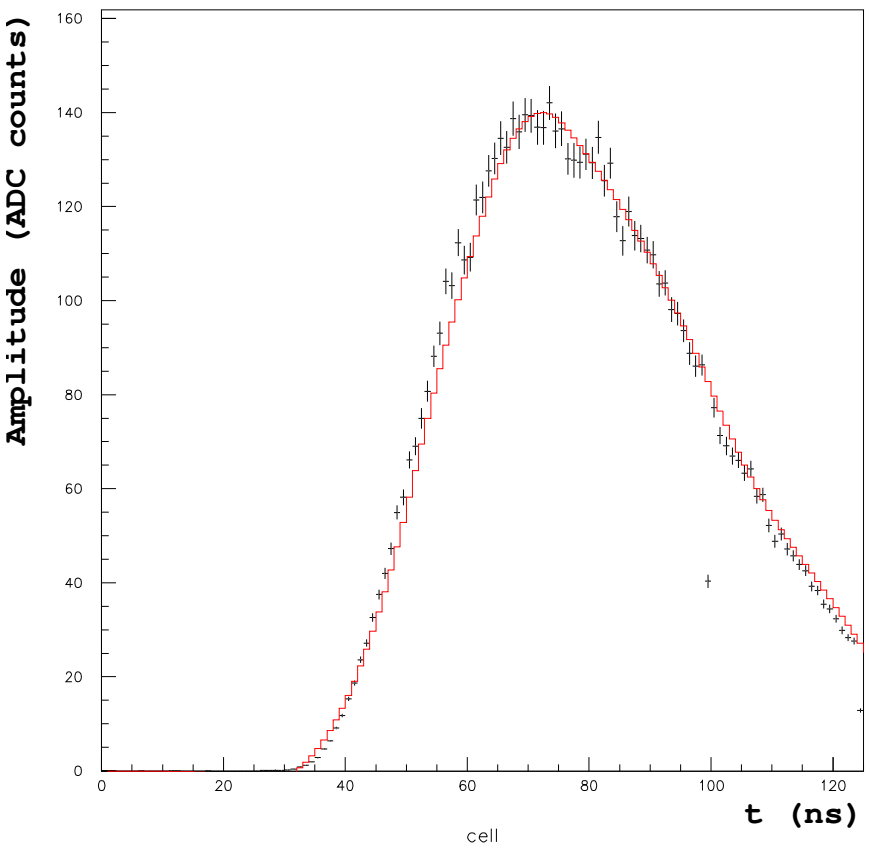

Figure 5.4: Physics pulse profile in a mid section cell before and after spline smoothing. $E = 120\,GeV$.

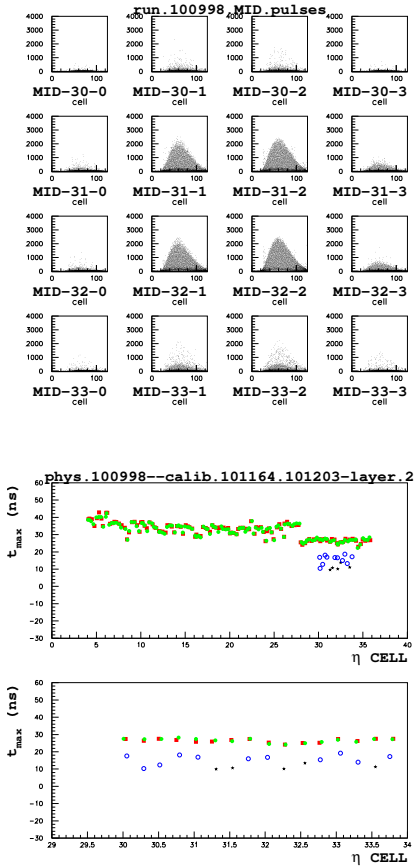

Figure 5.5: Lower: Time of the pulse peak for mid section cells, as a function of the η cell number, for two test pulse runs (grey squares; green and red if color copy) and for a $60\,GeV$ electron run (number 100998), with the beam pointing at the region $\eta = 2.2$ and gain HHH. Energy dominant cells are marked with full (black) stars and non-dominant ones with open (blue) circles. Physics pulses are shown on the upper half.

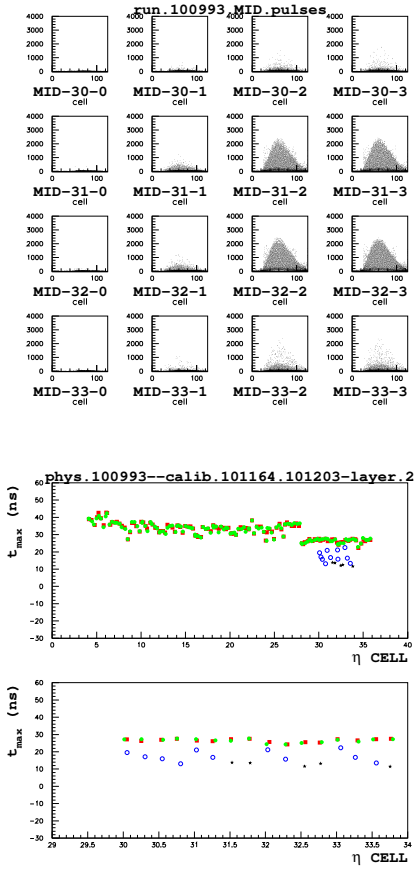

Figure 5.6: Lower: Time of the pulse peak for mid section cells, as a function of the η cell number, for two test pulse runs (grey squares; green and red if color copy) and for a $60\,GeV$ electron run (number 100993), with the beam pointing at the region $\eta = 2.2$ and gain HHH. Energy dominant cells are marked with full (black) stars and non-dominant ones with open (blue) circles. Physics pulses are shown on the upper half.

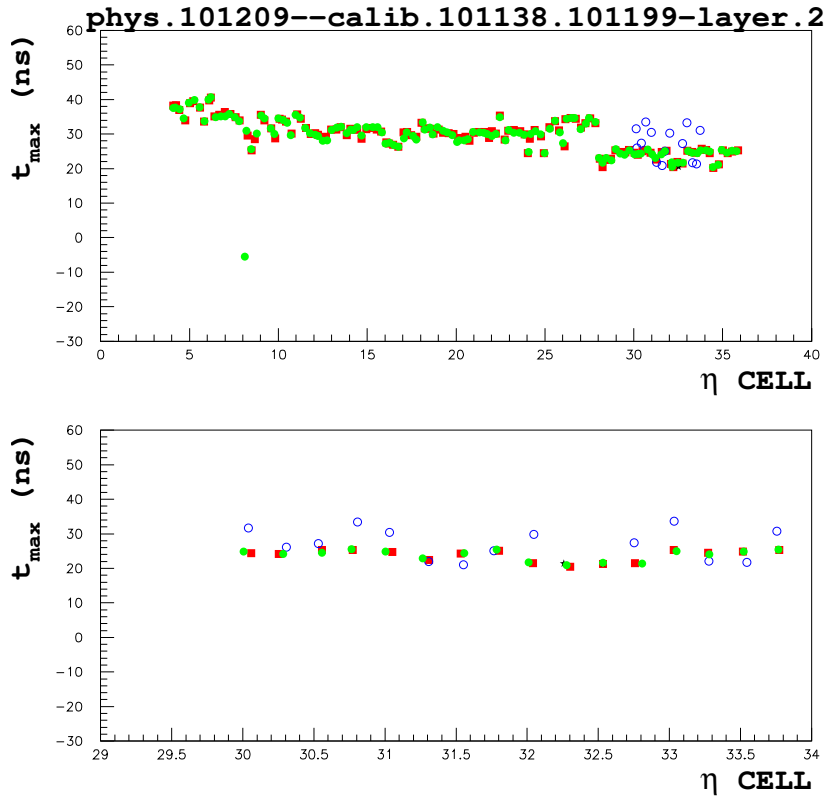

Figure 5.7: Time of the pulse peak for mid section cells, as a function of the η cell number, for two test pulse runs (grey full squares; green and red if color copy) and for a $150\,GeV$ electron run (number 101209), with the beam pointing at the region $\eta = 2.2$ and gain MMH. Full (black) stars are used for channels with larger energy signal and open (blue) circles for channels with smaller signals.

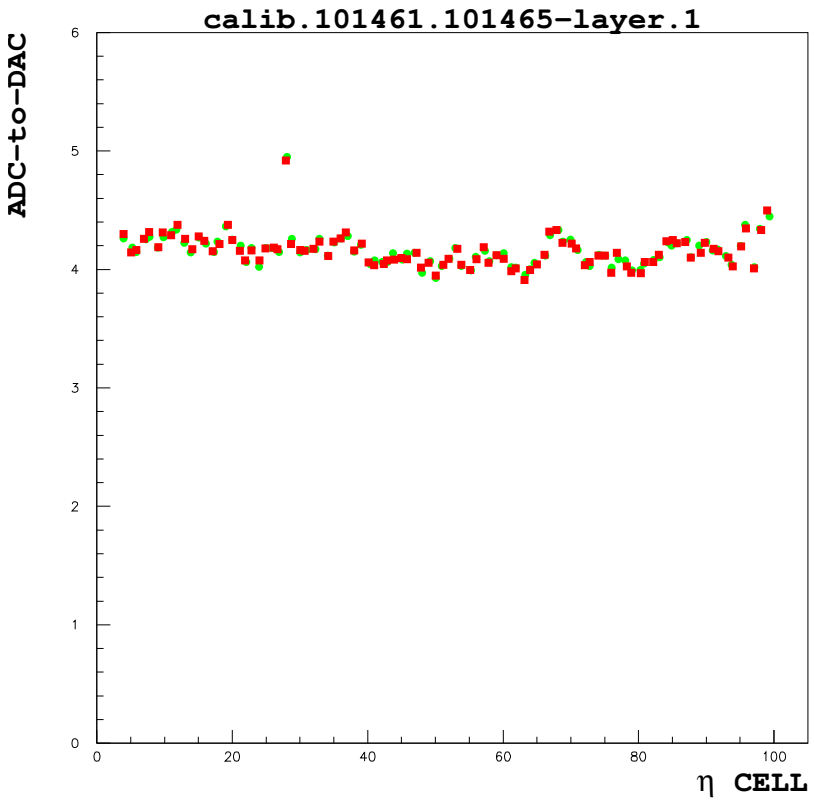

Figure 5.8: Conversion factor from ADC to DAC counts from two test pulse runs (grey squares; green and red if color copy) as a function of the cell η number. Front $cell_{\eta_1} = 1 - 100$ channels are shown.

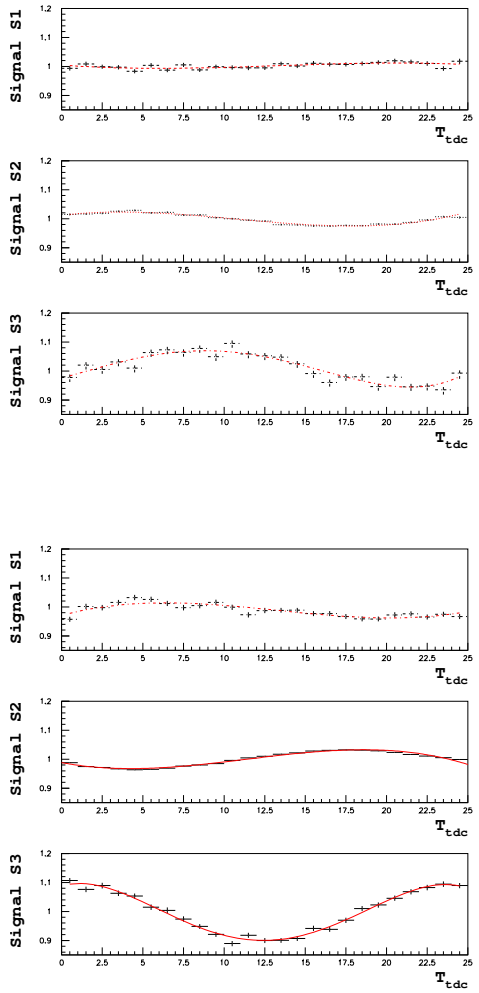

Figure 5.9: Signal seen at each detector section (S1 for front, S2 for mid, S3 for back) as a function of T_{tdc}. Run interval 100968-101005 (upper) and 101007-101210 (lower).

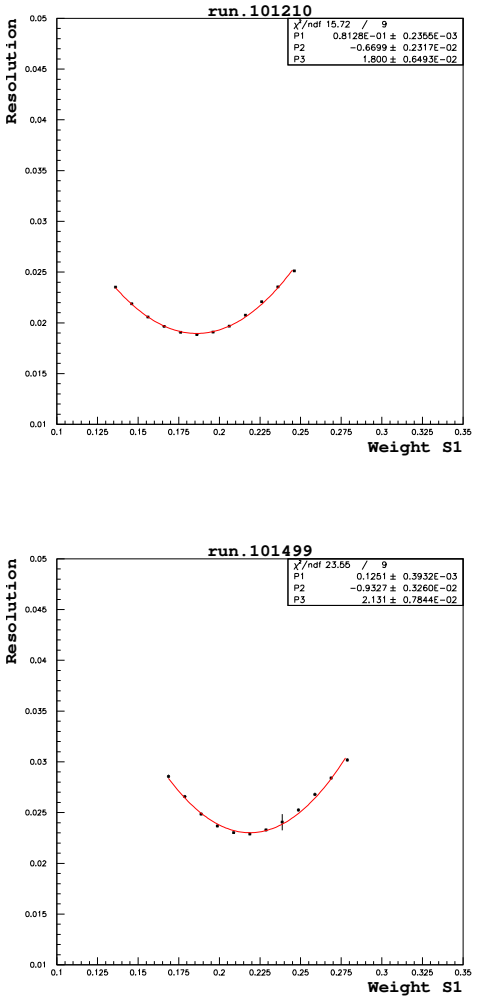

Figure 5.10: Energy resolution for different values of the weight α_1 applied to the front section in the addition of energy signals. Upper: electrons with $E = 120\,GeV$, gain MMH, $\eta = 2.2$. Lower: electrons with $E = 40\,GeV$, gain HHH, $\eta = 1.55$.

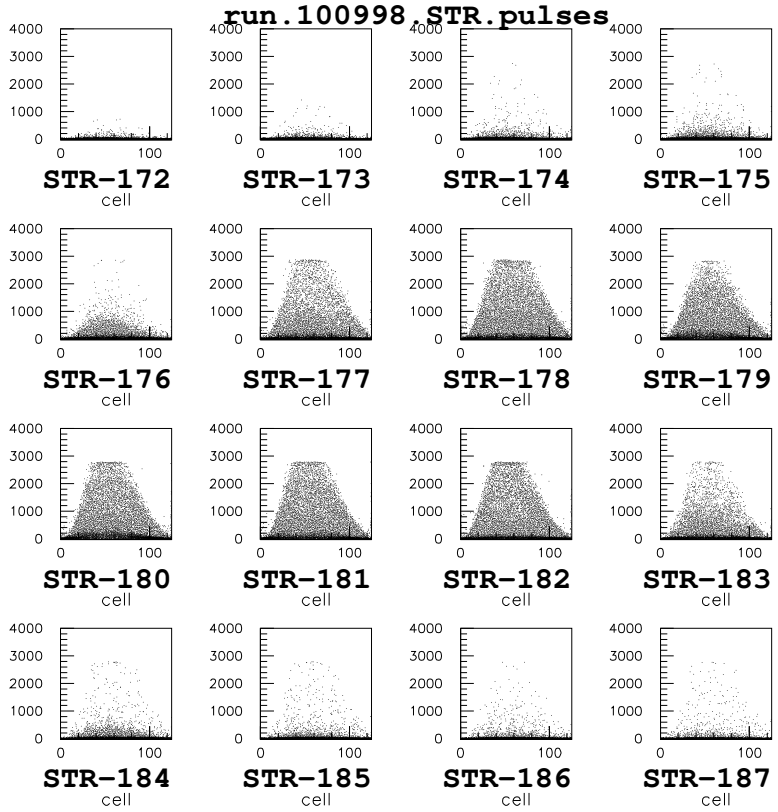

Figure 5.11: Pulses in the front section for a $60\,GeV$ run (number 100998) in the $\eta = 2.2$ region. Gain is HHH. Saturation is observed.

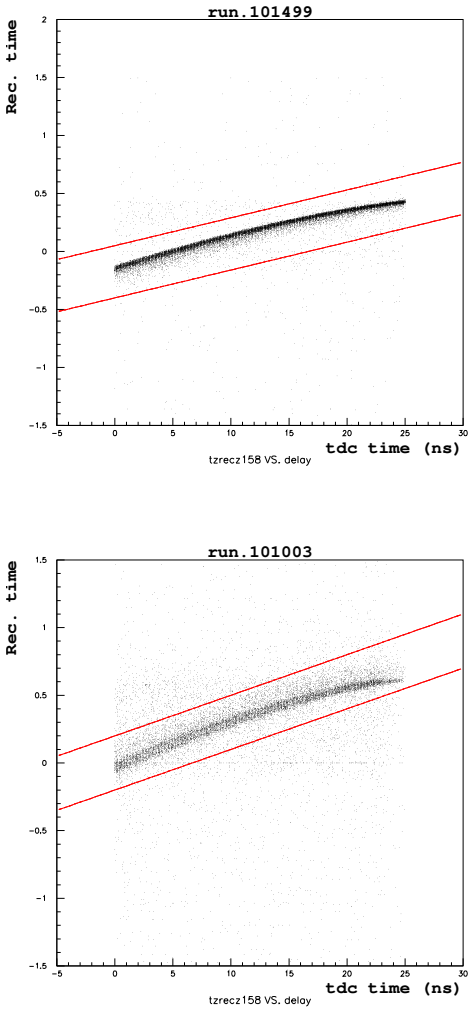

Figure 5.12: Reconstructed time (in arbitrary units) as a function of T_{tdc} for a run with few DAQ problems (top) and for one with many DAQ problems (bottom).

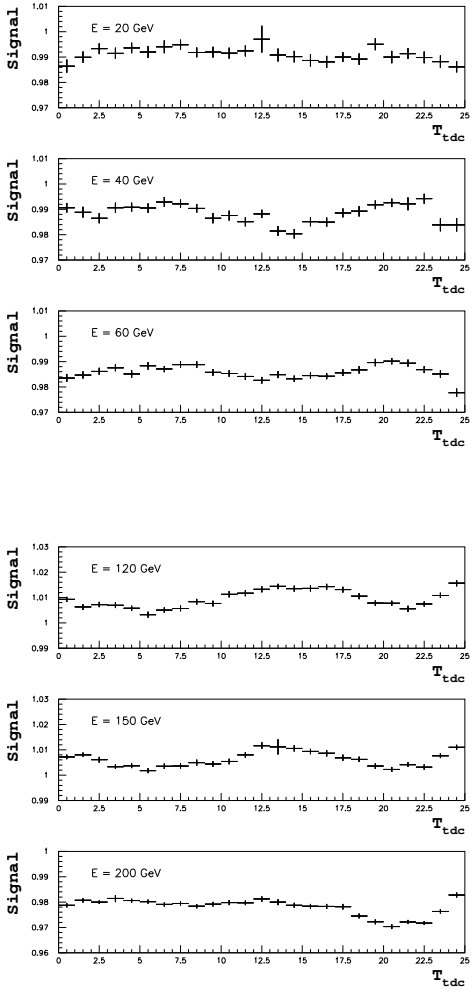

Figure 5.13: Total energy signal (normalized to the beam energy) as a function of T_{tdc} after first iteration correction has been applied to the signal at each detector section. Different beam energies are shown. Region $\eta = 2.2$.

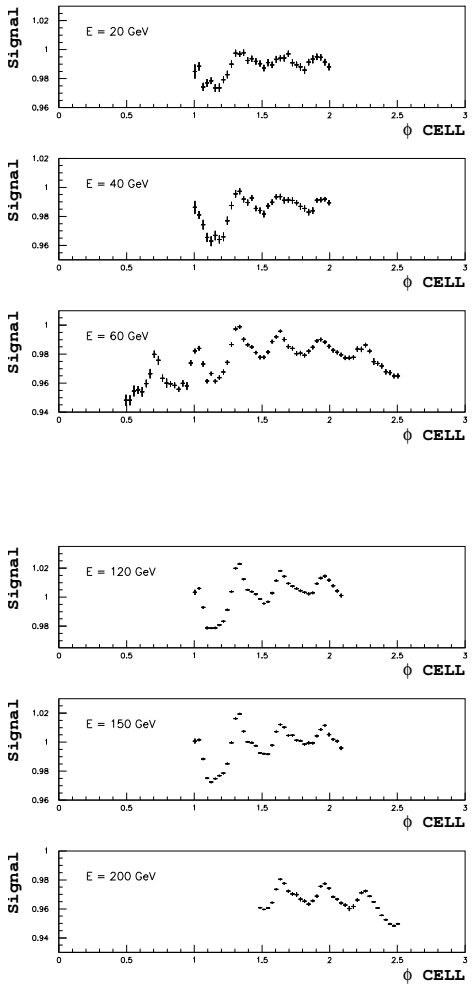

Figure 5.14: Total energy signal as a function of ϕ for different beam energies. Region $\eta = 2.2$.

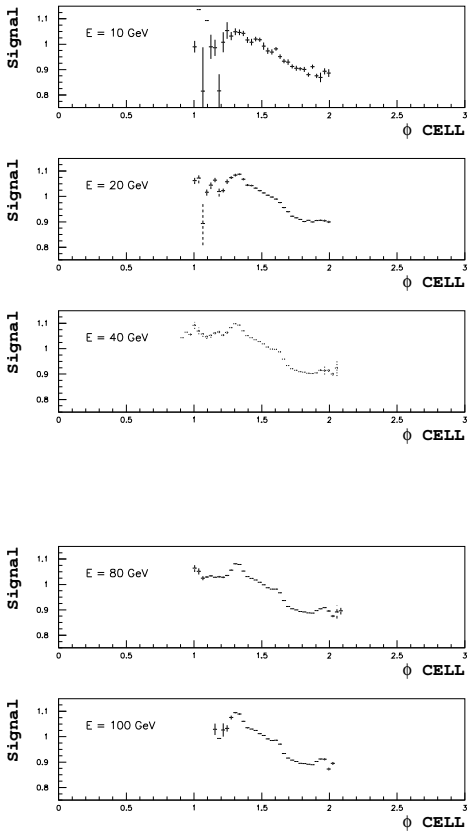

Figure 5.15: Dependence on ϕ of the energy signal at different energies for the region $\eta = 1.55$.

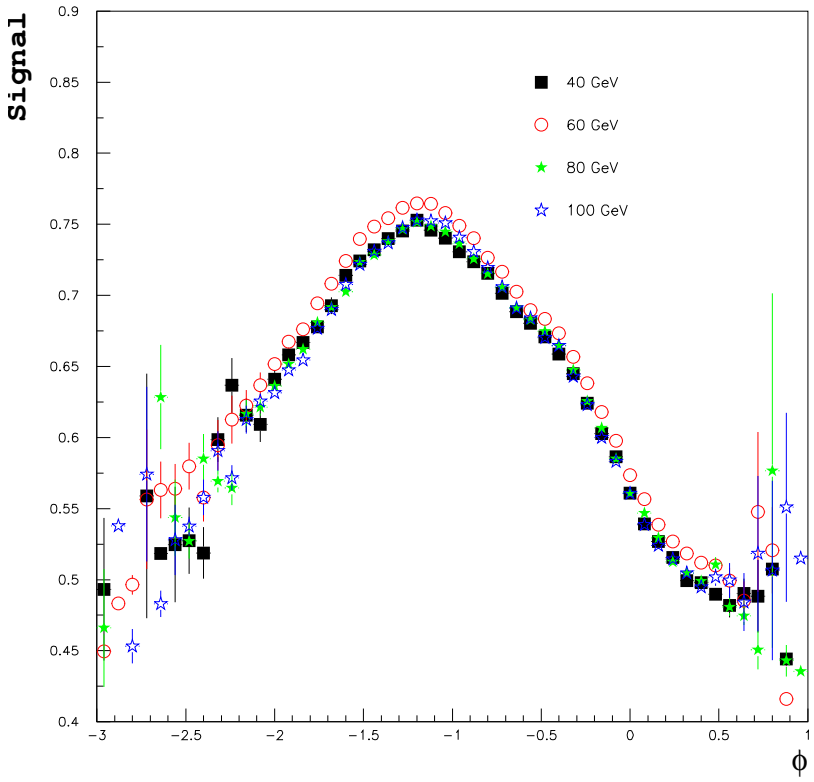

Figure 5.16: Dependence on ϕ (as given by the beam chamber) of the energy signal at different energies for the region $\eta = 2.9$.

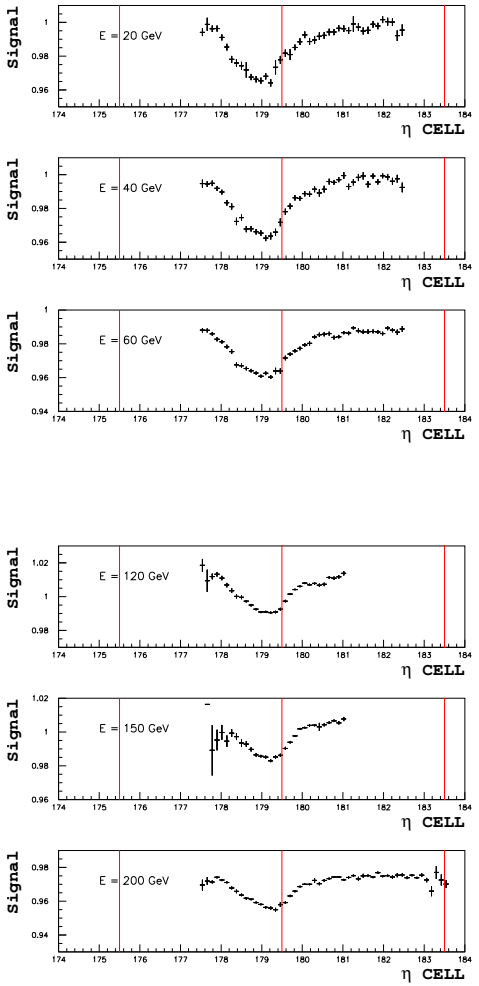

Figure 5.17: Total energy signal as a function of the η barycenter (calculated with the front section) for different beam energies. Vertical lines indicate mid section cell boundaries. The point $\eta = 2.2$ corresponds to the abscissa $cell_{\eta_1} = 179.5$.

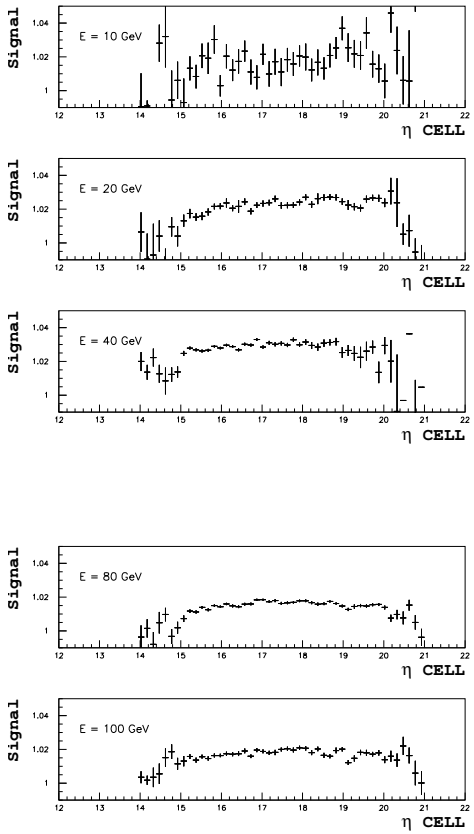

Figure 5.18: Dependence on η of the energy signal in the region $\eta = 1.55$ for different input beam energies.

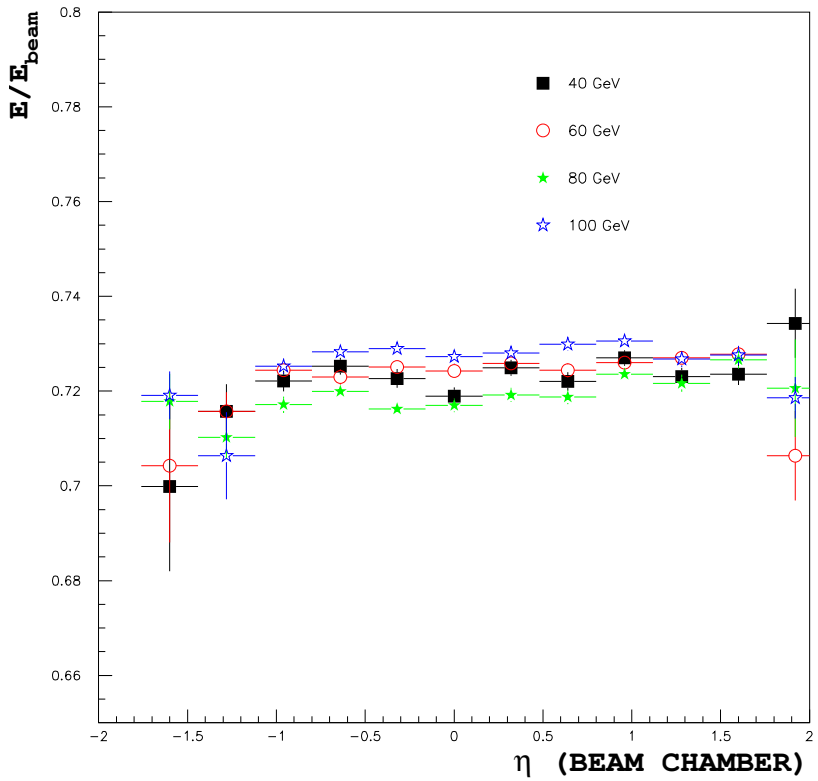

Figure 5.19: Dependence on η (arbitrary units as given by beam chamber) of the energy signal in the region $\eta = 2.9$ for different input beam energies.

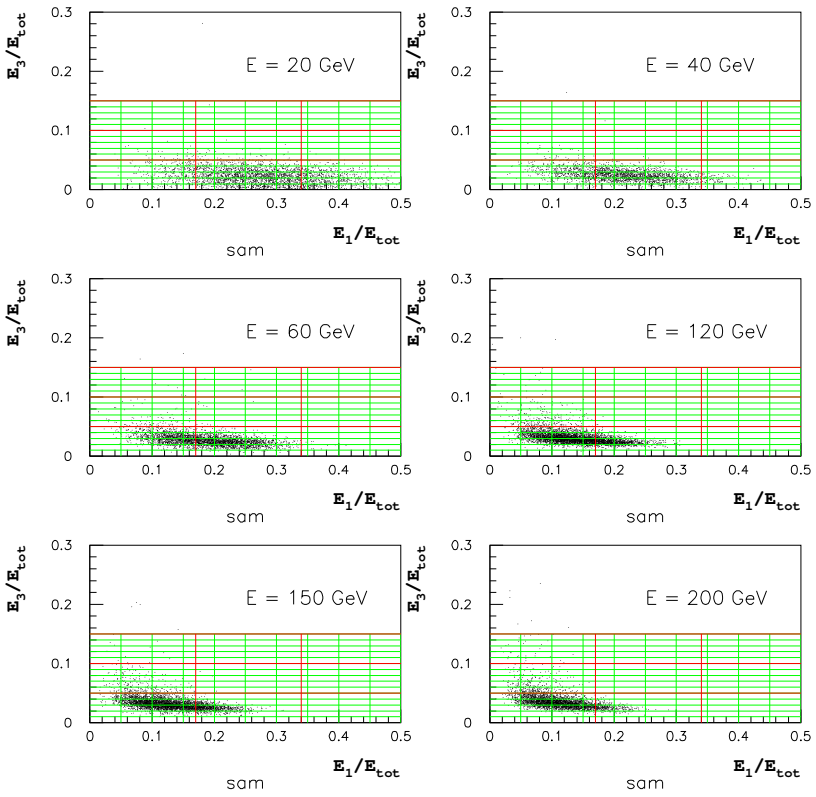

Figure 5.20: Events are represented as points in the (r_1, r_3) plane for different beam energies. Region $\eta = 2.2$.

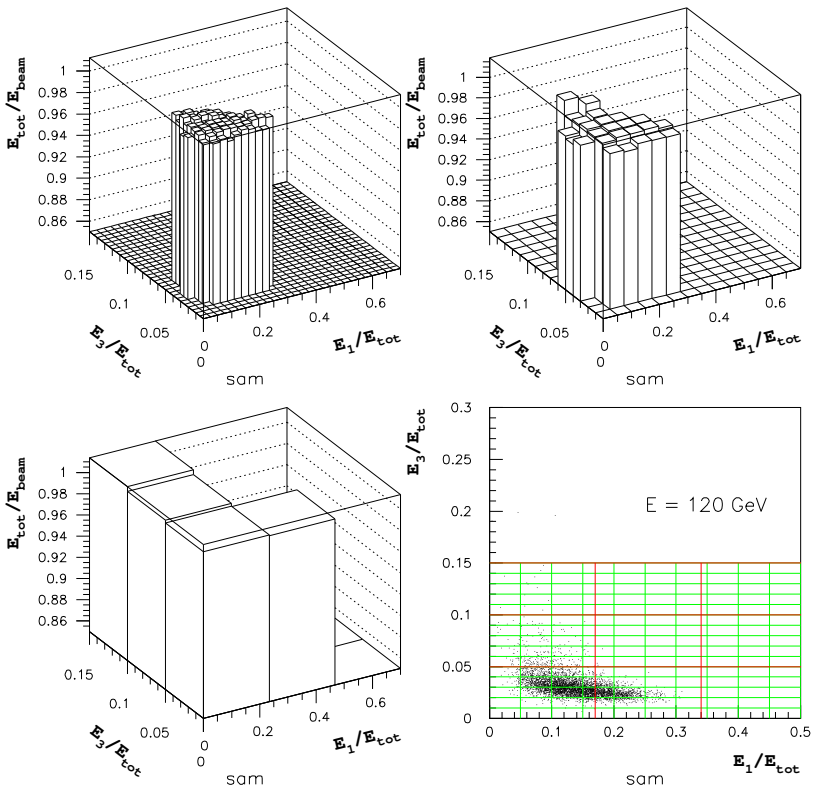

Figure 5.21: Average total observed signal (normalized to the beam energy) as a function of (r_1, r_3). Three different grids are used. $E = 120\,GeV$. The distribution of events in the (r_1, r_3) plane is also shown as a reference. Region $\eta = 2.2$.

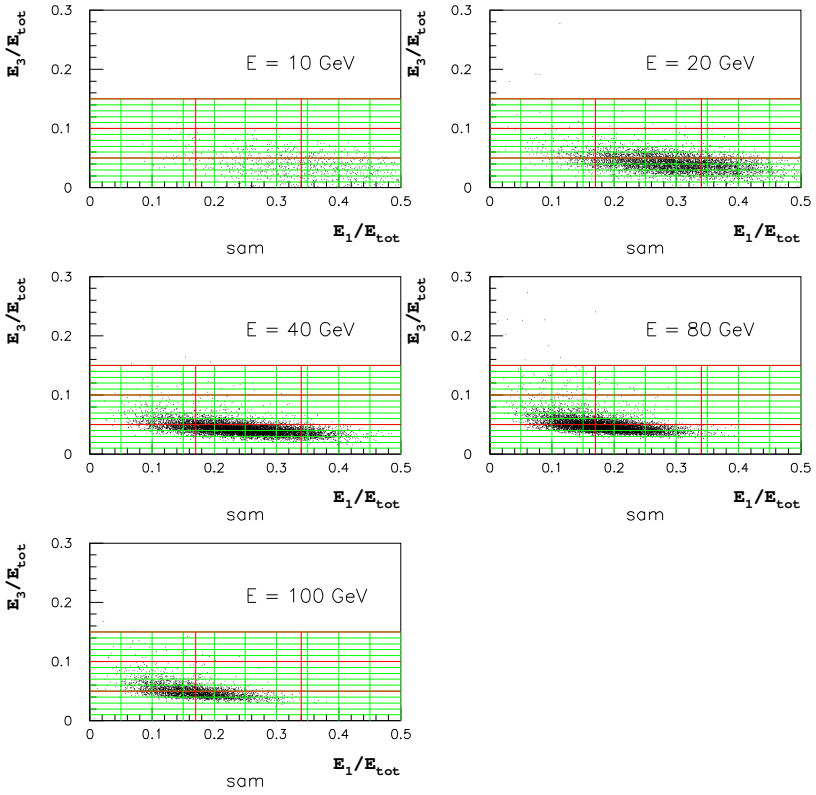

Figure 5.22: Region $\eta = 1.55$. Distribution of events in the (r_1, r_3) plane for different beam energies.

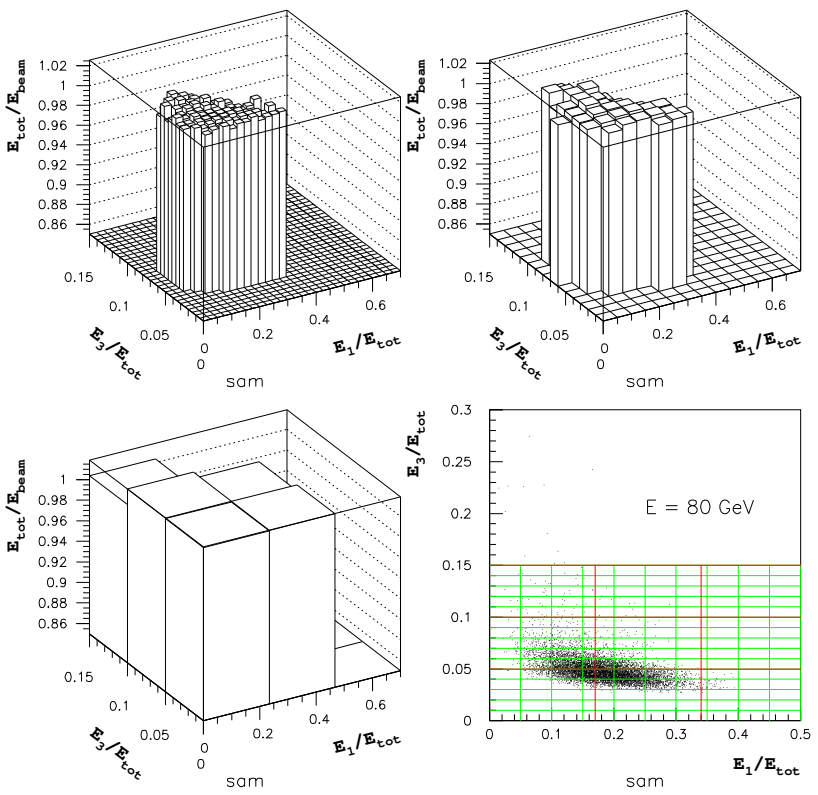

Figure 5.23: Region $\eta = 1.55$. Average total observed signal as a function of (r_1, r_3). Three different grids are used. $E = 80\,GeV$.

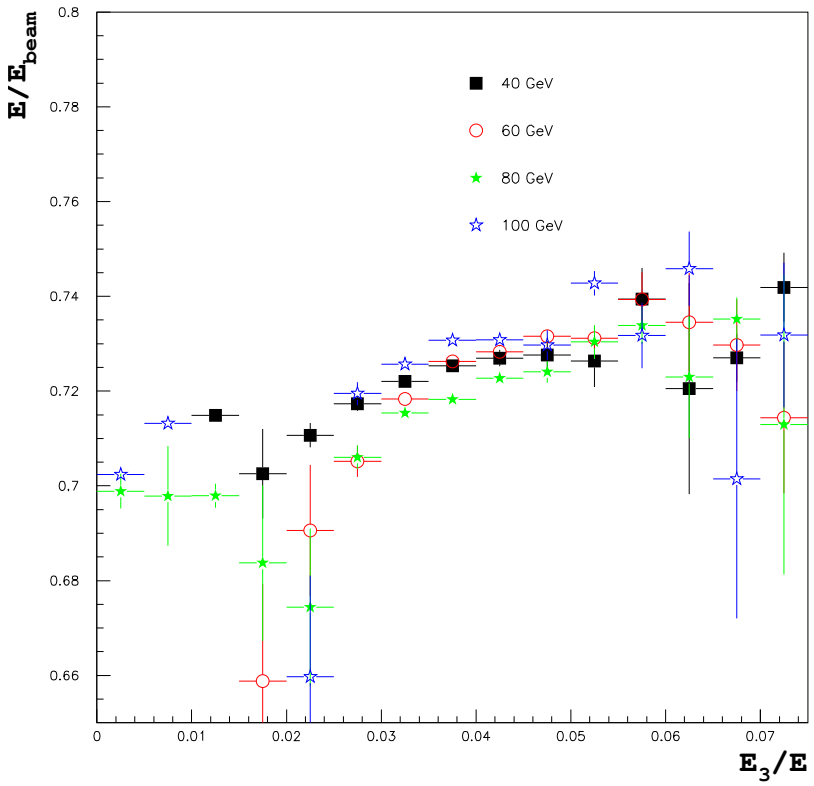

Figure 5.24: Average total observed signal as a function of r_3 in the region $\eta = 2.9$ for different beam energies.

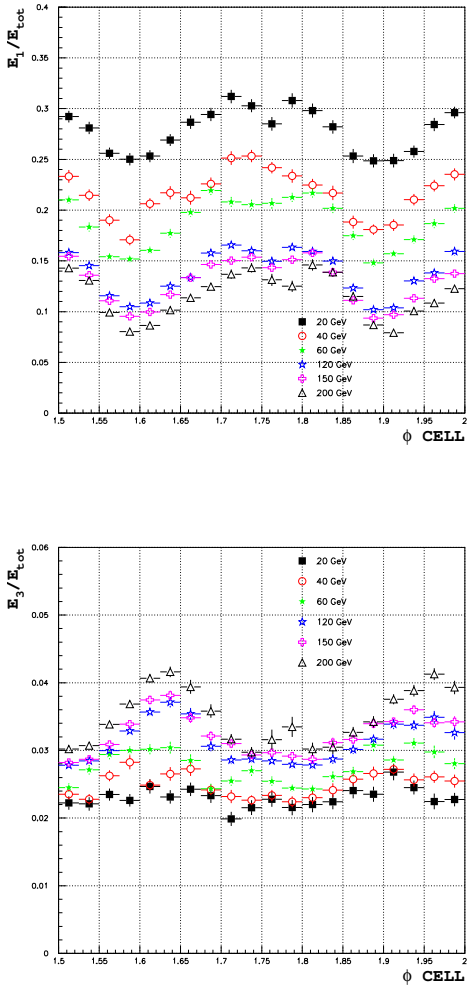

Figure 5.25: Parameter r_1 (top), r_3 (bottom) as a function of the ϕ cell number for different beam energies in the detector region $\eta = 2.2$.

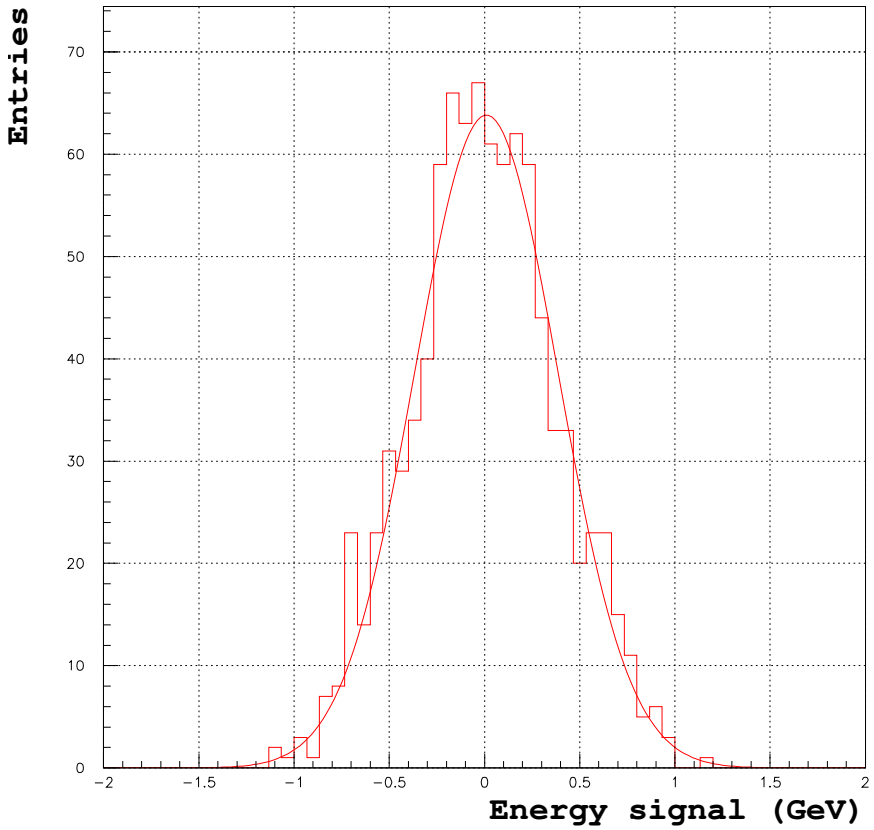

Figure 5.26: Noise spectrum for a 6×4 window, region $\eta = 2.2$, gain HHH.

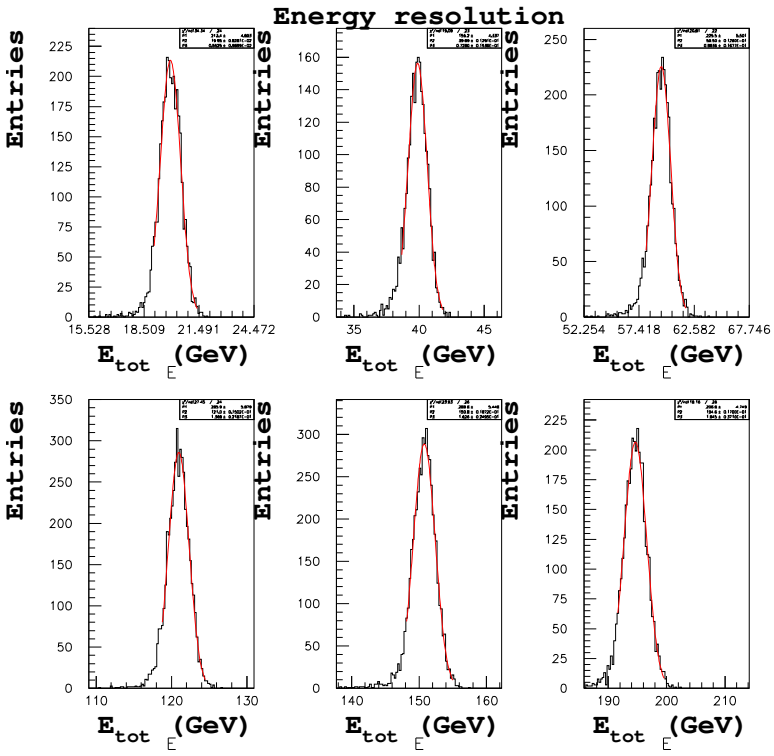

Figure 5.27: Energy signal reconstructed for different beam energies. Region $\eta = 2.2$. The spectra are fitted using gaussians.

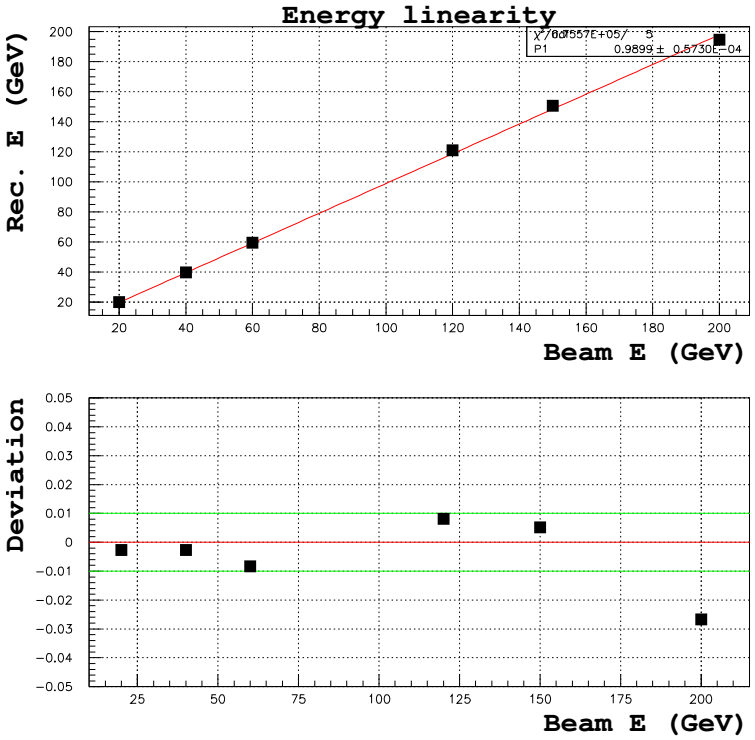

Figure 5.28: Measured energy as a function of beam energy (upper) and fractional deviations from linearity (lower). Region $\eta = 2.2$.

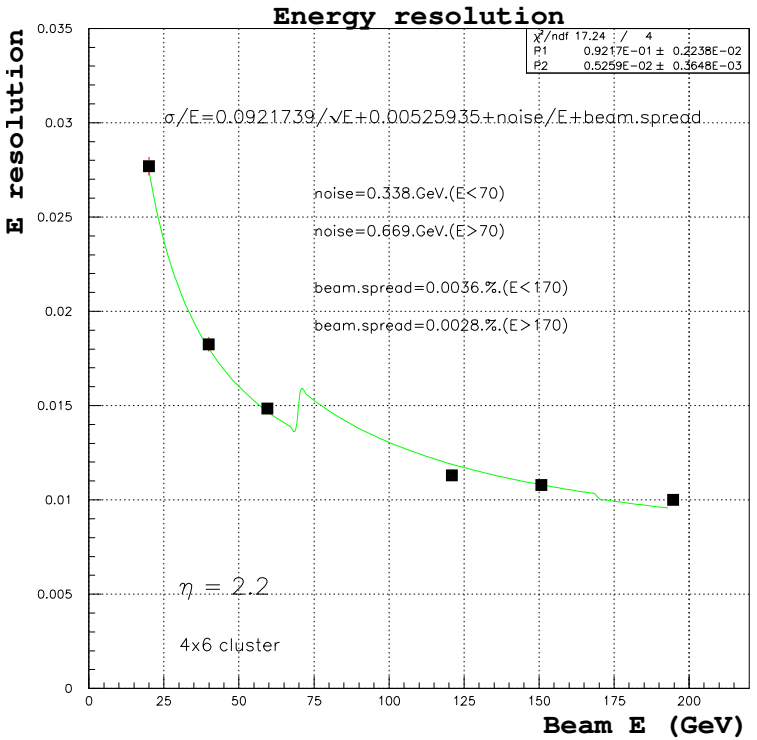

Figure 5.29: Energy resolution as a function of the input beam energy. Region $\eta = 2.2$. Window 6×4.

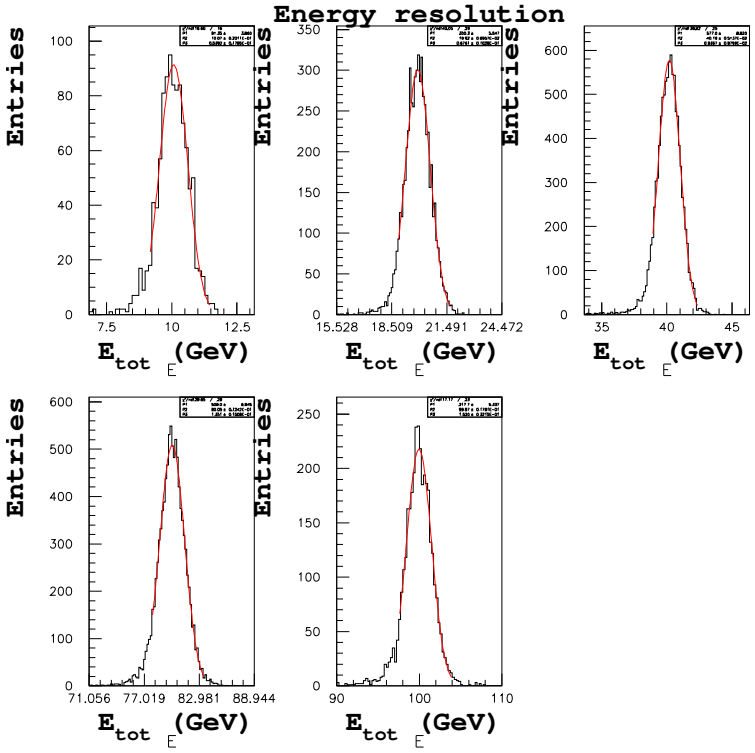

Figure 5.30: Energy signal spectra for different beam energies. Region $\eta = 1.55$.

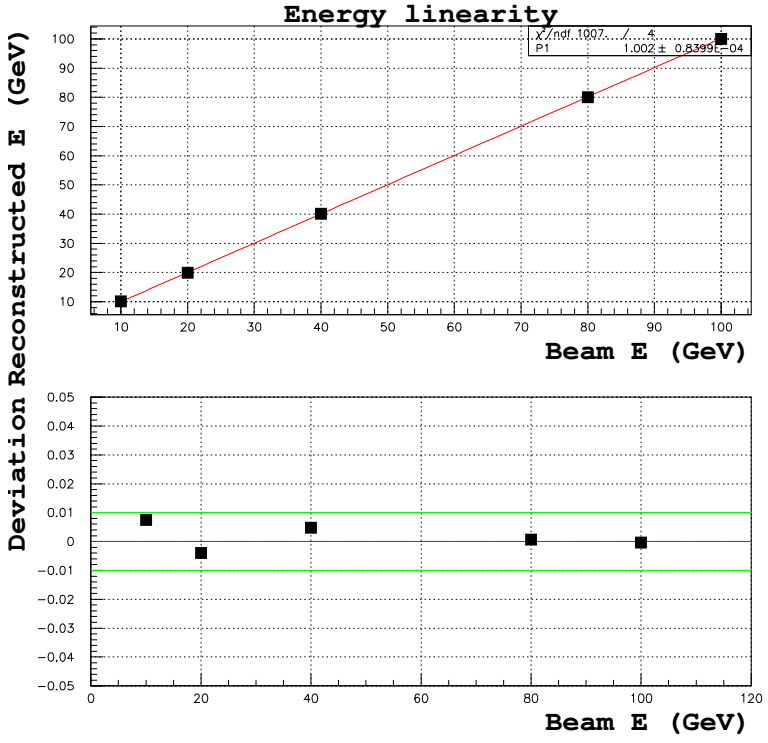

Figure 5.31: Linearity plot for the region $\eta = 1.55$.

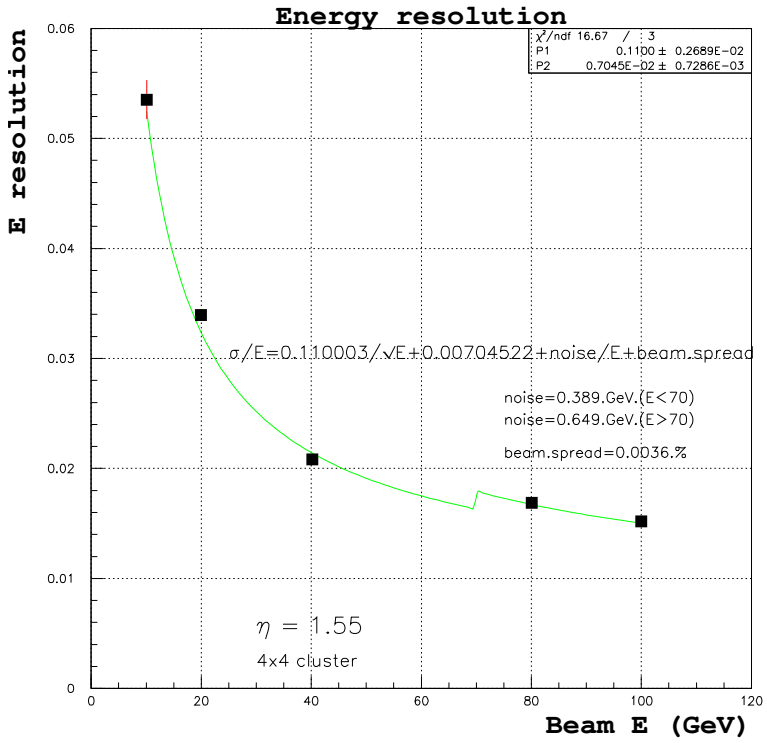

Figure 5.32: Energy resolution as a function of the input beam energy. Region $\eta = 1.55$. Window 4×4.

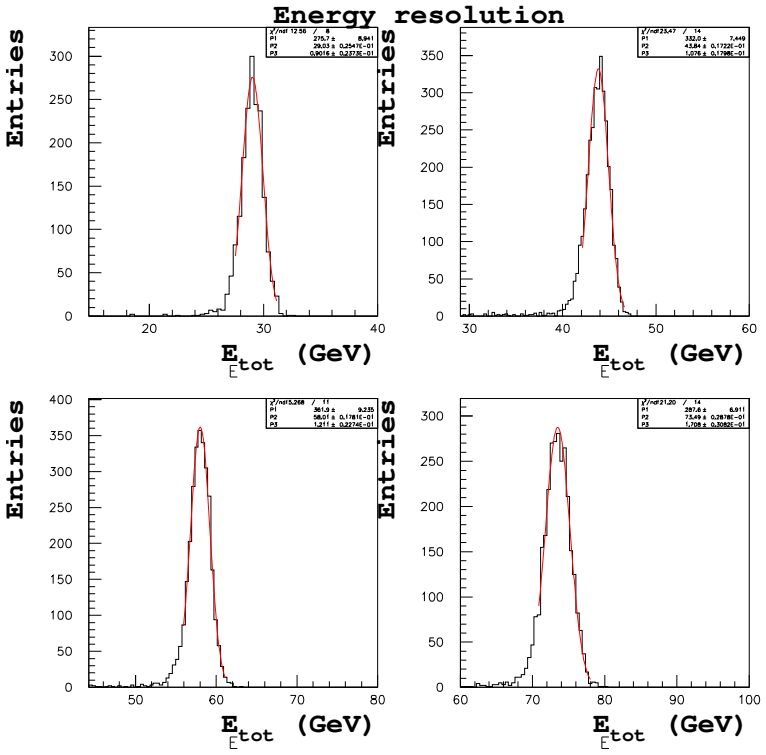

Figure 5.33: Energy signal reconstructed for different beam energies. Region $\eta = 2.9$. The beam energies of the four histograms are: 40, 60, 80, 100 GeV.

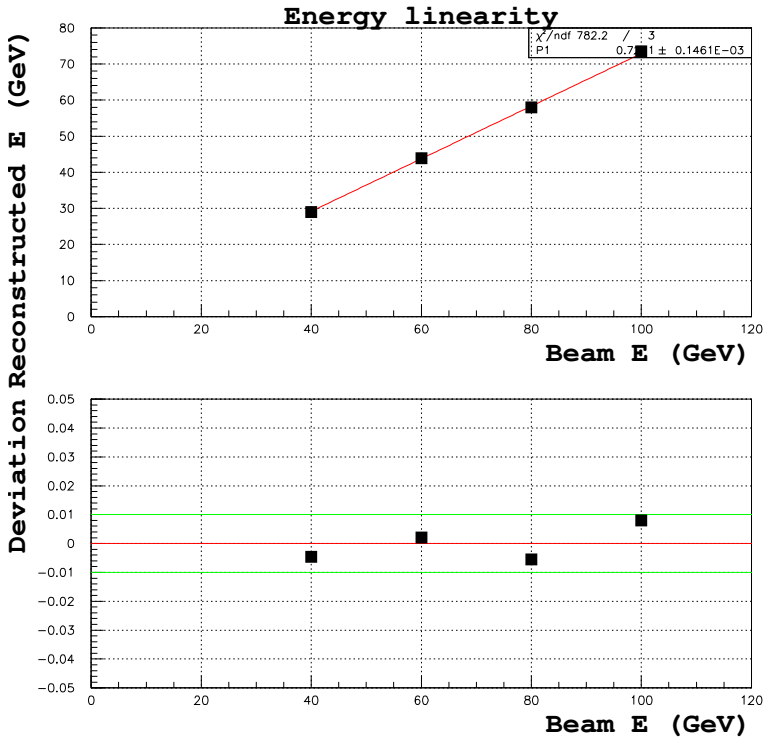

Figure 5.34: Linearity plot for the region $\eta = 2.9$.

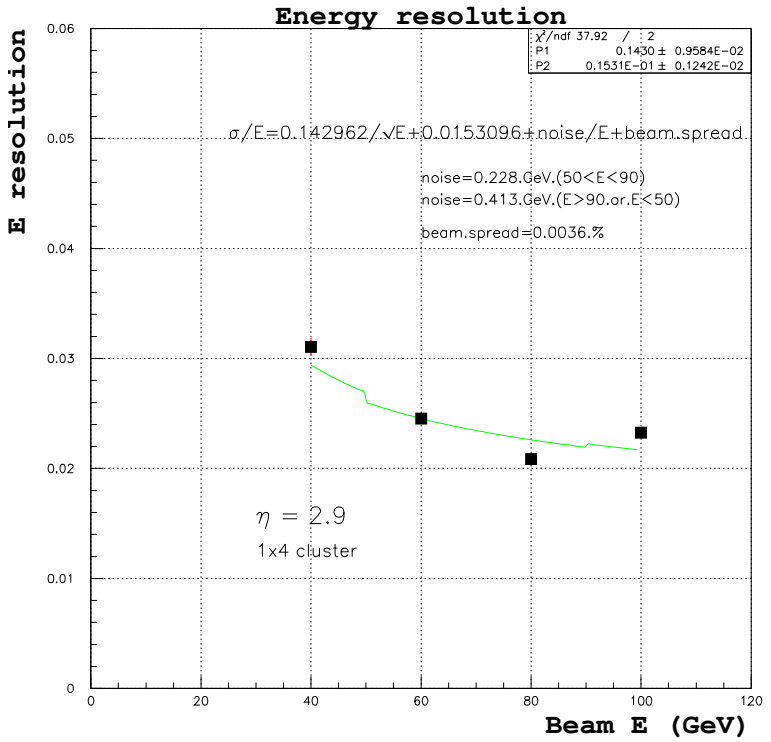

Figure 5.35: Energy resolution as a function of the input beam energy. Region $\eta = 2.9$. Window 4×1.

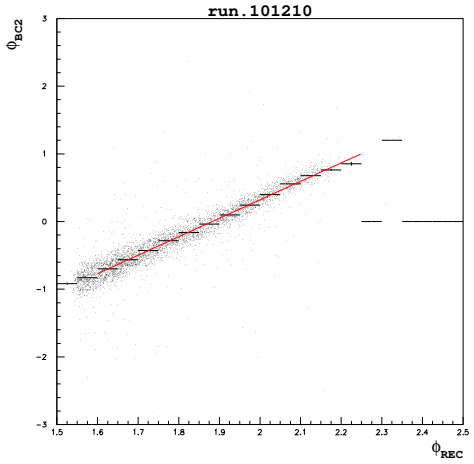

Figure 5.36: Coordinate ϕ provided by beam chamber 2 (arbitrary units) as a function of the reconstructed coordinate ϕ_{rec} (in mid section cell units), for a $120\,GeV$ electron run.

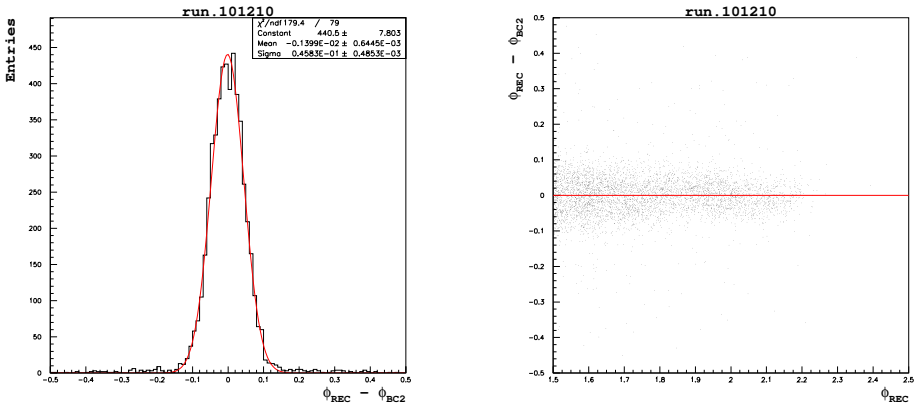

Figure 5.37: ϕ position resolution (in cell units) for a $120\,GeV$ electron run (left). $\overline{\phi_{rec}} - \phi_{bc}$ as a function of $\overline{\phi_{rec}}$ (right).

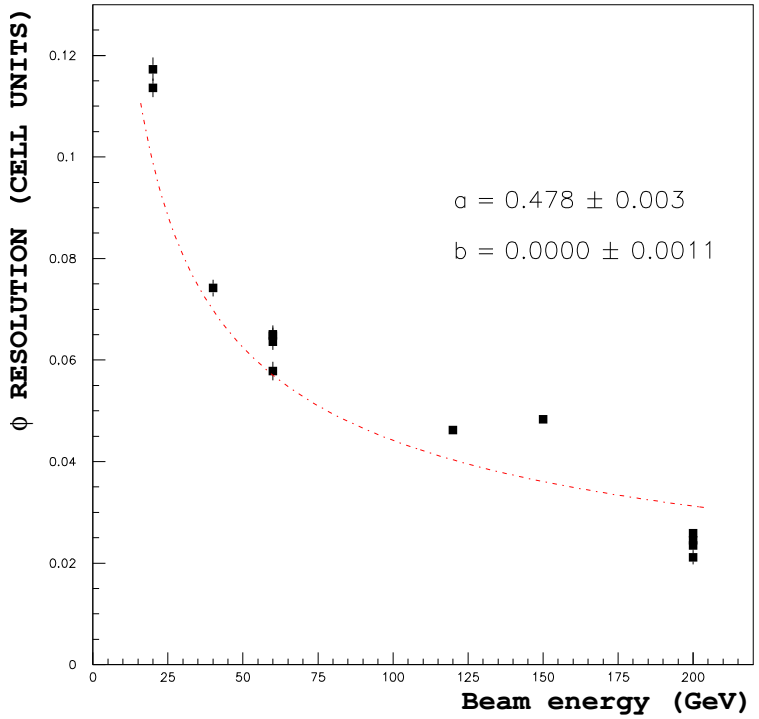

Figure 5.38: ϕ position resolution in cell units as a function of beam energy for particles from an electron beam injected in the region $\eta = 2.2$.

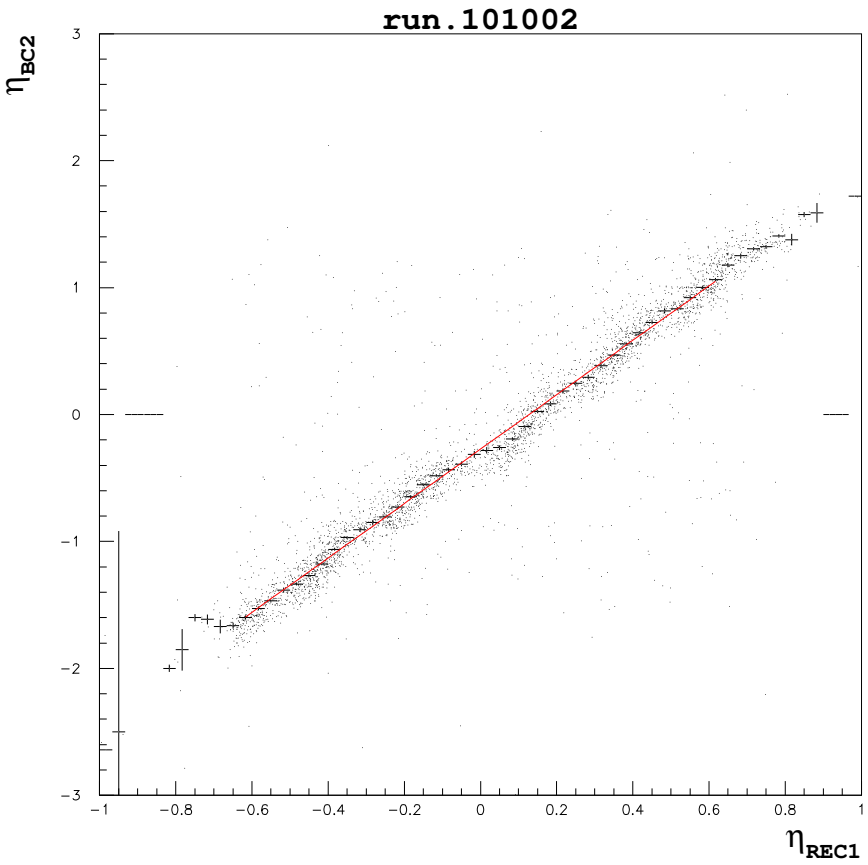

Figure 5.39: Coordinate η given by beam chamber 2 as a function of the barycenter reconstructed with the front section. $E = 60\,GeV$.

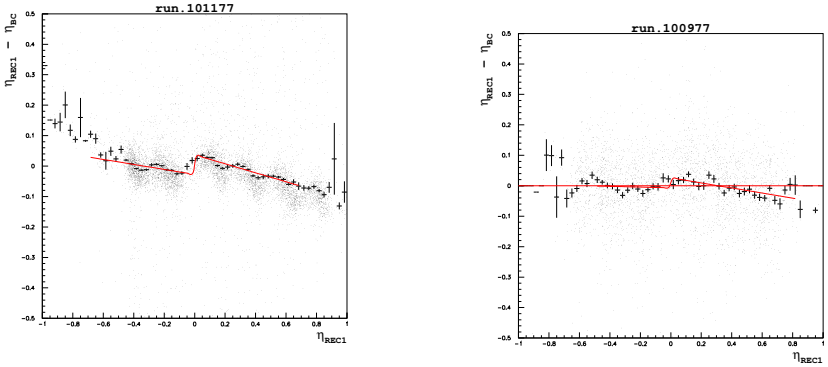

Figure 5.40: Difference between η barycenter reconstructed with the front section (η_{bar1}) and η_{bc}, as a function of η_{bar1}. $E = 200\,GeV$ (left), $20\,GeV$ (right).

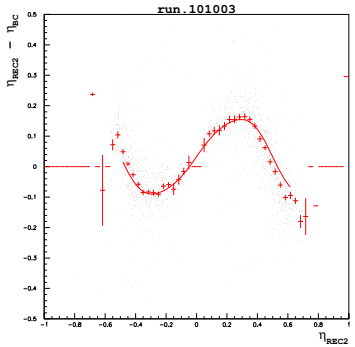

Figure 5.41: Difference between η barycenter reconstructed with the mid section (η_{bar2}) and η_{bc}, as a function of η_{bar2}. $E = 40\,GeV$.

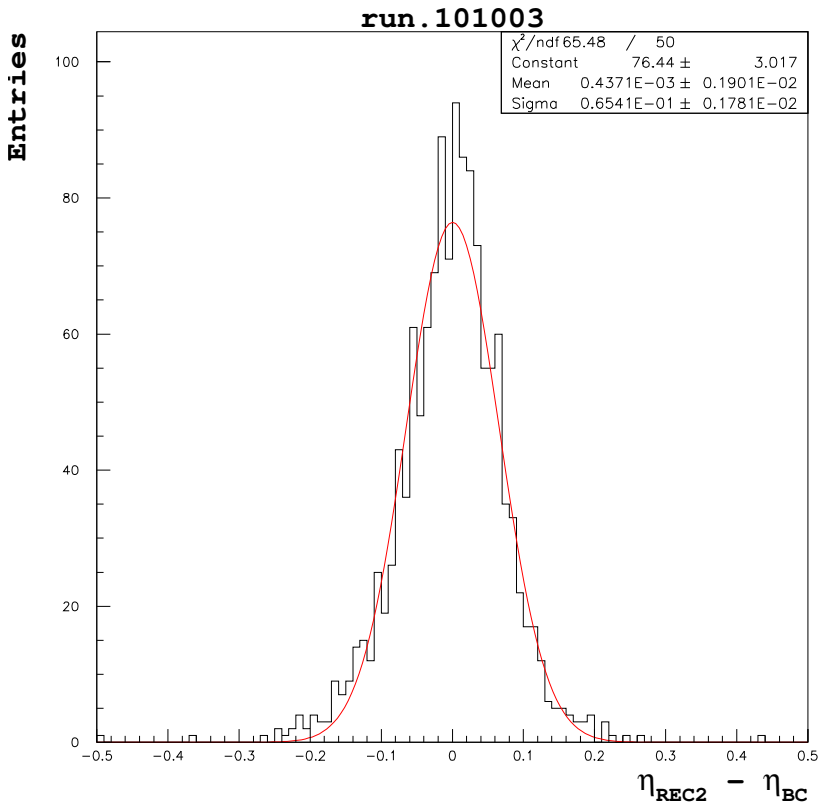

Figure 5.42: Distribution of the difference between η_2 and η_{bc}. $E = 40\,GeV$.

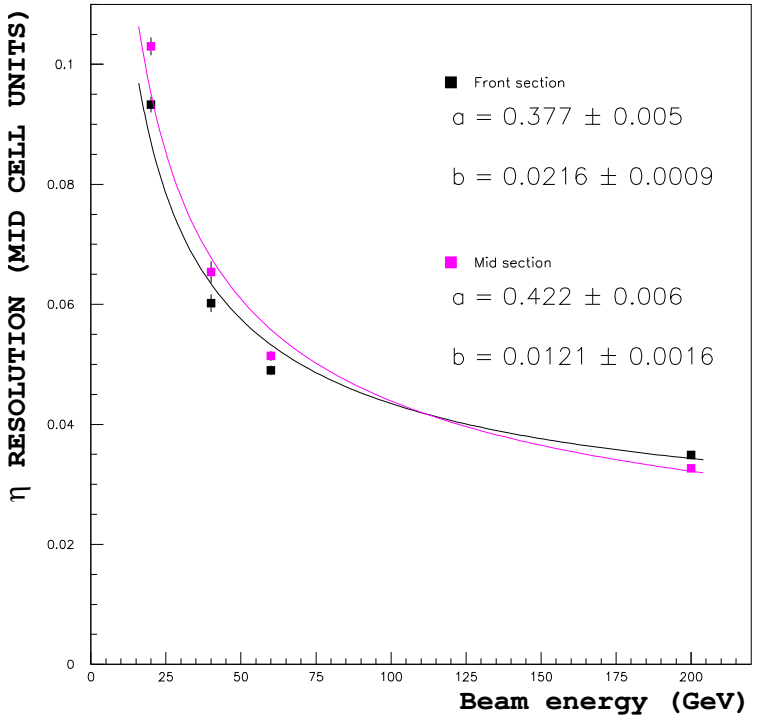

Figure 5.43: η position resolution as a function of beam energy with the front and with the mid section.

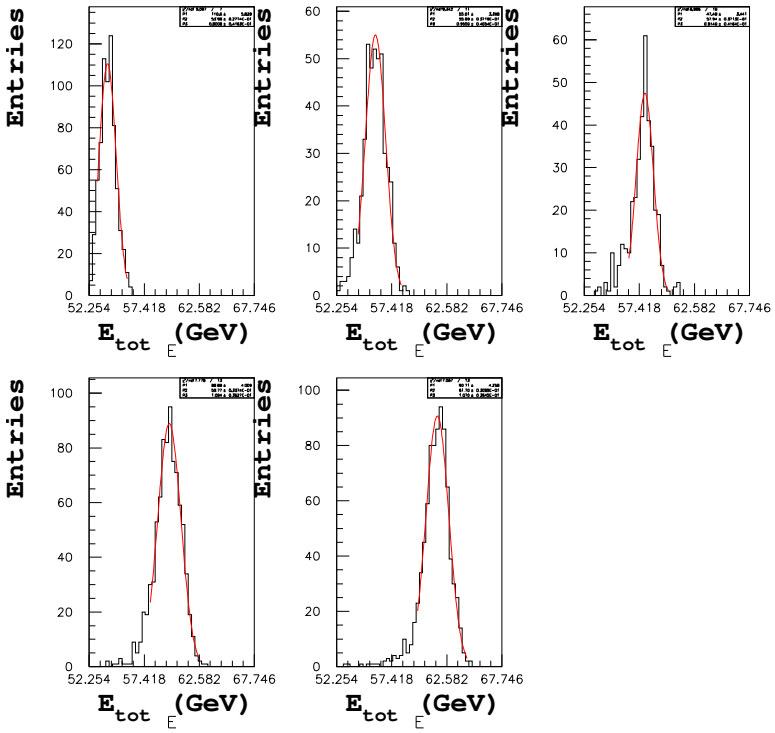

Figure 5.44: Energy signal spectra for different voltage values applied to the read out electrodes.

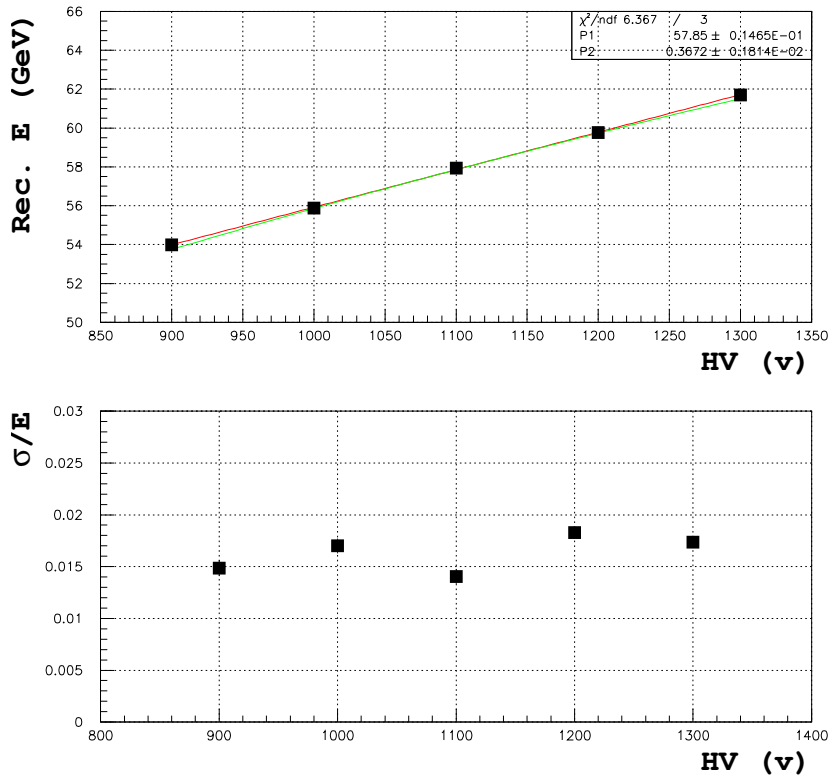

Figure 5.45: Energy signal as a function of the voltage applied to the read out electrodes (upper). Energy resolution obtained for the different voltage settings (lower).

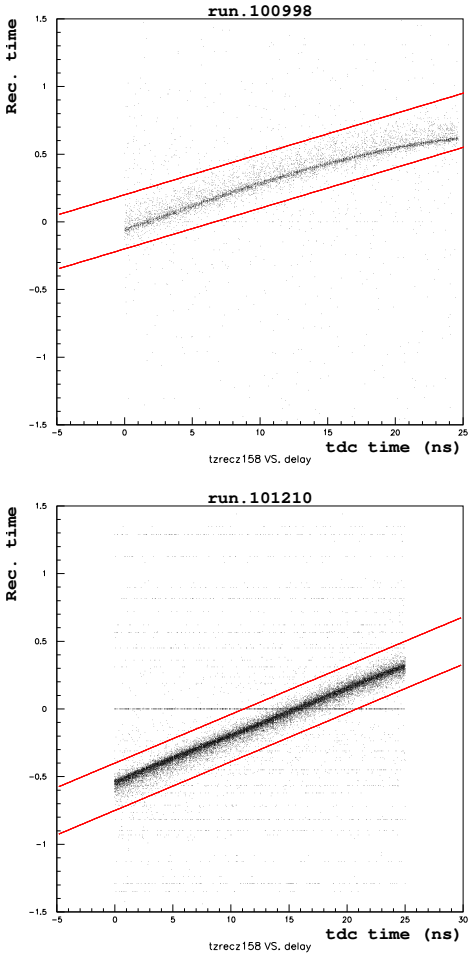

Figure 5.46: Reconstructed time (in arbitrary units) as a function of T_{tdc} for: a) A $60\,GeV$ electron run, prior to run 101006; b) A $120\,GeV$ electron run, after run 101006.

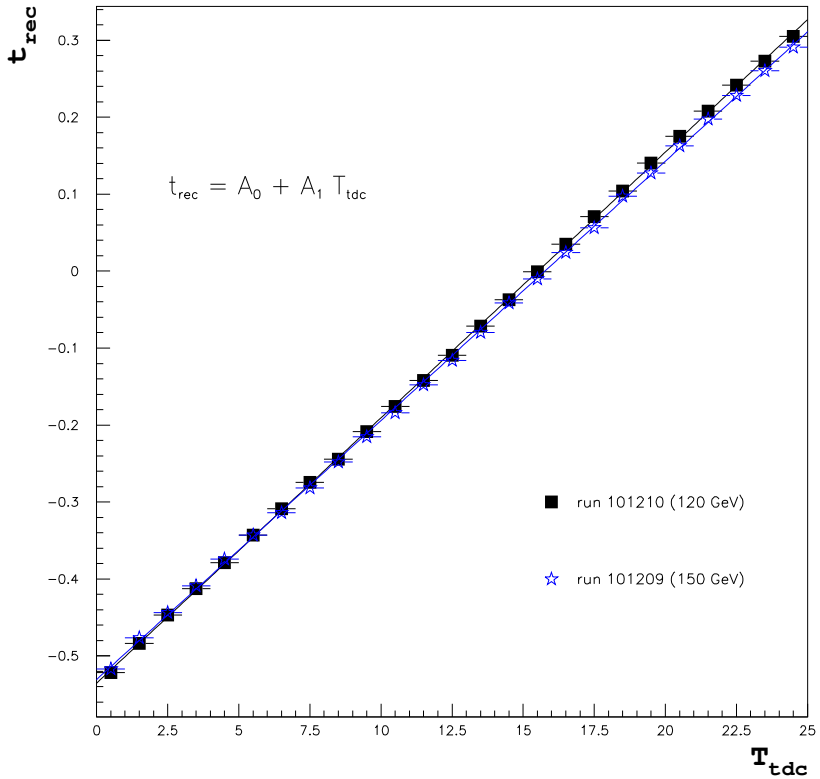

Figure 5.47: Reconstructed time (in arbitrary units) as a function of T_{tdc} for two different runs.

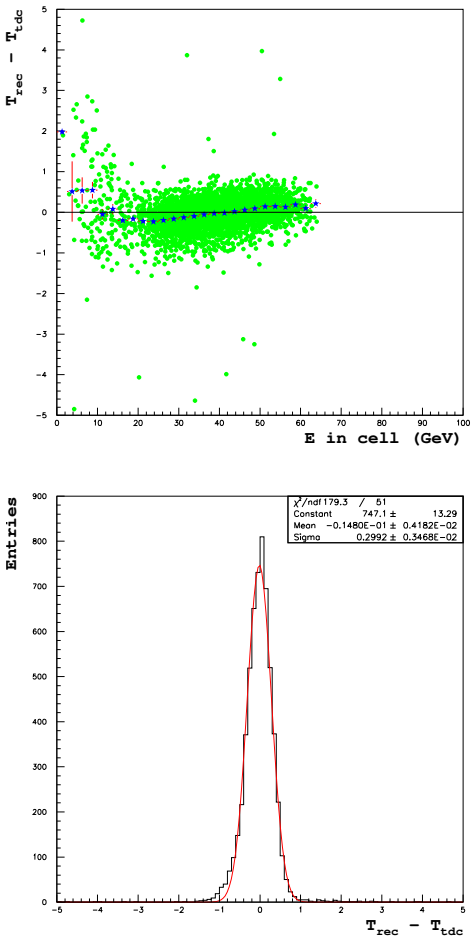

Figure 5.48: Error in time reconstruction as a function of the energy measured in the cell. Single events (dots) and bin averages (stars) are shown (upper). Distribution of the error (lower). A mid section cell is used. $E = 120\,GeV$. Time variables are in ns.

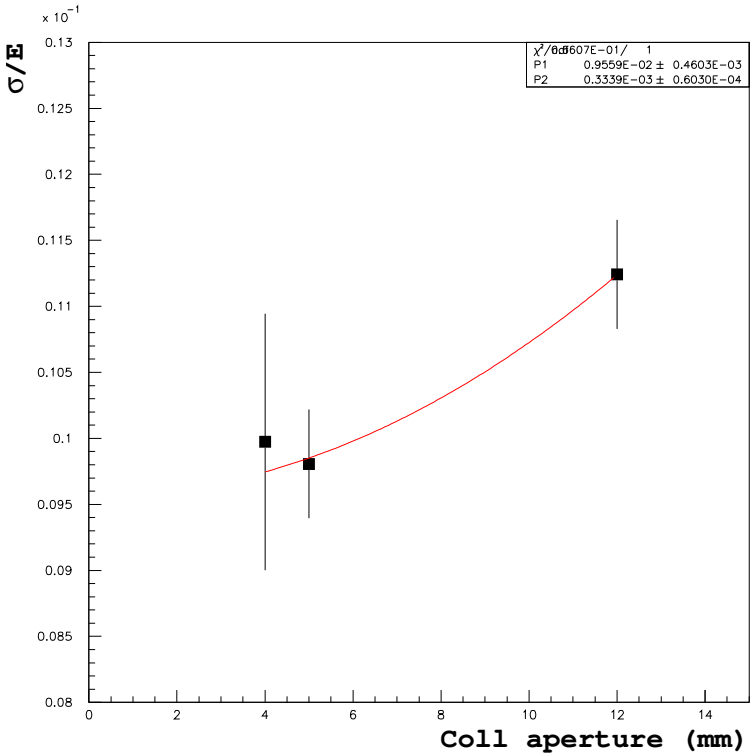

Figure 5.49: Energy resolution at $150\,GeV$, region $\eta = 2.2$, for different collimator apertures.

Part II

The Forward Plug Calorimeter of the ZEUS detector

In this part of the thesis the Forward Plug Calorimeter of the ZEUS experiment is described, beam test data are analyzed and the results discussed. Both the FPC and the ATLAS EMEC are calorimeters, but they have been designed for different purposes and using different techniques. A comparison of the two devices is therefore very fruitful. In addition to this, the FPC is able to measure the energy of both electromagnetic particles and hadrons. Therefore this part of the thesis enters the interesting (and extremely difficult) field of hadronic calorimetry.

The FPC [32] is a lead-scintillator sandwich calorimeter read out with WLS fibers and PMTs. It has been installed as a component of the ZEUS detector at the HERA ring (DESY, Hamburg), functioning in a stable way since the summer of 1998.

The installation of the FPC in ZEUS has increased its calorimetric coverage in pseudo-rapidity from $\eta \leq 4$ to $\eta \leq 5$. This, in turn, vastly increases the physics potential for diffraction in deep inelastic scattering. The mass range over which the dissociated photon system can be studied increases in fact by a factor of 1.7 .

The FPC was tested at the CERN SPS X5 beam facility with electrons and pions, covering an energy range from 10 to $100\,GeV$, and with $100\,GeV$ muons as well. Prior to this, a prototype consisting of half the electromagnetic section was tested at DESY with electron beams in the range $1 - 6\,GeV$.

Chapter 6 describes the ZEUS experiment, justifies the importance of installing the FPC in this environment and describes the FPC itself, along with its construction process. Chapter 7 summarizes the results of the beam test done at CERN [33], [34]. Data from the previous beam test at DESY [35] are used when convenient.

Chapter 6

The FPC in the ZEUS environment

6.1 Description of the ZEUS detector

ZEUS is a multipurpose detector installed at the HERA collider. In this accelerator facility two separate magnet systems guide electron and proton beams around a $6.3\,Km$ long ring. The smaller accelerators DESY and PETRA serve as injectors. The colliding beams have energies of 920 GeV (protons) and 27.5 GeV (electrons/positrons).

A view of the ZEUS detector is shown in Fig 6.1. Charged particles are tracked in ZEUS by the inner tracking system, consisting of a central tracking detector (CTD) and planar drift chambers in the forward and rear directions (FTD, RTD). A transition radiation detector (TRD) helps with electron identification in the forward direction. A thin superconducting solenoid surrounding the inner tracking system generates a magnetic field of 1.43 T. A compensator solenoid suppresses the effects on the beams.

The main component of the ZEUS detector from the point of view of this thesis is the uranium-scintillator calorimeter (UCAL), which can be seen in figure 6.1 enclosing the solenoid. It is subdivided mechanically into the forward (FCAL), barrel (BCAL) and rear (RCAL) calorimeters. Notice that the detector is clearly asymmetric. The FCAL (in the proton beam direction) is thicker than the RCAL (electron beam direction).

The UCAL covers 99.7% of the solid angle with the polar angle θ from 2.6^o to 176.1^o. In terms of pseudorapidity the calorimetric coverage is as follows: FCAL $4.3 > \eta > 1.1$; BCAL $1.1 > \eta > -0.75$; RCAL $0.75 > \eta > -3.8$. The FPC increases the coverage up to $\eta = 5.0$.

The UCAL consists of a total of 80 modules. Each module is made up of up to 185 layers of $3.3\,mm$ thick depleted uranium plates and $2.6\,mm$ thick scintillator plates. Wavelegth

shifter bars transport the light to PMTs. The modules are subdivided longitudinally into an electromagnetic (EMC) and two (one) hadronic (HAC) sections in FCAL, BCAL (RCAL) with a total depth of 7 to 4λ . The scintillator plates form $5 \times 20\,cm^2$ (10×20) cells in the EMC section and $20 \times 20\,cm^2$ in the HAC sections of FCAL, BCAL (RCAL). The total number of cells is 5918.

The calibration of the PMTs is monitored with the signal from the radioactivity of the uranium (UNO) to a precision below 0.2%. The heights of the pulses generated by an electron and a hadron of the same energy are equal to within 3%, i.e. $e/h = 1.00 \pm 0.03$, for momenta above 3 GeV. The energy resolutions measured in the test beam are $\sigma/E = 18\%/\sqrt{E}$ (electrons) and $\sigma/E = 35\%/\sqrt{E}$ (hadrons). In both cases the energy is in GeV.

After the first $3\,X_0$ of the FCAL and RCAL, a plane of $3 \times 3\,cm^2$ silicon diodes was introduced in an upgrade program. This device is called hadron-electron separator (HES).

A small tungsten-silicon calorimeter (BPC) positioned at the beampipe behind RCAL tags electrons with [1] Q^2 as small as 0.5 GeV^2.

The iron yoke serves as the absorber for the *backing calorimeter* and also as a muon filter. It is made of $7.5\,cm$ thick iron plates and it is instrumented with proportional tube chambers for measuring the energy not absorbed in the UCAL. For identification and momentum measurement of muons the yoke is magnetized to 1.6 T with copper coils. Large area Limited Streamer Tube (LST) chambers measure the position and direction of muons in front of and behind the iron yoke (BMUON, RMUON). In the forward direction a spectrometer of two iron toroids and drift-and LST chambers (FMUON) identifies muons and measures their momenta up to $100 - 150\,GeV$.

Luminosity is measured by observing the brehmesstrahlung process $ep \to e'p\gamma$ at very small angles w.r.t. the electron beam direction. The final state electron and photon are detected in coincidence in the electromagnetic calorimeters of the luminosity detector (LUMI), positioned at $33\,m$ (electron tagger) and $100\,m$ (photon tagger) downstream of the central detector in the electron beam direction.

Very forward scattered protons ($P_T < 1\,GeV$) are measured in the leading proton spectrometer (LPS) which uses the proton ring magnets for momentum analysis and detects the scattered protons in 6 stations with silicon strip detectors mounted very close to the beam at distances between 26 and $96\,m$ from the interaction point.

The forward neutron calorimeter (FNC) lies behind the LPS stations for very forward produced neutrons.

Particles produced by the proton beam upstream of the detector are detected in the VETOWALL. For monitoring the time structure and other properties of the two beams

[1] For the definition of Q^2 see section 6.2 below.

a ring counter C5 is used. It is made of two lead-scintillator layers and mounted on the beampipe behind RCAL. C5 registers the halo particles accompanying both beams.

More details about the ZEUS detector can be found in [2].

6.2 Diffractive physics with the ZEUS detector at HERA

6.2.1 Kinematics of deep inelastic scattering

Consider the inelastic process $ep \to eX$, in which an electron [2] interacts with a proton via neutral current exchange (NC) [3]. Let k, k' be the four-momenta of the incoming and outgoing electron. Let p, p_h be the four momenta of the incoming proton and of the outgoing hadron system X. The proton mass will be denoted as m_p. We can define the following quantities describing the kinematics of the process:

$$q = k - k' = p_h - p$$

$$\nu = \frac{p \cdot q}{m_p}$$

$$y = \frac{p \cdot q}{p \cdot k}$$

$$W^2 = (p + q)^2$$

$$s = (p + k)^2$$

The quantity s is the center-of-mass energy squared of the system proton-electron. The process under study can also be seen as collision between a proton and a virtual photon (emitted by the electron). The photon four-momentum is q and the center-of-mass energy squared of the system proton-photon is W^2. In the reference frame where the proton is

[2] We will use the word electron indistinctly for electron or positron.

[3] In terms of Feynman diagrams at tree level, this process would be described by the "exchange" of a photon or a Z boson.

at rest one can easily see that ν is the photon energy and y the fraction of the incident electron energy carried away by the photon.

In the quark-parton model, at lowest order, the process can be described as a hard interaction between the virtual photon and a parton (quark or gluon) inside the proton. The remaining partons act as spectators in the hard interaction. The struck parton enters the interaction as an essentially free particle.

If we are interested in the inclusive process $ep \to eX$, then conservation laws imply that the kinematics are described by only two independent quantities. Deep inelastic scattering (DIS) is usually studied using the Lorentz invariant variables Q^2 and x, defined as follows:

$$Q^2 = -q^2$$

$$x = \frac{Q^2}{2p \cdot q}$$

The quantity Q^2 is the (negative) mass squared of the virtual photon whereas x can be interpreted in the framework of the quark-parton model as the fraction of the proton momentum carried by the struck quark.

This choice is very well suited for the study of the scattering cross-section, since *Bjorken scaling* implies that the total inclusive cross section should factorize into two terms as follows:

$$\frac{d\sigma}{dQ^2 dx} \sim \frac{1}{x \cdot Q^4} \cdot F_2(x)$$

The, in principle, arbitrary function F_2 (the so-called *structure function*) depends only on the variable x. The structure function can be understood in terms of partonic densities.

This scaling law is valid as long as the energy scale running of the strong coupling constant α_s is not taken into account. Perturbative QCD calculations show that there should be logarithmic violations to Bjorken scaling, i.e. at constant x the structure function F_2 should evolve logarithmically with Q^2. This behaviour of the cross sections has been observed at HERA [36].

6.2.2 Kinematics of diffractive DIS

Let's focus now on a particular case of the set of reactions described in the previous section. We are interested in the process $ep \to epX$, which is usually referred to as the diffraction of a virtual photon by the proton. This nomencalture is due to the close relations between this process and the diffraction of light by a black disk. We are not interested at this point on events in which the photon is quasi-real, i.e. when the outgoing electron has almost the same direction as the incoming one. In a diffractive event the proton is practically unaffected and the photon dissociates into a hadron system X. A different way to visualize the reaction is considering it as an interaction of the virtual photon with a colorless object emitted by the proton. This colorless object can be related to the so-called *Pomeron* ($I\!P$) trajectory used in the framework of Regge theory [37] for the asymptotic behaviour of hadron-hadron cross sections. In the following we will refer to this object with the word *pomeron*, just in order to get a more plastic description of the kinematics.

The type of process that we are describing has a very characteristic feature: since the virtual photon interacts with a colorless object inside the proton, no colour flow takes place between the proton and the final hadronic system X. Therefore no energy deposition will be observed in the calorimeter in the region between the direction of the outgoing proton (that usually escapes undetected through the beampipe) and the energy signal deposition associated to the hadronic system. This void in the calorimeter will be called a *large rapidity gap* (LRG). Events with LRG have been observed in the ZEUS experiment [38].

In diffractive DIS the number of independent quantities required to describe the kinematics increases from two to four. We can choose two quantities from the set x, Q^2, W^2, defined above, to describe the lepton vertex, and include two more that can be chosen from the set M_X, t, $x_{I\!P}$, β, in order to describe the proton vertex. In this new set M_X is the invariant mass of the hadronic system X, that does not include the outgoing proton; t is the squared four-momentum transfer at the proton vertex

$$t = (p - p')^2$$

where p, p' are the four-momenta of the incoming and outgoing proton; $x_{I\!P}$ and β are defined by

$$x_{I\!P} = \frac{(p - p') \cdot q}{p \cdot q} \simeq \frac{M_X^2 + Q^2}{W^2 + Q^2}$$

$$\beta = \frac{Q^2}{2(p - p') \cdot q} = \frac{x}{x_{I\!P}} \simeq \frac{Q^2}{M_X^2 + Q^2}$$

If we carry our pictorical view of the process slightly further, we can consider the pomeron, emmited by the proton carrying a fraction $x_{I\!P}$ of the proton initial momentum, as composed by partons, one of which, with a fraction β of the pomeron momentum, enters the hard interaction with the photon, whereas the remaining partons act as spectators. Then M_X is the center-of-mass energy available for the photon-pomeron collision.

The quantity t is essentially related with the pomeron transverse momentum. For the type of events that can be studied with the ZEUS detector it can be regarded as negligible. The pomeron will thus be considered as essentially colinear with the proton.

Therefore all the events that we can identify as diffractive will be classified from the kinematical point of view according to three numbers, like for example Q^2, W^2 and M_X^2.

6.2.3 Models for diffractive DIS

The models which interpret diffraction as a photon-pomeron interaction, with the pomeron emitted by the proton, can be classified in two groups:

- The pomeron is dealt with following the same approach as for the proton in non-diffractive DIS. In analogy with the case of the proton, the diffractive structure function is introduced in the expression for the cross section as follows

$$\frac{d\sigma}{dx_{I\!P} d\beta dQ^2 dt} \sim \frac{1}{\beta Q^4} \cdot F_2^D$$

  The diffractive structure function is assumed to factorize into a flux factor and a term that is interpreted in terms of partonic densities (quarks and gluons). This is the approach followed by Ingelman and Schlein [39].

- The pomeron can be assumed to have pointlike couplings to pairs of quarks or gluons. This is a phenomenological point of view that leads to a very good description of the data with a very small number of parameters [40], [41].

These two families of models, as well as individual ones inside the first group, lead to different predictions for the diffractive differential cross section $d\sigma_{\gamma^* P}^{diff}/dM_X dW dQ^2$. The jet structure of the final hadronic state is also predicted to be different in various models.

The strategy to follow in order to test these models and, if possible, reject some of them, can be summarized in the following steps:

- Identify and select diffractive events. Three methods have been proposed, one of them based on the different behaviour with M_X of the diffractive and non-diffractive components of the cross section [42], another one based on the presence of a large rapidity gap in the energy deposition pattern observed in the calorimeter, and a third method based on the detection of the outgoing proton using the LPS.

- Classify diffractive events in bins of the three dimensional space spanned by, for instance, Q^2, W, M_X. Then the dependence of the cross section on these kinematical variables can be compared to model predictions.

- The jet structure of the events can also be studied and compared to theoretical predictions in the different kinematical regions.

6.2.4 Contribution of the FPC to diffractive physics at ZEUS

The variable M_X is especially interesting from the point of view of separating the events that can interpreted as a photon-pomeron hard interaction (i.e. diffractive events) from the rest (non-diffractive). Diffractive events are characterised by a lower M_X than the non-diffractive ones in a given W range. The kinematic region in M_X for which the diffractive contribution can be extracted with a reasonable contamination from non-diffractive processes is critically dependent on the calorimetric coverage in the forward direction of the detector. Using only the ZEUS UCAL the upper limit of the accessible region is $M_X^2 < 0.01 \cdot W^2$, which corresponds to $M_X = 15$ GeV at high W. The implementation of the FPC in the ZEUS environment has pushed this limit up to $M_X^2 < 0.03 \cdot W^2$, implying that a mass of $M_X = 25$ GeV can be reached.

It is very important to stress that the FPC also works as a veto for non-diffractive events. Diffractive events leave on average a very small fraction of the final hadronic system energy in the FPC ($E_{FPC} \simeq 12\,GeV$ for $M_X = 25\,GeV$), whereas in non-diffractive events the energy deposition increases dramatically as we move closer to the forward beam direction (we expect typically above 100 GeV in the FPC). Therefore a moderate energy resolution is enough in order to reject the undesired events. The precision in the measurement of M_X is little sensitive to the performance of the FPC. An energy resolution of

$$\frac{\sigma_E}{E} = \frac{100\%}{E} \oplus 10\%$$

for multihadronic systems is enough to achieve the proposed goals [32].

The observation of jet structure in LRG events reported by the ZEUS collaboration [43] was considered a very important result. A detailed study of the jet structure of the final

hadronic state X in diffractive events was hampered, before the FPC installation, by the acceptance of the calorimeter, which restricted the M_X range accessible. The invariant mass of the system X has to be above 8 to 10 GeV in order to clearly identify a two jet structure, judging from jet studies in e^+e^- annihilation. After the installation of the FPC, ZEUS is sensitive to the detection of three-jet structures.

A detailed review of the physics potential of the FPC can be found in [32].

6.3 Description of the FPC and performance requirements

The FPC is a lead-scintillator sandwich calorimeter read out by WLS fibers and PMTs [33], [34], [44]. This concept has been investigated in [45], [46], [47]. It has been installed in the $20 \times 20\,cm^2$ beam hole of the ZEUS FCAL [48], [49] (Fig 6.1). The FPC has a $63\,mm$ diameter central hole to accomodate the HERA beampipe.

The thickness ratio lead to scintillator was chosen to be 6:1. Results from a lead-scintillator calorimeter of similar composition [12] showed that the FPC should provide equal response to hadrons and electrons (compensating calorimeter). The thickness of the lead and scintillator plates is $15\,mm$ and $2.6\,mm$ respectively. The WLS fibers have $1.2\,mm$ diameter and go through $1.4\,mm$ diameter holes arranged on a $12\,mm$ step square grid (Fig 6.2).

The FPC is divided longitudinally into an EMC and a HAC section (Fig 6.3) which are read out separately. The EMC part consists of 10 lead-scintillator layers corresponding to $26.5\,X_0$ ($0.9\,\lambda$). The HAC section is five times deeper leading to a total of $5.4\,\lambda$ for the whole calorimeter.

The scintillator plates are subdivided into tiles forming cells which are read out independently. The cell sizes are $24 \times 24\ mm^2$ (EMC) and $48 \times 48\ mm^2$ (HAC). The 8 (4) innermost EMC (HAC) cells follow the circular shape given by the beam hole (see Fig 6.2). Every HAC cell has 4 EMC cells in front of it (except for the 4 innermost ones, which have only 3). The total number of read out channels is therefore $(EMC + HAC)$: $60 + 16 = 76$.

The WLS fibers of the EMC section are glued to clear fibers ($1.4\,m$ length) at the front part. These fibers are bent by 180^o and guided to the PMTs along the outer side of the FPC in order to transport the light to the light mixers at the PMTs placed behind the detector, at the exit from the calorimeter. The WLS fibers in the HAC section are routed directly to the PMTs (see Fig 6.3). All 4 (16) fibers corresponding to an EMC (HAC) cell are connected to the same PMT through a light mixer. An additional fiber is connected to each PMT through the same light mixer bar in order to inject light pulses from a light

unit layer	$15\,mm$ Pb, $2.6\,mm$ scint, $0.4\,mm$ paper
effective thickness of layer	$14.84\,mm$ Pb, $2.86\,mm$ plastic
transversal dimensions	$192 \times 192\,mm^2$
EMC section, 10 layers	$180\,mm$
HAC section, 50 layers	$900\,mm$
diameter beam hole	$63\,mm$
number of cells	
EMC + HAC	60 + 16
average density	$9.6\,g/cm^3$
radiation length	$0.68\,cm$
absorption length	$20\,cm$
Moliere radius	$2.0\,cm$
total length	$1080\,mm$
total weight	$400\,kg$
total radiation length:	
EMC + HAC	$26.5 + 133.0 = 159.5 X_0$
total absorption length:	
EMC + HAC	$0.9 + 4.5 = 5.4\ \lambda$

Table 6.1: Summary of FPC parameters.

emission diode (LED) and a laser for monitoring of the stability of PMTs and read out electronics.

The active part of the FPC has outer dimensions $192 \times 192 \times 1080\ mm^3$. The FPC is mechanically subdivided into two identical half modules. In ZEUS they are attached to the bottom and top half parts of the FCAL innermost module [32]. The FCAL halves, and therefore also the FPC halves, are moved apart for beam injection in order to reduce the radiation load on the calorimeters.

A summary of FPC parameters is given in table 6.1.

The requirements posed on the detector performance by the physics goals are stated below:

- Absolute calibration uncertainty: below 5%.
- Cell to cell signal variation: below 5%.
- Position resolution for hadrons: $1\,cm$ (EMC), $3\,cm$ (HAC).

- Energy resolution for multihadron systems: $100\%/\sqrt{E} \oplus 10\%$.

The FPC is therefore not intended to be a precise electromagnetic calorimeter, like the ATLAS EMEC. Its main purpose is to extend the calorimetric coverage of ZEUS near the forward (proton) beam direction, mainly in order to measure energy deposited by hadrons. Since the detector has small transverse dimensions, the energy of the hadronic showers is shared with the surrounding FCAL. The FPC is a low-cost complement of the FCAL. The lead-scintillator technique is a good choice, since it can provide signal compensation, and since a very accurate energy measurement of electromagnetic showers (that can be achieved with LAr or crystal calorimeters) is not needed.

Further details on the detector design and its physics potential can be found in [32].

6.4 Construction of the FPC

In this section the procurement and assembly of the different components of the FPC are summarized.

The passive material was taken to be lead, containing a small fraction of antimony (4%) in order to provide the hardness required for hole drilling. The dimensional tolerances for the lead plates were $0.1\,mm$ (thickness) and $0.2\,mm$ (contour). The wholes were drilled with tolerances of $0.05\,mm$ (diameter and position).

The scintillator used was the polystyrene based SCSN81T2. It turned out to be the best choice in terms of light yield and radiation stability [50]. Tiles were manufactured with a tolerance of $0.2\,mm$ (thickness and contour) and holes were drilled mechanically with the same tolerance as in the case of lead plates. These tolerances are determined by the required performance of the calorimeter and by the assembly procedure. The scintillator tiles were wrapped with tyvek paper in order to improve the light collection efficiency.

For the WLS fibers the model Y11200(dc) has been chosen. It has a polystyrene core and a double cladding (PMMA and fluorinated PMMA) which produces a substantial increase in light output. Its absorption spectrum matches best the SCSN81T2 emission spectrum.

The PMT chosen for the FPC is the Hammamatsu R5600U, a tube with metal channel dynodes. It is relatively insensitive to a magnetic field and its small dimensions ($16 \times 16 \times 16\,mm^3$) are well suited for the limited space available in ZEUS. Tests done at DESY prior to the beam tests [32] showed that it fulfills well the constraints on dynamic ranges placed by the required FPC performance in the HERA environment. For the combination SCSN81T2/Y11200(dc)/clear fiber/R5600U, 12 photoelectrons per minimum ionizing particle traversing the EMC section are expected, while a minimum of 8 are required so that the light yield does not dominate the energy resolution.

In each FPC half section the lead plates were placed upright on a $4\,mm$ thick aluminum baseplate. The plates and holes were aligned and the former glued with epoxy to the baseplate. The scintillator tiles were inserted between the lead plates and the fibers were threaded through the holes layer by layer. Finally a stainless steel sheet of $0.2\,mm$ thickness was glued to the lead plates along each of the three sides.

The FPC has four $2.5\,mm$ diameter brass tube holes, parallel to the ones containing the fibers. They are used to introduce a ^{60}Co source located at the tip of a long steel wire, used for long term stability monitoring of the scintillator, fibers and PMTs. A brief description of this monitoring system may be found in [33].

The PMTs are housed in four separate iron frames of shape and transverse size similar to that of the lead plates. The four structures correspond to the EMC and HAC sections of both halves. These frames are placed behind the hadronic section, first the one containing the HAC PMTs and behind it the one with the EMC ones (see Fig 6.3). The EMC PMTs are arranged in their support frames in such a way that they do not line up with their respective calorimeter cell. This is important for the monitorization of muon signals in the EMC cells.

In the beam tests Standard LeCroy units were used to provide HV to the PMTs. Note that these HV supplies are different from the NIKHEF CW type ones used in ZEUS [51]. The voltage was fed to the tubes using flat cables. The typical voltage value of operation was 900 v.

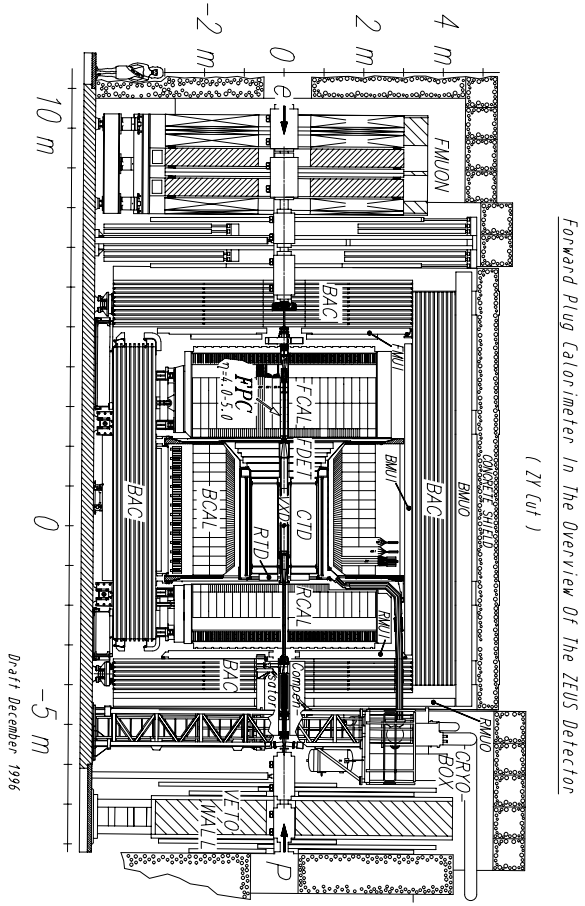

Figure 6.1: The ZEUS detector at HERA. The FPC can be seen at the beam hole across the FCAL.

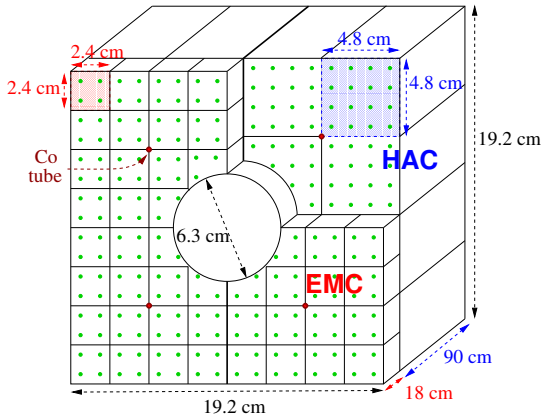

Figure 6.2: View of the FPC. The read out cells and the position of WLS fibers are shown. Notice that there is one HAC read out cell behind each group of 2×2 EMC ones, except in the 4 innermost hadronic cells.

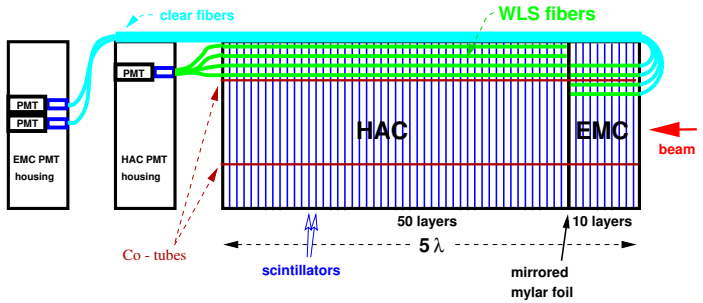

Figure 6.3: Side view of the FPC.

Chapter 7

Beam test of the FPC

The FPC was tested at CERN in the summer of 1997. Prior to this a prototype was tested at DESY. The results of both tests are presented in this chapter. Emphasis is put on the CERN test, whereas data from the DESY test are used as a reference for comparison. The author of the thesis was strongly involved in both.

7.1 Set up, data taken and signal processing

7.1.1 Beam test set up

The FPC was tested in the X5 beam of the CERN SPS. It was installed surrounded by three FCAL modules (see Fig 7.1). These are uranium-scintillator calorimeter units, similar to the ones implemented at ZEUS (see [48]), that surround the FPC. The detector complex (FPC plus FCAL) was placed on a structure movable in X and Y, in order to point at the desired position with the particle beam.

Fig 7.2 sketches the beam test set up. In front of the FPC a *Delay Line Wire Chamber* (DLWC) gave precise position information for each single event. The relative position of the FPC detector w.r.t. the DLWC coordinates was established to within about one millimeter for each run by looking at the DLWC coordinate dependence of the signal in a given cell. Cuts on DLWC coordinates were used in offline analysis in order to select particles hitting a given region of the detector.

Also in front of the FPC, two scintillator paddles, a thin finger and a paddle with a hole used as a veto, were used for the trigger. Two different trigger conditions were used along the beam test: a coincidence of the two paddles was used with a defocused beam in order

to obtain events covering a wide region of the FPC; for the focused beam, coincidence of the finger and anticoincidence of the veto were required in addition. In both cases triggers could be inhibited by a *busy* signal delivered by the read out system to provide the time necessary for signal digitization after an event was accepted.

Behind the FPC an additional paddle (which will be referred to as B5), was installed mainly for offline identification of muons. The three paddles, veto and finger were read out with PMTs. Their charge pulses were fully integrated and digitized. All of them showed the Landau-like spectrum expected from a correct behaviour.

All devices other than the FPC and FCAL modules (that is, trigger counters, B5 paddle and DLWC) stayed fixed, centered on the beam trajectory.

7.1.2 The data taken during the test

Runs with $100\,GeV$ muons, and with pion and electron beams of different energies were taken as described below.

Muons with an energy of $100\,GeV$ were used to scan the whole FPC for HAC cell calibration and uniformity tests. More than 10,000 events were collected with the beam pointing at each of the HAC cells.

The FPC was scanned with electrons of 10 and $60\,GeV$ resulting in several thousand events per 2×2 EMC cell group. The beam spot was wide enough to cover a region larger than the 2×2 EMC cluster. After tilting the FPC by an angle of 1.7^0 (which is the typical angle of incidence for a particle that reaches the FPC once installed at ZEUS) an additional scan was performed at $80\,GeV$, with more than 10,000 events per 2×2 EMC cell group. Electrons at different energies (10, 20, 30, 40, 60, 80, $100\,GeV$) were directed to a limited region (the lower left hemisphere) for different detector conditions: tilted and untilted, with and without inactive material in front. In all cases an unfocused beam was used. Only at the beginning of the test a focused $40\,GeV$ electron beam was directed to the center of each EMC cell for HV tuning of EMC channels.

The FPC was scanned with pions of 30, 60, 80 and $100\,GeV$. In addition to this, pions of 10, 20 and $40\,GeV$ were directed to the lower left hemisphere. Again, data were collected with the FPC tilted and untilted, with and without inactive material in front. In this case more events were collected than for the electron beam. However, the purity of the pion beam turned out to be poorer, chiefly due to muon contamination at high energy. After fiducial cuts, statistics available for hadrons were still higher than those for electrons.

7.1.3 Signal processing

In order to achieve the same working conditions as at ZEUS, a fraction of 20% of the FPC PMTs pulse charge was splitted away from the read out chain, using the charge splitters that are used in ZEUS. This fraction of the signal is used for the first level trigger.

The pulse containing the remaining 80% of the charge was reshaped and sampled eight times with a period of $96\,ns$, as is done for the ZEUS UCAL [49]. Typically there is one sampling at the rising slope of the charge pulse and another one at the falling side. A sampling previous to these two is used for baseline subtraction. Since the output of the shapers has a well known profile and samplings are taken with similar timing relative to the pulse for all events at ZEUS, a simple linear combination of the samplings at the falling and rising slopes (after baseline subtraction) gives a very stable measurement of the total pulse charge [1]. Nevertheless a third degree polynomial correction is used to eliminate the residual dependence of the signal on the precise timing of a given event. At the beam test the pulse was sampled every $96\,ns$ using an external clock (i.e. the samplings were not synchronized with the pulse). Therefore the timing of the samplings relative to the pulse was measured and used as an input of the residual corrections. The time was determined using the phase of the signal at the trigger counters relative to the sampling clock.

The charge collected with each of the eight samplings was stored in an analog pipeline. The charges of the triggered events were transferred to the digital cards, equipped with ADCs, for digitization. Finally the ADCs were read out by a VME transputer system. At the test beam site, the digitized data from the counters and calorimeters were then transfered to a UNIX workstation for offline analysis. A PC running Linux and two EXABYTE units were used for mass data handling and storage.

7.2 Calibration

7.2.1 Calibration of the EMC and HAC section

Relative calibration of the EMC cells was done in two steps:

- HV settings were tuned to the proper value in order to obtain an approximately uniform response across all EMC cells with a reference electron beam.

[1] If the eight sampled amplitudes are denoted as h_0, h_1, ..., h_7, the pulse height is reconstructed as $A_{peak} = (h_2 - h_0) + 1.8 \cdot (h_3 - h_0)$

Beam energy (GeV)	α_{min}
20	1.20 ± 0.05
30	1.18 ± 0.04
60	1.13 ± 0.04
80	1.18 ± 0.04

Table 7.1: Value of α_{min} for several beam energies.

- Calibration constants were calculated to refine the result obtained with the previous step. The constants were calculated using electron beam data.

Absolute calibration of the EMC section was done using electron data with different beam energies in the range $10 - 100\,GeV$. The uncertainty of the whole method was estimated to be 2%.

The hadronic section could not be calibrated using pion beam data, due to transverse leakage. The signal of $100\,GeV$ muons was used instead. The calibration was done by comparing the data to the prediction of MC. The uncertainty of the method was estimated to be at the level of 5%, mainly due to the MC description of pair production and brehmesstrahlung processes, that become relevant for high energy muons.

7.2.2 Calibration cross-check with pion data

In this section the validity of the calibration procedure for the HAC section described above is tested, which relied on the MC prediction for the FPC response to muons. To this end the method presented in [48] for the ZEUS FCAL is used, which is based on the optimization of the pion energy resolution.

In absence of leakage and for a compensating calorimeter, if our cell calibration method is correct, in order to measure the energy of pions hitting the FPC, the EMC and HAC signals should be added linearly, i.e. $E_{FPC} = E_{HAC} + \alpha E_{EMC}$, with $\alpha = 1$, where E_{EMC} and E_{HAC} are calibrated energy signals.

Fig 7.3 shows the normalized pion energy resolution (see section 7.4 for technical details) as a function of the value of α used for signal reconstruction. Results for pion beams of different energies are shown. An optimum value of α was obtained for each energy by fitting the dependence of the energy resolution on α to a parabola. The results are shown in table 7.1.

In all cases the value obtained is larger than unity. The weighted mean yields

$$\alpha_{min} = 1.17 \pm 0.02$$

This can be taken as an indication that the calorimeter is not compensating or that the effect of leakage is non-negligible.

7.3 FPC performance with an electron beam

7.3.1 Uniformity

The read out scheme used in the FPC generates non-uniformity effects, investigated in [46]. When an electron is incident near the position of a fiber, photons are more efficiently captured, giving rise to a signal enhancement. This effect was studied using beam test data. Fig 7.4 shows a signal cartography of an EMC cell. The fiber positions are clearly seen. The enhancement in the region closest to the fiber is at the level of 20%.

7.3.2 Linearity

Electron data at several different beam energies were available for the lower left part of the FPC (cells 46-60). For each cell the DLWC information was used to select events inside a cell-centered square of $1.2 \times 1.2\,cm^2$ at all available beam energies. In each case the cell signal distribution was fitted by a gaussian. Linearity was checked in the following way:

- The mean signal seen in pC, as obtained from the gaussian fit, was determined as a function of the beam energy. The data were fitted to a straight line going through (0,0).
- For each energy the ratio between the measured and the fitted signal was determined along with its error.
- If all ratios are consistent with, for example, the range 1.00 ± 0.01, then we will say that the cell considered shows deviations from linearity of less than 1%.

Fig 7.5 shows the result for a typical cell. Except for a few problematic cells, linearity holds to within 1%.

7.3.3 Energy resolution

The purpose of this section is to study the energy resolution for electrons. Data for this type of analysis can be chosen in several ways:

- Events hitting the center of an electromagnetic cell.
- Events hitting a broader area inside a cell. The difference with the previous case is that now some events are hitting the fiber area.
- The same study was performed with the FPC tilted, plus inactive material in front of it.

The results for the different configurations are discussed in this section.

Energy resolution at the center of a cell

Events hitting a cell-centered region of $8 \times 8\, mm^2$ were selected using the DLWC. In order to reject muon contamination, the signal from the back leakage paddle B5 was used.

Energy resolution was determined either using only the signal at the cell hit by the beam or adding up all signals inside a 3×3 cluster. The spectra for both cases are shown in Fig 7.6. The relative widths of these gaussian fits, using the 3×3 cell cluster, are plotted versus the beam energy in Fig 7.7. The data are fitted to the standard quadratic sum of a sampling and a constant term. Lower energy DESY data taken with an FPC prototype are included for comparison.

The DESY data lie systematically below the fitted curve. This can be explained by light losses produced in the coupling of the WLS with the clear fiber. In the prototype the WLS fibers of the EMC section were routed directly to the PMTs and therefore the effect did not occur. Light losses imply larger photostatistics fluctuations. The sampling term measured for the prototype was $a_{DESY} = 30.0 \pm 0.5$ %, which includes a contribution from photostatistics (measured using LED data) of $a^{ph}_{DESY} = 10 \pm 2$ %. If we assume that the sampling term measured at CERN, $a_{CERN} = 34 \pm 3$ %, owes its increase only to photostatistics fluctuations, one finds $a^{ph}_{CERN} = 19 \pm 4$ %. In fact LED data taken in the cells used for the electron energy resolution analysis show photostatistics fluctuations around 15 %, in good agreement with the estimate presented above.

Conditions	Sampling term (%)	Constant term (%)
Center of cell	34 ± 3	1.8 ± 0.7
Full cell	37.7 ± 1.5	2.9 ± 0.3
with inactive mat.	36.9 ± 1.7	3.0 ± 0.4
FPC tilted	36.3 ± 1.9	3.5 ± 0.3
DESY data	30.0 ± 0.5	–

Table 7.2: Electron energy resolution for different data sets.

Energy resolution with non-uniformities

If events are selected inside a cell-centered square of $1.6 \times 1.6\, cm^2$, i.e. a square containing the four fibers that go through the cell, the resolution deteriorates. Fig 7.8 illustrates this effect. DESY data of this type are only available at $3\, GeV$. In this case the energy resolution is calculated and plotted both using only the signal at the central cell and the 3×3 cluster. As expected, the sampling term improves dramatically when using a 3×3 cluster.

The results obtained, compared to the previous case, show a substantial energy resolution deterioration due to non-uniformities.

Other configurations

The energy resolution for electrons at different energies was also measured after placing inactive material [2], with roughly the same number of radiation lengths as in the final set up at ZEUS, in front of the FPC. The same type of measurement was done as well with the detector tilted by 1.7^o w.r.t. the beam axis. The results obtained were compatible in all cases.

Conclusion on electron energy resolution

The results obtained with the different setups are summarized in Fig 7.9. The result of the fit for each case is given in table 7.2.

The results obtained with different detector conditions are all compatible. Non-uniformity

[2] In this case the energy resolution was slightly improved by usage of the FPC *presampler*, which was removed from the detector after the CERN beam test.

Cluster	Signal containment (%)
1×1	56.0
3×3	93.8
5×5	100
7×7	100

Table 7.3: Energy signal containment for electron showers in EMC section cell clusters of different sizes.

due to the presence of the fibers is seen to contribute significantly to the energy resolution. The sampling and constant term obtained in the most general case are

$$a = 0.369 \pm 0.017$$

$$b = 0.030 \pm 0.004$$

7.3.4 Shower width

The fine segmentation of the FPC electromagnetic section allows to study the energy deposition pattern of electromagnetic showers in the transverse plane.

In order to study shower signal containment inside a cluster of $n \times n$ EMC cells it is necessary to limit the data sample to electron events whose incident point is close to the center of a given cell. Selecting electron events hitting a cell-centered squared region of $0.5 \times 0.5\,cm^2$, one can compare the mean signal for the entire FPC EMC section (i.e. adding up all cells) to that contained in a cluster of $n \times n$ cells.

Energy signal containment inside one cell for $60\,GeV$ electrons was observed to be 56 %. A 3×3 cluster contains 94 % of the signal. The results on energy signal containment are summarized in table 7.3.

The transverse profile of the shower can be studied in more detail by looking at the density of deposited energy as a function of the distance to the impact point. DLWC information was used to isolate electrons hitting a small region of the detector, lying at a given distance from a reference EMC cell. The signal at that cell is then a good approximation to the energy deposition density at the given distance of the impact point. This information is given in Fig 7.10, where the expected exponential behaviour is observed

$$\frac{dE}{dR} \sim e^{-bR}$$

$$b = 0.813 \pm 0.008\,cm^{-1}$$

at $60\,GeV$. Notice that the $10\,GeV$ data are rescaled for a better comparison with the $60\,GeV$ ones. The shower shape in the transverse plane is energy independent within the statistical errors.

7.3.5 Position reconstruction

Description of the algorithm

Position reconstruction is done in the following way for each event:

- The electromagnetic cell with maximum energy signal is searched for. The event is accepted if around this cell a 3×3 cluster can be defined *inside the FPC*.
- Once the 3×3 cluster is selected, a linear algorithm is used to obtain a first approach to the correct position. The formula applied is

  $$X_{bar} = \frac{\sum_{i=1}^{9} x_i S_i}{\sum_{i=1}^{9} S_i}$$

  where i runs across the 9 cells, x_i are the x coordinates of the cells and S_i the energy signals. The same is done for Y.
- The resulting X_{bar} (the same holds for Y), when plotted versus the true X coordinate as given by the DLWC, shows a characteristic S-shape shown in Fig 7.11. After applying a suitable correction to X_{bar} one obtains X_{rec} that, as shown in Fig 7.11 is an unbiased estimate of the true X. The correction is of the type

  $$X_{rec} = P_1 + P_2 tanh(P_3 X_{bar})$$

  The values of the parameters for the different beam energies are given in table 7.4. The errors quoted are those given by the PAW package.

Beam energy (GeV)	$P_1\,(cm)$	$P_2\,(cm)$	$P_3\,(cm^{-1})$
10	1.372 ± 0.019	1.32 ± 0.05	2.1 ± 0.2
20	1.318 ± 0.010	1.266 ± 0.019	2.37 ± 0.11
40	1.313 ± 0.012	1.38 ± 0.02	2.01 ± 0.09
60	1.302 ± 0.007	1.264 ± 0.013	2.54 ± 0.08
80	1.281 ± 0.006	1.235 ± 0.017	2.62 ± 0.09
100	1.321 ± 0.009	1.297 ± 0.013	2.32 ± 0.07

Table 7.4: Values obtained for the parameters entering the position reconstruction correction for different beam energies.

The plots show all individual events (dots), and effective points that are calculated averaging out, in order to obtain a better fit (full squares). The correction applied at this stage is approximately energy-independent, as one could expect from the fact that the shower transverse profile is energy invariant (see 7.3.4).

The method used is very similar to the one described in 5.8.2 for η reconstruction with the mid section of the ATLAS EMEC. S-shapes are a large effect in both cases due to the fact that cell boundaries are parallel to the beam trajectory along the full detector depth, and that the cell size is comparable to the transverse width of the shower.

Position resolution at different energies

The algorithm for electron position reconstruction explained above was applied to a large data sample taken from the CERN beam test. Events with maximum energy deposition in a given cell were selected. The expected $1/\sqrt{E}$ scaling law for the resolution is observed, as can be seen in Fig 7.12 for the X coordinate. The same behaviour is seen for Y. Position resolution calculated from lower energy data taken at DESY are also included. Notice that, despite the differences between the two types of data, the agreement is excellent. The fit is done putting all the data together. The constant term of the position resolution is below $1\,mm$ (i.e. 4% of the cell size).

7.4 FPC performance with pions

This section describes the performance of the FPC with a pion beam. At high energies the pion beam provided by the CERN test beam facility showed a substantial muon contamination. Muons were rejected from the data sample by applying suitable cuts.

7.4.1 Linearity

Fig 7.13 shows the mean value of the signal generated by pions of energies between 10 and $100\,GeV$ in the HAC section, in the whole FPC and adding up also the surrounding FCAL modules. Linearity holds fairly well both for the FPC and FPC + FCAL setups. In the latter case Fig 7.14 shows linearity to hold at the 2% level.

7.4.2 Energy resolution

Introduction

An important feature of the FPC is that the typical width of hadronic showers for any energy is comparable to the transverse dimensions of the detector. A rough estimate for the fraction of the shower energy that leaks transversely to the surrounding FCAL modules can be obtained from Fig 7.13. It is around 25-30% for pion energies between 10 and $100\,GeV$. Therefore, the energy measurement for hadrons must be done combining the information from the FPC and the adjacent FCAL modules.

After installation inside ZEUS, the FPC is completely surrounded by FCAL modules. Therefore almost all energy leaking transversely out of the FPC is expected to be recuperated in the FCAL. In contrast, in the CERN test beam set up, FCAL modules were present only at the two sides of the FPC (see Fig 7.1). For this reason the energy resolution obtained with the test beam data is a pessimistic upper limit of the FPC performance after installation in ZEUS.

The pion samples used in this analysis were selected by imposing suitable cuts. In particular, DLWC information was used in order to isolate beam particles hitting a limited region inside the FPC.

Ratio e/h

As discussed above the absolute calibration of FPC EMC cells was done with electrons, and the calibration of the HAC cells was established with muons detected in the HAC section. Assuming the e/h ratio to be 1 [32], [12], i.e. a compensating FPC, then the signals from the FPC and adjacent FCAL modules can be combined as follows

$$E_{total} = E_{FCAL} + \beta E_{FPC}$$

with $\beta = 1$. Notice that the energy scale of the compensating FCAL modules is accurately

Beam energy (GeV)	β_{min}
30	0.73 ± 0.18
60	0.88 ± 0.16
80	0.91 ± 0.08

Table 7.5: Optimal value of the parameter β for different beam energies.

known from previous beam tests [48].

The compensating FPC hypothesis was investigated by studying the value of β that yields the minimum pion energy resolution for each input beam energy. This analysis is similar to the one presented in 7.2.2.

Fig 7.15 shows the normalized pion energy resolution as a function of β for several beam energies. An optimum value of β was obtained for each beam energy by fitting the β dependence of the energy resolution to a parabola. The results are shown in table 7.5.

The weighted mean yields

$$\beta_{min} = 0.88 \pm 0.07$$

significantly below unity. The result suggests some deviation to the compensating behaviour or might be due to the transverse leakage in the set up, consistently with the similar analysis performed in 7.2.2 using only energy deposited at the FPC.

Beam energy dependence of the pion energy resolution

Energy resolution for pions was measured at several beam energies ranging from 10 to $100\,GeV$. Fig 7.16 shows the signal spectra measured by the FPC alone at all beam energies available (upper) and, for the sake of clarity, again for two selected energies (lower). The signal is gaussian at low and moderate energies and starts developing low energy tails due to longitudinal leakage as the beam becomes very energetic. Fig 7.17 shows the corresponding distributions obtained when combining the signals from FPC and FCAL. They feature similar characteristics as those from the FPC alone.

Fig 7.18 shows the beam energy dependence of the pion energy resolution. A large improvement is seen when including the energy deposited in the FCAL modules surrounding the FPC. The curves show fits done with the usual parametrization. Using the FPC alone the fitted sampling and constant terms are

$$a = 0.99 \pm 0.03$$

$$b = 0.112 \pm 0.007$$

For the $FPC + FCAL$ case the results are

$$a = 0.702 \pm 0.016$$

$$b = 0.055 \pm 0.005$$

Notice that by adding the FCAL information, the constant term (b) is reduced by a factor of two. The sampling term is also substantially improved. Pion energy resolution is thus observed to be well below the value required for physics analyses [32].

Pion energy resolution was measured with the detector tilted and with inactive material in front of it, the same as for electrons. Again the resolution does not vary significantly.

Conclusions on pion energy resolution

Pion events were successfully reconstructed from test beam data. Combining the signals from the FPC and the surrounding FCAL modules resolution was observed to be around

$$\frac{\sigma}{E} = \frac{70\%}{\sqrt{E}} \oplus 5\%$$

with both tilted and not tilted FPC, with and without inactive material in front.

7.4.3 Position reconstruction

Position reconstruction for pions was studied using techniques similar to those explained for electrons. The resolution was parametrized as follows

$$\sigma(Y) = \frac{a}{\sqrt{E}} \oplus b$$

The result obtained using the hadronic section of the FPC was

$$a = 4.60 \pm 0.16\ cm$$

$$b = 0.60 \pm 0.03\ cm$$

and using the EMC part

$$a = 5.3 \pm 0.5\ cm$$

$$b = 1.1 \pm 0.8\ cm$$

The technical details may be found in [34].

7.5 Conclusions on the beam test of the FPC

The Forward Plug Calorimeter, now installed in the ZEUS detector at the electron-proton collider HERA, was tested at DESY and CERN with particle beams in the range 1 to $100\,GeV$. The results of these tests have been used to determine the calibration of the FPC. The FPC performance in terms of energy signal linearity, energy and position resolution, both for hadrons and electrons, fulfill the physics requirements stated in the FPC proposal.

Energy resolution for electrons was found to be

$$\frac{\sigma}{E} = \frac{38\%}{\sqrt{E}} \oplus 4\%$$

Pion energy resolution combining FPC and FCAL is

$$\frac{\sigma}{E} = \frac{70\%}{\sqrt{E}} \oplus 5\%$$

Electron position resolution is

$$\sigma(X) = \frac{8.23}{\sqrt{E}} \oplus 0.64\ mm$$

Pion position resolution is around

$$\sigma(X) = \frac{5}{\sqrt{E}} \oplus 1\ cm$$

using the EMC or the HAC section.

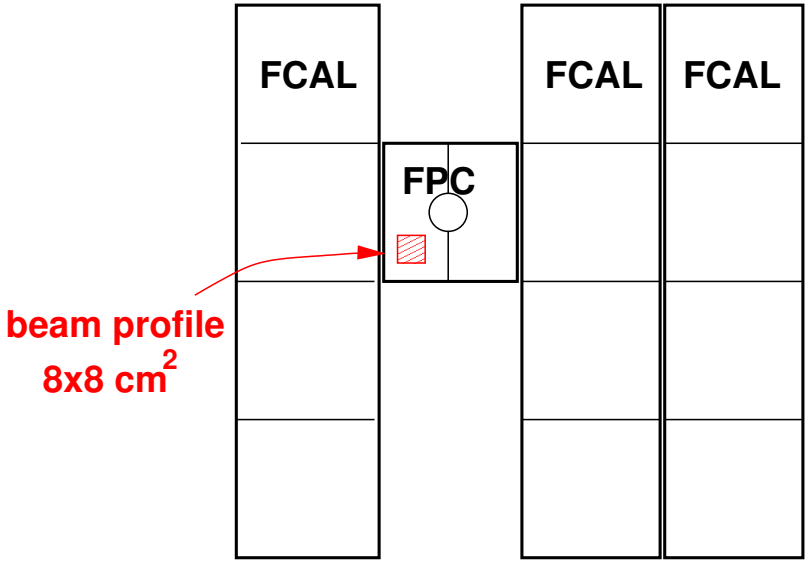

Figure 7.1: Front view of the FPC at the test beam site, surrounded by three FCAL modules.

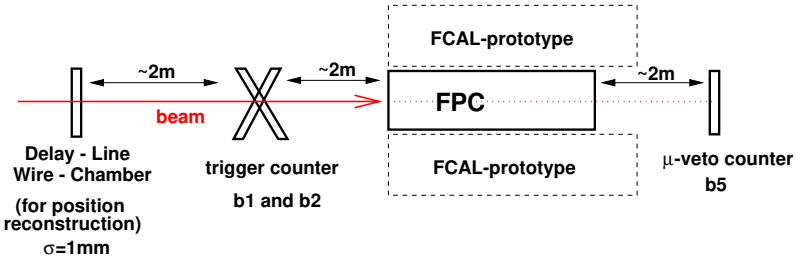

Figure 7.2: Sketch of the beam test set up.

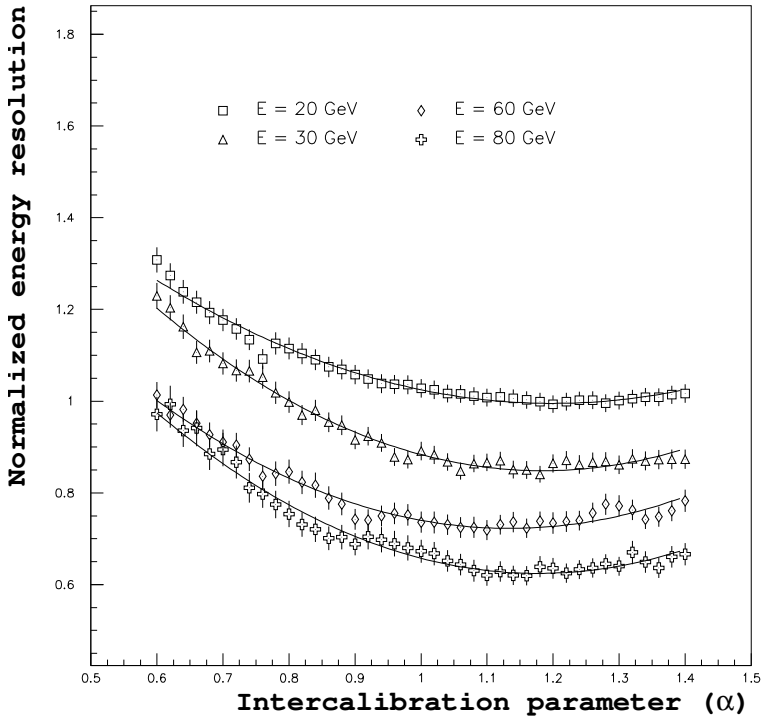

Figure 7.3: Pion energy resolution for different values of the intercalibration parameter α. Resolution is normalized to an arbitrary reference value.

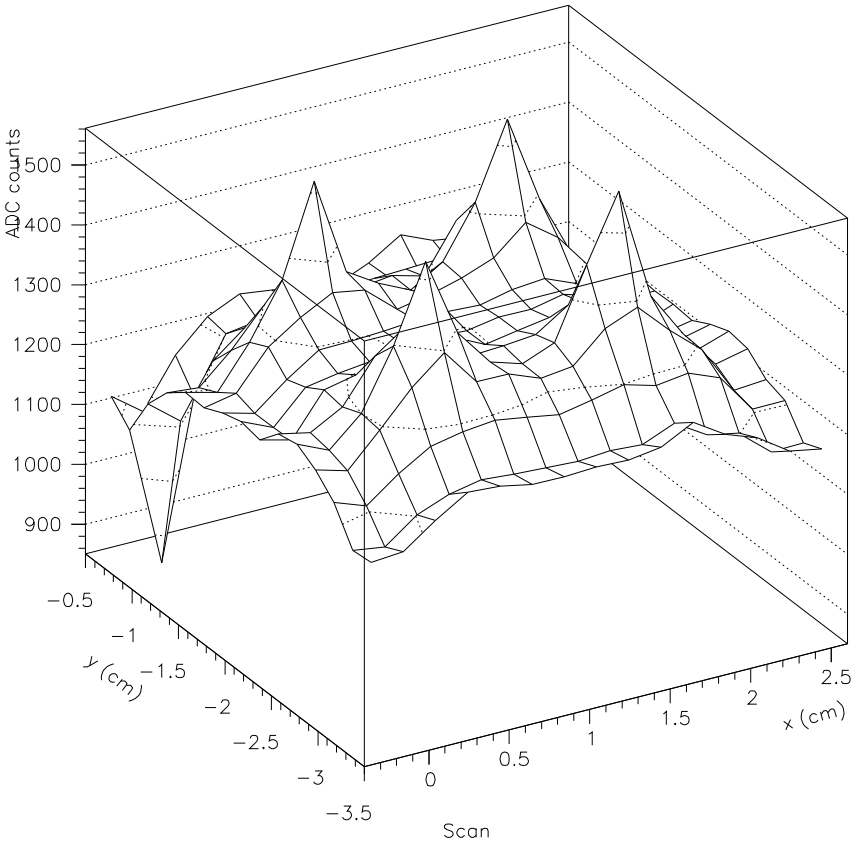

Figure 7.4: Energy signal cartography of an electromagnetic cell, done with $3\,GeV$ electrons.

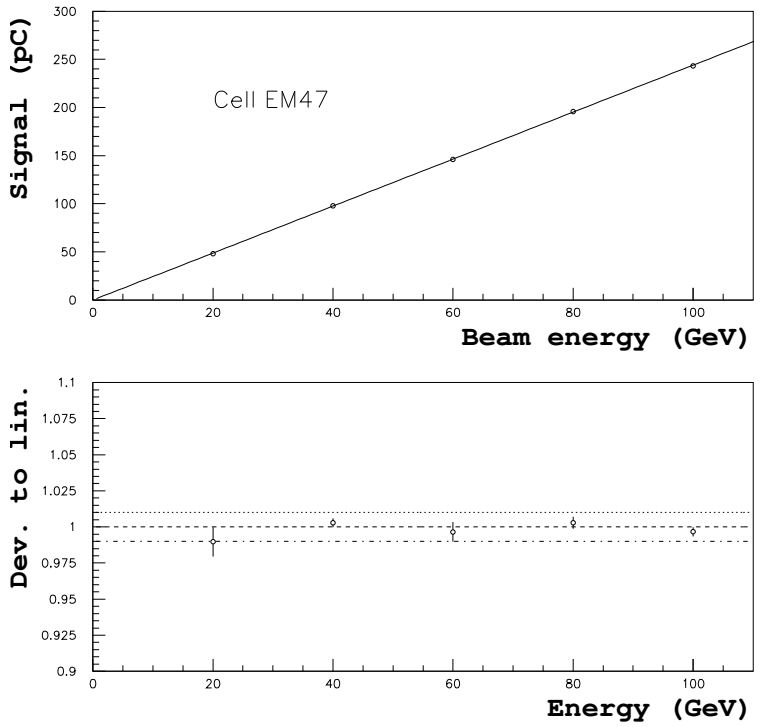

Figure 7.5: Linearity plot for a typical EMC cell.

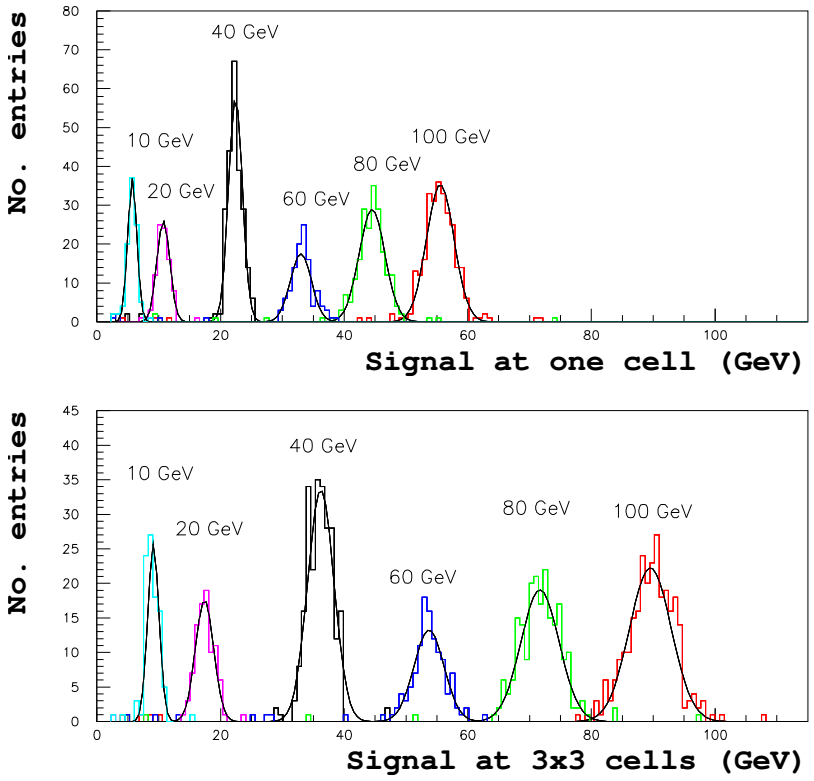

Figure 7.6: Electron energy signals measured in the central cell (upper) and in the 3×3 cluster (lower). The electrons entered the center of the central cell, covering a $0.8 \times 0.8\,cm^2$ square.

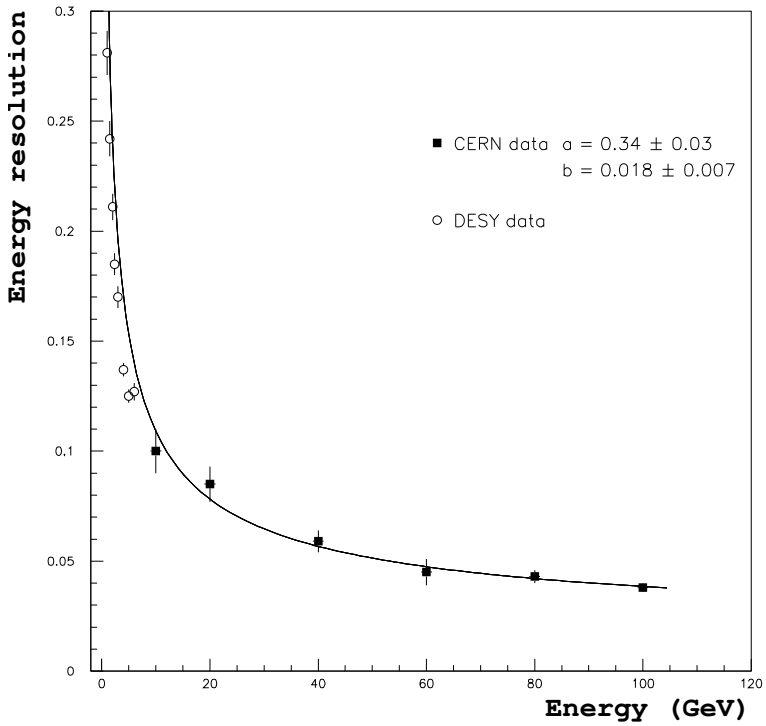

Figure 7.7: Electron energy resolution for a 3×3 cell cluster. Fit done only with CERN data. DESY data shown for comparison. The electrons entered the center of the central cell, covering a $0.8 \times 0.8\,cm^2$ square.

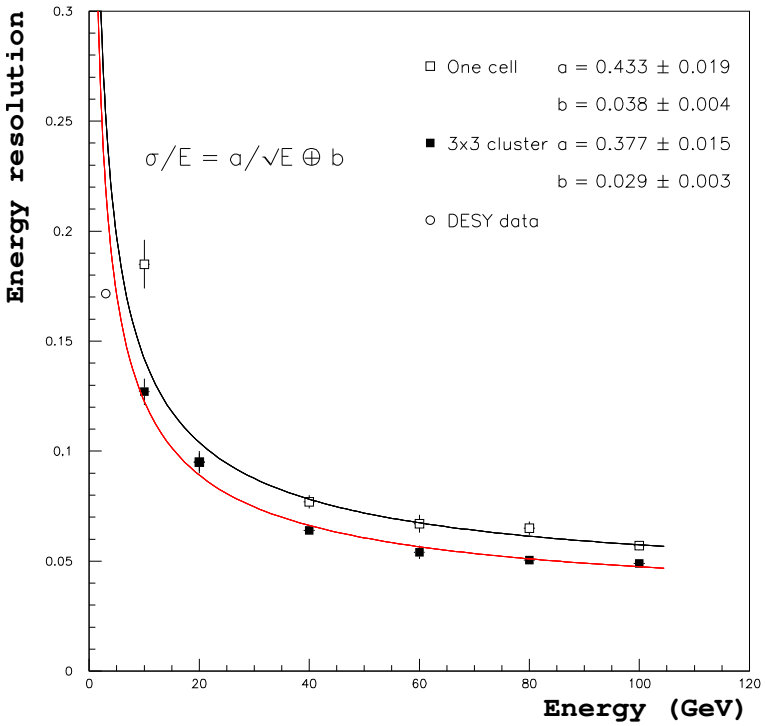

Figure 7.8: Electron energy resolution for the central cell, for a 3×3 cluster and for the prototype (DESY data) using a 3×3 cluster. The electrons entered the center of the central cell, covering a $1.6 \times 1.6\,cm^2$ square.

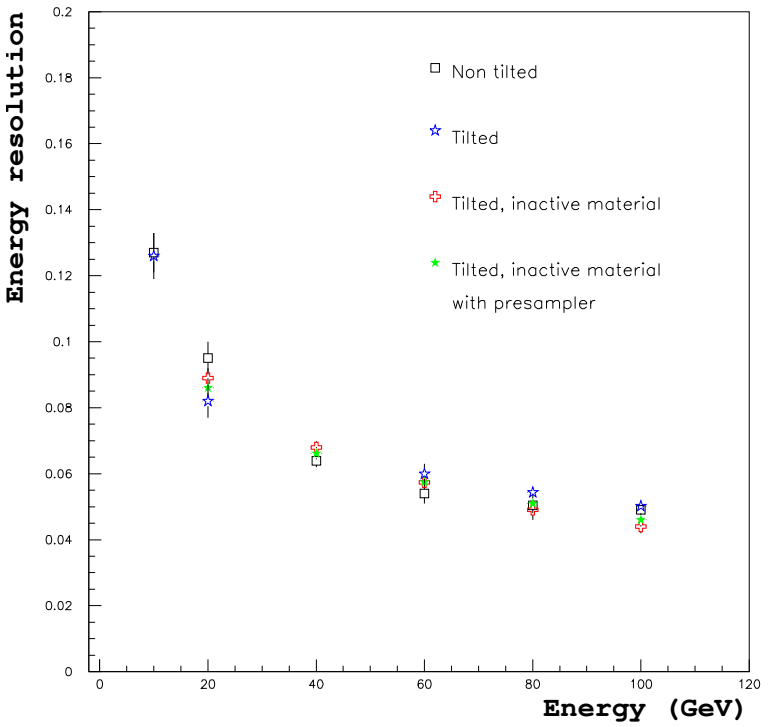

Figure 7.9: Energy resolution for electrons with a 3×3 cluster. The electrons entered the center of the central cell, covering a $1.6 \times 1.6\,cm^2$ square. Results for different setups.

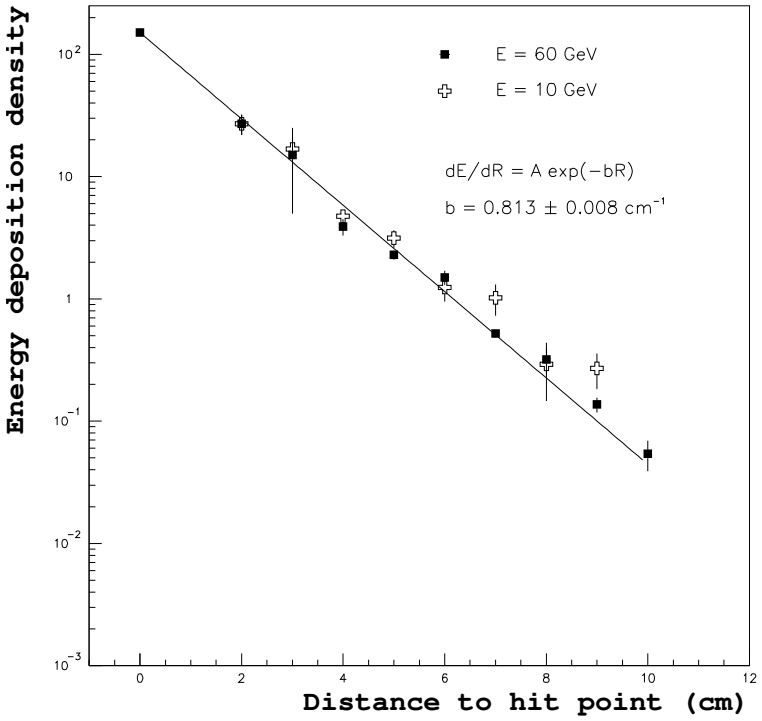

Figure 7.10: Shower energy deposition density (in arbitrary units) as a function of the distance from the impact point. Fit done with $60\,GeV$ data.

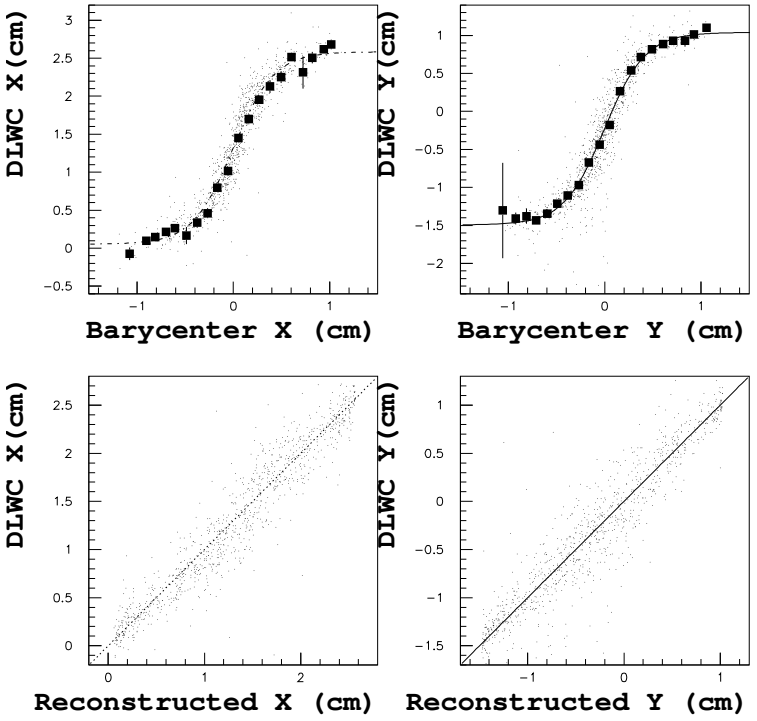

Figure 7.11: X and Y position reconstruction for $20\,GeV$ electrons before (upper) and after (lower) correcting for the S-shape

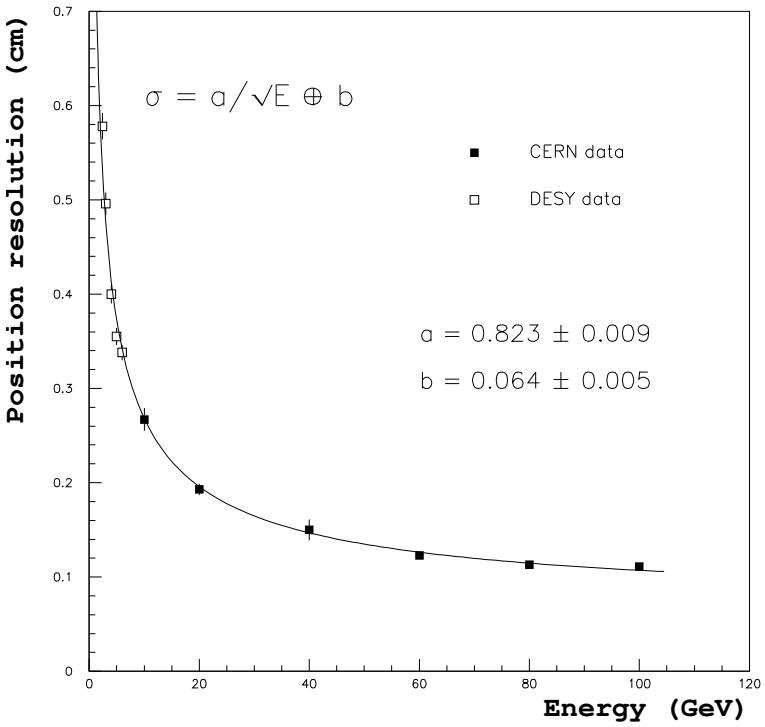

Figure 7.12: Energy dependence of position resolution.

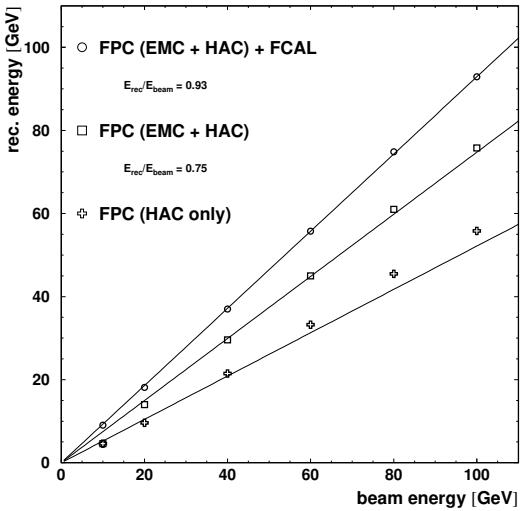

Figure 7.13: Total signal as a function of the pion beam energy for FPC + FCAL set up. Contributions from the different sections of the detectors are given.

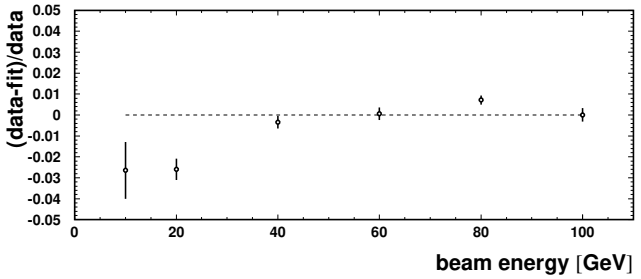

Figure 7.14: Deviations from linearity for the total FPC + FCAL signal.

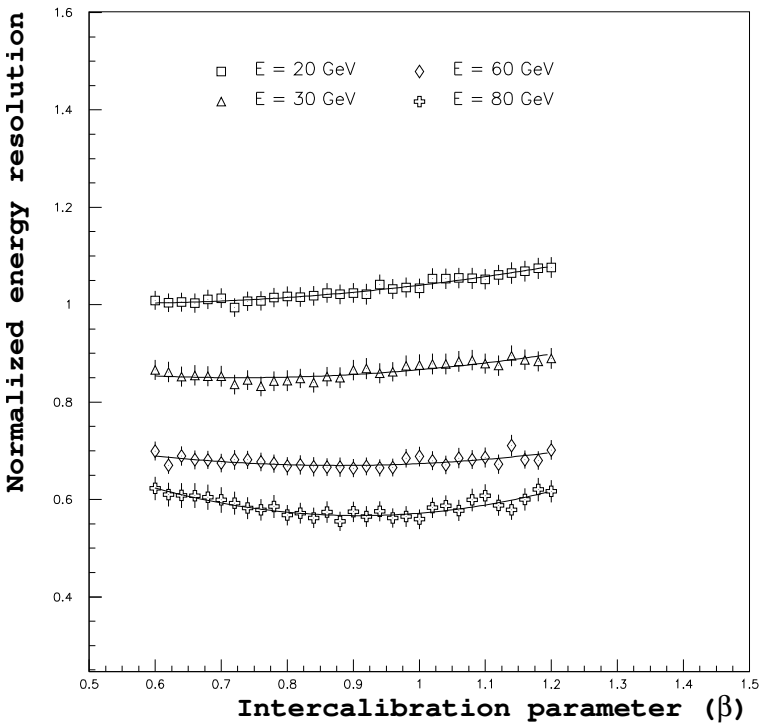

Figure 7.15: Normalized pion energy resolution adding up signals at FPC and FCAL, with different values of the intercalibration parameter β.

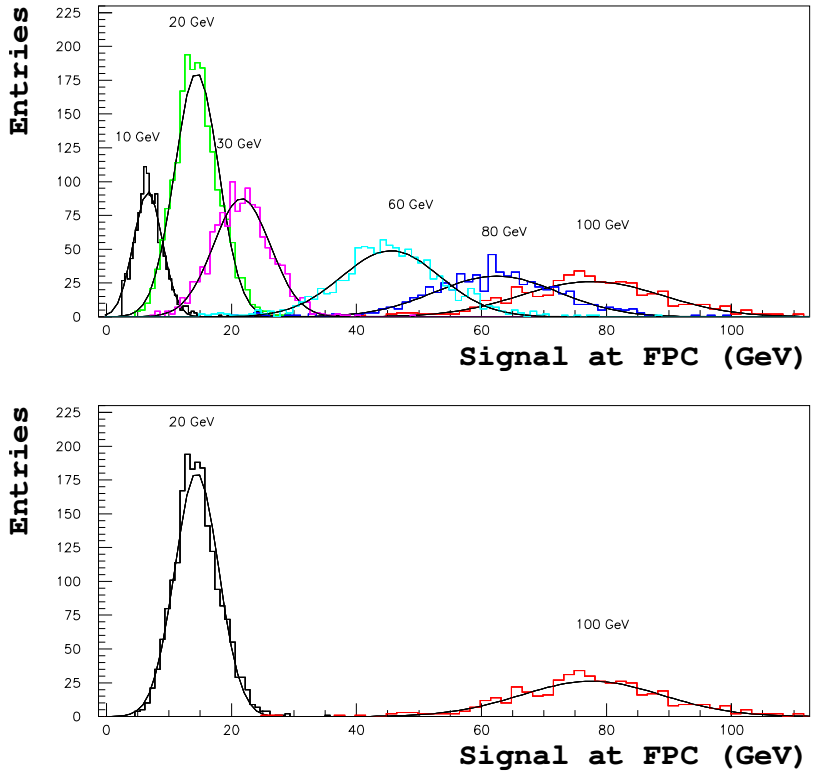

Figure 7.16: Pion signal observed in the FPC for pion energies of 10, 20, 30, 60, 80 and $100\,GeV$. The results for 20 and $100\,GeV$ are displayed again in the lower half of the figure.

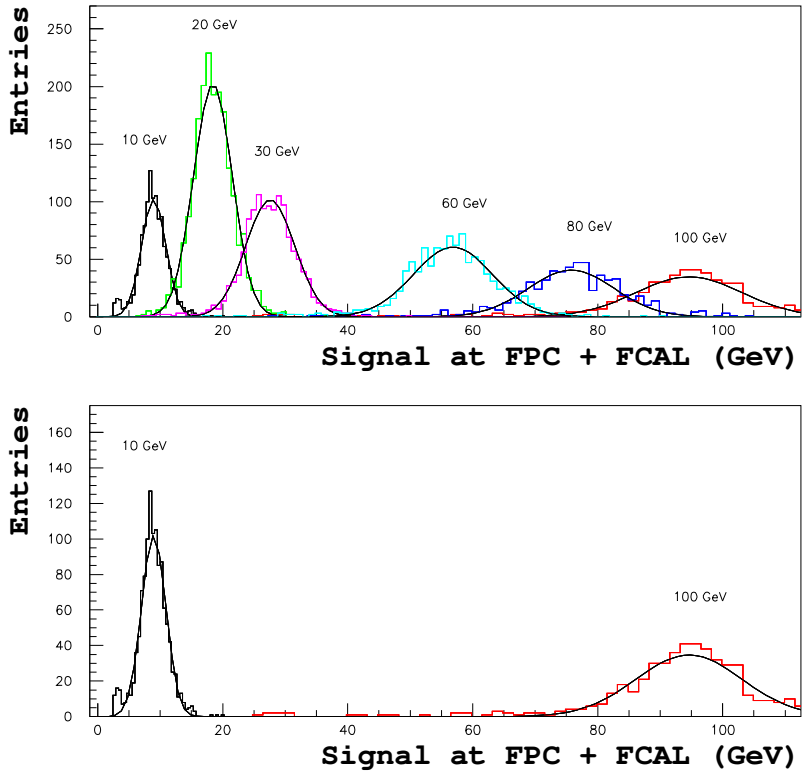

Figure 7.17: Pion signal observed in the FPC + FCAL for pion energies of 10, 20, 30, 60, 80 and 100 GeV. The results for 10 and 100 GeV are displayed again in the lower half of the figure.

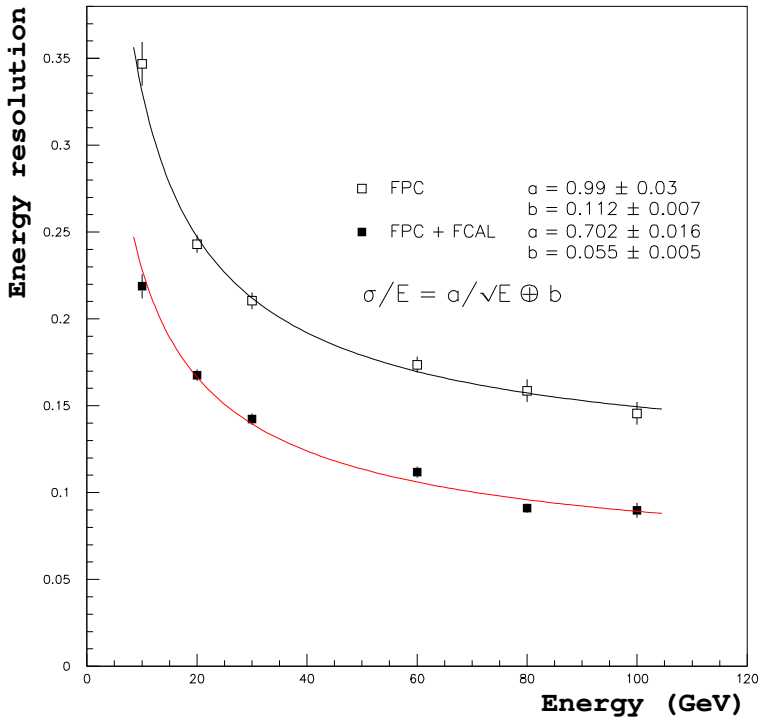

Figure 7.18: Pion energy resolution versus beam energy for the FPC and FPC + FCAL.

Chapter 8

Global comparison between the two calorimeters

We finalize this thesis by comparing the relevant features of the performance of the two calorimeters studied. The differences between the two devices are understood in terms of the principles of calorimetry explained in chapter 1.

8.1 Energy resolution for electromagnetic showers

The energy resolutions measured for electrons with the EMEC and the FPC are shown in table 8.1. The difference comes from the following sources:

- The constant term of $\sim 3\%$ for the FPC comes partly from non-uniformities due to the fiber read out scheme. The remaining difference from $\sim 2\%$ down to $\sim 0.5\%$

Detector	Sampling term (%)	Constant term (%)
ATLAS EMEC	9.2 ± 0.2	0.53 ± 0.04
ZEUS FPC (center cell)	34 ± 3	1.8 ± 0.7
ZEUS FPC (whole cell)	37.7 ± 1.7	2.9 ± 0.3

Table 8.1: Electron energy resolution for the ATLAS EMEC and the ZEUS FPC. For the latter, the resolution is shown separately for the detector region less affected by non-uniformities due to fibers.

comes from mechanical imperfections and reflects the enormous effort done by the ATLAS Collaboration on pushing the EMEC mechanics to the limit.

- The different thickness of the lead layers (see 1.2.2) induces an increase of the sampling term by a factor of 3 from the EMEC to the FPC. This would imply a sampling term at the level of 30% for the FPC. The remaining difference can be understood in terms of photostatistics fluctuations, present for the scintillator-WLS-PMT scheme, which does not have a counterpart in the LAr technique. These fluctuations were measured to be at the level of 15% for the FPC (see 7.3.3). The quadratic sum of the two contributions yields 33.5%, in good agreement with the observed sampling term for the FPC in the region less affected by the fibers.

8.2 Position resolution for electromagnetic showers

Let us suppose that we try to reconstruct position using only energy deposition in one detector cell. In this case, we would assign to each particle the coordinate of the center of the cell with maximum energy deposition. The resolution of the measurement would be of the order of the cell size, independently of any other considerations [1]. Let us now move to the usual situation in which position reconstruction is carried out by calculating an energy weighted barycenter of the positions of the cells in which the shower of a given particle has deposited energy. Provided we have cell sizes comparable to the transverse width of the shower, and using a cluster of a reasonable size for the position measurement, it is sensible to think that, working in cell size units, position resolution should depend mainly on the features of the electromagnetic shower. Therefore we can expect a certain universality to hold.

This interesting idea is not pushed forward in this thesis, but just used as a qualitative argument to justify the comparison of the position resolutions measured with the ATLAS EMEC and the ZEUS FPC. The results of the comparison can be seen in Fig 8.1. A few comments are in order:

- The data correspond to the FPC (measured at CERN), FPC prototype (measured at DESY), EMEC ϕ and η; in the latter case, with the front (η_1) and with the mid (η_2) detector section.
- All position resolutions are expressed in units of the cell size used for the reconstruction, except for η_1, which is expressed in mid section η cell units.

[1] To be more precise, considering a uniform probability density across the cell, the resolution would be $\Delta x = a/\sqrt{12}$, where a is the cell size.

- At high energy position resolution might be affected by the finite resolution of the beam chambers used in order to obtain the *true* position. This effect has not been evaluated.
- Among the EMEC data, the two ϕ position resolution points at 120 and 150 GeV are above the expected result due to beam chamber instabilities.
- Again in the EMEC, η_1 resolution is similar to η_2 because of the compensation of two effects going in opposite directions: energy containment and granularity. Therefore, for the purpose of this section, the agreement of the η_1 resolution with the rest of the data shall be regarded as a coincidence.

Taking into account the dramatic differences between the two types of data, the similarity of the results is extremely remarkable. A deeper discussion of the consequences and limitations of the comparison is out of the scope of this thesis.

8.3 Conclusion

Two different calorimeters have been built and tested with high energy particle beams. The ATLAS LAr accordion EMEC is an extremely abitious, very expensive and difficult to build, high precision electromagnetic calorimeter. Its energy resolution for electrons was measured to be

$$\frac{\sigma}{E} = \frac{9.2\%}{\sqrt{E}} \oplus 0.5\%$$

where E is in GeV. The ZEUS FPC is a simple and robust extension of the more sophisticated ZEUS UCAL, for electromagnetic and hadronic shower energy measurement, cheap and easy to build. Its energy resolution for electrons is

$$\frac{\sigma}{E} \simeq \frac{38\%}{\sqrt{E}} \oplus 3\%$$

The difference is understood in terms of the larger thickness of the FPC lead layers, the additional contribution from photostatistics fluctuations, the non-uniformities due to the fiber read out scheme and the mechanical imperfections.

The electron shower position resolution is, on the other hand, comparable for both detectors when expressed in cell units.

Both the FPC, successfully integrated in ZEUS since 1998, and the ATLAS EMEC, now moving into the phase of series production, have achieved their design performance goals.

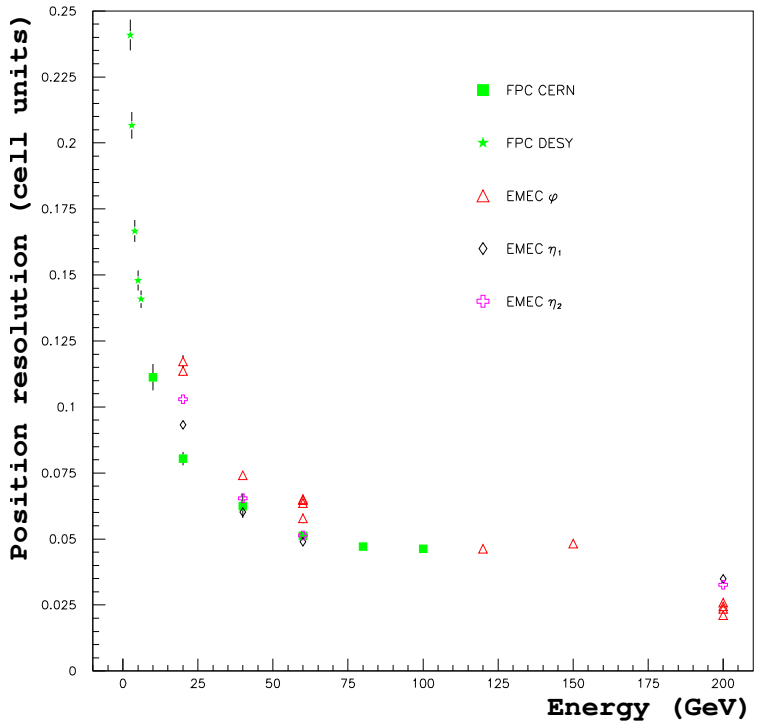

Figure 8.1: Position resolution measured in cell size units for the ZEUS FPC and ATLAS EMEC.

Acknowledgements

I am very grateful to my supervisor Luis Labarga. His scientific advise and human support have been essential for the fulfillment of this thesis. I am also grateful to the UAM group leader, Fernando Barreiro, for his support.

In different parts of the thesis I worked in close collaboration with different people of the Madrid group, that complemented the work of my supervisor. With Luis Hervás I learned a lot of mechanics and electronics. José del Peso taught me many things about computing and calorimetry, and guided me in my first beam tests. I had useful discussions with the rest of the people from the group. I must mention as well that much of my technical skill was learned from our technician Francisco Gallardo (Pachi).

Within the ZEUS collaboration, I am very indebted to all the people of the FPC group, very especially Günther Wolf, Matthias Kasemann, Yuji Yamazaki and Florian Goebel. We worked very hard together. In my last period at Hamburg I got a lot of help from Ignacio Redondo and especially Mario Martínez.

Within ATLAS, I am indebted in the first place to Daniel Fournier: over this period of almost four years he read my internal notes and listened to my talks (some of them very long !) at CERN. In ATLAS I had the chance to work with a number of people belonging to different groups. I am very grateful to all of them. I would like to mention explicitly Philippe Schwemling and the technicians from LPNHE (among them, my friend Philippe Laloux). I am also particularly grateful to Sylvain Tisserant and the CPPM group. I worked and learned a lot with all of them, particularly Pascal Pralavorio, Fares Djama, Dominique Sauvage (to whom I asked *a lot* of questions, that he always answered), Delphine Nicod and Chafik Benchouk. I really enjoyed working (and also not working) with them. I would also like to mention the names of other people from different groups whose help was important: Sascha Chekhtman, Stefan Simion, Jerome Schwindling and Michal Seman.

Bibliography

[1] ATLAS Collaboration, *ATLAS Technical Proposal*, CERN/LHCC 94-43.

[2] ZEUS Collaboration, *The ZEUS detector, Status Report 1993*; Editor Uwe Holm, February 1993.

[3] U. Amaldi, *"Fluctuations in Calorimetry Measurements", Physica Scripta*, Vol. 23 pp.409-424 (1981).

[4] C. Fabjan, *"Experimental techniques in High Energy Physics"*. CERN, Geneva, 1985. CERN-EP/85-84.

[5] L. Landau, J. Phys. USSR 8, 201 (1944).

[6] J. del Peso, E. Ros, NIM A 276 (1989) 456.

[7] C. Fabjan, *"Calorimetry in High Energy Physics", Techniques and Concepts of High Energy Physics-III, T. Ferbel, ed. Plenum Pub. Corp.*, 1985.

[8] R. Wigmans, NIM A 259 (1987) 389.

[9] T. A. Gabriel et al., NIM, A 134 (1976) 271.

[10] H. Brückmann, B. Anders, U. Behrens, *"Hadron Sampling Calorimetry - A Puzzle of Physics"* DESY, Hamburg, 1986. DESY 86-155.

[11] C. Fabjan et. al., NIM 141 (1977) 61-80.

[12] ZEUS Collaboration, E. Bernardi et al., NIM A 262 (1987) 229.

[13] ALEPH Collaboration, *"Search for neutral Higgs bosons in e^+e^- collisions at $\sqrt{s}$ up to 196 GeV"*, ALEPH 99-075, CONF 99-047.

[14] *ATLAS Letter of Intent for a General-Purpose pp Experiment at the Large Hadron Collider at CERN*, CERN/LHCC/92–4, LHCC/I2 (1992).

[15] ATLAS Collaboration, *ATLAS Calorimeter Performance Technical Design Report* , CERN/LHCC 96-40.

[16] ATLAS Collaboration, *ATLAS Liquid Argon Calorimeter Technical Design Report* , CERN/LHCC 96-41.

[17] P. Romero, *"On some aspects of the design and construction of the ATLAS electromagnetic end cap calorimeter"*, PhD thesis, Universidad Autónoma Madrid.

[18] Gastón García, *"Energy signal ϕ-modulation in the liquid argon electromagnetic calorimeter"*, ATLAS internal note LARG-NO-098.

[19] A. Cravero et al., NIM A 344 (1994) 39-46.

[20] A.M. Kalinin et al., *"Temperature and electric field strength dependence of electron drift velocity in liquid argon"*, ATLAS internal note LARG-NO-058.

[21] C. Scheel, *"Simulation Results comparing constant and variable thickness lead plates in the EMEC Calorimeter"* , ATLAS internal note CAL-NO-079.

[22] A. Dell'Acqua, *"DICE manual version 0.10*, ATLAS internal note SOFT-95-011.

[23] ATLAS offline software group, *"Draft ATLAS ATRECON manual (version 0.015)"*, ATLAS internal note SOFT-94-015.

[24] B. Canton et al. *"Analysis and results of the measurements of the plate thickness, done at the factory, during the production of the lead for the module-0 of the Barrel and End-Cap ATLAS electromagnetic calorimeters"*, ATLAS internal note LARG-NO-076.

[25] Gastón García, L. Hervás, *"Lead thickness control system for the ATLAS end cap production"*, ATLAS internal note LARG-NO-069.

[26] Gastón García et al., NIM A 418 (1998) 513-521.

[27] L. Labarga, P. Romero, *"Analysis of the quality control measurements performed on the absorbers produced for the module 0 of the ATLAS electromagnetic end cap calorimeter"*, ATLAS internal note LARG-99-004.

[28] Gastón García *"Lead absorber production for the end cap module-0"*, ATLAS internal note LARG-NO-074.

[29] M. Vázquez et al. *"Analisis of the thickness measurements on lead plates corresponding to the absorbers of modules 1 and 2"*, ATLAS internal note in preparation.

[30] Gastón García, *"Data analysis of the ATLAS EMEC module-0 calorimeter September 1998 beam test"*, ATLAS internal note ATL-LARG-99-017.

[31] J. F. de Trocóniz, C. Liapis, ATLAS LARG note in preparation.

[32] ZEUS Collaboration, *"A Forward Plug Calorimeter for the ZEUS Detector"*, ZEUS-Note 97-007, DESY-PRC-97-02.

[33] Gastón García et al.,*"The ZEUS Forward Plug Calorimeter with lead-scintillator plates and WLS-fiber read out"*, DESY 99-194, submitted to NIM.

[34] Gastón García et al., *"Data analysis of the ZEUS Forward Plug Calorimeter beam test at CERN"*, ZEUS-Note 2000-001.

[35] Gastón García et al., *"Test of a FPC prototype at DESY"*, ZEUS-Note 98-068.

[36] ZEUS Collaboration; M.Derrick et al., *Zeitschrift f. Physik* C65 (1995) 379-398.

[37] P.D.B. Collins, A.D. Martin, *Hadron Interactions*, Adam Hilger, 1964.

[38] ZEUS Collaboration, M. Derrick et al., *Phys. Lett.* B315 (1993) 481.

[39] G. Ingelman, P. Schlein, *Phys. Lett.* B152 (1985) 256.

[40] J. Vermaseren, F. Barreiro, L. Labarga, F. J. Yndurain, *Phys. Lett.* B418 (1998) 363.

[41] ZEUS Collaboration; J.Breitweg et al., *Phys. Lett.* B421 (1998) 368.

[42] ZEUS Collaboration; M. Derrick et al., *Z. Phys.* C70 (1996) 391.

[43] ZEUS Collaboration, M. Derrick et al., *Phys. Lett.* B332 (1994) 228.

[44] Gastón García for the ZEUS Coll., *"The Forward Plug Calorimeter of the ZEUS detector"*, in *Proceedings of the VIII International Conference on Calorimetry in High Energy Physics*, to be published by *World Scientific*.

[45] H. Fessler et al., NIM A 240 (1985) 284.

[46] L. Labarga, E. Ros, NIM A 249 (1986) 228.

[47] F.Barreiro, B.Loehr, E.Ros, S.Weissenrieder, NIM A 257 (1987) 145.

[48] Zeus Calorimeter Group (U. Behrens et al.), NIM A 289 (1990), 115.

[49] L. Hervás, *"The Pipelined Readout for the ZEUS Calorimeter"*, DESY R35D-91-01.

[50] T. Hasegawa et al., NIM A 311 (1992) 498.

[51] M. Gospic, H. Groenstege, *"A remote controlled high voltage supply system for photomultiplier tubes"*, ZEUS-Note 96-006.

List of Figures

2.1 View of the ATLAS detector. 37
2.2 View of the ATLAS calorimetry. 38
2.3 One half of the LAr calorimeter. 39
2.4 One half of the barrel cryostat. 40
2.5 Sketch of the accordion structure of the EM calorimeter. 41
2.6 End cap cryostat. 42
2.7 General view of the EMEC calorimeter, with a few absorbers to give an idea of the accordion structure. 43
2.8 EMEC calorimeter module. Each of the two EMECs consists of eight such modules. 44
2.9 EMEC outer wheel absorber. 45
2.10 EMEC inner wheel absorber. 45
2.11 Bending press for inner-wheel EMEC absorbers. 46
2.12 Cross section of a kapton electrode. 46
2.13 HV layer of an outer-wheel EMEC electrode (before bending). 47
2.14 HV layer of an inner-wheel EMEC electrode (before bending). 47

3.1 Various contributions to the energy resolution. Simulation done with photons of $E_T = 50\,GeV$. Figure taken from [15]. 57
3.2 ϕ-modulation effect before and after applying a multiplicative correction. . 58

3.3 Transverse energy signal distribution before and after correcting for ϕ-modulation. . . . 58

3.4 Energy signal ϕ-modulation at $\eta = 1.7$. $E_T = 200\,GeV$. . . . 59

3.5 Energy signal ϕ-modulation at $\eta = 1.8$. $E_T = 200,\, 80\,GeV$. . . . 59

3.6 Energy signal ϕ-modulation at $\eta = 1.9$. $E_T = 200\,GeV$. . . . 60

3.7 Energy signal ϕ-modulation at $\eta = 2.0$. $E_T = 200\,GeV$. . . . 60

3.8 Energy signal ϕ-modulation at $\eta = 2.1$. $E_T = 200\,GeV$. . . . 61

3.9 Energy signal ϕ-modulation at $\eta = 2.2$. $E_T = 200,\, 80\,GeV$. . . . 61

3.10 Energy signal ϕ-modulation at $\eta = 2.3$. $E_T = 200\,GeV$. . . . 62

3.11 Side view of the EMEC. The η coordinate is given for the most relevant features of the detector. . . . 63

3.12 η dependence of Fourier coefficients (EMEC outer wheel). $E_T = 200\,GeV$. . 64

3.13 Energy resolution at several η values before and after correcting for ϕ-modulation (EMEC outer wheel). $E_T = 200\,GeV$. . . . 64

3.14 ϕ position resolution as a function of energy in units of the spacing between consecutive absorbers. A mid section read out cell corresponds to 3 spacings. In order to read the resolution in cell units the numbers in the ordinate axis must be divided by 3. . . . 65

3.15 η dependence of Fourier coefficients at $80\,GeV$ (barrel). . . . 66

3.16 η dependence of Fourier coefficients at $200\,GeV$ (barrel). . . . 66

3.17 Improvement in energy resolution after correcting for ϕ-modulation (barrel). 67

3.18 Energy resolution improvement for $E_T = 80\,GeV$ photons at different η values, applying a correction optimized at that energy or at $200\,GeV$. . . . 67

3.19 Energy resolution improvement for $E_T = 50\,GeV$ photons at different η values, applying an energy independent ϕ-modulation correction and an energy dependent one. . . . 68

3.20 Energy signal ϕ-modulation at $\eta = 2.3$. $E_T = 200\,GeV$. Three different windows are compared. . . . 68

4.1 $z_{Pal} - z_k$ vs. z_k. Fit to a straight line ($v_k = 2.238 Km/s$). . . . 93

4.2 Stability of the thickness measurement versus time of operation at four different points of a plate. . . . 93

4.3 Distribution of measurement oscillations at the same point for six plate scans done the same day. . . . 94

4.4 Temperature dependence of the thickness measurement. Data taken at four different points. . . . 94

4.5 Absorber lead shape and lead plate coordinate system. . . . 95

4.6 Thickness map of two lead plates. . . . 95

4.7 Calibration control: difference between u-thickness and p-thickness for all plates. . . . 96

4.8 Calibration control: difference between u-thickness and p-thickness for plates classified by their nominal thickness. . . . 96

4.9 Calibration control: difference between u-thickness and p-thickness for $1.7\,mm$-thick plates measured by different operators. The upper left plot corresponds to the period during which no information about the person doing each individual measurement was kept. . . . 97

4.10 U-thickness mean and RMS of all small absorbers. . . . 98

4.11 U-thickness mean and RMS of all large absorbers. . . . 98

4.12 Correlations between u-thickness mean and RMS of all small (upper) and large (lower) absorbers. . . . 99

4.13 U-thickness measurements and maps of two small absorbers. . . . 100

4.14 U-thickness measurements and maps of two large absorbers. . . . 101

4.15 U-thickness RMS values of large absorbers classified by rolls (upper) and RMS and mean for roll 10 as a function of position on the roll. . . . 102

4.16 Thickness measured with ultrasounds (upper) and with X-rays (lower) for a large absorber. . . . 103

4.17 U-thickness, x-thickness and difference at the same point (with the smoothed ultrasound value). . . . 104

4.18 Mean thickness of absorbers: correlation between ultrasound and X-ray (left); difference between the two methods (right). Rolls 8 and 9. . . . 105

4.19 Mean thickness of absorbers: correlation between ultrasound and X-ray (left); difference between the two methods (right). Rolls 10 and 11. 106

4.20 Mean thickness of absorbers with low and high RMS (roll 10): correlation between ultrasound and X-ray (left); difference between the two methods (right). Roll 10. 107

4.21 All thicknesses measured with ultrasounds on large (upper) and small (lower) absorbers produced for module-0. 108

4.22 Histograms for the deviations w.r.t. nominal of the measured half-wave surface angle at eight different scan lines. Data from all the module-0 large absorbers are shown. RMS tolerances are given in radians. The lowest Y value is at the obtuse side of the absorber; the highest Y is at the acute side. 109

4.23 Stacking frame. 110

4.24 Vaccuum lifter. Notice the shape of the suckers, adapted to the absorber folds. 110

4.25 Stacking frame once closed after module assembly. A void can be seen in the place where the module should have been mounted. 111

4.26 Spatule. 111

5.1 Five samplings of two pulses in a mid section cell, for $60\,GeV$ electrons, before (upper) and after (lower) applying T_{tdc} time shift. 157

5.2 Pulse profiles obtained with a medium gain test pulse run, pulsing at all channels at the same time, with 25 delay steps of $1\,ns$. DAC value selected was 8400. 158

5.3 Pulse profiles obtained with a $150\,GeV$ electron run. The beam points at the region $\eta = 2.2$. Gain MMH. 159

5.4 Physics pulse profile in a mid section cell before and after spline smoothing. $E = 120\,GeV$. 160

5.5 Lower: Time of the pulse peak for mid section cells, as a function of the η cell number, for two test pulse runs (grey squares; green and red if color copy) and for a $60\,GeV$ electron run (number 100998), with the beam pointing at the region $\eta = 2.2$ and gain HHH. Energy dominant cells are marked with full (black) stars and non-dominant ones with open (blue) circles. Physics pulses are shown on the upper half. 161

5.6 Lower: Time of the pulse peak for mid section cells, as a function of the η cell number, for two test pulse runs (grey squares; green and red if color copy) and for a $60\,GeV$ electron run (number 100993), with the beam pointing at the region $\eta = 2.2$ and gain HHH. Energy dominant cells are marked with full (black) stars and non-dominant ones with open (blue) circles. Physics pulses are shown on the upper half. 162

5.7 Time of the pulse peak for mid section cells, as a function of the η cell number, for two test pulse runs (grey full squares; green and red if color copy) and for a $150\,GeV$ electron run (number 101209), with the beam pointing at the region $\eta = 2.2$ and gain MMH. Full (black) stars are used for channels with larger energy signal and open (blue) circles for channels with smaller signals. 163

5.8 Conversion factor from ADC to DAC counts from two test pulse runs (grey squares; green and red if color copy) as a function of the cell η number. Front $cell_{\eta_1} = 1 - 100$ channels are shown. 164

5.9 Signal seen at each detector section (S1 for front, S2 for mid, S3 for back) as a function of T_{tdc}. Run interval 100968-101005 (upper) and 101007-101210 (lower). 165

5.10 Energy resolution for different values of the weight α_1 applied to the front section in the addition of energy signals. Upper: electrons with $E = 120\,GeV$, gain MMH, $\eta = 2.2$. Lower: electrons with $E = 40\,GeV$, gain HHH, $\eta = 1.55$. 166

5.11 Pulses in the front section for a $60\,GeV$ run (number 100998) in the $\eta = 2.2$ region. Gain is HHH. Saturation is observed. 167

5.12 Reconstructed time (in arbitrary units) as a function of T_{tdc} for a run with few DAQ problems (top) and for one with many DAQ problems (bottom). 168

5.13 Total energy signal (normalized to the beam energy) as a function of T_{tdc} after first iteration correction has been applied to the signal at each detector section. Different beam energies are shown. Region $\eta = 2.2$. 169

5.14 Total energy signal as a function of ϕ for different beam energies. Region $\eta = 2.2$. 170

5.15 Dependence on ϕ of the energy signal at different energies for the region $\eta = 1.55$. 171

5.16 Dependence on ϕ (as given by the beam chamber) of the energy signal at different energies for the region $\eta = 2.9$. 172

5.17 Total energy signal as a function of the η barycenter (calculated with the front section) for different beam energies. Vertical lines indicate mid section cell boundaries. The point $\eta = 2.2$ corresponds to the abscissa $cell_{\eta_1} = 179.5$. 173

5.18 Dependence on η of the energy signal in the region $\eta = 1.55$ for different input beam energies. 174

5.19 Dependence on η (arbitrary units as given by beam chamber) of the energy signal in the region $\eta = 2.9$ for different input beam energies. 175

5.20 Events are represented as points in the (r_1, r_3) plane for different beam energies. Region $\eta = 2.2$. 176

5.21 Average total observed signal (normalized to the beam energy) as a function of (r_1, r_3). Three different grids are used. $E = 120\,GeV$. The distribution of events in the (r_1, r_3) plane is also shown as a reference. Region $\eta = 2.2$. . 177

5.22 Region $\eta = 1.55$. Distribution of events in the (r_1, r_3) plane for different beam energies. 178

5.23 Region $\eta = 1.55$. Average total observed signal as a function of (r_1, r_3). Three different grids are used. $E = 80\,GeV$. 179

5.24 Average total observed signal as a function of r_3 in the region $\eta = 2.9$ for different beam energies. 180

5.25 Parameter r_1 (top), r_3 (bottom) as a function of the ϕ cell number for different beam energies in the detector region $\eta = 2.2$. 181

5.26 Noise spectrum for a 6×4 window, region $\eta = 2.2$, gain HHH. 182

5.27 Energy signal reconstructed for different beam energies. Region $\eta = 2.2$. The spectra are fitted using gaussians. 183

5.28 Measured energy as a function of beam energy (upper) and fractional deviations from linearity (lower). Region $\eta = 2.2$. 184

5.29 Energy resolution as a function of the input beam energy. Region $\eta = 2.2$. Window 6×4. 185

5.30 Energy signal spectra for different beam energies. Region $\eta = 1.55$. 186

5.31 Linearity plot for the region $\eta = 1.55$. 187

5.32 Energy resolution as a function of the input beam energy. Region $\eta = 1.55$. Window 4×4. 188

5.33 Energy signal reconstructed for different beam energies. Region $\eta = 2.9$. The beam energies of the four histograms are: 40, 60, 80, 100 GeV. 189

5.34 Linearity plot for the region $\eta = 2.9$. 190

5.35 Energy resolution as a function of the input beam energy. Region $\eta = 2.9$. Window 4×1. 191

5.36 Coordinate ϕ provided by beam chamber 2 (arbitrary units) as a function of the reconstructed coordinate ϕ_{rec} (in mid section cell units), for a 120 GeV electron run. 192

5.37 ϕ position resolution (in cell units) for a 120 GeV electron run (left). $\overline{\phi_{rec}} - \phi_{bc}$ as a function of $\overline{\phi_{rec}}$ (right). 192

5.38 ϕ position resolution in cell units as a function of beam energy for particles from an electron beam injected in the region $\eta = 2.2$. 193

5.39 Coordinate η given by beam chamber 2 as a function of the barycenter reconstructed with the front section. $E = 60\,GeV$. 194

5.40 Difference between η barycenter reconstructed with the front section (η_{bar1}) and η_{bc}, as a function of η_{bar1}. $E = 200\,GeV$ (left), 20 GeV (right). 195

5.41 Difference between η barycenter reconstructed with the mid section (η_{bar2}) and η_{bc}, as a function of η_{bar2}. $E = 40\,GeV$. 195

5.42 Distribution of the difference between η_2 and η_{bc}. $E = 40\,GeV$. 196

5.43 η position resolution as a function of beam energy with the front and with the mid section. 197

5.44 Energy signal spectra for different voltage values applied to the read out electrodes. 198

5.45 Energy signal as a function of the voltage applied to the read out electrodes (upper). Energy resolution obtained for the different voltage settings (lower). 199

5.46 Reconstructed time (in arbitrary units) as a function of T_{tdc} for: a) A 60 GeV electron run, prior to run 101006; b) A 120 GeV electron run, after run 101006. 200

5.47 Reconstructed time (in arbitrary units) as a function of T_{tdc} for two different runs. 201

5.48 Error in time reconstruction as a function of the energy measured in the cell. Single events (dots) and bin averages (stars) are shown (upper). Distribution of the error (lower). A mid section cell is used. $E = 120\,GeV$. Time variables are in ns. 202

5.49 Energy resolution at $150\,GeV$, region $\eta = 2.2$, for different collimator apertures. 203

6.1 The ZEUS detector at HERA. The FPC can be seen at the beam hole across the FCAL. 220

6.2 View of the FPC. The read out cells and the position of WLS fibers are shown. Notice that there is one HAC read out cell behind each group of 2×2 EMC ones, except in the 4 innermost hadronic cells. 221

6.3 Side view of the FPC. 221

7.1 Front view of the FPC at the test beam site, surrounded by three FCAL modules. 238

7.2 Sketch of the beam test set up. 238

7.3 Pion energy resolution for different values of the intercalibration parameter α. Resolution is normalized to an arbitrary reference value. 239

7.4 Energy signal cartography of an electromagnetic cell, done with $3\,GeV$ electrons. 240

7.5 Linearity plot for a typical EMC cell. 241

7.6 Electron energy signals measured in the central cell (upper) and in the 3×3 cluster (lower). The electrons entered the center of the central cell, covering a $0.8 \times 0.8\,cm^2$ square. 242

7.7 Electron energy resolution for a 3×3 cell cluster. Fit done only with CERN data. DESY data shown for comparison. The electrons entered the center of the central cell, covering a $0.8 \times 0.8\,cm^2$ square. 243

7.8 Electron energy resolution for the central cell, for a 3×3 cluster and for the prototype (DESY data) using a 3×3 cluster. The electrons entered the center of the central cell, covering a $1.6 \times 1.6\,cm^2$ square. 244

7.9 Energy resolution for electrons with a 3×3 cluster. The electrons entered the center of the central cell, covering a $1.6 \times 1.6\,cm^2$ square. Results for different setups. 245

7.10 Shower energy deposition density (in arbitrary units) as a function of the distance from the impact point. Fit done with $60\,GeV$ data. 246

7.11 X and Y position reconstruction for $20\,GeV$ electrons before (upper) and after (lower) correcting for the S-shape 247

7.12 Energy dependence of position resolution. 248

7.13 Total signal as a function of the pion beam energy for FPC + FCAL set up. Contributions from the different sections of the detectors are given. . . 249

7.14 Deviations from linearity for the total FPC + FCAL signal. 249

7.15 Normalized pion energy resolution adding up signals at FPC and FCAL, with different values of the intercalibration parameter β. 250

7.16 Pion signal observed in the FPC for pion energies of 10, 20, 30, 60, 80 and $100\,GeV$. The results for 20 and $100\,GeV$ are displayed again in the lower half of the figure. 251

7.17 Pion signal observed in the FPC + FCAL for pion energies of 10, 20, 30, 60, 80 and $100\,GeV$. The results for 10 and $100\,GeV$ are displayed again in the lower half of the figure. 252

7.18 Pion energy resolution versus beam energy for the FPC and FPC + FCAL. 253

8.1 Position resolution measured in cell size units for the ZEUS FPC and ATLAS EMEC. 259

List of Tables

5.1 List of HV problems in the detector regions that were tested. 116

5.2 t_{max} prescription for all the runs. 123

5.3 Optimal value of α_1 for the region $\eta = 2.2$. 126

5.4 Optimal value of the weights α_1 and α_3^{12} for the region $\eta = 1.55$ in the MMH gain configuration. 127

5.5 Optimal value of α_1 for the region $\eta = 1.55$ in the HHH gain configuration. 127

5.6 Global calibration factor for the region $\eta = 2.2$. 128

5.7 Global calibration factor for the region $\eta = 1.55$. 129

5.8 Noise measurement for different detector regions and gain configurations. . 138

5.9 Noise measurement and sampling and constant term of the energy resolution (after noise subtraction) for two different window sizes. 139

5.10 Resolution in the ϕ position measurement for different runs. 146

6.1 Summary of FPC parameters. 217

7.1 Value of α_{min} for several beam energies. 226

7.2 Electron energy resolution for different data sets. 229

7.3 Energy signal containment for electron showers in EMC section cell clusters of different sizes. 230

7.4 Values obtained for the parameters entering the position reconstruction correction for different beam energies. 232

7.5 Optimal value of the parameter β for different beam energies. 234

8.1 Electron energy resolution for the ATLAS EMEC and the ZEUS FPC. For the latter, the resolution is shown separately for the detector region less affected by non-uniformities due to fibers. 255